Version 2.0
July 1997

Near Infrared Camera and Multi-Object Spectrometer Instrument Handbook

SPACE
TELESCOPE
SCIENCE
INSTITUTE

STScI
3700 San Martin Drive
Baltimore, Maryland 21218

User Support

For prompt answers to any question, please contact the Science Support Division Help Desk.

- **E-mail:** help@stsci.edu
- **Phone:** (410) 338-1082
          (800) 544-8125 (U.S., toll free)

World Wide Web

Information and other resources are available on the NICMOS World Wide Web page:

- **URL:** http://www.stsci.edu/ftp/instrument_news/NICMOS/topnicmos.html

NICMOS Instrument Team

Name	Title	Phone	e-mail
Bill Sparks	Group Lead	(410) 338-4843	sparks@stsci.edu
David J. Axon	Instrument Scientist	(410) 338-4892	axon@stsci.edu
Daniela Calzetti	Instrument Scientist	(410) 338-4518	calzetti@stsci.edu
Luis Colina	Instrument Scientist	(410) 338-5086	colina@stsci.edu
John W. MacKenty	Instrument Scientist	(410) 338-4559	mackenty@stsci.edu
Keith Noll	Instrument Scientist	(410) 338-1828	noll@stsci.edu
Al Schultz	Instrument Scientist	(410) 338-5044	schultz@stsci.edu
Chris Skinner	Instrument Scientist	(410) 338-5057	skinner@stsci.edu
Alex Storrs	Instrument Scientist	(410) 338-4903	storrs@stsci.edu
Anatoly Suchkov	Instrument Scientist	(410) 338-4979	suchkov@stsci.edu
L. Eddie Bergeron	Data Analyst	(410) 338-1018	bergeron@stsci.edu
Doris Daou	Data Analyst	(410) 338-4485	daou@stsci.edu
Diane Gilmore	Data Analyst	(410) 338-4947	dgilmore@stsci.edu
Sherie Holfeltz	Data Analyst	(410) 338-4418	holfeltz@stsci.edu
Christine Ritchie	Data Analyst	(410) 338-5042	ritchie@stsci.edu

Revision History

Version	Date	Editors
1.0	June 1996	D.J. Axon, D. Calzetti, J.W. MacKenty, C. Skinner
2.0	July 1997	J.W. MacKenty, C. Skinner, D. Calzetti, and D.J. Axon

Acknowledgements

Citation

In publications, refer to this document as:

MacKenty, J.W.. et al., 1997, "NICMOS Instrument Handbook", Version 2.0, (Baltimore: STScI).

Table of Contents

CHAPTER 6 Exposure Time Calculations 89

CHAPTER 7 NICMOS Detectors 105

CHAPTER 8 Detector Readout
Modes 119

CHAPTER 9 Overheads and Orbit Time
Determination 133

CHAPTER 10 Techniques for Dithering, Background Measurement and Mosaicing

CHAPTER 11 Imaging Reference Material

xi   Contents

PART 1

Introduction

The chapters in this part explain how to use this handbook, where to go for help, and describe special considerations for using NICMOS in Cycle 7.

CHAPTER 1

Introduction

The Near Infrared Camera and Multi-Object Spectrometer, NICMOS, is a second-generation instrument installed on the Hubble Space Telescope during the Second Servicing Mission in February 1997. NICMOS provides HST with infrared imaging and spectroscopic capabilities between 0.8 and 2.5 microns. From above the earth's atmosphere, NICMOS provides access to this complete spectral range without hindrance from atmospheric emission or absorption at a sensitivity and angular resolution not possible from the ground.

This Handbook provides the instrument specific information you need to propose HST observations (Phase 1), design accepted proposals (Phase 11), and understand NICMOS in detail. It has been revised to include the results of the on-orbit checkout program (SMOV) available as of July 7, 1997.

This chapter explains the layout of the Handbook and how to get additional help and information through the Help Desk and STScI World Wide Web pages.

Purpose

The *NICMOS Instrument Handbook* is the basic reference manual for the Near Infrared Camera and Multi-Object Spectrometer and describes the instrument's properties, expected performance, operations, and calibration. The Handbook is maintained by scientists at STScI. Dr. R.I. Thompson, the Principal Investigator for NICMOS, and scientific staff at Steward Observatory and Ball Aerospace kindly provided information and test data in support of this Handbook.

We designed the document to serve three purposes:

- To provide instrument-specific information for preparing Cycle 7 and Cycle 7-NICMOS observing proposals with NICMOS.

- To provide instrument-specific information to support the design of Phase II proposals for accepted NICMOS proposals (in conjunction with the Phase II Proposal Instructions).

- To provide technical information about the operation and performance of the instrument, which can help in understanding problems and interpreting data acquired with NICMOS.

This Handbook is not meant to serve as a manual for the reduction and analysis of data taken with NICMOS. Late in 1997, we will publish an addition to the *HST Data Handbook* describing how to work with NICMOS data.

A significant change from the first version of the *NICMOS Instrument Handbook* is that the fundamental source of photometric performance is now the NICMOS Exposure Time Calculator (ETC) available on the World Wide Web (see Chapter 6).

Document Conventions

This document follows the usual STScI convention in which terms, words, and phrases which are to be entered by the user in a literal way on a form are shown in a typewriter font (e.g., `BRIGHT-RETURN`, `PP-SPLIT`). Names of software packages or commands (e.g., **synphot**) are given in bold type.

Wavelength units in this Handbook are in microns (µm) and fluxes are mainly given in Janskys (Jy).

Layout

NICMOS has a variety of imaging modes. The instrument provides direct imaging in broad, medium, and narrow-band filters at a range of spatial resolutions in the near infrared from 0.8 to 2.5 microns, together with broad-band imaging polarimetry, coronographic imaging and maskless grism spectroscopy. To guide you through NICMOS's capabilities and help optimize your scientific use of the instrument we have divided this Handbook into four parts: Part I - Introduction; Part II - Users's Guide; Part III - Supporting Material; and Part IV - Calibration. Figure 1.1 provides a roadmap to navigating the document; following the roadmap is a list of chapters and their contents.

Figure 1.1: Roadmap for Using the NICMOS Instrument Handbook

```
┌──────────┐        🚚        ┌──────────────────────┐
│  Start   │  ────────────▶  │   Review Special     │
│          │                 │ Cycle 7-NICMOS Issues│
└──────────┘                 └──────────────────────┘
 Chapter 1                              Chapter 2
                                        │
                                        ▼
                     ┌──────────────────────┐ ◀---▶ ┌──────────────────┐
                     │ Obtain Overview of   │        │  Information on   │
                     │ NICMOS Capabilities  │        │ NICMOS Detectors │
                     │    and Operation     │        └──────────────────┘
                     └──────────────────────┘                 Chapter 7
                         Chapter 3
            ┌────────────────┴────────────────┐
            ▼                                  ▼
  ┌──────────────────┐            ┌──────────────────────┐
  │ Select Imaging & │            │ Select Coronography, │
  │ Estimate Exposure│            │ Polarimetry, or      │
  │      Times       │            │ Grisms & Estimate    │
  └──────────────────┘            │   Exposure Times     │
      Chapter 4, 11               └──────────────────────┘
            │                            Chapter 5
            └──────────────┬─────────────┘
                           │
                           │        ┌──────────────────────┐
                           ◀---▶    │  Detailed Exposure   │
                           │        │ Time Calculations?   │
                           │        └──────────────────────┘
  ┌──────────────────────┐ │                  Chapter 6
  │ Using NICMOS to      │◀│                  ⇕
  │ Measure Backgrounds  │ │        ┌──────────────────────┐
  │ or Make Maps?        │ │        │ Additional Reference │
  └──────────────────────┘ │        │      Material        │
       Chapter 10          │        └──────────────────────┘
                           │                Chapter 11, 12
                           ▼
                 ┌──────────────────┐
                 │ Select Data-Taking│
                 │      Mode        │
                 └──────────────────┘
                      Chapter 8
                           │        ┌──────────────────────┐
                           ◀---▶    │  Information on       │
                           │        │ NICMOS Calibrations   │
                           │        └──────────────────────┘
                           │              Chapters 13, 14, 15
                           ▼
  ┌──────────┐  🚚  ┌──────────────────────┐
  │  Finish  │◀──── │ Determine Overheads  │
  │          │      │ and Calculate Phase 1│
  └──────────┘      │ Orbit Time Request   │
                    └──────────────────────┘
                            Chapter 9
```

The chapters of this Handbook are as follows:

Part I - Introduction

- Chapter 1, *Introduction* on page 3.

- Chapter 2, *Special Considerations for Cycle 7–NICMOS* on page 11, describes special considerations for the use of NICMOS during Cycle 7-NICMOS.

Part II - Users Guide

- Chapter 3, *Overview of NICMOS* on page 19, provides an introduction to the full capabilities of NICMOS. A discussion is provided to help guide you through the technical details you will need to consider in choosing the optimum NICMOS configuration and in determining the number of orbits to request.

- Chapter 4, *Imaging* on page 39, provides a description of NICMOS's imaging capabilities including camera resolutions and throughputs.

- Chapter 5, *Coronography, Polarimetry and Grism Spectroscopy* on page 67, provides detailed information on coronographic imaging, grism spectroscopy, and polarimetry.

- Chapter 6, *Exposure Time Calculations* on page 89, describes how to perform signal to noise calculations, either by using pencil and paper, or using software tools that are provided on the World Wide Web (WWW).

- Chapter 7, *NICMOS Detectors* on page 105, describes the basic properties of the detectors used in the three cameras including their physical characteristics, capabilities and limitations.

- Chapter 8, *Detector Readout Modes* on page 119 explains the data taking modes which take advantage of the non-destructive readout capabilities of the NICMOS arrays. While nearly all observers will choose to use MULTI-ACCUM mode, we give advice the observer should consider in choosing the most appropriate mode.

- Chapter 9, *Overheads and Orbit Time Determination* on page 133, provides information to convert from a series of planned science exposures to an estimate of the number of orbits, including spacecraft and NICMOS overheads. This chapter applies principally to the planning of Phase 1 proposals.

Part III - Supporting Material

- Chapter 10, *Techniques for Dithering, Background Measurement and Mosaicing* on page 145, gives a guide to measuring the sky background when observing with NICMOS. This chapter describes the implementation of a pre-defined set of patterns which accomplish dithering and chopping from the field of interest, and allow easy generation of large mosaic images.

- Chapter 11, *Imaging Reference Material* on page 161, provides summary information and filter transmission curves for each imaging filter, ordered by camera and increasing wavelength.

- Chapter 12, *Flux Units and Line Lists* on page 209, provides formulae and tables for the conversion of flux units, and a list of common infrared spectral lines.

Part IV - Calibration

- Chapter 13, *Calibration Pipeline* on page 231, briefly describes the processing of NICMOS data by the STScI pipeline and the data that will be sent to observers.

- Chapter 14, *Expected Calibration Accuracies* on page 243 summarizes the accuracies expected for NICMOS data calibrated by the STScI pipeline during Cycle 7-NICMOS.

- Chapter 15, *Calibration Plans* on page 245, provides a summary of the status and results from the Servicing Mission Observatory Verification (SMOV) and an overview of the Cycle 7 calibration plan.

NICMOS Proposal Preparation

Use the *NICMOS Instrument Handbook* and the *Cycle 7-NICMOS Call for Proposals & Phase I Proposal Instructions* (CP) when assembling your NICMOS Phase I Proposal. The CP provides policy and instructions for proposing; the *NICMOS Instrument Handbook* contains technical information about NICMOS, describing its expected performance, and presenting suggestions for use. The next chapter in the Handbook describes special considerations for Cycle 7-NICMOS.

If your Phase I proposal is accepted, you will be asked to submit a Phase II proposal in which you specify the exact configurations, exposure times and sequences of observations that NICMOS and the telescope should perform. To assemble your Phase II proposal, you should use the *NICMOS Instrument Handbook* in conjunction with the *Phase II Proposal Instructions*. These instructions describe the rules and syntax that apply to the planning and scheduling of NICMOS observations and provide relevant observatory information.

▽ At this time, predictions of the performance of NICMOS should be treated as provisional, and users should adopt conservative expectations for the performance of the instrument in Cycle 7-NICMOS. See Chapter 2 for a detailed discussion of issues which are unresolved as this is written.

The Help Desk at STScI

STScI maintains a Help Desk. The Help Desk staff at STScI quickly provide answers to any HST-related topic, including questions regarding NICMOS and the Cycle 7 proposal process. The Help Desk staff has access to all of the resources available at the Institute, and they maintain a database of answers so that frequently asked questions can be immediately answered. The Help Desk staff also provide STScI documentation, in either hardcopy or electronic form, including instrument science reports, instrument handbooks, and the like. Questions sent to the Help Desk during normal business hours are answered within one hour. Questions received outside normal business hours will be answered the next business day. Usually, the Help Desk staff will reply with the answer to a question, but occasionally they will need more time to investigate the answer. In these cases, they will reply with an estimate of the time needed to supply a full answer.

We ask that you please send all initial inquiries to the Help Desk. If your question requires a NICMOS Instrument Scientist to answer it, the Help Desk staff will put a NICMOS Instrument Scientist in contact with you. By sending your request to the Help Desk, you are guaranteed that someone will provide you with a timely response.

To contact the Help Desk at STScI:

- **Send e-mail (preferred method)**: help@stsci.edu
- **Phone**: 1-410-338-1082

The Space Telescope European Coordinating Facility (ST-ECF) also maintains a help desk. European users should generally contact the ST-ECF for help: all other users should contact STScI. To contact the ST-ECF Help Desk:

- **Send e-mail**: stdesk@eso.org

The NICMOS Instrument Team at STScI

STScI maintains a team of Instrument Scientists, Scientific Programmers, and Data Analysts who support the development, operation and calibration of NICMOS. The team is also responsible for supporting NICMOS users. The table inside the front cover of this Handbook lists the current members of the NICMOS Instrument Team at STScI.

Supporting Information and the NICMOS Web Site

The NICMOS Instrument Team at STScI maintains a World Wide Web page, as part of the STScI home page. The URL for the STScI NICMOS page is:

`http://www.stsci.edu/ftp/instrument_news/NICMOS/topnicmos.html`

The STScI NICMOS web page includes:

- **Advisories**: This is where we will post updates to instrument performance as these are produced through ground testing and on-orbit investigations.

- **Documentation**: An electronic version of this Handbook will be maintained on the WWW site. In addition, more detailed technical information (not needed to propose for Cycle 7) concerning the development, performance, ground testing, operation and calibration of NICMOS itself are found in a series of NICMOS instrument science and calibration reports maintained on the web, while others can be obtained upon request from the Help Desk.

- **User Support**: Will contain general information on data reduction and support for HST users.

- **Software**: Some software can be retrieved or run directly over the web, including an exposure time calculator, and a flux units conversion program.

- **Frequently Asked Questions**: A list of frequently asked questions about NICMOS, and their answers, ranging from proposal preparation to data analysis.

CHAPTER 2

Special Considerations for Cycle 7–NICMOS

HST's second servicing mission successfully installed two second-generation instruments, NICMOS and STIS (the Space Telescope Imaging Spectrograph) while removing the Faint Object Spectrograph (FOS) and Goddard High Resolution Spectrograph (GHRS). In addition, a Fine Guidance Sensor (FGS) was replaced and a solid state data recorder installed. The increased data capacity of the new recorder, exploited through a series of changes to the ground system, considerably increases the capacity of HST to handle large volumes of data.

While NICMOS has demonstrated its capability for excellent scientific observations, problems within its cryogenic cooling system resulted in some degradation of the Camera 3 capability and a significantly shortened life expectancy. As discussed in the Cycle 7-NICMOS call for proposals (CP), this special CP is being issued to maximize the scientific return from NICMOS within its predicted lifetime. To solicit, select, and prepare proposals within the timescale necessary to accelerate the NICMOS science program, this Handbook is being prepared before the Servicing Mission Observatory Verification (SMOV) period is completed and its results fully analyzed. Thus, this Handbook represents a snapshot of our current but evolving understanding of NICMOS. While observers should rely upon this Handbook (except where noted) when preparing proposals for Cycle 7-NICMOS, they are advised to seek updated information when preparing Phase II proposals and analyzing NICMOS observations.

NICMOS is a New Instrument

While planning your Cycle 7-NICMOS observations, keep in mind that NICMOS is a *new capability*, as well as a new instrument for HST. The sensitivities, brightness limits, and optical performance contained in this Handbook are based on our initial calibration and test observations (and in many instances also rely upon ground-based tests). *You should rely upon the WWW based Exposure Time Calculator (ETC) for the best available estimates of NICMOS performance, as these may still change.*

HST's performance as an infrared telescope is now significantly better characterized than it was prior to the installation of NICMOS. The level of thermal emission from the telescope is considerably lower than was predicted in the previous version of this Handbook (see Chapter 3).

As NICMOS is experiencing difficulties with both cryogen lifetime and Camera 3 focus, observers should pay careful attention to its status, the limitations imposed by this situation, and the resulting policies which have been adopted to maximize its scientific return.

Information Updates for Cycle 7-NICMOS

Updates with new results from SMOV will be posted to the STScI NICMOS WWW site (see "Supporting Information and the NICMOS Web Site" on page 9) as soon as they become available. Additional updates, applicable only to *accepted* Cycle 7-NICMOS proposals, will be provided prior to Phase II Submission as required.

Because the SMOV testing of the coronograph is underway as this Handbook is being completed, a summary of the coronograph performance will be posted on the STScI NICMOS WWW site on August 1, 1997.

▽ Your Cycle 7-NICMOS HST proposal must be based on the Exposure Time Calculator (ETC) predictions of NICMOS performance. The ETC is accessible from the STScI NICMOS WWW site and has been updated to reflect the on-orbit performance of NICMOS.

NICMOS Status Summary

Early on-orbit tests of NICMOS revealed dynamic changes to its characteristics and performance. On-orbit expansion of the solid nitrogen in the dewar (used to cool the detectors) has deformed the dewar leading to a thermal contact between the instrument cold well (which contains the three detectors inside the solid nitrogen dewar) and the inner vapor-cooled shield and also causing changes in focus for all three NICMOS cameras. The expected lifetime of the NICMOS cryogen has been significantly reduced as a result. Best estimates are that, if the current rate of cryogen loss continues, NICMOS will remain operational until late 1998 or early 1999. If the thermal contact breaks and the cryogen loss rate is consequently decreased, that time could be longer. NICMOS camera 3 (NIC3) has suffered the largest performance loss. Cameras 1 and 2 (NIC1, NIC2) are performing well and can meet most observational requirements. Based on our best estimates of the current situation, we are working from the following set of assumptions:

- *Lifetime:*

  - The useful lifetime of NICMOS will be reduced; we are planning for NICMOS observations to end by about November 1998.

- *Focus Issues:*

  - Image quality in NIC1 and NIC2 is excellent. Both cameras are, however, very slightly vignetted.

  - The best focus positions for NIC1 and NIC2 are different, but the image quality of NIC1 at NIC2's focus or NIC2 at NIC1's focus is only marginally degraded.

  - NIC3 cannot currently be brought into focus using the internal NICMOS focus mechanism. The image quality is very poor when either NIC1 or NIC2 are in focus as the prime camera. NIC3 is vignetted over approximately 25% of the detector (although this vignetting may be reduced as a result of ongoing experiments with the internal optical alignment of the NICMOS optics).

  - NIC3 may return to focus as cryogen is depleted, but when and if this will occur is difficult to predict. NIC3 can be placed into focus by adjusting the OTA focus mechanism although other instruments would then be (temporarily) out of focus.

  - The spectral resolution and sensitivity of the grisms are seriously degraded for point sources when NIC3 is out of focus. For extended sources the loss of performance is less severe.

- *Thermal Background:*

  - Thermal backgrounds are much lower than estimated in Version 1.0 of the *NICMOS Instrument Handbook* (see Chapter 3).

- *Coronograph:*

  - The coronograph performance in NIC2 is slightly degraded as the coronographic hole is no longer confocal with the detector (a compromise focus is presently being explored and results should be available on the WWW by August 1, 1997).
  - The position of the coronographic hole is changing with time. A flight software modification is being developed in time for Cycle 7-NICMOS which will locate the hole prior to a coronographic acquisition with minimal overhead cost.

- *Detector Issues:*

  - A small percentage of pixels in each camera have reduced throughput, probably from debris on the detectors. The pattern of affected pixels is time variable and therefore difficult to fully calibrate.
  - The bias level exhibits enhanced signal after periods of non-use which presently cannot be fully calibrated out. Excess signal levels of ~10 DN are not uncommon. Laboratory testing is ongoing to validate an improved detector operation method which may reduce or eliminate this effect.

Recommendation Summary

We give here a summary of general recommendations. However, observers are strongly advised to read the technical sections that follow and develop an optimal observation strategy based on the demands of their individual scientific goals.

- Proposers should attempt to use NIC1 or NIC2 if their scientific objectives can be met. Proposals which require NIC3 (e.g., for its field of view or spectroscopic capabilities) should recognize the scheduling limitation which campaigns may impose.

- Proposers should weigh the use of the grisms in NIC3 against using narrow band filters in NIC2 or NIC1 to meet their science goals.

- Proposers should dither observations that could be adversely affected by bad pixels.

- Proposers should eliminate restrictive scheduling requirements (e.g., ORIENT) wherever possible to decrease the chance that their program will fail to be scheduled before the NICMOS cryogen supply is exhausted.

Supported NICMOS Capabilities for Cycle 7-NICMOS

As was done for both NICMOS and STIS for Cycle 7, we have established a set of core scientific capabilities of NICMOS which will be supported for Cycle 7-NICMOS science. These capabilities cover an enormous range of science applications. In practice, the supported capabilities will be phased in during Cycle 7, as our understanding of the instrument and on-orbit performance grows. This phasing will optimize the likelihood that observations are successfully executed and assure that the requisite calibration observations are obtained.

NICMOS has additional capabilities that are not supported for Cycle 7-NICMOS. These capabilities are "available" in the form of *Engineering-only* modes, upon consultation with a NICMOS Instrument Scientist. If you find that your science *cannot* be performed with the capabilities described in this handbook, you may wish to consider an unsupported capability. The use of these capabilities requires approval from STScI and support for calibration may be limited or non-existent.

Supported capabilities include:

- NIC1, NIC2 observations in any filter or polarizer.

- NIC3 observations in campaign mode (i.e., in-focus NIC3 observations).

- MULTIACCUM and ACCUM detector readout modes (but see Chapter 8 for a discussion of the problems that can be faced when using ACCUM mode).

  - The defined MULTIACCUM SAMP-SEQ exposure time sequences,
  - A subset of the ACCUM exposure times as defined in Chapter 8.
  - ACCUM NREAD=1 or 9 values only.

- Coronographic observations including on-board target acquisitions.

Unsupported ("available") capabilities include:

- The Field Offset Mirror (FOM).

- BRIGHTOBJ readout mode. The calibration and linearity of this mode is problematic.

- The RAMP readout mode. This detector readout mode is similar to a limited version of the MULTIACCUM mode with the processing carried out within the NICMOS instrument computer and only the final processed image downlinked.

- Any non-standard ACCUM exposure time or any MULTIACCUM exposure times not incorporated in one of the standard sequences of exposures (SAMP-SEQ). ACCUM with NREAD other than 1 or 9.

Use of unsupported modes comes at a price, and these modes should be used only if the need and scientific justification are particularly compelling. Proposers should be aware of the following caveats in the use of unsupported modes:

- Calibrations for unsupported capabilities will not be provided by STScI. Observers must either determine that they can create calibration files from data in the HST Archive or they must obtain calibrations as part of their observations. The STScI pipeline will not calibrate data taken in unsupported modes but will deliver uncalibrated FITS files (or in some cases partially calibrated FITS files) to the observer and the HST Archive.

- STScI adopts a policy of *shared risk* with the observer for the use of unsupported capabilities. Requests to repeat failed observations taken using unsupported capabilities will not be honored if the failure is related to the use of the unsupported capability.

- User support from STScI for the reduction and analysis of data taken using unsupported capabilities will be limited and provided at a low priority. Users taking data with unsupported capabilities should be prepared to shoulder the increased burden of calibration, reduction, and analysis of these data.

Cycle 7-NICMOS proposals which include use of unsupported NICMOS capabilities must include a justification of why the science cannot be done with a supported configuration, must include a request for any observing time needed to perform calibrations, must justify the added risk of using an unsupported mode in terms of the science payback, and must include a demonstration that the observers are able to shoulder the increased burden of calibration, reduction, and analysis of their data.

PART 2

User's Guide

The chapters in this part describe the basics of observing with NICMOS. Included are: a description of the instrument layout and basic operation; the imaging and spectroscopic capabilities of NICMOS; exposure time calculations; the performance and limitations of its detectors; and overhead and orbit request determination.

CHAPTER 3
Overview of NICMOS

In this Chapter we provide an overview of the basic properties and capabilities of NICMOS. We describe the optical and mechanical layout and the basic operation of the instrument. For those not familiar with IR array technology we compare the characteristics of these detectors with CCDs. In the final section in this chapter, we present a flowchart and a discussion to help you design a technically feasible and scientifically optimized NICMOS observing proposal.

Instrument Capabilities

NICMOS, the Near Infrared Camera and Multi-Object Spectrometer, is an HST axial instrument, containing three cameras designed for simultaneous operation. The NICMOS optics present the detectors with three adjacent but not spatially contiguous fields-of-view of different image scales. The instrument covers the wavelength range from 0.8 to 2.5 microns, and contains a variety of filters, grisms, and polarizers. Each camera carries a complement of 19 optical elements, selected through independent filter wheel mechanisms, one per camera.

The basic capabilities of the instrument, and the chapters which discuss them are:

- *IR imaging*: NICMOS provides its highest sensitivity from 1.1 to ~2 microns, where it is superior to that achievable on an 8m class telescope, and better sensitivity than the WFPC2 for all observations for wavelengths longward of 0.9 microns. Chapter 4 discusses the overall throughput of NICMOS and the optical elements available in each camera. The low back-

ground will allow deep photometry. Our estimates of limiting sensitivities per pixel to give a 5 σ detection in a 60 minute integration are given in Table 3.1.

Table 3.1: Limiting Sensitivities per Pixel in Janskys for 5 σ Detection in 60 Minutes (assumes point source centered on pixel)

Camera	Filter			
	F110W	F140W	F160W	F240M
bandwidth (microns)	0.8 to 1.35	0.8 to 1.8	1.4 to 1.8	2.3 to 2.5
NIC1	2.4×10^{-7} (J~23.9)	2.3×10^{-7} (J~24.6)	5.5×10^{-7} (H~23.1)	—
NIC2	8.5×10^{-8} (J~25.1)	—	1.8×10^{-7} (H~24.3)	5.2×10^{-6} (K~20.1)
NIC3	6.5×10^{-8} (J~25.3)	—	7.8×10^{-8} (H~25.2)	2.8×10^{-6} (K~20.7)

- *Grism Spectroscopy*: Camera 3, NIC3, has three grisms which provide a multi-object spectroscopic capability with a resolving power of R ~200 over the full field of view of the camera. Their wavelength ranges are 0.8 to 1.2 microns, 1.1 to 1.9 microns, and 1.4 to 2.5 microns. Because the grisms are slitless, the spectra of spatially resolved objects are confused and multiple objects can overlap.

- *Imaging Polarimetry*: Three polarizing filters with pass directions of 0, 120, and 240 degrees are provided for the wavebands 0.8–1.2 microns in Camera 1, NIC1, and 1.9–2.1 microns in Camera 2, NIC2.

- *Coronography*: A 0.3 arcsec radius occulting spot and cold mask, in the intermediate resolution Camera 2, NIC2, provides a coronographic imaging capability.

Chapter 5 discusses these three special capabilities.

Instrument Design

Physical Layout

NICMOS is an axial bay instrument which replaced the FOS in the HST aft shroud during the Second HST Servicing Mission in February 1997. Its enclosure contains four major elements: a graphite epoxy bench, the dewar, the fore-optics bench, and the electronics boxes. The large bench serves to establish the alignment and dimensional stability between the HST optics (via the latches or fittings), the room temperature fore optics bench, and the cryogenic optics and detectors mounted inside the dewar. The NICMOS dewar uses solid nitrogen as a

cryogen for a design lifetime of approximately +5 +/- 0.5 years. Cold gas vented from the dewar is used to cool the vapor cooled shield (VCS) which provides a cold environment for both the dewar and the transmissive optical elements (i.e., the filters, polarizers, and grisms). The VCS is itself enclosed within two layers of thermal electrically cooled shells (TECs).

Figure 3.1 is an overview of the NICMOS instrument; Figure 3.2 shows details of the dewar.

Figure 3.1: Instrument Overview

Figure 3.2: Solid Nitrogen Dewar
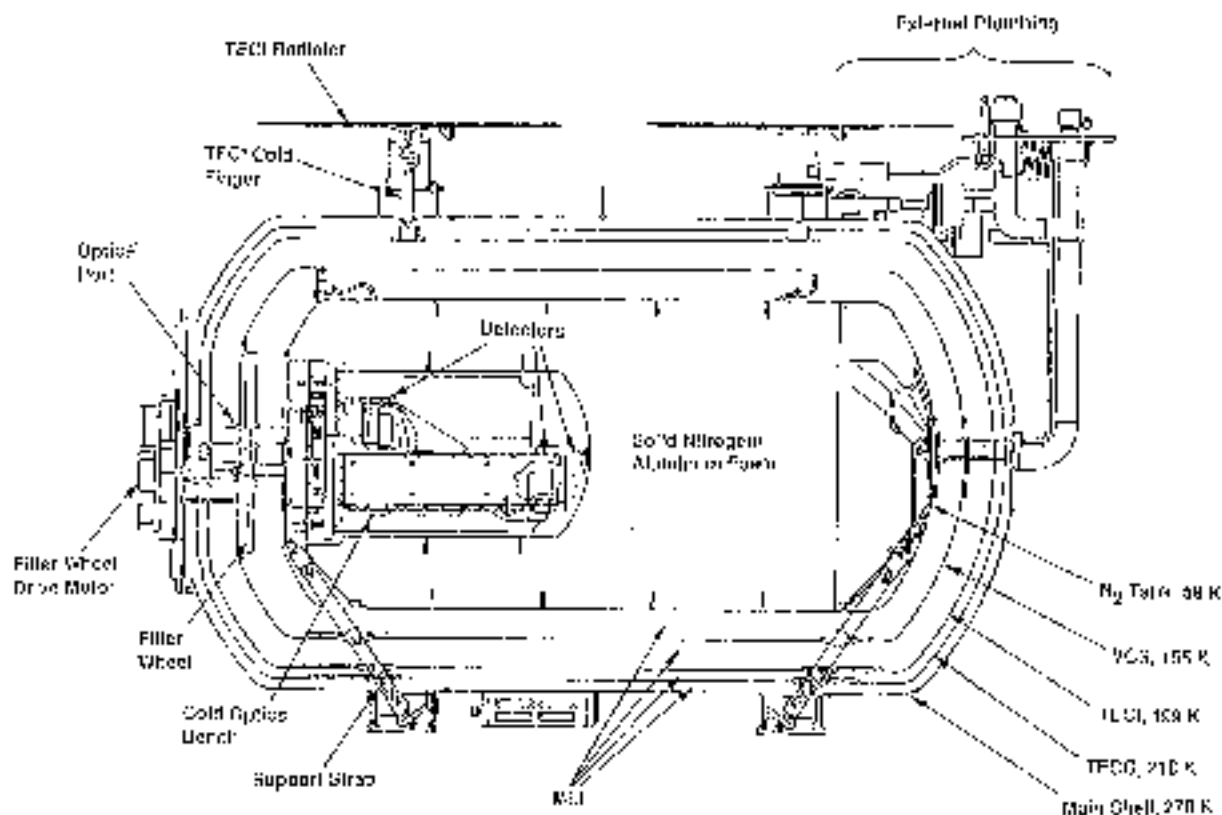
Dewar Anomaly

The NICMOS dewar was filled with about 240 pounds of liquid nitrogen which was then solidified (in stages) by passing cold helium gas through a coil located at the aft end (the fore end has the "A" latch and the entrance aperture). This reduced the temperature of the nitrogen to about 40K. During testing and storage, the block of solid nitrogen increased in temperature as expected (from passive heat inputs). To avoid reaching the triple point (at ~63K) the block was recooled approximately every 6-8 weeks using the helium cooling coil. After several iterations of this procedure, it was observed that the focal position of the detectors was moving both with the change in temperature and over the thermal cycles. It became clear that solid nitrogen with aluminum foam (a 1% by volume material included to assure good thermal conductivity as the nitrogen sublimated on orbit), was both structurally quite strong and that the recooling cycle was resulting in cryopumping at the aft (colder) end of the dewar. That is, nitrogen vapor, evaporating from the "warm" fore end of the nitrogen block, froze onto the cooling coil at the aft end. This reduced the vapor pressure at the aft end, pumping more vapor to this end, and prompting more evaporation at the fore end. This process pumped nitrogen from the fore end to the aft end. As the dewar was allowed to warm up, the ice at the aft end pushed in the interior surfaces of the

dewar, expanding it. By mid-1996 the three cameras in NICMOS were no-longer confocal although there were good reasons to expect that they would return to a nearly confocal state after a fraction of the nitrogen had evaporated on orbit. At that time a total deformation of ~4 mm had been observed and steps were taken to both assure that the dewar remained flightworthy and that subsequent recooling cycles did not stretch the dewar further. Also, the internal optical alignment and focus mechanism (the Pupil Alignment Mechanism—PAM) was replaced with a version permitting twice the focus range and a demonstrated capability for frequent movement. The PAM, originally intended to align the input beam onto the corrective optic and to bring NICMOS into confocality with the WFPC2 (the only HST instrument without an internal focus mechanism), would be used to support unique focus setting for each NICMOS camera and to switch between them routinely.

After NICMOS was installed in HST, the dewar expanded considerably further than it had on the ground for reasons still not understood. A maximum motion of ~11 mm was observed in March 1997 and a slow contraction since then has occurred. The motion history of NICMOS and the resulting image quality are discussed in Chapter 4.

This unexpectedly large deformation has several undesirable effects:

- The NIC3 camera's focus has moved outside of the focus range of the PAM. While it is presently moving back toward being within the focus range, the rate of motion is slow and unpredictable. The present extrapolation would result in an acceptable focus becoming available in late 1997.

- The three cameras now have significantly different foci, hence parallel observations are degraded (although the difference between the NIC1 and NIC2 foci is sufficiently small that an intermediate focus yields good quality images in both cameras).

- Due to the off-axis optical design, the relative positions of the fields of view change with the position of the PAM mirror as it is moved to adjust the focus. This increases the calibration burden somewhat.

- Lateral motion of the detectors relative to the field divider assembly (located outside the dewar) has resulted in a slight (~20 rows) vignetting in all three cameras.

- NIC3 has an additional vignetting which effects ~25% of its field of view. It is presently expected that adjustment of the FOM mirror will reduce or remove this vignetting, and an experiment is being implemented to test this.

- Lateral motion of the detectors in the focal plane results in a variable position for the coronographic hole in NIC2. New flight software is being developed to rapidly locate this hole as part of the target acquisition process. This software should be available for Cycle 7-NICMOS.

- Finally, the motion of the inner shell of the dewar was sufficiently large that it made physical contact with the vapor cooled shield. This resulted in a thermal short which increased the heat flux into the inner shell (and there-

fore the solid nitrogen) by a factor of 2.5 and has thereby reduced the expected lifetime of NICMOS from 4.5 to < 2 years. The expected and present thermal states of NICMOS are shown in Table 3.2.

Table 3.2: Dewar Thermal State (° K)

	Expected	Present
Cold Well	58	60
VCS	155	101
TEC1	199	190
TEC0	218	217
Dewar Shell	270	270

Imaging Layout

The NICMOS fore-optics assembly is designed to correct the spherically aberrated HST input beam. As shown in the left hand panel of Figure 3.3 it comprises a number of distinct elements. The Pupil Alignment Mechanism/mirror (PAM) directs light from the telescope onto a re-imaging mirror, which focuses an image of the OTA pupil onto an internal Field-Offset Mechanism (FOM) comprising a pupil mirror that provides a small offset capability (26 arcsec). An internal flat field source is also provided. The FOM provides correction for conic error in the OTA pupil.

After the FOM, the Field Divider Assembly provides three separate but closely-spaced imaging fields, one for each camera (right hand panel of Figure 3.3). The dewar itself contains a series of cold masks to eliminate stray IR emission from peripheral warm surfaces.

A series of relay mirrors generate different focal lengths and magnifications for the three cameras, each of which contains a dedicated 256 x 256 pixel HgCdTe detector array that is developed from the NICMOS 3 design. NICMOS achieves diffraction limited performance in the high resolution Camera 1, NIC1, longward of 1.0 microns, and in Camera 2, NIC2, longward of 1.75 microns.

The operation of each camera is separate from the others which means that filters, integration times, readout times and readout modes can be different in each, even when two or three are used simultaneously. The basic imaging properties of each of the cameras is summarized in Table 3.3.

Camera 1

Camera 1 (NIC1) provides the highest available spatial resolution with an 11 x 11 arcsec field of view and 43 milliarcsec sized pixels (equivalent to the WFPC2 PC pixel scale). The filter complement includes broad and medium band

Figure 3.3: Ray Diagrams of the NICMOS Optical Train. The left panel shows the fore-optics. The right panel shows the field divider and re-imaging optics for the three cameras.
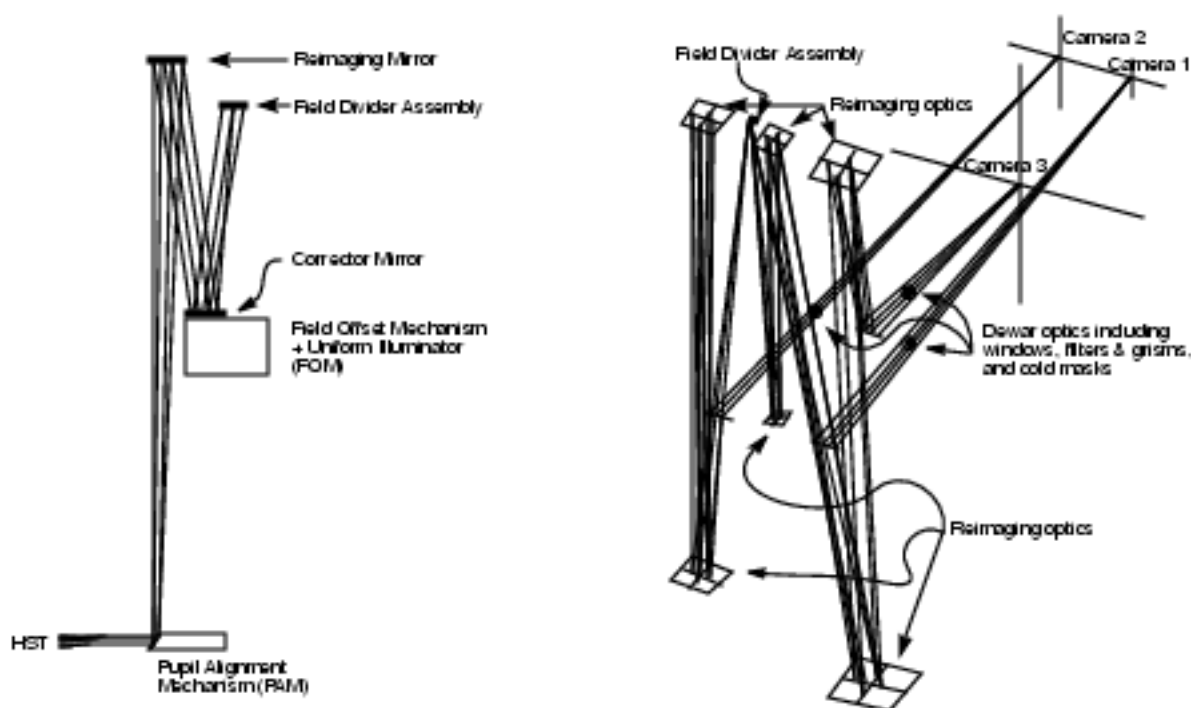
Table 3.3: Basic Imaging Parameters

Parameter	Camera 1	Camera 2	Camera 3
Pixel Size (arcsec)	0.043	0.075	0.2
Field of View (arcsec x arcsec)	11 x 11	19.2 x 19.2	51.2 x 51.2
Diffraction Limited Wavelength (μm)	1.0	1.75	...

filters covering the spectral range from 0.8 to 1.8 microns and narrow band filters for Paschen α, He 1, [Fe 11] λ 1.64μm, and [S 111] λ 0.953 μm, both on and off band. It is equipped with the short wavelength polarizers (0.8 to 1.3 microns).

Camera 2

Camera 2 (NIC2) provides an intermediate spatial resolution with a 19.2 x 19.2 arcsec field of view and 75 mas pixels. The filters include broad and medium band filters covering the spectral range from 0.8 to 2.45 microns. The filter set also includes filters for CO, Brackett γ, H_2 S2 (1-0) λ 2.122 μm, Paschen α, HCO_2 + C_2, and the long wavelength polarizers (1.9–2.1 microns). Camera 2 also provides a coronographic mask with a 300 milliarcsec radius.

Camera 3

Camera 3 (NIC3) provides the lowest spatial resolution with a large 51.2 x 51.2 arcsec field of view and 200 milliarcsec pixels. It includes broad filters covering the spectral range 0.8 to 2.3 microns, medium band filters for the CO band (and an adjacent shorter wavelength continuum region), and narrow band filters for H_2 S2 (1-0), [Si VI] λ 1.962 μm, Paschen-α, [Fe II] λ 1.64 μm, and He I λ 1.083 μm. Camera 3 also contains the multi-object spectroscopic capability of NICMOS with grisms covering the wavelength ranges 0.8–1.2 microns, 1.1–1.9 microns, and 1.4–2.5 microns.

Placement and Orientation of Cameras

The placement and orientation of the NICMOS cameras in the HST focal plane is shown in Figure 3.4. Notice that the cameras are in a straight line pointing radially outward from the center of the telescope focal plane. From the observer's point of view the most important aspect of the layout of NICMOS comes when trying to plan an observation of an extended source with all three cameras simultaneously, when the user must bear in mind the relative positions and orientations of the three cameras. Note that the gaps between the cameras are large, and therefore that getting good positioning for all cameras may be rather difficult.

Note that the position of the NICMOS cameras relative to the HST focal plane (i.e., the FGS frame) depends strongly on the focus position of the PAM. Since independent foci and their associated astrometric solutions are supported for each camera, this is transparent to the observer.

Comparison to WFPC2 and STIS

In addition to NICMOS, between 0.8 and 1.0 microns HST offers the WFPC2 camera for wide field imaging. These two cameras complement each other. The Wide Field CCDs of WFPC2 have an imaging plate scale of ~0.1 arcsec per pixel over each of the three chips, while the PC offers a plate scale of ~0.045 arcsec per pixel on one CCD. The WFPC2 CCDs cover a much larger area of the sky (nearly 160 x 160 arcsec) compared with NICMOS. On the other hand, NICMOS has increasingly higher sensitivity as we move towards 1.0 microns.

A unique feature of the WFPC2 is the presence of ramp filters which permit observations in any narrow bandpass up to 9800Å. These filters are limited to a ~10 x 10 arcsec field of view. The WFPC2 has a narrow band methane filter at 8920Å. Both WFPC2 and NICMOS have [S III] filters. NICMOS offers an adjacent off-band (or slightly redshifted) complementary continuum filter.

In Table 3.4, we summarize the sensitivities of WFPC2 and NICMOS in their region of overlap. In this wavelength region WFPC2's sensitivity is dropping rapidly with increasing wavelength, while NICMOS's is rising. The signal to noise achievable in one hour on a V=20 A0 star is seen to be comparable in the overlap region, and so the choice of which instrument to use is likely to be driven

Figure 3.4: NICMOS Field Arrangement
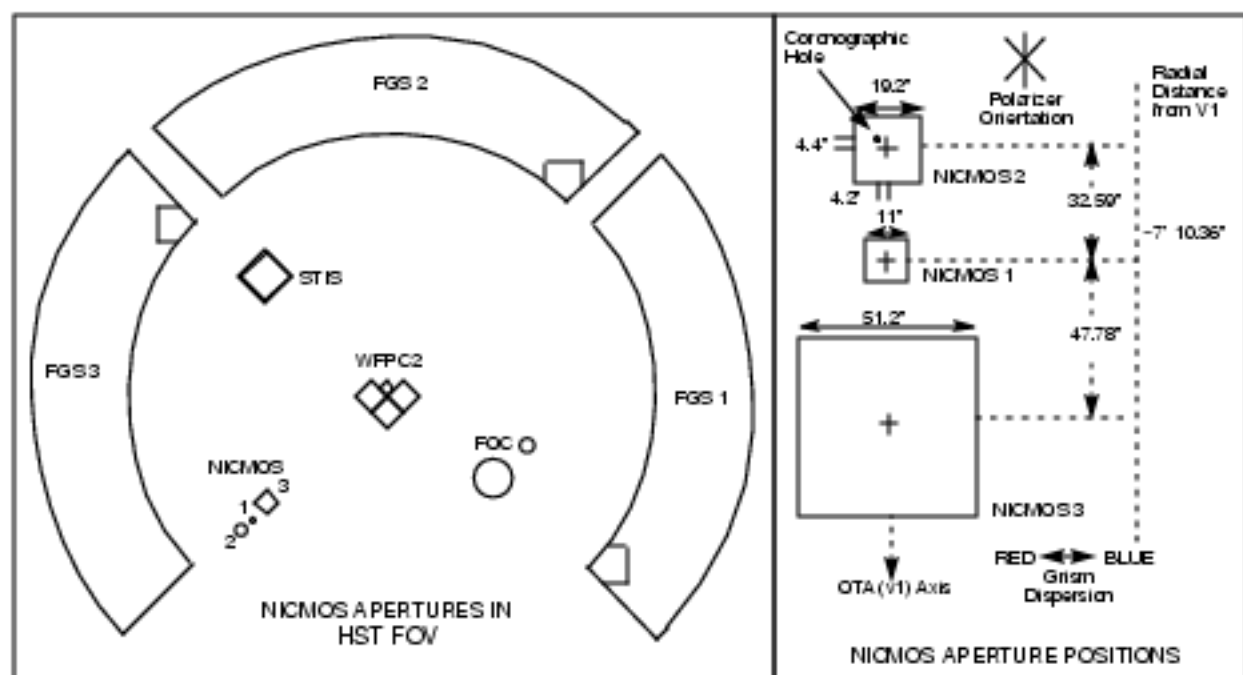
by the field of view desired (WFPC2's is much larger) and whether any further observations are required at either shorter (WFPC2) or longer (NICMOS) wavelengths. NIC3 observations assume that it is in focus.

The Space Telescope Imaging Spectrograph (STIS) also offers CCD based imaging to 1.1 μm with 0.05" pixels and higher quantum efficiency than WFPC2 (although without a useful filter set). Additionally, STIS offers a large complement of slit and slitless spectroscopic capabilities that could complement near-infrared NICMOS science.

Basic Operations

NICMOS employs three low-noise, high QE, 256x256 pixel HgCdTe arrays in a passive dewar using solid N_2 as a coolant. The detector design is based on the NICMOS 3 design that many IR observers may have used; however, there are differences between the two (see Chapter 7). Here we summarize the basic properties of the NICMOS detectors most relevant to the planning of your observations.

The NICMOS detectors have dark current of less than 0.05 electrons per second and effective readout noise for a single exposure of approximately 35 electrons.

Table 3.4: Comparison of WFPC2 and NICMOS Sensitivities for V=20 A0 Star

Instrument	Filter	Mean Wavelength (μm)	Effective Width (μm)	Count Rate (e⁻/sec)	S/N in one hour
WFPC2	F785LP	0.9366	0.2095	14	215[a]
	F791W	0.8006	0.1304	30	314[a]
	F814W	0.8269	0.1758	33	333[a]
	F850LP	0.9703	0.1670	7.1	150[a]
	FQCH4N (QuadD)	0.8929	0.0064	0.47	34,29[a,b]
	F953N	0.9546	0.0052	0.21	19,15[a,b]
	F1042M	1.0443	0.0611	0.20	18,15[a,b]
	LRF[c]	0.8000	0.0105	1.5	66
		0.9000	0.0113	0.64	40
		0.9762	0.0126	0.23	20
NICMOS	F090M[d]	0.8970	0.1885	1.5[e]	68
	F095N[d]	0.9536	0.0088	0.074	7.3
	F097N[d]	0.9715	0.0094	0.085	8.1
	F108N (Camera 1)	1.0816	0.0094	0.088	8.5
	F110W (Camera 1)	1.1022	0.5920	5.4	135
	F110W (Camera 2)	1.1035	0.5915	15	220
	F110W (Camera 3)	1.1035	0.5915	32	340

a. Assumes two 1800 second exposures for cosmic ray removal.
b. Values given for WFC and PC.
c. LRF filter is continuously tunable from 0.371μm to 0.9762μm. LRF field of view is 10"x10".
d. These NICMOS filters are available only on Camera 1 which has field of view of 11"x11".
e. Count rates are for the central pixel on NICMOS.

The NICMOS detectors are capable of very high dynamic range observations and have no count-rate limitations. The dynamic range, for a single exposure, is limited by the depth of the full well, or more correctly the onset of non-linearity, which limits the total number of electrons which can usefully be accumulated in any individual pixel during an exposure to ~160,000 electrons.

NICMOS has four detector read-out modes that may be used to take data (see Chapter 8) plus a target acquisition mode (ACCUM, MULTIACCUM, BRIGHTOBJ, RAMP, and ACQ). For Cycle 7-NICMOS, only ACCUM, MULTIACCUM, and ACQ are supported and ACCUM mode observations are strongly discouraged.

The simplest mode is ACCUM which provides a single integration on a source. A second mode, called MULTIACCUM, provides intermediate read-outs during an integration that subsequently can be analyzed on the ground. A third mode, BRIGHTOBJ, has been designed to observe very bright targets that would

otherwise saturate the detector. BRIGHTOBJ mode reads-out a single pixel at a time. Due to the many resets and reads required to map the array there are substantial time penalties involved. BRIGHTOBJ mode may *not* be used in parallel with the other NICMOS detectors. BRIGHTOBJ mode appears to have significant linearity problems and has not been tested, characterized, or calibrated on-orbit. RAMP mode implements a subset of the MULTIACCUM mode with onboard processing to avoid the transfer of large volumes of data. With the successful installation of the Solid State Recorder during the Second Servicing Mission, this mode is not necessary, has not been tested, and is not supported.

Users who require time-resolved images will have to use either ACCUM where the minimum exposure time is expected to be 0.6 seconds, and the minimum time between successive exposures is 20 seconds, or MULTIACCUM where the shortest spacing between exposures can be reduced to 0.203 seconds.

It is expected that MULTIACCUM *mode will be used for most observations.* It provides the best dynamic range and correction for cosmic rays, since post-observation processing of the data can make full use of the multiple readouts of the accumulating image on the detector. However, a sequence of ACCUM mode observations potentially offers a significant advantage for read noise limited observations using the NREADS option to decrease the effective read noise by up to a factor of ~2 (see Chapter 8). To enhance the utility of MULTIACCUM mode and to simplify the implementation, execution, and calibration of MULTIACCUM observations, a set of predefined MULTIACCUM sequences has been defined. The observer needs only to specify the name of the sequence and the number of samples which should be obtained (with defines the total duration of the exposure). For a set of fairly long exposure times these include sequences which accomplish an equivalent readout noise reduction to the use of ACCUM with multiple reads.

Comparison to CCDs

These arrays, while they share some of the same properties as CCDs, are not CCDs and offer their own set of advantages and difficulties. Users unfamiliar with IR arrays should therefore not fall into the trap of treating them like CCDs. For convenience we summarize the main points of comparison:

- As with CCDs, there is noise (read-noise) and time (read-time) associated with the reading out. In addition, there is an effect called *shading* which is an extraneous bias generated by the readout amplifiers. Furthermore, the dark current associated with NICMOS arrays, while low for IR arrays, is quite substantial compared to that produced by the current generation of CCDs.

- Unlike a CCD, the individual pixels of the NICMOS arrays are strictly independent and can be read-out non-destructively. Read-out modes have been designed which take advantage of the non-destructive read capabilities of the detectors to yield the optimum signal to noise for your science observations (see Chapters 7 and 8). Because the array elements are independently addressed, the NICMOS arrays do not suffer from some of the

artifacts which afflict CCDs, such as charge transfer smearing and *bleeding* due to filling the wells. If, however, they are illuminated to saturation for sustained periods they retain a *memory* of the object in the saturated pixels. This is only a concern for the photometric integrity of back to back exposures of very bright targets, as the ghost images take many minutes to be flushed from the detectors.

Target Acquisition Modes

Most target acquisitions can be accomplished by direct pointing of the telescope. The user should use target coordinates which have been measured with the Guide Star Astrometric Support Package (GASP) to ensure the best accuracy with respect to the HST Guide Star Catalog. Particular care must be exercised with targets in Camera 1 due to its small field of view.

However, direct pointing will not be sufficient for coronographic observations since the achieved precision (~1 arcsec rms) is much larger than the 0.3 arcsec radius coronographic spot. *Note that this is a function of the total HST pointing error and not only the result of uncertainties in the target's coordinates.*

There are three target acquisition options for coronographic observations:

- An on-board acquisition (ACQ mode) can be obtained. This commands NICMOS to obtain an image of the target and rapidly position the brightest source in a restricted field of view behind the coronographic spot (see Chapter 5).

- The RE-USE TARGET OFFSET special requirement can be used to accomplish a positioning relative to an early acquisition image.

- A real time acquisition (INT-ACQ) can be obtained although this is costly in spacecraft time and is a limited resource.

While ACQ mode is restricted to coronographic observations in Camera 2, the last two target acquisition modes may be useful for positioning targets where higher than normal (1–2 arcsec) accuracy is required (e.g., crowded field grism exposures).

Attached Parallels

While the three NICMOS cameras are no longer at a common focus, under many circumstances it is desirable to obtain data simultaneously in multiple cameras. Generally, Cameras 1 and 2 will be used simultaneously while Camera 3 will be used by itself.

Since some programs by their nature do not require more than one camera (e.g., studies of isolated compact objects), to make the most of the limited lifetime of NICMOS, observers are encouraged to add exposures to their proposals to obtain the maximum amount of NICMOS data consistent with efficiently accomplishing their primary science program. Detailed instructions for this process will be included in the Phase II proposal instructions. Internal NICMOS

parallel observations obtained under this policy will be known as *attached parallels* and will be delivered to the prime program's observer and will have the usual proprietary period.

▽ This section applies only to Phase 11 proposals—you need not worry about this for your Phase 1 proposal.

The recommendations attached below are intended for General Observers (GOs) who do not establish a scientific rationale for observations with the non-prime NICMOS camera(s) in their Phase 1 submission to the TAC. They are subject to revision.

Table 3.5: Attached Parallel Recommendations

Pointing	Camera 1	Camera 2
Extragalactic	F160W	F110W, F160W
Galactic Clouds	F164N, F166N	F110W, F160W, F205W
(if <= 4 orbits)	F164N, F166N	F212N, F215N
Galactic Plane	F160W	F110W, F160W
(add if > 1 orbit)	F110W	F205W

Pointings are defined as:

- Extragalactic: > 5 degrees above the galactic plane.
- Galactic Clouds: Dark/molecular cloud regions (e.g., OMC, rho Oph, etc.)
- Galactic Plane: all pointings not Extragalactic or Galactic Clouds.

The Infrared Background

From the ground, the infrared background is affected by telluric absorption and emission which limits the depth of astronomical imaging. As is well known, between 1 and 2.5 microns there are a number of deep molecular absorption bands in the atmosphere (top panel of Figure 3.5), and the bandpasses of the conventional near-IR bands of JHK were designed to sit in the gaps between these opaque regions (middle panel of Figure 3.5). Unfortunately, outside the absorption features there is also considerable background emission in both lines and continuum. Most of the background between 1 and 2 microns comes from OH and O_2 emission produced in a layer of the atmosphere at an altitude ~ 87 km (bottom panel of Figure 3.5).

Figure 3.5: Atmospheric Absorption and Emission Line Spectrum in NICMOS Operational Range
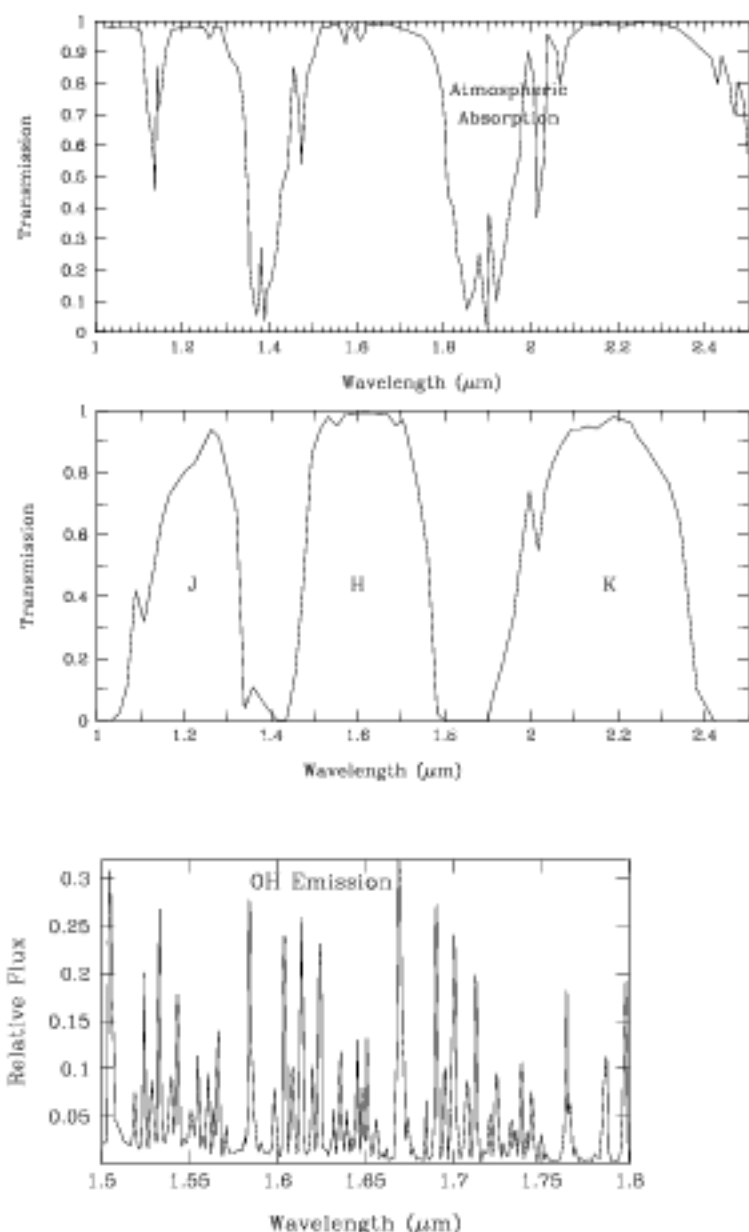
The location of HST above the atmosphere removes these terrestrial effects from the background. Now, the dominant sources of background radiation will be the zodiacal light at short wavelengths and the thermal background emission from the telescope at long wavelengths. The sum of these two components will be a minimum at 1.6 microns (roughly the H band). All three NICMOS cameras carry broad-band filters which are centered on this wavelength.

At the shorter wavelengths, sensitivities will be affected by the zodiacal background which is, of course, strongly spatially dependent (see Table 3.6).

Observations by the COBE satellite have implied that at positions 45 degrees out of the ecliptic the zodiacal background can be approximated as:

$$5.0 \times 10^8 / \lambda^{1.09} + 6 \times 10^{-8} B_\lambda(\lambda, T) \text{ photons cm}^{-2} \text{ } \mu m^{-1} \text{ steradian}^{-1}$$

Where λ is the wavelength in μm and B_λ is the blackbody function for the zodiacal dust temperature T (roughly 265 K).

Table 3.6: Sky Brightness (V mag arcsec^{-2}) as a Function of Heliocentric Ecliptic Latitude and Longitude. "SA" denotes that the target is unobservable due to solar avoidance.

| Heliocentric Ecliptic Longitude	Ecliptic Latitude						
	0°	15°	30°	45°	60°	75°	90°
180°	22.1	22.4	22.7	23.0	23.2	23.4	23.3
165°	22.3	22.5	22.8	23.0	23.2	23.4	23.3
150°	22.4	22.6	22.9	23.1	23.3	23.4	23.3
135°	22.4	22.6	22.9	23.2	23.3	23.4	23.3
120°	22.4	22.6	22.9	23.2	23.3	23.3	23.3
105°	22.2	22.5	22.9	23.1	23.3	23.3	23.3
90°	22.0	22.3	22.7	23.0	23.2	23.3	23.3
75°	21.7	22.2	22.6	22.9	23.1	23.2	23.3
60°	21.3	21.9	22.4	22.7	23.0	23.2	23.3
45°	SA	SA	22.1	22.5	22.9	23.1	23.3
30°	SA	SA	SA	22.3	22.7	23.1	23.3
15°	SA	SA	SA	SA	22.6	23.0	23.3
0°	SA	SA	SA	SA	22.6	23.0	23.3

At wavelengths longer than 1.6 microns the thermal background of the telescope rises and may have to be removed by obtaining off-source images. By using filtering techniques such as median filtering any contaminating sources in these offset fields can be removed in a composite background frame which can then be subtracted from the data.

Figure 3.6 shows the HST background for each of the three cameras (the solid line represents Camera 1, the dotted line represents Camera 2, the dashed line represents Camera 3) as a function of wavelength. This background has been calculated assuming a zodiacal light contribution consistent with the mean observed by COBE for an ecliptic latitude of 45°, and also includes thermal emission by the HST primary and secondary mirrors, and the NICMOS optics, based on-orbit data and the transmission of all the NICMOS fore-optics. It does not include the transmission of any filter, nor the response of the detectors.

We are presently obtaining direct observations to measure and establish the stability of the thermal contribution to the background during SMOV and early in Cycle 7.

On-orbit measurements now indicate that the prelaunch estimates for the HST thermal emission were overly conservative. The emissivity of the OTA appears to be close to 4% leading to a significant reduction in the expected thermal

Figure 3.6: HST Background for Each Camera
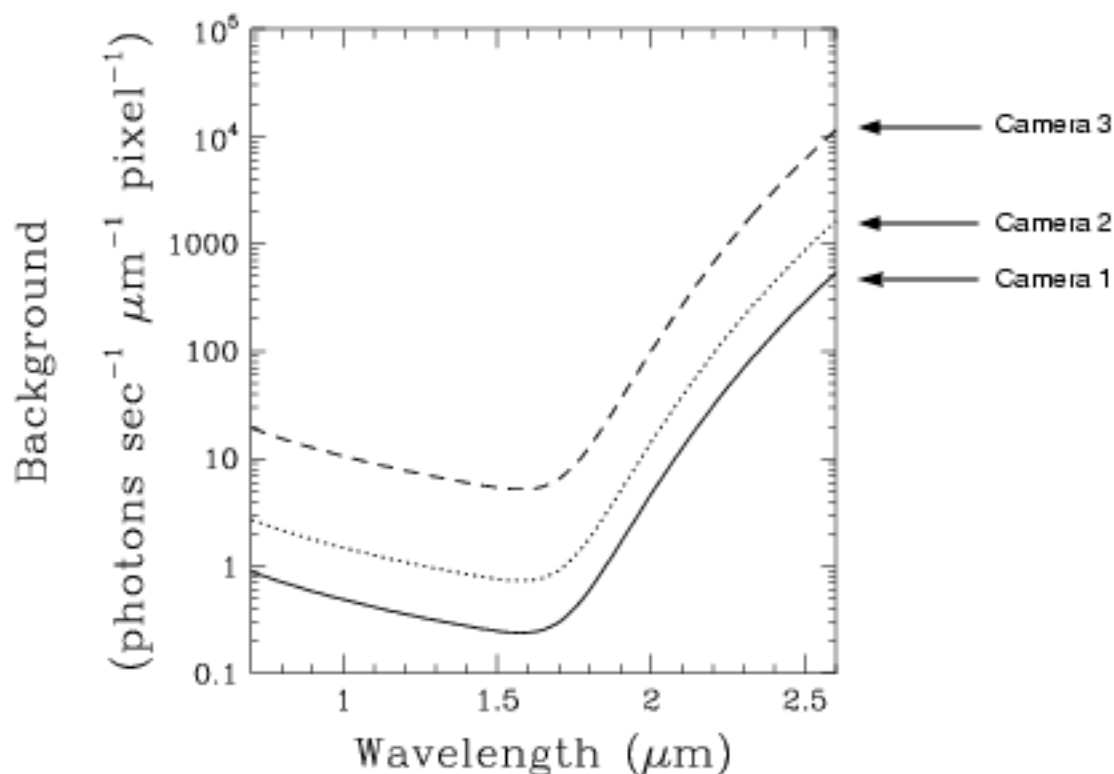
background for all filters longward of 1.5 microns. (In addition, it appears that the contribution to the background from the zodiacal dust was overestimated by a factor of two, a change that affects all filters.) These changes result in significant improvements in the sensitivity of NICMOS at the longest wavelengths where the background count rates are reduced by the largest amount.

Table 3.7 compares the predicted background rates in several filters in NIC2 before SMOV with the revised rates resulting from the first on orbit test. The exposure time calculator tool on the STScI NICMOS WWW page has been updated to reflect the newly measured background rates. Background count rates for any filter/camera combination may be obtained by selecting Input Info on the exposure time calculator results page.

Table 3.7: Background count rates for selected filters in NIC2

Filter	Predicted Background (e-/s/pix)	Revised Background (e-/s/pix)
F110W	0.19	0.10
F160W	0.39	0.088
F180M	0.33	0.039
F190N	0.27	0.027
F207M	20	2.0
F215N	5.1	0.50
F222M	74	7.8
F237M	279	31

For pointings very close to the Earth, the zodiacal background may be exceeded by the earthshine. The brightness of the earthshine falls very rapidly with increasing angle from the Earth's limb, and for most observations only a few minutes at the beginning and end of the target visibility period will be significantly affected. The major exception to this behavior is a target in the continuous viewing zone (CVZ). Such a target will always be rather close to the Earth's limb, and so will always see an elevated background (at the shorter wavelengths where zodiacal emission would ordinarily dominate). For targets faint enough that the background level is expected to be much brighter than the target, the observer is recommended to specify the LOW−SKY option. This will increase the minimum allowed Earth avoidance angle, requiring scheduling during a time for which the zodiacal background is no greater than 30% above the minimum achievable level, at the cost of a slight decrease of the available observing (visibility) time during each orbit. Note that this restriction is only helpful when observations are background limited.

Conversion Between Fluxes and Magnitudes

Throughout the NICMOS documentation we will frequently use flux units of Janskys (Jy). A detailed discussion of the conversion between various units and Janskys is given in Chapter 12. Here we summarize the central wavelengths and zero-point fluxes for the more commonly encountered photometric bands in Table 3.8, using the most commonly encountered photometric systems, the CIT and the UKIRT systems.

Designing NICMOS Observations

In the preceding sections, we provided you with an overview of the scientific capabilities of NICMOS and the basic layout and operation of the instrument. Subsequent chapters will provide detailed information about the performance and operation of the instrument. In this section, we describe the conceptual steps you

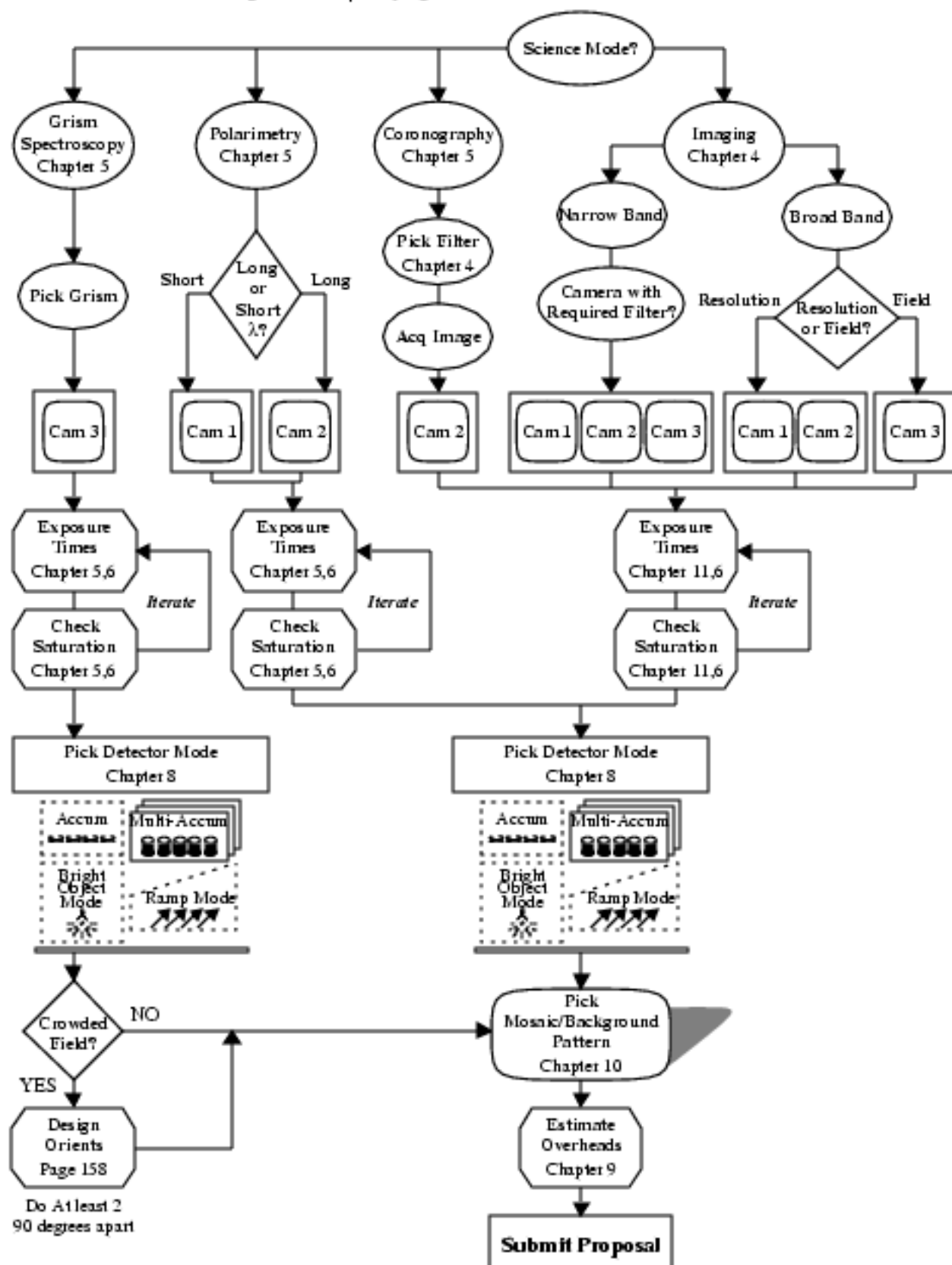**Table 3.8:** Effective Wavelengths and Zero-points for Photometric Bands

Band	λ[μm]	F_o[Jy](CIT)	F_o[Jy] (UKIRT)
V	0.56	3540	3540
R	0.70	2870	-
I	0.90	2250	-
J	1.25	1670	1600
H	1.65	980	1020
K	2.2	620	657
L	3.4	280	290
L'	3.74	-	252
M	4.8	150	163
N	10.1	37	39.8
Q	20.0	10	10.4

will need to take when designing a NICMOS observing proposal. The basic sequence of steps in defining a NICMOS observation are shown in flow diagram form in Figure 3.7, and are:

- Identify your science requirements and select the basic NICMOS configuration to support those requirements (e.g., imaging, polarimetry, coronography). Refer to the detailed accounts given in Chapter 4 and Chapter 5.

- Select the wavelength region of interest and hence determine if your observations will be Background or Read-Noise limited using the Exposure Time Calculator available on the STScI NICMOS WWW page (see Chapters 4 and 6).

- Establish which MULTIACCUM sequence you need to use. Detailed descriptions of these are provided in Chapter 8. This does not need to be specified in a Phase 1 proposal. However, if you require a readout mode other than MULTIACCUM this should be justified in the Phase 1 proposal.

- Estimate the exposure time to achieve the required signal to noise ratio and check feasibility (i.e., saturation and bright object limits). To determine your exposure time requirements and assess whether you are close to the brightness and dynamic range limitations of the detectors, use the Exposure Time Calculator.

- If necessary choose a chop and dithering pattern either to measure the background or to enable mapping of areas bigger than the field of view of the NICMOS cameras you plan to use. See Chapter 10.

- If you are doing coronographic observations, additional target acquisition exposures will be required to center your target in the aperture to the accuracy required for your scientific aims (e.g., you may wish to center the nucleus of a galaxy in a crowded field behind the coronographic spot).

- Calculate the total number of orbits required, taking into account the overheads. In this, the final step, you combine all your exposures (science and non-science, alike) into orbits, using tabulated overheads, and determine the total number of orbits you require. Refer to Chapter 9 when performing this step.

Figure 3.7: Specifying a NICMOS Observation

Imaging

This chapter provides the information needed to construct an imaging proposal. Filter transmission curves are presented. The sensitivity curves and exclusion curves available from the Exposure Time Calculator are described. Instructions and examples for calculating exposure times and signal to noise ratios are provided in Chapter 6.

Filters & Optical Elements

Each camera has 20 filter positions on a single filter wheel: 19 filters and one blank. As a result, not all filters are available in all cameras. Moreover, the specialized optical elements, such as the polarizers and grisms, cannot be crossed with other filters, and can only be used in fixed bands. In general the filters have been located in a way which best utilizes the characteristics of NICMOS, thus at shorter wavelengths the most important narrow band filters are located in Camera 1 so that the diffraction limited performance can be maintained wherever possible, while those in Camera 2 have been selected to work primarily in the longer wavelength range where it will also deliver diffraction limited imaging.

Table 4.1 through Table 4.3 list the available filters and provide an initial general description of each, starting with Camera 1 and working down in spatial resolution to Camera 3. Figure 4.1 through Figure 4.3 show the percentage transmission of each optical element plotted against wavelength. Chapter 11 provides further details and the individual filter transmission curves.

Nomenclature

The name of each optical element starts with a letter or group of letters identifying what kind of element it is: filters start with an "F", grisms with a "G", and polarizers with "POL". Following the initial letter(s) is a number which in the case of filters identifies its approximate central wavelength in microns, e.g., F0951 implies a central wavelength of 0.95 microns. A trailing letter identifies the filter width, with "W" for wide, "M" for medium and "N" for narrow. In the case of grisms, the initial "G" is followed by a number which gives the center of the free-spectral range of the element, e.g., G206. For the polarizers, a somewhat different notation is used, with the initial "POL" being followed by a number which gives the PA of the principal axis of the polarizer in degrees, and a trailing letter identifying the wavelength range it can be used in, which is either "S" for short (0.8-1.3 microns) or "L" for long (1.9-2.1 microns).

Figures 4.1, 4.2, and 4.3 show the transmission curves of all of the NICMOS filters for Cameras 1, 2, and 3, respectively. The wide, medium, and narrow bandwidth filters are plotted separately for each camera. Only the filter transmission is shown—the efficiency of other optical elements or the detectors has not been included. Different line styles have been used for the different filters only to help differentiate them.

Table 4.1: Camera 1 Filters

Name	Central Wavelength (μm)	Bandwidth (μm)	Comment	See also
Blank	N/A	N/A	blank	
F110W	1.025	0.8–1.35		page 166
F140W	1.3	0.8–1.8	Broad Band	page 168
F160W	1.55	1.35–1.75		page 170
F090M	0.9	0.8–1.0		page 161
F110M	1.1	1.0–1.2		page 165
F145M	1.45	1.35–1.55	Water	page 169
F165M	1.6	1.55–1.75		page 172
F170M	1.7	1.6–1.8		page 174
F095N	0.953	1%	[S III]	page 162
F097N	0.97	1%	[S III] continuum	page 163
F108N	1.083	1%	He I	page 164
F113N	1.13	1%	He I continuum	page 167
F164N	1.644	1%	[Fe II]	page 171
F166N	1.66	1%	[Fe II] continuum	page 173
F187N	1.87	1%	Paschen α	page 175
F190N	1.90	1%	Paschen α continuum	page 176
POL0S	1.1	0.8–1.3	Short λ Polarizer	page 76
POL120S	1.1	0.8–1.3	Short λ Polarizer	page 76
POL240S	1.1	0.8–1.3	Short λ Polarizer	page 76

Figure 4.1: Filters for Camera 1
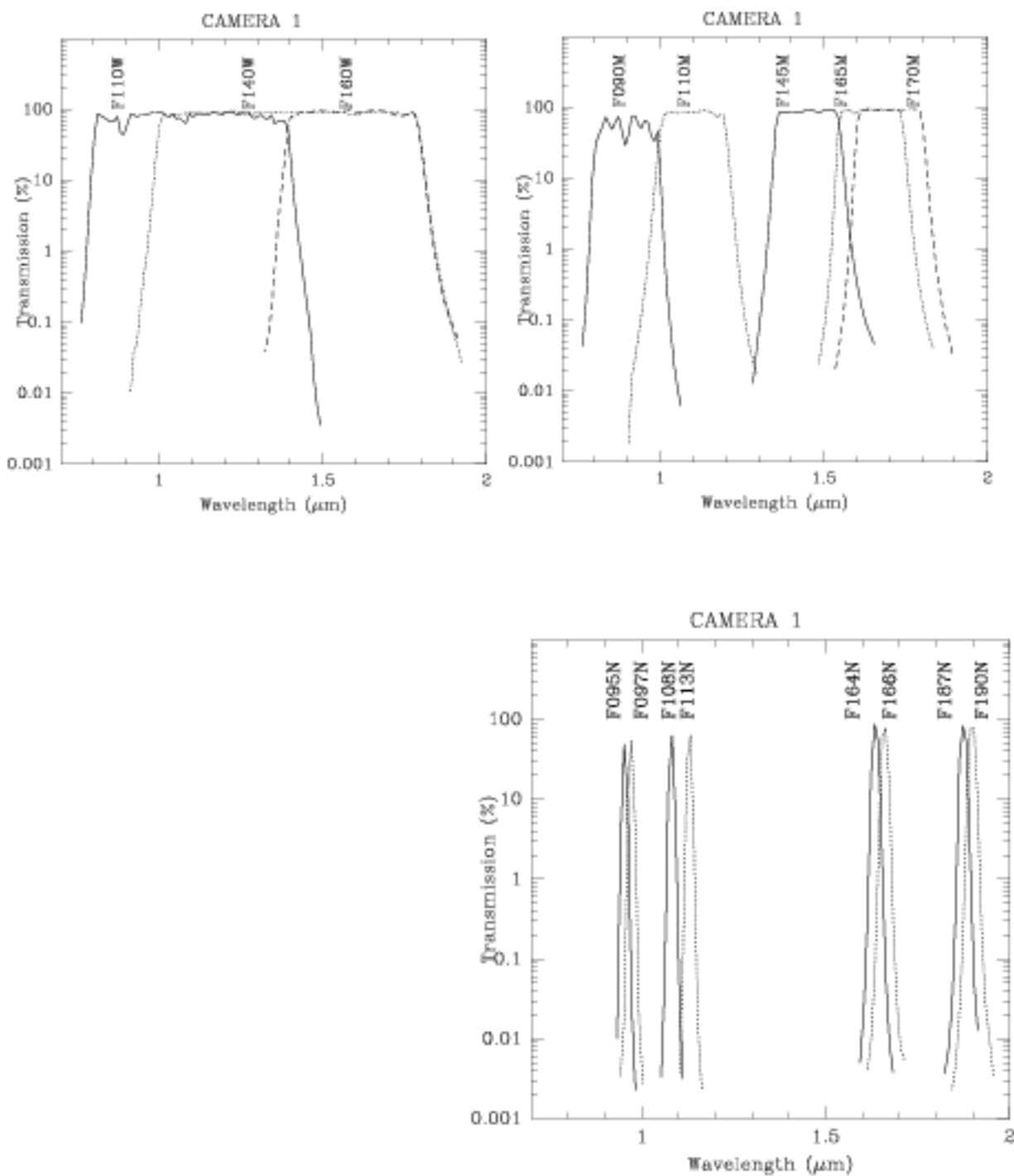
Table 4.2: Camera 2 Filters

Name	Central Wavelength (µm)	Bandwidth (µm)	Comment	See also
Blank	N/A	N/A	blank	
F110W	1.1	0.8–1.4		page 177
F160W	1.6	1.4–1.8	Minimum background	page 178
F187W	1.875	1.75–2.0	Broad	page 183
F205W	1.9	1.75–2.35	Broad Band	page 186
F165M	1.7	1.55–1.75	Planetary continuum	page 179
F171M	1.715	1.68–1.75	HCO_2 and C_2 continuum	page 180
F180M	1.80	1.765–1.835	HCO_2 and C_2 bands	page 181
F204M	2.04	1.9–2.09	Methane imaging	page 185
F207M	2.1	2.0–2.15		page 187
F222M	2.3	2.15–2.30	CO continuum	page 191
F237M	2.375	2.3–2.45	CO	page 192
F187N	1.87	1%	Paschen α	page 182
F190N	1.9	1%	Paschen α continuum	page 184
F212N	2.121	1%	H_2	page 188
F215N	2.15	1%	H_2 and Br γ continuum	page 189
F216N	2.165	1%	Brackett γ	page 190
POL0L	2.05	1.9–2.1	Long λ polarizer	page 76
POL120L	2.05	1.9–2.1	Long λ polarizer	page 76
POL240L	2.05	1.9–2.1	Long λ polarizer	page 76

Figure 4.2: Filters for Camera 2
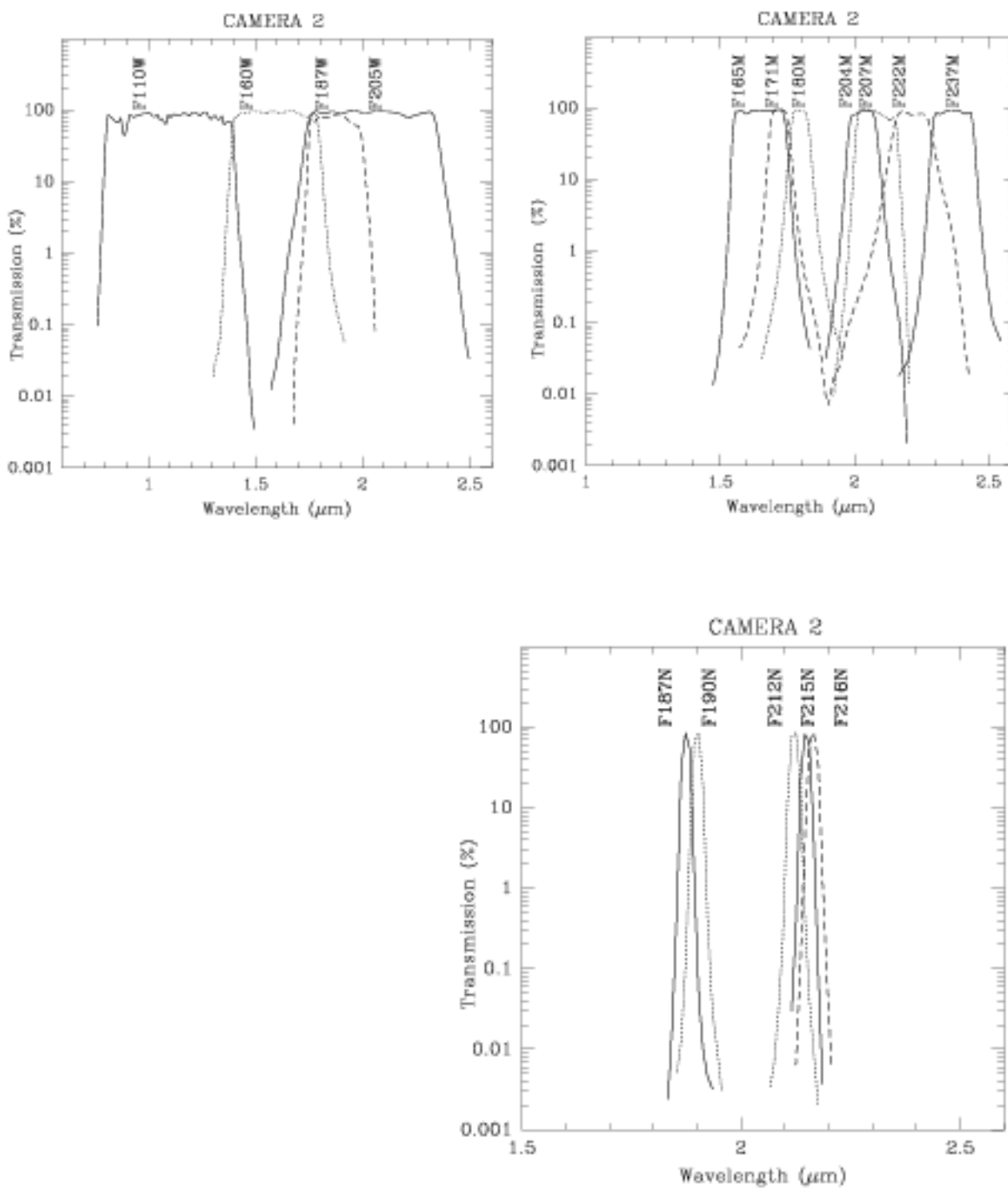
Table 4.3: Camera 3 Filters

Name	Central Wavelength (μm)	Bandwidth (μm)	Comment	See also
Blank	N/A	N/A	blank	
F110W	1.1	0.8–1.4		page 194
F160W	1.6	1.4–1.8	Minimum background	page 197
F175W	1.75	1.2–2.3		page 200
F222M	2.3	2.15–2.3	CO continum	page 207
F240M	2.4	2.3–2.5	CO band	page 208
F108N	1.0830	1%	He I	page 193
F113N	1.13	1%	He I continum	page 195
F164N	1.644	1%	[Fe II]	page 198
F166N	1.66	1%	[Fe II] continum	page 199
F187N	1.875	1%	Paschen α	page 201
F190N	1.9	1%	Paschen α continum	page 202
F196N	1.962	1%	[Si VI]	page 203
F200N	2.0	1%	[Si VI] continum	page 204
F212N	2.121	1%	H_2	page 205
F215N	2.15	1%	H_2 continum	page 206
F150W	1.5	1.1–1.9	Grism B continum	page 196
G096	0.9673	0.8–1.2	GRISM A	page 84
G141	1.414	1.1–1.9	GRISM B	page 85
G206	2.067	1.4–2.5	GRISM C	page 86

Figure 4.3: Filters for Camera 3
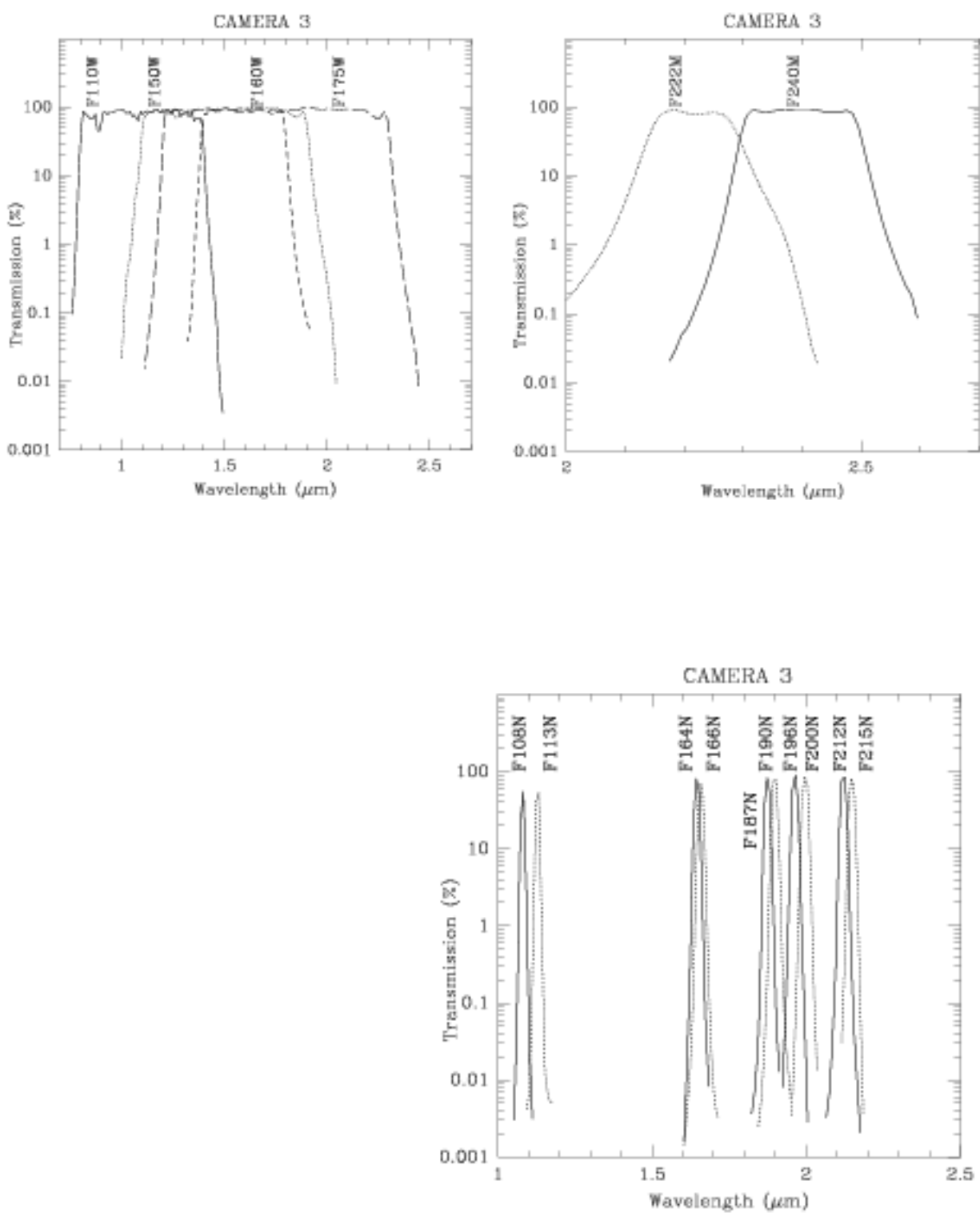
Filter Sensitivity Curves

Detailed information and transmission curves are provided for each filter (Chapter 11) and for the grisms and polarizers (Chapter 5). Performance information may be obtained from the Exposure Time Calculator (ETC). In this section we explain the formats and outline the use of the Figures from the ETC. For many purposes, these Figures may take the place of detailed calculations and permit observers to quickly determine the feasibility or appropriateness of an observation.

▽ Caution: The Figures in this section and in Chapter 5 are shown as examples and are based on preliminary *estimates* of the NICMOS sensitivities, noise characteristics, and backgrounds—observers should rely upon the ETC for their performance predictions.
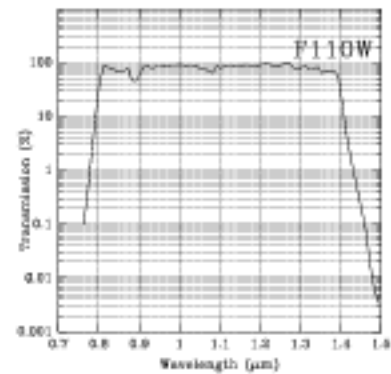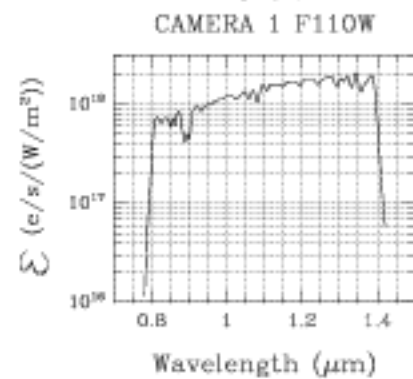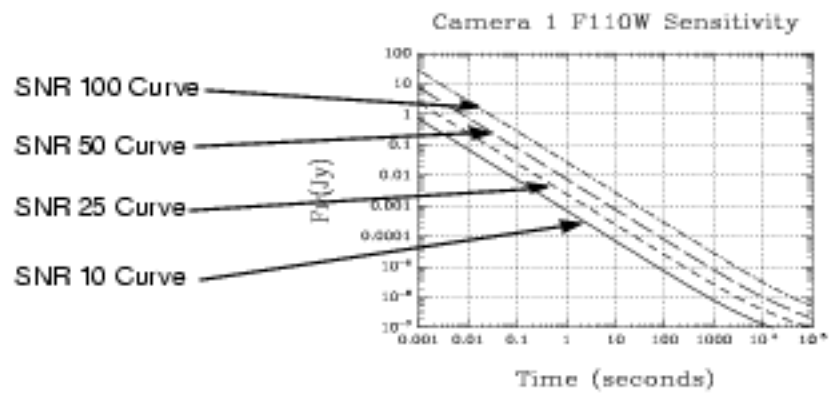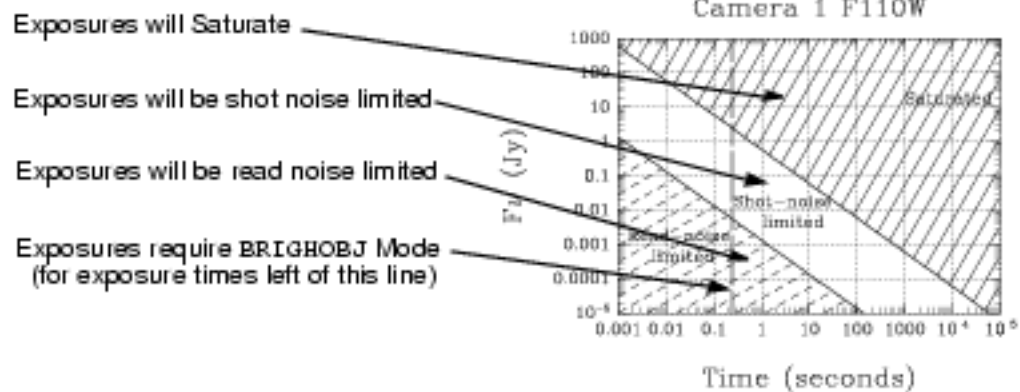
The Handbook provides the following (see Chapters 11 and 5):

- A *summary* of the basic filter parameters:

    - Central wavelength
    - Mean wavelength
    - Peak wavelength
    - Full Width at Half Maximum transmission (FWHM)
    - Spectral range
    - Maximum transmission
    - Fraction of light falling on the central pixel for a point source centered on the pixel.

- A *filter transmission curve*. The spectral characteristics of the NICMOS flight filters were measured at cryogenic temperature and normal incidence at Ball Aerospace. All filters had their spectral transmission measured from 0.5 to 2.7 microns with a step size of 0.001 microns.

The Exposure Time Calculator should be used to obtain:

- *An epsilon diagram*. For each filter we have calculated $\varepsilon(\lambda)$ to permit simple determination of the response of NICMOS to a monochromatic emission line within the filter's useful bandpass. This single parameter encompasses the wavelength dependent DQE, filter transmission, mirror reflectivities (including both the NICMOS fore-optics and the HST primary and secondary mirrors), and dewar window transmission. This parameter is calculated in units of $e^- \ s^{-1} \ (W \ m^{-2})^{-1} \ pixel^{-1}$. Given a line flux in $W \ m^{-2}$, the flux per pixel can be determined using the pixel fraction for point sources or the pixel area for extended sources. Then the $\varepsilon(\lambda)$ parameter provides the count rate in $e^- \ s^{-1}$. Additional discussion and examples of this calculation are provided in Chapter 6.

Figure 4.4: Example Sensitivity and Exclusion Curves

Filter Transmission Curve

Epsilon Diagram

CAMERA 1 F110W

Sensitivity Curves

Camera 1 F110W Sensitivity

SNR 100 Curve

SNR 50 Curve

SNR 25 Curve

SNR 10 Curve

Observational Exclusion Diagrams

Time to saturate

Camera 1 F110W

Exposures will Saturate

Exposures will be shot noise limited

Exposures will be read noise limited

Exposures require BRIGHOBJ Mode
(for exposure times left of this line)

- *Sensitivity curves for point and extended sources*. These present spectral flux density (F_ν) as a function of time to achieve a signal to noise ratio (S/N) of 10, 25, 50, and 100 (solid, short dash, long dash, and dot-dash lines, respectively). These curves incorporate the expected backgrounds and presently understood noise characteristics of the detectors. To use these plots select a camera and filter combination, locate the flux of your source and read across the figure to determine the exposure time for a given S/N.

- *Observational exclusion diagrams* for point and extended sources. These again show flux (F_ν) as a function of time. The useful limits of the instrument are shown. Sources falling in the upper right hand region will be saturated (see the discussion of MULTIACCUM mode to observe both bright and fainter sources in the same exposure). Sources falling in the lower left region of the plot will be read noise rather than shot noise limited. Finally, sources to the left of the vertical dashed line at 0.203 seconds must be observed using the BRIGHTOBJ mode.

Out-of-Band Leaks in NICMOS Filters

In order to make use of the high spatial resolution of HST, many observers will wish to use NICMOS to observe very red objects (e.g., protostars) at relatively short wavelengths. By their very nature, these very red objects have very low effective color temperatures. Thus if we observe such an object at a wavelength of 1.0 microns, we can expect that its flux at 2.5 microns will be orders of magnitude larger than its flux at the desired wavelength. In such a case, exceptionally good out-of-band blocking is required from the filter. We have therefore investigated whether the measured filter transmissions would allow any sources with extreme colors to yield erroneous photometry due to out-of-band leaks.

We have calculated the effects of filter leaks for sources with color temperatures from 700K to 10,000K. At this juncture we note that the reddest of the kinds of sources likely to be observed with NICMOS may have color temperatures lower than 400K, while the bluest sources (probably reflection nebulae) can be significantly bluer than a 10,000K blackbody. We find that significant leaks may occur for nine of the filters. No photometric errors as large as 1% were found for any filters using the hottest (i.e., 10,000K) spectrum (however, as noted above some reflection nebulae may have bluer spectra than this, and we cannot rule out the possibility of errors as large as a few percent in this case, for a few filters). For the reddest source considered here (with a color temperature of 700K), the photometric errors might be as large as an order of magnitude in a few filters. There are still some uncertainties regarding the measured transmission curves, and so the information presented here should be regarded only as cautionary.

▽ On-orbit tests will be performed as part of the Cycle 7 Calibration program and the results posted on the STScI NICMOS WWW pages as they become available—this is not likely to be before the Cycle 7-NICMOS Phase 1 deadline.

The nine filters for which these leaks might be a problem are: F090M, F095N, F097N, F108N, F110M, F110W, F113N, F187N, F190N. We recommend that observers using these filters for sources with extremely red colors observe them in a number of filters to minimize the likelihood of filter leaks causing errors.

Image Quality and Focus

The Pupil Alignment Mechanism

The Pupil Alignment Mechanism, or PAM, consists of an adjustable mirror in the NICMOS optical train that can be moved to make small corrections to the NICMOS focus and serves to properly position the pupil image of the telescope primary mirror onto the corrective optic. The motion of the PAM is limited to +/- 10mm in focus travel from its zero position. The NICMOS cameras were designed to share a common focus with the PAM close to its zero position. In the current state of the dewar, cameras 1 and 2 (NIC1 and NIC2) can each be focussed within the range of the PAM. Camera 3 (NIC3), however, cannot be focussed by motions of the PAM alone. Throughout this document we will use the PAM mirror position as the measure of focus position of the three NICMOS cameras.

The focus positions of all three NICMOS cameras have changed since launch with motion in the dewar. The positions are measured by observations of stars over a range of focus settings on a frequent basis. Phase retrieval is used, especially for NIC3, to determine the optimal focus positions. The focus history since shortly after launch is shown in Figure 4.5.

Cameras 1 and 2

The changes in dewar geometry leading to the lack of focus in NIC3 have also affected NIC1 and NIC2. By measuring the PSFs of stars at a series of PAM positions it has been determined that the optimal focus for NIC1 occurs for a PAM position of ~+2 mm and the optimal focus for NIC2 at ~0.5 mm. This difference is significant enough that NIC1 and NIC2 are no longer considered to be parfocal. A separate PAM position at the optimal focus is defined and maintained for each camera. The main effects of this decision are to similarly degrade the image quality of either NIC1 or NIC2 when used in parallel and to add overhead associated with changes from NIC1 to NIC2.

The encircled energy profiles for NIC1 and NIC2 at representative wavelengths are shown in Figure 4.6 through Figure 4.9.

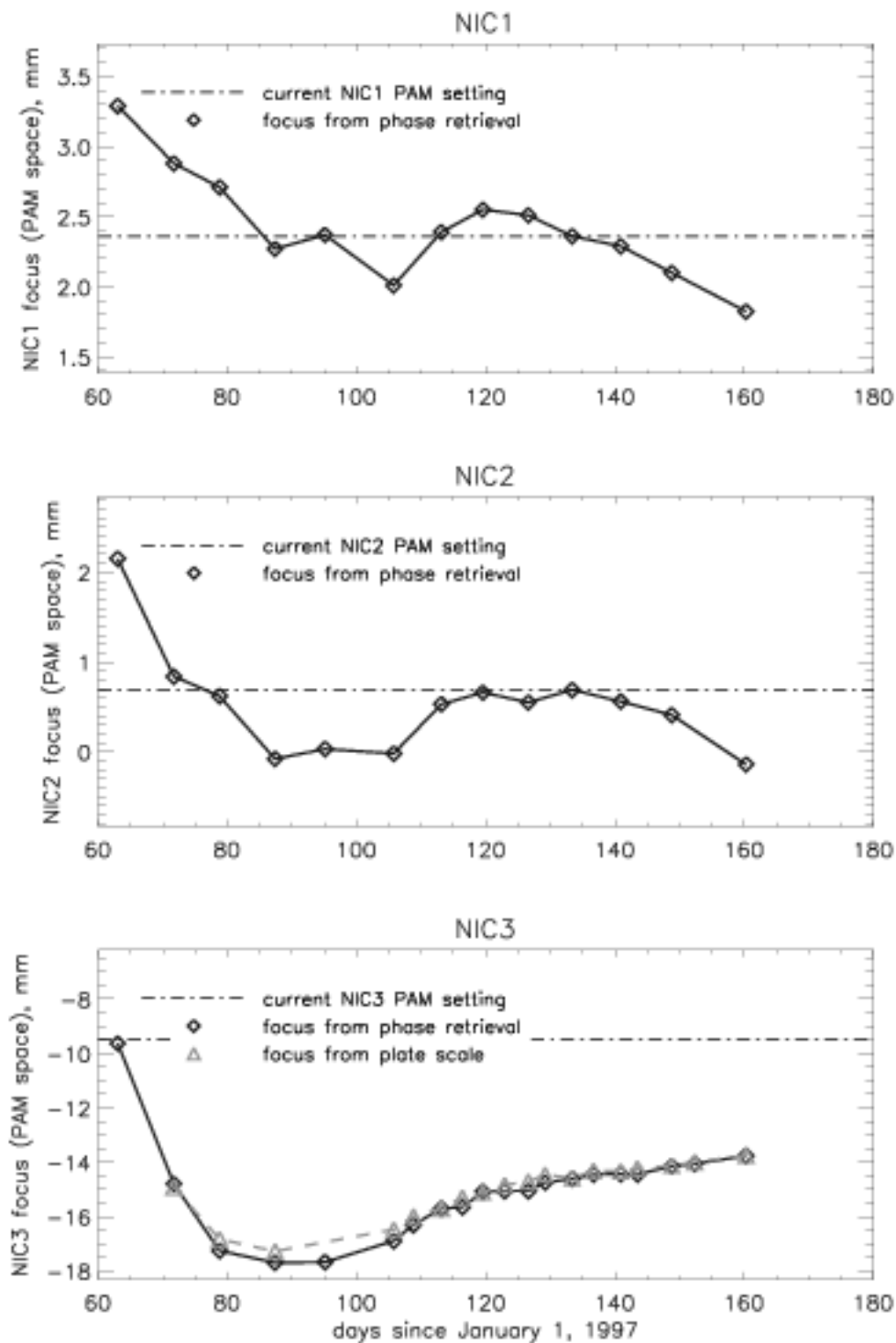**Figure 4.5: NICMOS Focus History as of June 9, 1997.**
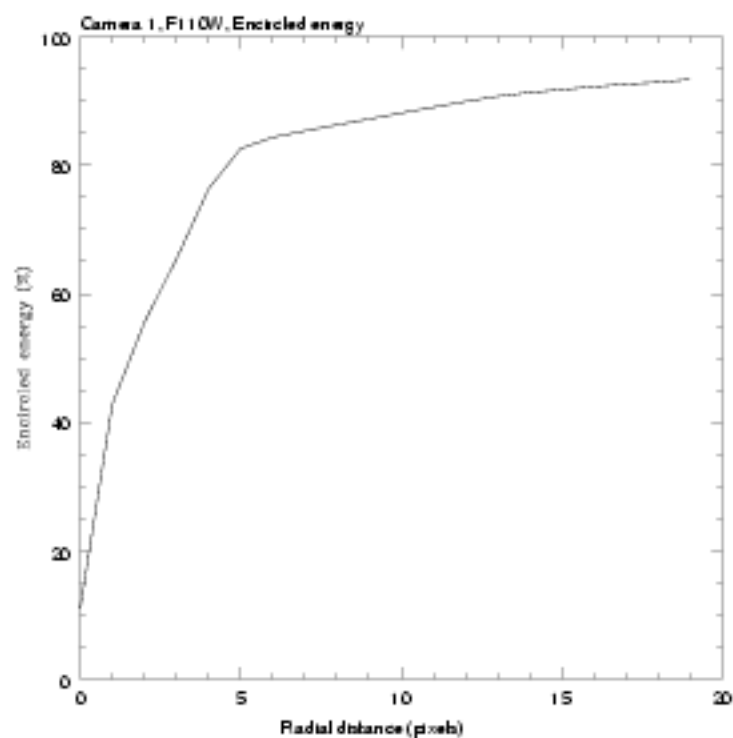
Figure 4.6: Encircled Energy for Camera 1, F110W.

Camera 1, F110W, Encircled energy

Figure 4.7: Encircled Energy for Camera 1, F160W.

Camera 1, F160W, Encircled energy
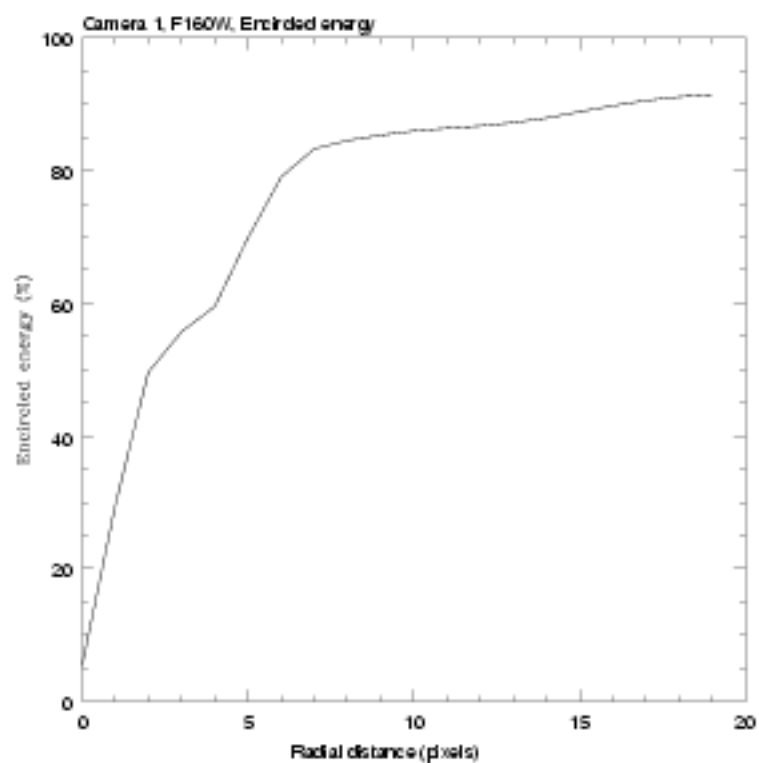
Figure 4.8: Encircled Energy for Camera 2, F110W.

Camera 2, F110W, Encircled energy

Encircled energy (%)

Radial distance (pixels)
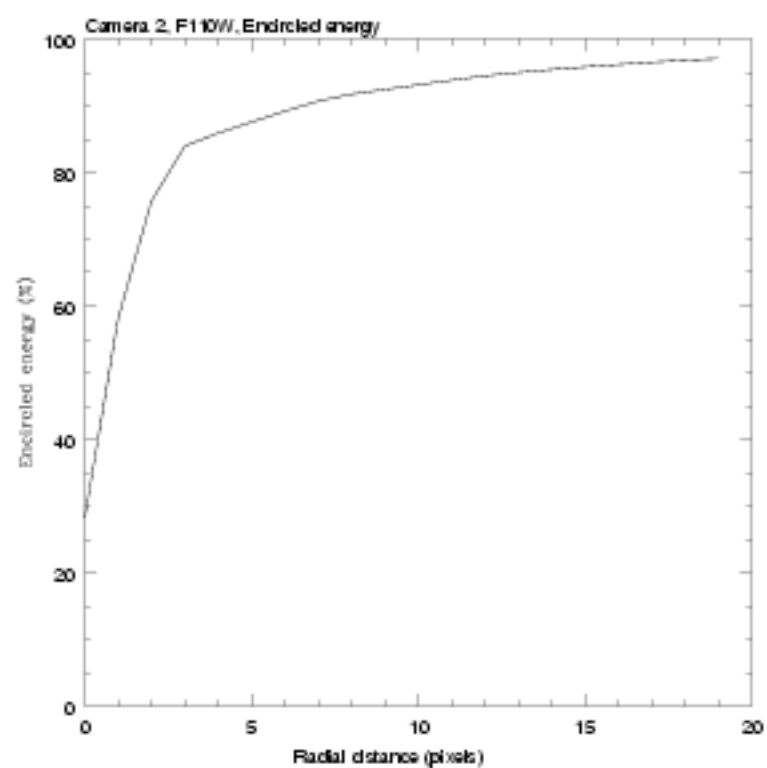
Figure 4.9: Encircled Energy for Camera 2, F160W.

Camera 2, F160W, Encircled energy

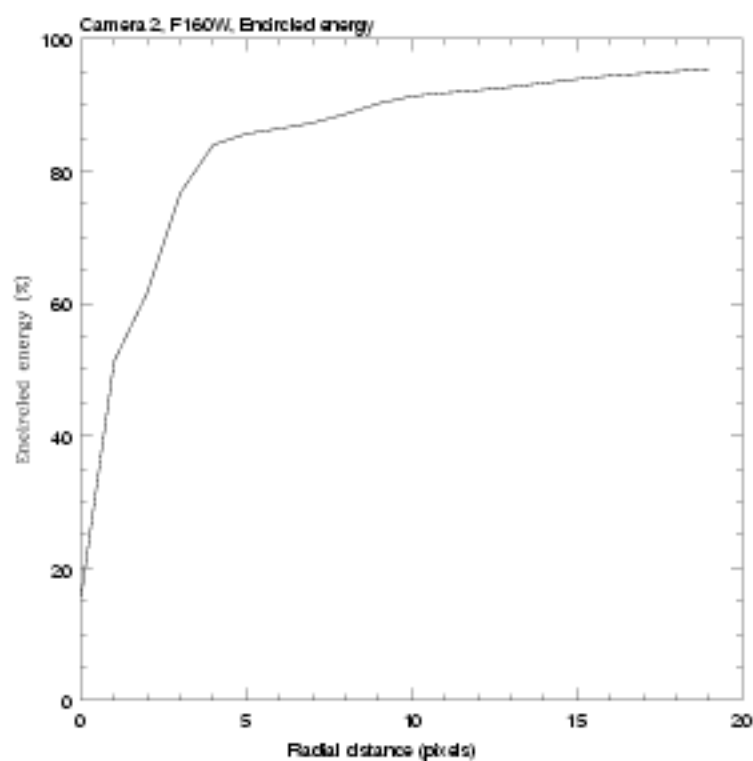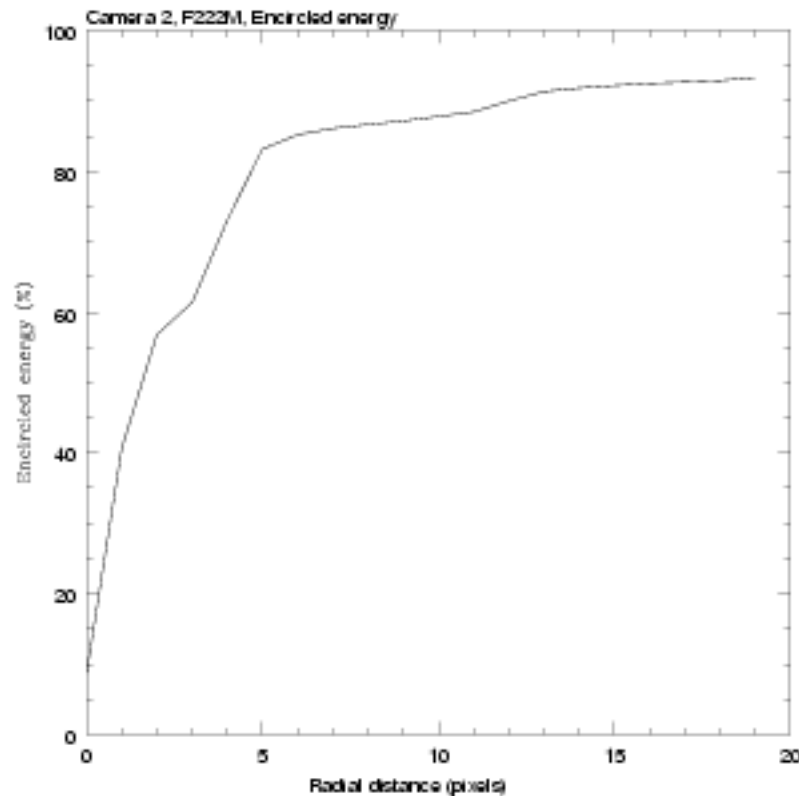Encircled energy (%)

Radial distance (pixels)

Figure 4.10: Encircled Energy for Camera 2, F222M.

The NIC1 and NIC2 foci are sufficiently close that reasonably good quality images will be obtained by each when the PAM is positioned at the optimal focus of the other camera. The slightly defocussed images in NIC1 or NIC2 in parallel will be sufficiently good that parallel observations are strongly encouraged, as discussed below and in Chapter 3.

The PAM mirror must be moved when switching between NIC1 and NIC2 resulting in a 240 second instrument overhead. This may result in slightly less time available for science exposures, particularly if frequent shifts between NIC1 and NIC2 are made during an orbit. Efforts are now underway to reduce this additional overhead, but observers can minimize the impact of any such overheads by reducing the number of switches between NIC1 and NIC2 to a minimum. A compromise focus that shares the wavefront error equally between NIC1 and NIC2 is also supported.

Vignetting in NIC1 and NIC2

The lateral shifts of the NICMOS dewar have resulted in vignetting in cameras 1 and 2 in addition to NIC3. In the case of NIC1 and NIC2, the source of the vignetting is most likely the Field Divider Assembly (FDA) mask. Relatively small losses in throughput are observed near the edges of both NIC1 and NIC2 as shown in Figure 4.11 and Figure 4.12.

Figure 4.11: The curve below shows one column of a ratio between a recent NIC1 flat field at 1.1 µm and a flat field taken during thermal vacuum testing before launch. The overall normalization of the y-axis ratio scale is arbitrary. The approximately 6% decrease seen in rows near the bottom of the detector (labelled Line on this figure) shows the region of the NIC1 detector where vignetting has affected the throughput. The step-like edge near y=128 may be related to a quadrant boundary.
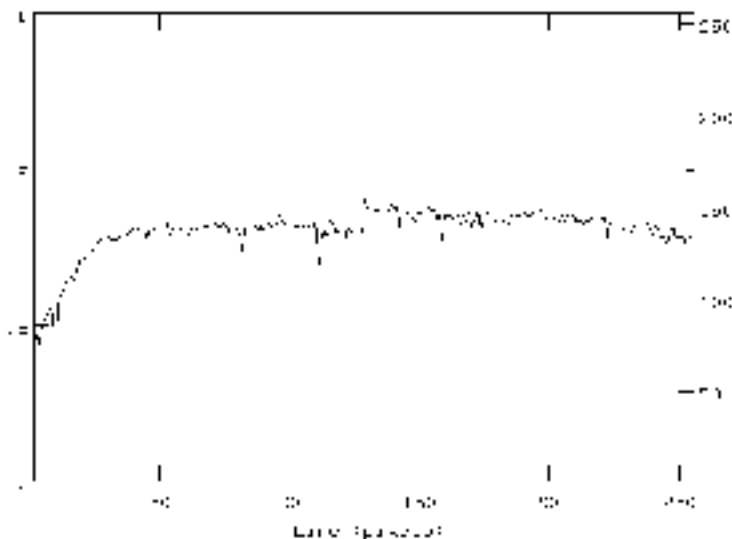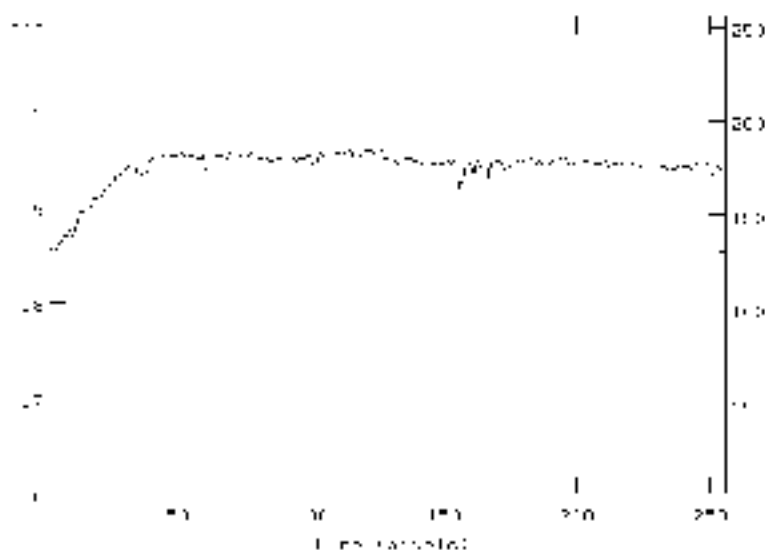

Figure 4.12: Similar to 4.11, this curve shows an approximately 10% decrease in throughput in rows near the bottom of NIC2 from vignetting by the FDA mask.

Camera 3

NIC3 has suffered the largest shift in focus, now estimated to be at a location equivalent to a ~-14 mm motion of the PAM from its nominal position after reaching a maximum of -17.7 mm in late March. Because the PAM is limited to motions of +/- 10 mm, NIC3 cannot now be focussed with the PAM alone.

Figure 4.13 shows a series of measured star images over a range of PAM focus positions. The images were taken in steps of 1 mm of PAM motion from +8 mm on the left to -8 mm on the right. The current (June 30, 1997) best focus positions are +1.68 +/- 0.49 mm (NIC1), −0.32 +/- 0.43 mm (NIC2), and −14.00 +/- 0.06 mm (NIC3). Consequently, at either the NIC1 or NIC2 focus positions, the NIC3 image quality is very poor.

Using the TinyTIM software package it is possible to calculate model PSFs for any PAM position, including positions not reachable by the actual PAM mechanism. The model PSFs produced in this way agree well with the observed PSFs as shown in Figure 4.14, produced by R. Fosbury, R. Hook, and W. Freudling of the ST-ECF.

Figure 4.13: A series of NIC3 images of two stars at different PAM positions ranging from +8 mm to -8 mm (left to right). The upper star is located near the top of NIC 3 (y=225). The lower star is located near the bottom of NIC3 (y=15) in the vignetted region of the detector. Each subimage is centered in a 20 by 20 pixel box (i.e. 4 by 4 arcsec). These images were obtained during the coarse alignment test before the peak expansion of the dewar. The NIC3 focus was estimated to be at a PAM mirror offset of -14.8 mm at that time, similar to the focus at the time of this writing. An image of a point source in NIC3 when NIC2 is prime would be similar to the star images in the sixth or seventh subimage from the left. When NIC1 is prime a NIC3 point source image will be similar to the image in the eighth or ninth subimage from the left. The full range of the PAM mirror extends to -10 mm or two steps farther to the right than covered by this focus sweep.
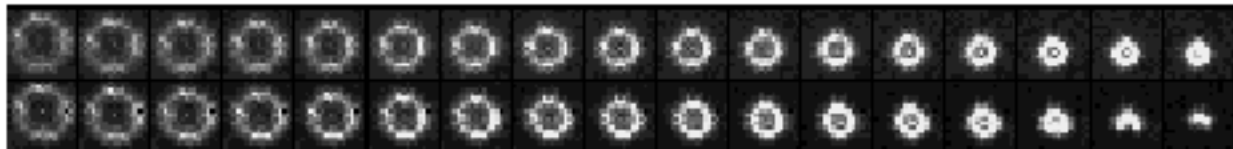
Figure 4.14: Model PSFs computed for NIC3 and several positions of the PAM mirror are shown in the ST-ECF figure reproduced below. Since the figure was produced, the camera 3 focus was moved to ~-14 mm.
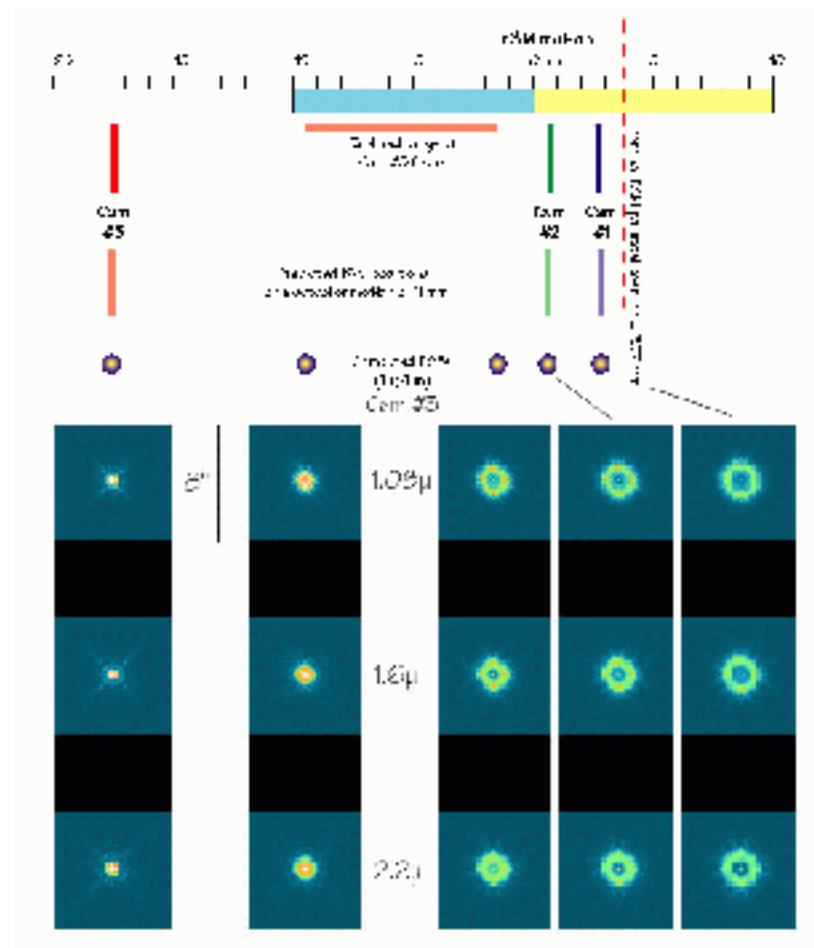
Using the TinyTim models (provided by Richard Hook of the ST-ECF), Figure 4.15 through Figure 4.17 show the encircled energy for Camera 3 in three passbands the infocus, -2mm, and -4 mm defocus positions. The -4 defocus curve corresponds approximately to what can presently be achieved with Camera 3 at the limit of the PAM focus range.

Figure 4.15: Encircled Energy at Three Focii for Camera 3, F110W.
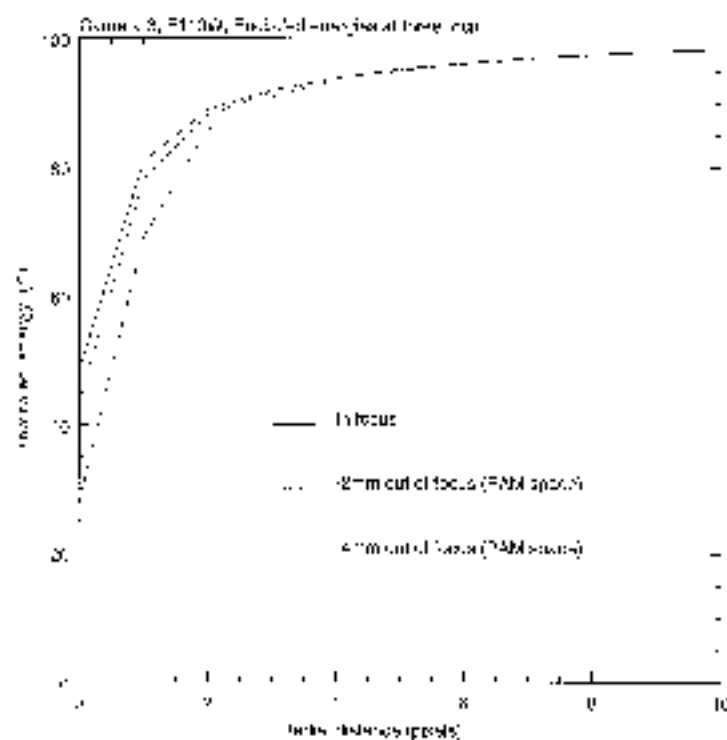
Figure 4.16: Encircled Energy at Three Focii for Camera 3, F160W.
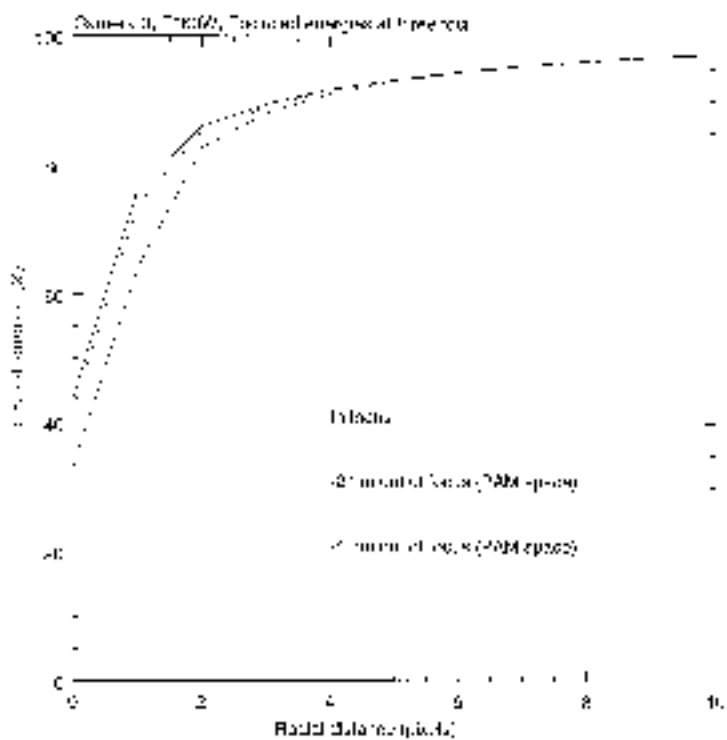
Figure 4.17: Encircled Energy at Three Focii for Camera 3, F222M.
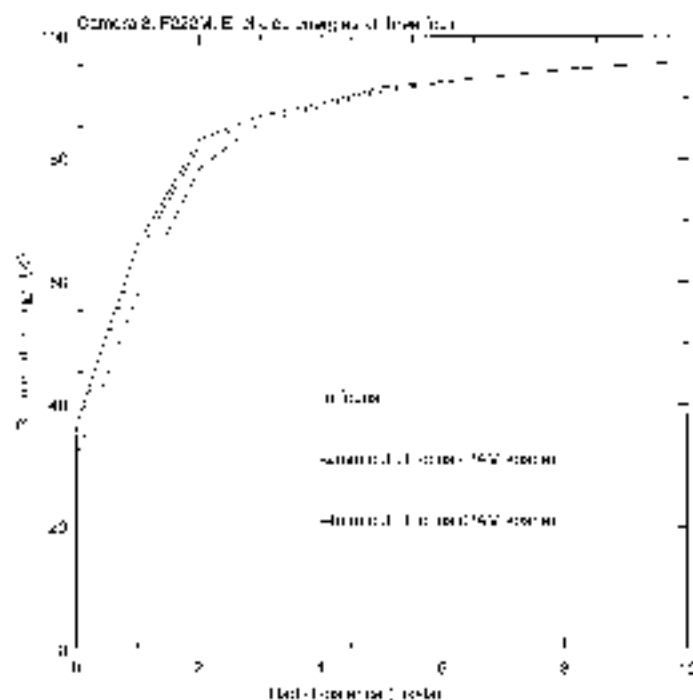
To illustrate the impact on parallel observations, the predicted encircled energy for NIC3 observations of a point source at the three different PAM mirror positions are shown in Figure 4.18. These curves have been derived from model PSFs generated by TinyTim. Observed PSFs are in good agreement with the model PSFs generated by TinyTim. Although Figure 4.18 overstates the present situation (-17.15 vs. the current -14mm focus for NIC3), it shows the limitations of NIC3 parallels when at the NIC1 or NIC2 focus positions.

Figure 4.18: Three curves showing the encircled energy in NIC3 for PAM mirror positions corresponding to -9.5 mm (dashed curve) and the NIC2 (dotted curve) and NIC1 best focus positions (solid curve). The TinyTim program was used to generate the PSFs for an assumed best NIC3 focus corresponding to a PAM mirror offset of -17.5 mm.
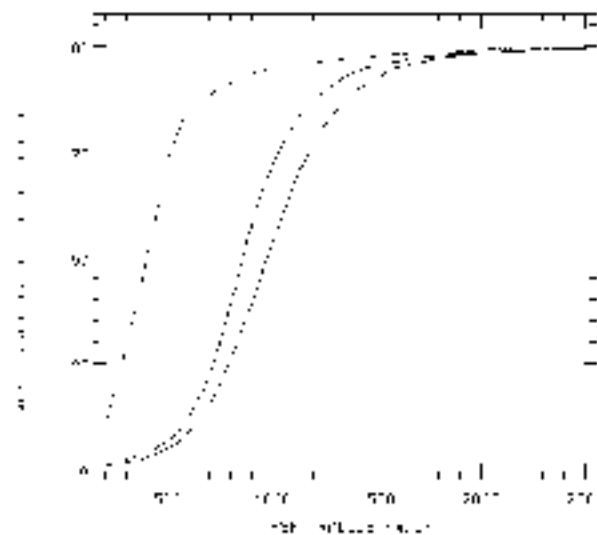
NIC3 Vignetting

In addition to the loss of focus, there is evidence of significant vignetting of the NIC3 field of view. As the PAM mirror is moved to shift the focus forwards or backwards, it simultaneously translates the field of view laterally, moving one or more obstructions into the field of view. The observed vignetting in NIC3 is most likely a combination of a warm bulkhead edge, far from focus, which affects the lower ~1/4 of the detector (in y) and a portion of a mask on the NICMOS field divider assembly (FDA) that results in a decrease in throughput over a smaller portion of the detector. The approximate extent of the warm component of the vignetting is shown in Figure 4.19 and Figure 4.20. This also delineates the portion of the detector where degraded PSFs are observed. Figure 4.21 shows the decrease in throughput over a smaller area caused by the FDA mask.

The vignetting is a function of the PAM mirror position. The figures shown are for a PAM position of -9.5 mm, the closest to focus position available for NIC3. At this focus the vignetting is substantial. However, when NIC3 is observed with the PAM positioned for either NIC1 or NIC2, we do not detect any evidence of vignetting. This effect can be seen in Figure 4.13 where the star images in the lower row show the effects of vignetting at PAM positions of -6, -7 and -8 mm. Repositioning the Field Offset Mirror (FOM) would allow observations in NIC3 with reduced vignetting. Tests sufficient to enable general use of this option are planned for August and September 1997. Should this prove successful, then the new FOM position would be adopted as the default for all Camera 3 observations.

Figure 4.19: A NIC3 flat field at 2.4 µm measured on-orbit divided by a flat field measured during thermal vacum testing shows enhanced thermal background in the lower quarter of the NIC3 detector. This emission is due to vignetting by a warm bulkhead edge that is far from focus. A line plot of a row average is shown in Figure 4.20. Over the same portion of the detector, the PSF is degraded, as shown by the lower set of images in Figure 4.13.
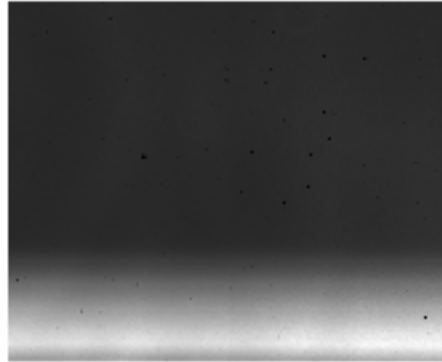

Figure 4.20: The average countrate as a function of row for the NIC3 2.4 µm flat field ratio shown in Figure 4.19 is plotted showing the range of the detector where increased thermal background and degraded PSFs occur. This component of the vignetting is thought to be produced by a warm, out-of-focus bulkhead edge.
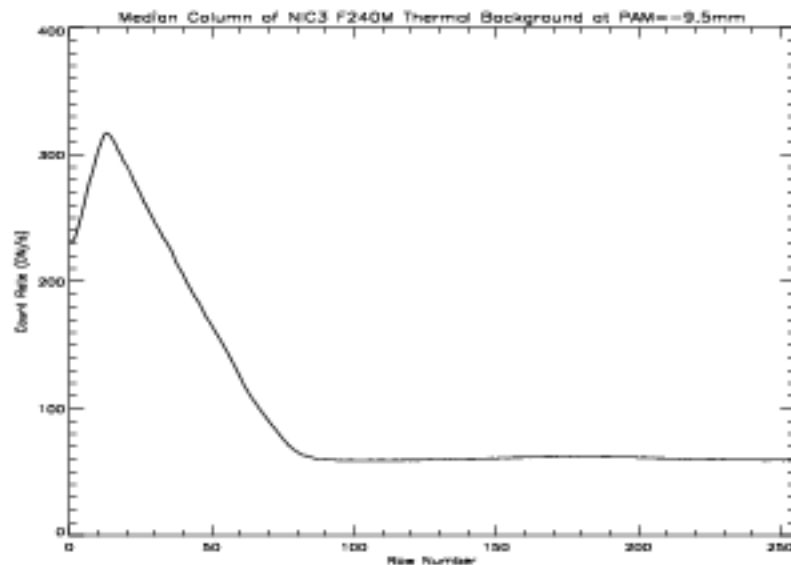
Figure 4.21: A second component of the vignetting in NIC3 is shown in this ratio of a recently measured NIC3 flat to a flat measured during thermal vacuum testing. At 1.1 μm no enhanced thermal emission is detected. However, at rows near the bottom of the NIC3 detector a loss of throughput as large as 60% is evident.
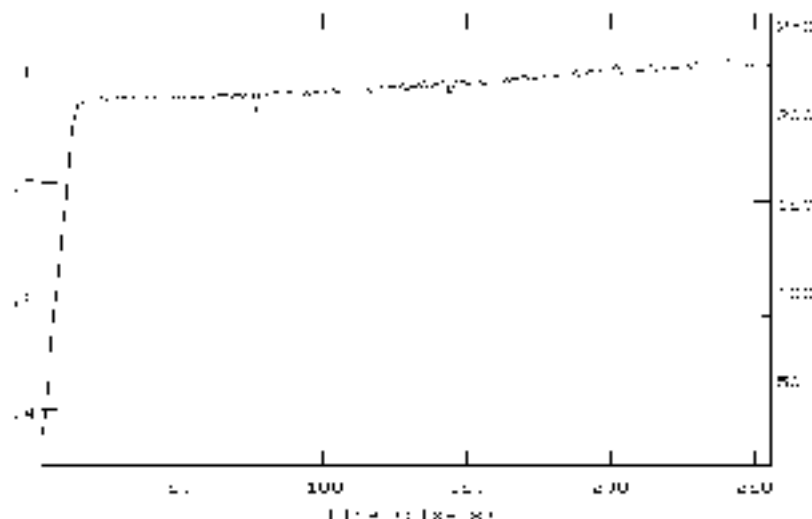
Paths to Recovery of NIC3 Capability

It is possible that at some point the ongoing, normal loss of cryogen from NICMOS will result in a relaxation of the forces on the dewar that have led to the loss of focus for NIC3. If the present trend in the motion of the NIC3 focus position continues, NIC3 may return to focus by late 1997 or early 1998. Even if this does not occur, it will still be possible to obtain optimal focus for NIC3, by refocusing the HST itself. Since motions of the HST secondary mirror impact the operation of other science instruments (e.g., the WFPC2 does not have an internal focusing capability), if an HST refocus is required then NIC3 observations will be performed in one or two "campaigns" during Cycle 7-NICMOS.

▽ Observers are advised to seriously consider the necessity for NIC3 observations and to plan programs with NIC1 or NIC2 whenever possible. It is particularly important to minimize scheduling and orientation restrictions for NIC3 observations.

Field Dependence

The PSF is at least to some extent a function of position in the OTA field of view. Preliminary data indicate that this effect is extremely small and that only a small degradation will be observed. Movement of the FOM, on the other hand, is

expected to have a greater effect on the PSF quality. Since use of FOM motions is an "available" mode (i.e., not supported), an extensive calibration of this is not planned. Initial tests indicate that the PSFs are not strongly effected by FOM motion and some further testing is presently planned.

Transient Bad Pixels

Flat fields taken on orbit show a population of pixels with very low count rates. In some cases, pixels with low count rates in one flat field will be normal in the subsequent one. A working hypothesis is that the bad pixels are caused by debris lying on top of the detectors. Paint flecks from the optical baffles are one possible source of this debris. The largest of these areas of bad pixels occurs in NIC1 and is shown in Figure 4.22 below. Approximately 100 pixels in each of NIC1 and NIC2 are affected by this debris and a similar number are expected to be affected in NIC3. As described below, dithering is recommended for observers who believe that these and other pixel defects could adversely affect their science goals.

Figure 4.22: A portion of a NIC1 flat field image shows the largest of the groups of pixels affected by debris. This bit of "grof' is roughly 5 by 9 pixels and is located in the upper left quadrant of NIC1. This particular group of bad pixels has remained constant for several weeks. Other features are transient on week time scales.
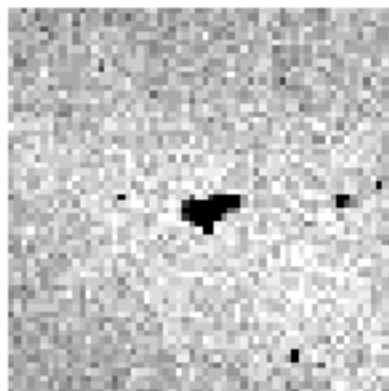
NICMOS Aperture Definitions

Each HST Science Instrument requires its own local coordinate system and apertures to support both target acquisition and small angle motions (SAMs). Apertures are calibrated locations in the HST focal plane relative to the FGS frame. All acquisitions and SAMs are relative to apertures. Any location within the field of view of a NICMOS camera can be specified by the POSTARG special requirement (described in the HST Phase II Proposal Instructions).

Aperture Definitions

The basic philosophy of the NICMOS aperture definitions follows that used by WF/PC-1 and WFPC2. Each NICMOS camera has two primary apertures. One is positioned at the geometric center of the detector and the other at an *optimal* position close to the center. The first of these apertures is anchored to that fixed location, while the second may be moved in the future. In this way the optimal aperture may be shifted to avoid array defects, even if these are time dependent. Observers with large targets which fill the field of view of a particular camera are generally advised to use the first type of aperture, while for observers with smaller targets the second type is recommended

Additional apertures are defined in Camera 2 for use in the Mode 2 coronographic acquisition.

Standard Apertures

The names of the defined apertures are listed in Table 4.4 along with a description of their function and their initial location.

Table 4.4: NICMOS Aperture Definition

Aperture Name	Description	Position (detector pixels)
NIC1	Optimal center of Camera 1	162,100
NIC1-FIX	Geometric center of Camera 1	128,128
NIC2	Optimal center of Camera 2	149,160
NIC2-FIX	Geometric center of Camera 2	128,128
NIC2-CORON	Center of Coronographic Mask	
NIC2-ACQ	Center of Mode 2 ACQ region	
NIC3	Optimal center of Camera 3	140,135
NIC3-FIX	Geometric center of Camera 3	128,128

NICMOS Coordinate System Conventions

Figure 4.24 shows how the NICMOS cameras are arranged in the HST field of view. The alignment of each camera is not exact, and the internal coordinate systems attached to each of them will differ by small rotations (probably <2 degrees). The FITS format data files generated for NICMOS observers will have a World Coordinate System specified appropriately for each camera. The adopted coordinate system for the 3 cameras is summarized in Figure 4.23.

Figure 4.23: Common NICMOS Coordinate System
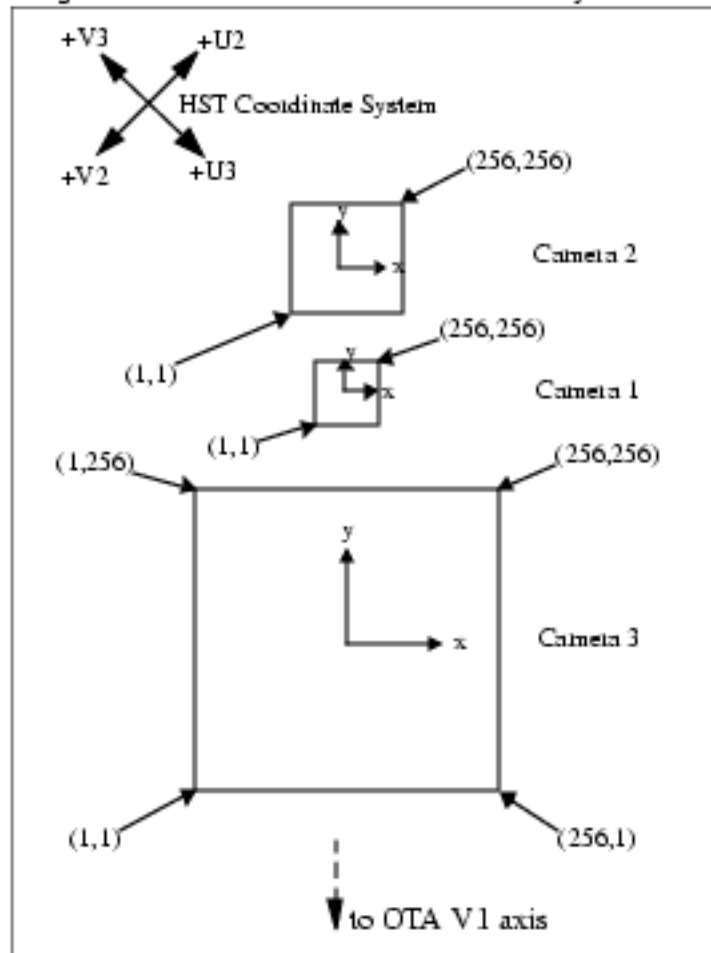
Orients

NICMOS orientations are specified relative to the +y axis shown in Figure 4.23. Eastward rotations are counterclockwise (in the usual astronomical convention). Spacecraft orientations are rotated by 225 degrees from the NICMOS coordinate system.

Due to the linear arrangement of the 3 NICMOS cameras on the sky, it will often be advantageous to consider the specification of a unique telescope orientation. Observers should be aware that such constraints may decrease the duration and number of scheduling opportunities for their observations and, under some circumstances, may make the identification of suitable guide stars impossible.

Figure 4.24: Definition of Orient for NICMOS
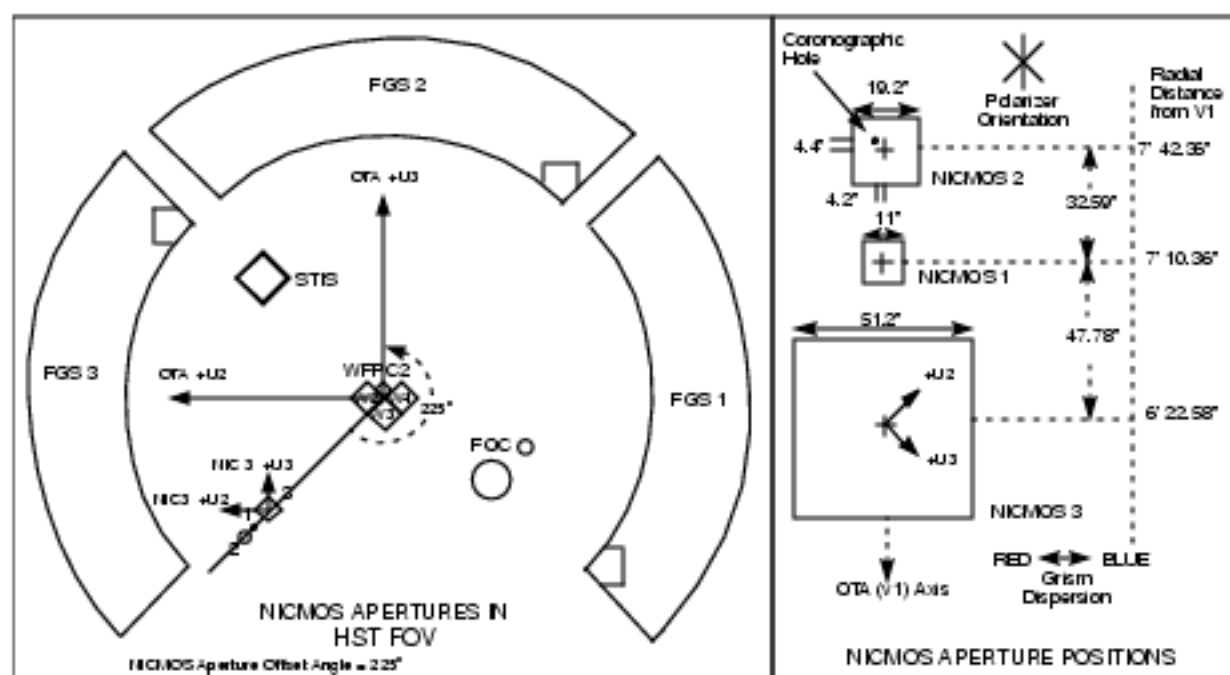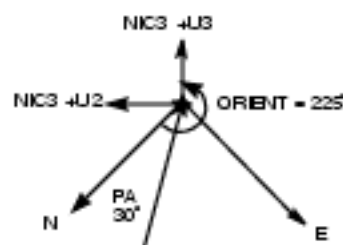
While the Phase II proposal instructions contain the definitive instructions and examples for specifying the desired orientation for HST. We provide a simple example in Figure 4.24. A binary star with a position angle (PA) 30 degrees measured east from north is to be positioned with the southern star in Camera 3 and the northern star in Camera 2. That is, we want the line connecting the two stars to lie along the NICMOS +y axis. The resulting HST orientation is 225 + 30 = 255 degrees. (HST ORIENT = PA + 225 for NICMOS).

Coronography, Polarimetry and Grism Spectroscopy

This chapter provides information on three specialized uses of NICMOS, namely, coronography, polarimetry, and grism spectroscopy.

Coronography

A coronographic imaging mode is available in NIC2. This camera has 0.075 arcsec pixels, covering a 19.2 x 19.2 arcsec region of the sky. The coronographic spot imaged onto the focal plane provides a circular occulted region 0.3 arcsec in radius. At this radius, in an idealized Point Spread Function, a natural break occurs in the encircled energy profile at 1.6 microns with 93 percent of the energy in the PSF being enclosed. Beyond, the encircled energy profile flattens out toward larger radii.

The Camera 2 coronograph comprises two elements. A 170 micron diameter hole has been laser ablated out of the Camera 2 mirror in the NICMOS field divider assembly, which is at the image plane. (Small irregularities within a 10 microns annulus at the edge of the hole may be a source of residual scattered light in the images.) An oversized cryogenic pupil-plane mask screens out residual radiation from the edges of the HST primary and secondary mirrors and the secondary mirror support structures (pads, spider, and mounts.). This mask

obscures approximately 15% of the primary mirror area. (Scattering by dust on the primary mirror may affect the overall image contrast, and while this is expected to be a small effect it can only be quantified on-orbit.).

▽ The SMOV measurements of coronographic performance were being carried out as this version of the *NICMOS Instrument Handbook* was written. A preliminary description of the results of the SMOV tests will be placed on the STScI NICMOS WWW page on August 1, 1997.

Initial indications are that the coronograph meets or exceeds expectations.

Coronographic Acquisitions

Coronographic imaging requires an acquisition sequence at the beginning of the observation to center the target onto the occulting spot since the size of the occulting spot is smaller than typical HST blind-pointing errors. The procedure for a coronographic observation is to first acquire the target on the NIC2-ACQ aperture using an onboard, reuse target offset, or interactive acquisition.

The science exposures are then specified using any of the NICMOS observing modes with the target positioned on the NIC2-CORON aperture (which is behind the coronographic spot).

Onboard Acquisition (ACQ mode)

The NICMOS flight software includes an automatic target acquisition mode. A coronographic acquisition is requested through the proposal interface (exposure logsheet), as an ACQ exposure using the NIC2-ACQ aperture as described in the NICMOS Phase II Proposal Instructions. In this process, after pointing to the field and acquiring guide stars, two images of the target are taken (for cosmic ray removal), and the brightest object is located in a 128 x 128 pixel sub-array in the coronographic acquisition aperture (see Chapter 8). The NICMOS flight software will then request a vehicle slew to move the spacecraft to place this object in the center of the occulting spot. This is illustrated in Figure 5.1 which shows a schematic representation of the Camera 2 acquisition aperture. The observer must select the filter type and the exposure time (see the flow chart in Figure 5.4). The telescope is pointed so that the target nominally appears at the aperture NIC2-ACQ which is located in a 128 x 128 logical acquisition aperture. The acquisition software, analyzes this aperture, locates the center of the target, and offsets the telescope so that the target is placed behind the occulting spot.

Figure 5.1: Acquisition Process
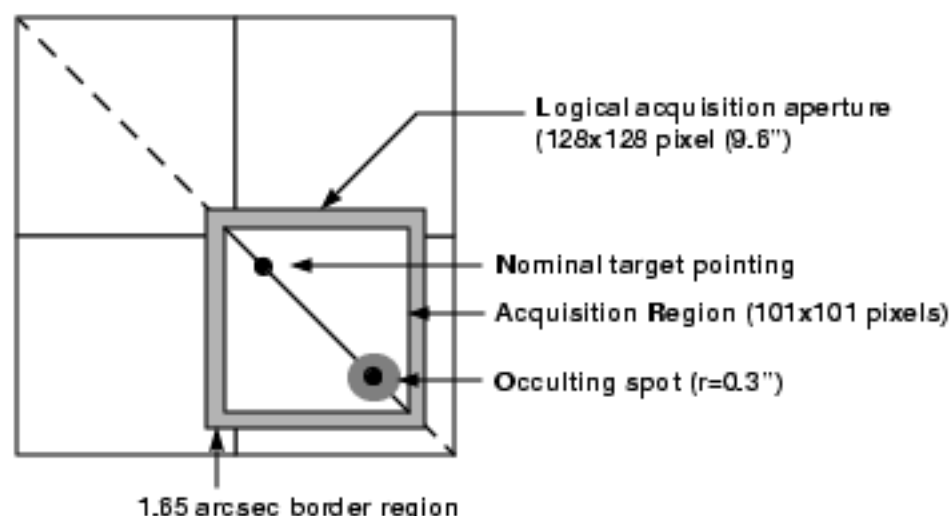
Very bright targets might cause saturation, leading to poor results in the centroid solution, and in the subsequent placement behind the occulting spot. To avoid this, a narrow band filter may have to be used to cut down the target flux. Since the NICMOS filters are in the pupil plane there should not be a shift introduced by using a different filter than needed for the science observations.

For observations longer than ~5 minutes the probability of cosmic ray hits occurring in the same pixel in each of the two acquisition images is sufficiently high that observers must instead use an early acquisition image to avoid their observation failing due to a false center determination. Early acquisitions are described in the next section. In practice, this should not be a severe restriction as in the F160W filter one will reach a signal-to-noise of 50 at H=17 in only 2–3 minutes.

Reuse Target Offset and Interactive Acquisitions

In crowded fields, or for extended objects, the coronographic acquisition should not be relied on, since by necessity the on-board centering algorithm is rather simple. Whenever you know *a priori* that this is the situation, or the complexity of the field is unknown, we recommend obtaining an acquisition image before the scientific observation instead, even though this will require slightly more HST observations to accomplish your program. The telescope control system has the ability to re-use the same pair of guide stars as were used for the acquisition exposure, and from the accurate coordinates you have obtained, it is then possible to blind-offset the source onto the coronographic spot (RE-USE TARGET OFFSET). This can be obtained a few orbits or days prior to the science exposure. Alternatively, a real-time, interactive acquisition (INT-ACQ) can be obtained although the number of these are limited and must be justified in the Phase 1 proposal. This will mainly be necessary for time critical observations.

Detector and Coronographic Hole Motion Issues

Since the coronographic hole is located in the field divider assembly (FDA) external to the dewar, the position of the image of the hole on the NIC2 detector will change with any relative motions between the FDA and NIC2. Some motion was expected due to the release of gravity but continuing motion has occurred on both long and short (orbits) timescales. Figure 5.2 graphically shows the offset.

Figure 5.2: A ratio of a recent flat field taken on-orbit and a flat field measured during thermal vacuum testing shows the change in position of the coronographic hole in that interval. Approximately half of this motion was expected relaxation in zero-G, the remainder has resulted from the deformation of the NICMOS dewar. The bright spot marks the location of the spot at the time of the on-orbit flat field; the dark spot shows its location during thermal vacuum testing before launch. More recent observations show the coronographic spot moving back towards its expected on-orbit position. The bright region near the bottom of the detector shows the area of the detector that is vignetted by a mask on the field divider assembly.
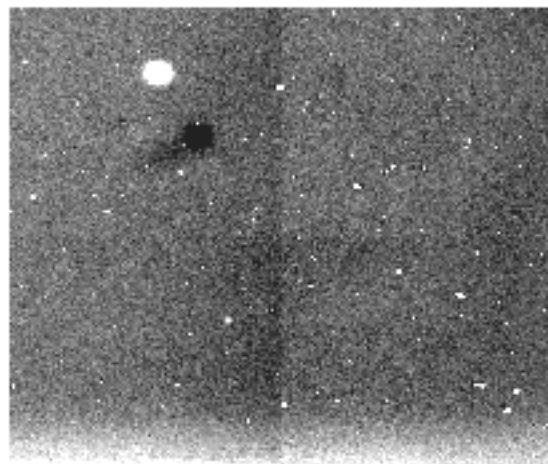
While the motion during a single orbit appears to be <0.25 pixels, a method of locating the coronographic hole's image on the NIC2 detector as part of the target acquisition process is underway and will be supported in Cycle 7-NICMOS.

PSF Centering

Both the total encircled energy rejection (from the occulted core of the PSF) and the local contrast ratio obtainable in a coronographic image depend on the accuracy of the target centering on the occulting spot. The goal is to center the PSF of the occulted source to a precision of a quarter pixel. The decrease in the fractional encircled energy due to imprecise centering of the core of an idealized PSF in the occulting spot is 0.3 percent for a 1/4 pixel offset, and 4.4 percent for a 1 pixel (75 milliarcseconds) offset at 1.6 microns. The predicted fractional decrease in the encircled energy relative to that for a perfectly centered PSF is plotted against the shift of the center of the PSF from the center of the hole in Figure 5.3.

Figure 5.3: Contrast Decrease Due to PSF De-centering

Shift of PSF from coronographic center (milliarcsec)
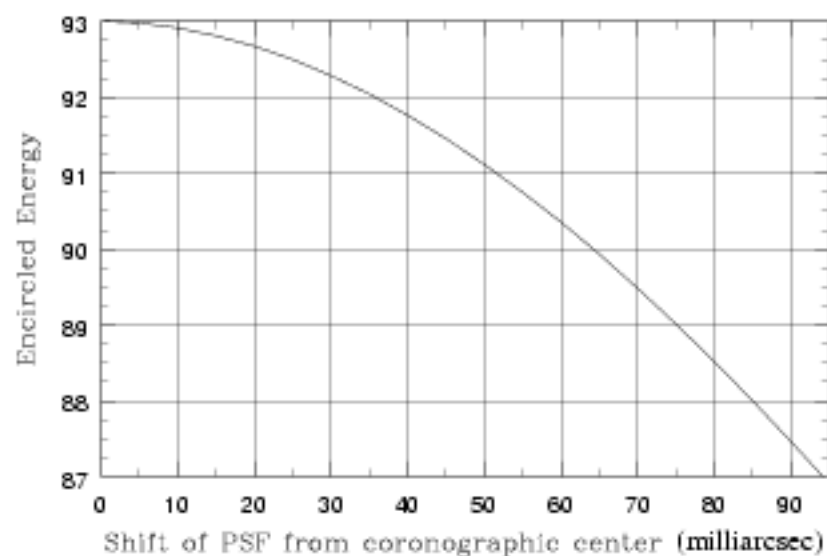
However, a small error in target centering will create an asymmetric displacement of the PSF zonal structures both in and out of the occulting spot, leading to position dependent changes in the local image contrast ratios.

Coronographic Decision Chart

The decision chart given in Figure 5.4 leads you through the selection process to construct a coronographic observation.

Figure 5.4: Coronographic Decision Chart
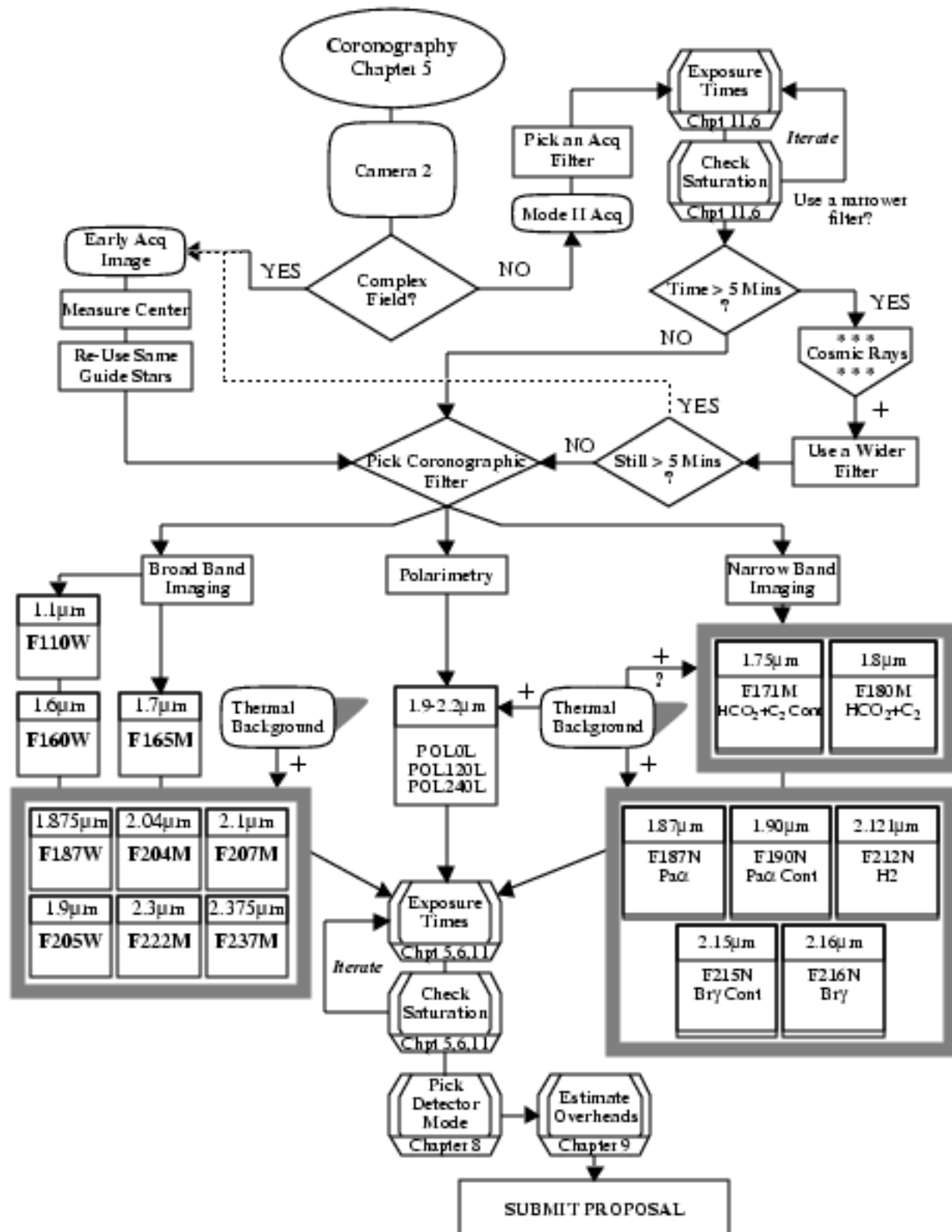
Polarimetry

Cameras NIC1, and NIC2, each contain 3 polarizers, whose principal axes of transmission are separated by 120 degrees. Observations in all three polarizers will provide the Stokes parameters of linearly polarized light. The spectral coverage is fixed for each camera, and the polarizers cannot be crossed with other optical elements. For Camera 1, the polarizers cover the wavelength range 0.8 to 1.3 microns, and for Camera 2, 1.9 to 2.1 microns.

Instrumental Polarization

Since there are a number of internal reflections in NICMOS prior to reaching the polarizers there will be instrumental polarization, estimated to be 1 to 2 percent. It should, however, be quite stable. Measurements of polarized and unpolarized standard stars will be obtained as part of the Cycle 7 calibration program and these will be used to measure the instrumental polarization and the zero position angle for each polarizer (remember the actual zero point will depend on your spacecraft orient).

Theory

The raw polarimetric images obtained through the three polarizers will be routinely processed by the first stage of the pipeline like any other exposure. The resulting images will have been placed onto a common intensity scale by correcting for the relative transmissions of each of the polarizers. If we define the intensity and statistical uncertainties (including read-noise) obtained in the 3 polarizers after processing by the pipeline to be I_0, I_{120} and I_{240} and σ_0, σ_{120}, σ_{240} respectively, then we may obtain the total intensity I from:

$$I = \frac{2}{3}(I_0 + I_{120} + I_{240})$$

and the Stokes parameters Q and U:

$$Q = \frac{2}{3}(2I_0 - I_{240} - I_{120})$$

$$U = \frac{2}{\sqrt{3}}(I_{240} - I_{120})$$

The statistical uncertainties are obtained by straightforward propagation of errors:

$$\sigma_I = \frac{2}{3}\sqrt{[\sigma_0^2 + \sigma_{240}^2 + \sigma_{120}^2]}$$

$$\sigma_U = \frac{2}{\sqrt{3}}\sqrt{[\sigma_{240}^2 + \sigma_{120}^2]}$$

$$\sigma_Q = \frac{2}{3}\sqrt{[+\sigma_0^2 + \sigma_{240}^2 + \sigma_{120}^2]}$$

The Stokes parameters can then be combined to yield the polarized intensity, I_p:

$$I_p = [Q^2 + U^2]^{1/2}$$

and the degree, P, and position angle of polarization, θ, using:

$$P = \frac{I_p}{I}$$

$$\theta = 28.648\tan^{-1}\left(\frac{U}{Q}\right)$$

Polarimetry Decision Chart

The decision chart given in Figure 5.5 leads you through the selection process to construct a polarimetry observation.

Figure 5.5: Polarimetry Decision Chart
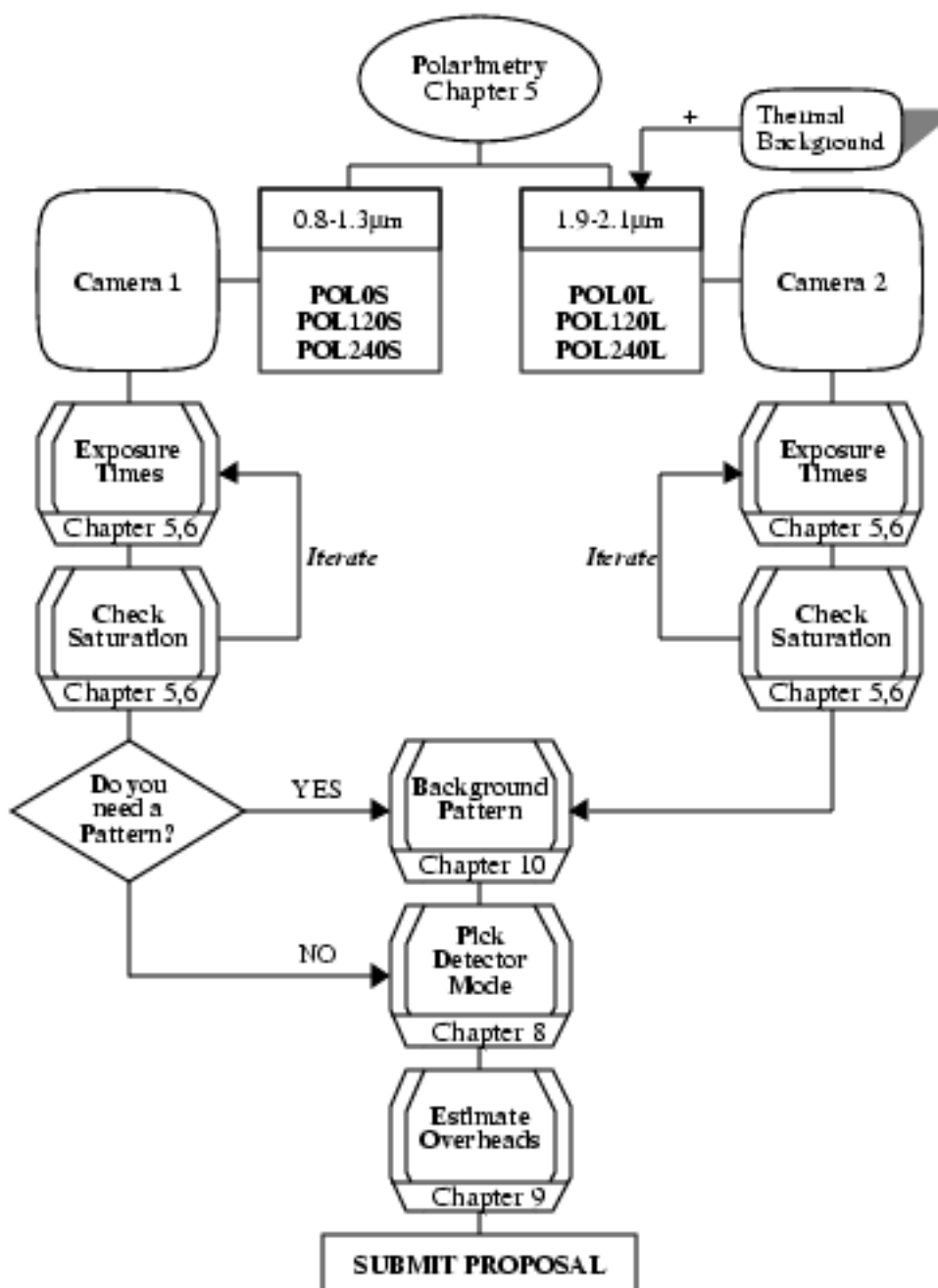
Polarimetric Sensitivity

As with the imaging filters, sensitivity information for the two sets of polarizers may be obtained from the Exposure Time Calculator. It gives the same information as was described in Chapter 4: namely a sensitivity curve, plotted as flux against time for a constant S/N ratio and an exposure *exclusion* curve for both point and extended sources. To use these, look up the integration time required for your source flux on the sensitivity curve for the signal to noise you want (see Chapter 12 if you need to convert the units). Then go to the associated *exclusion* curve and check that you are not in the shaded areas. If you are, adjust your integration time appropriately until you are in the clear area. If you are to the left of the vertical dashed line then you must use bright object mode. Work out how many integrations you need to get your desired S/N. To get the total exposure time required for a polarimetric observation multiply your final answer by 3 to account for the fact that you need to use 3 polarizers to get a measurement. Note that the transmission curves are for a 100% polarized source while all the sensitivity information here is calculated for a single polarizer image, assuming an unpolarized source.

The polarizers have yet to be extensively tested or calibrated – this will be accomplished as part of the Cycle 7 calibration program. Current estimates are than single observations will have ~1% uncertainties implying 3-5% accuracy for polarization measurements.

In NIC1 the POL120 filter only has 48% transmission while the POL0 filter has 98%. Observers may wish to consider using POL0 at multiple spacecraft roll angles rather than POL120. Further, there is some indication of ghost images in the polarizers.

Further information on the performance of the polarization capability should become available in August 1997 and will be posted on the STScI NICMOS WWW page as soon as possible.

Camera 1, Polarizers

The polarizers consist of 3 identical elements at relative angles of 0, 120, and 240 degrees.

Central (microns)	Mean (microns)	Peak (microns)	FWHM (microns)	Range (microns)	Principal Tr percent	Pixel fraction
1.0450	1.0384	1.0245	0.4750	0.8–1.3	77.60	0.048

Figure 5.6: Throughput of Short Wavelength Polarizers
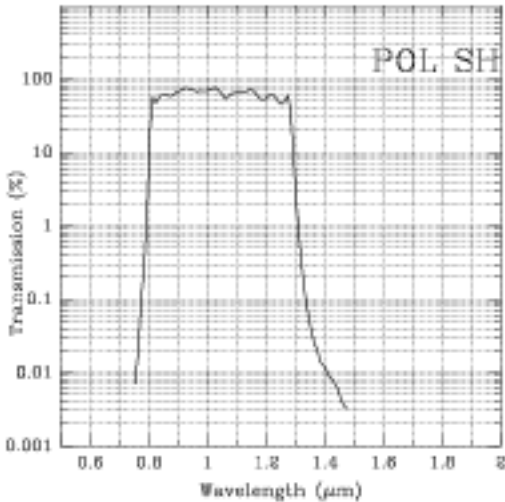
Camera 2, Polarizers

The polarizers consist of 3 identical elements at relative angles of 0, 120, and 240 degrees. Thermal background is important.

Central (microns)	Mean (microns)	Peak (microns)	FWHM (microns)	Range (microns)	Principal Tr	Pixel Fraction
1.9943	1.9946	1.9100	0.2025	1.9—2.1	96.67	0.33

Figure 5.7: Throughput of Long Wavelength Polarizers
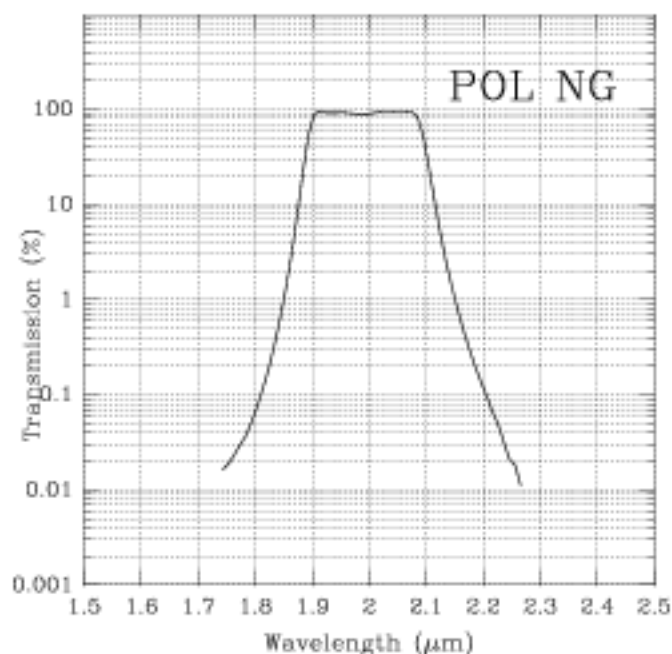
Grism Spectroscopy

A grism is a combination of a prism and grating arranged to keep light at a chosen central wavelength undeviated as it passes through the grism. Grisms are normally used to create spectra in a camera by inserting the grism into the normal camera beam. The grism then creates a dispersed spectrum centered on the location of the object in the camera field of view. The resolution of a grism is proportional to the tangent of the wedge angle of the prism in much the same way as the resolution of gratings are proportional to the angle between the input and the normal to the grating.

NICMOS uses this mode of operation without any slit or aperture at the input focus so that all objects in the field of view display their spectra for true multi-object spectroscopy. The NICMOS grisms operate in the spectral range between 0.8 and 2.5 μm. The grisms reside in the filter wheel for Camera 3, therefore the spatial resolution of the spectroscopy is similar to the spatial

resolution of Camera 3. The filter wheel contains three grisms, of infrared grade fused silica, which cover the entire NICMOS wavelength range with a spectral resolving power of ~200 per pixel.

▽ Since the Grisms are located exclusively in Camera 3, they are subject to the same limitations and policies as all other NIC3 observations.

Also, so far all SMOV grism tests have been obtained with NIC3 significantly out of focus. These data *suggest* that the grisms will perform as expected.

The two shorter wavelength grisms exploit the low natural background of HST while the longest wavelength grism is subject to the thermal background emission from HST.

The NICMOS grisms have an interference filter coated on their entrance faces to limit the bandpass of the spectrum. This is necessary to prevent overlap of orders and reduce thermal background from the telescope. Since the NICMOS grisms do not have an input slit or aperture, there is not a reduction of the background flux found in slit dispersing systems. This is not a significant problem in the shorter wavelengths, but the long wavelength grism has a high background flux.

The basic parameters of the NICMOS grisms are given in Table 5.1.

Table 5.1: Grism Characteristics

Grism	Resolution per Pixel	Central Wavelength	Wedge Angle	Bandpass	Lines per mm
A	200	0.964	5.219	0.8 - 1.2	45.0
B	200	1.401	5.5889	1.1 - 1.9	30.769
C	200	2.058	5.6944	1.4 - 2.5	21.05

Relationship Between Wavelength and Pixel

Table 5.2 gives the dispersion relationship in the form:

wavelength = m*pixel + b,

where wavelength is in microns and the 0 pixel is at the central wavelength. The relationship is plotted in Figure 5.8. The actual location of the plus and minus pixels will be dependent on the grism orientation and the location of the source in the image. The grisms are aligned as accurately as possible along a row or column of the array. We do not expect any distortion or curvature in the spectrum.

The orientation and position of the spectra relative to the direct object has been measured in orbit and has been confirmed to be identical to the Thermal Vacuum measurements. The current best estimates of the dispersion relations are those measured before launch.

Table 5.2: Wavelength to Pixels Relationship (prelaunch)

Grism	m	b
1	-0.005126312	0.9638530
2	-0.007379983	1.4098832
3	-0.010506387	2.0583025

Figure 5.8: Wavelength Versus Pixel Number for each Grism. Note that the actual location of the central wavelength on the detector depends on the position of the source.
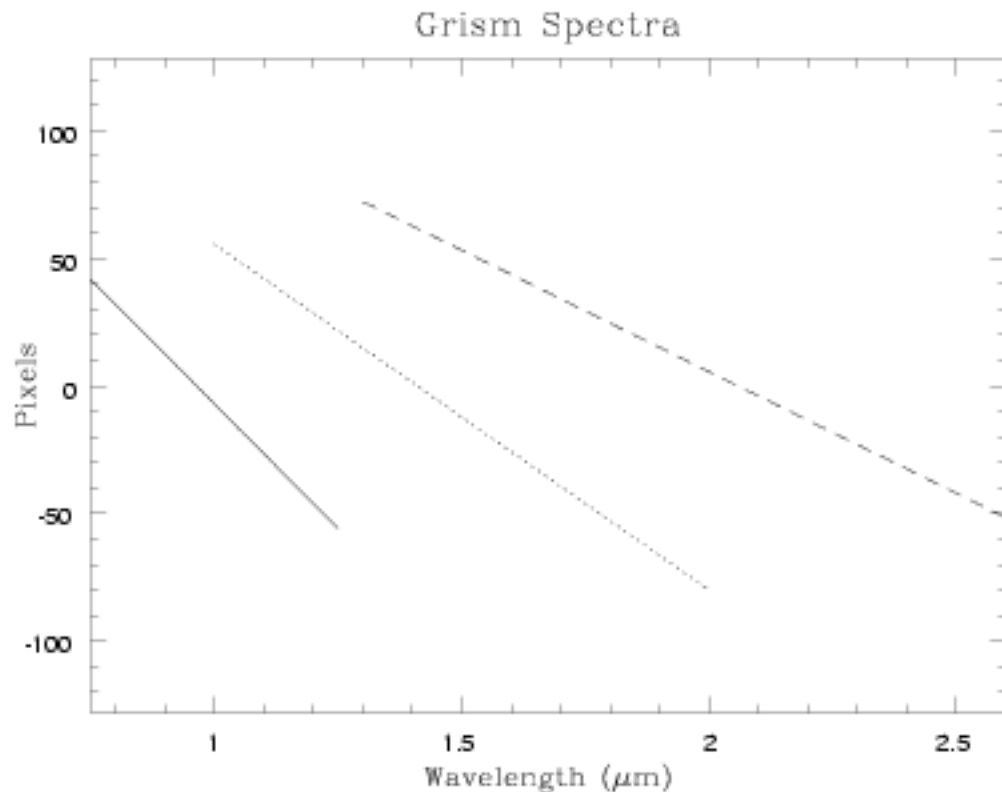
Multi-Object Spectroscopy

Grism observations are carried out in the same manner as any of the imaging operations discussed earlier. In multi-object spectroscopy one of the grisms in the filter wheel for NIC3 will be selected. The observations then proceed via one of the readout and operation modes discussed later.

Although multi-object spectroscopic observations can stand alone with no supporting observations, we recommend pairing them with an image in Camera 3, through an appropriate filter, at the same pointing. This provides the location of each object in the field and aids in the identification of their individual spectra. Because of this natural pairing it is anticipated that most spectroscopy observations will be in at least a two image sequenced observation.

The direction of dispersion is perpendicular to the radial direction in Camera 3 where the radial direction is defined by a vector originating at the center of the field of view for Camera 3 and pointing toward the center of the OTA axis. In complex fields, such as extended objects and crowded fields, individual spectra of targets may overlap and cause confused images. In such cases, it may be possible to alleviate the superposition of spectra by requesting a specific orientation of the telescope during the Phase II Proposal submission. For complex fields, several different orientations may be necessary so that the individual spectra can be deconvolved from those of other sources in the field. It should be recognized that specifying an orientation for a grism observation creates constraints on the number of visibility windows available for scheduling. If different orientations are needed to unscramble the source spectra, then this will make telescope scheduling difficult.

Since Camera 3 may only be available for use during one or two campaigns (at presently unknown dates), some orientation constraints could easily prove impossible to satisfy.

Grism Decision Chart

The decision chart given in Figure 5.9 leads you through the construction of a grism observation.

Figure 5.9: Grism Decision Chart
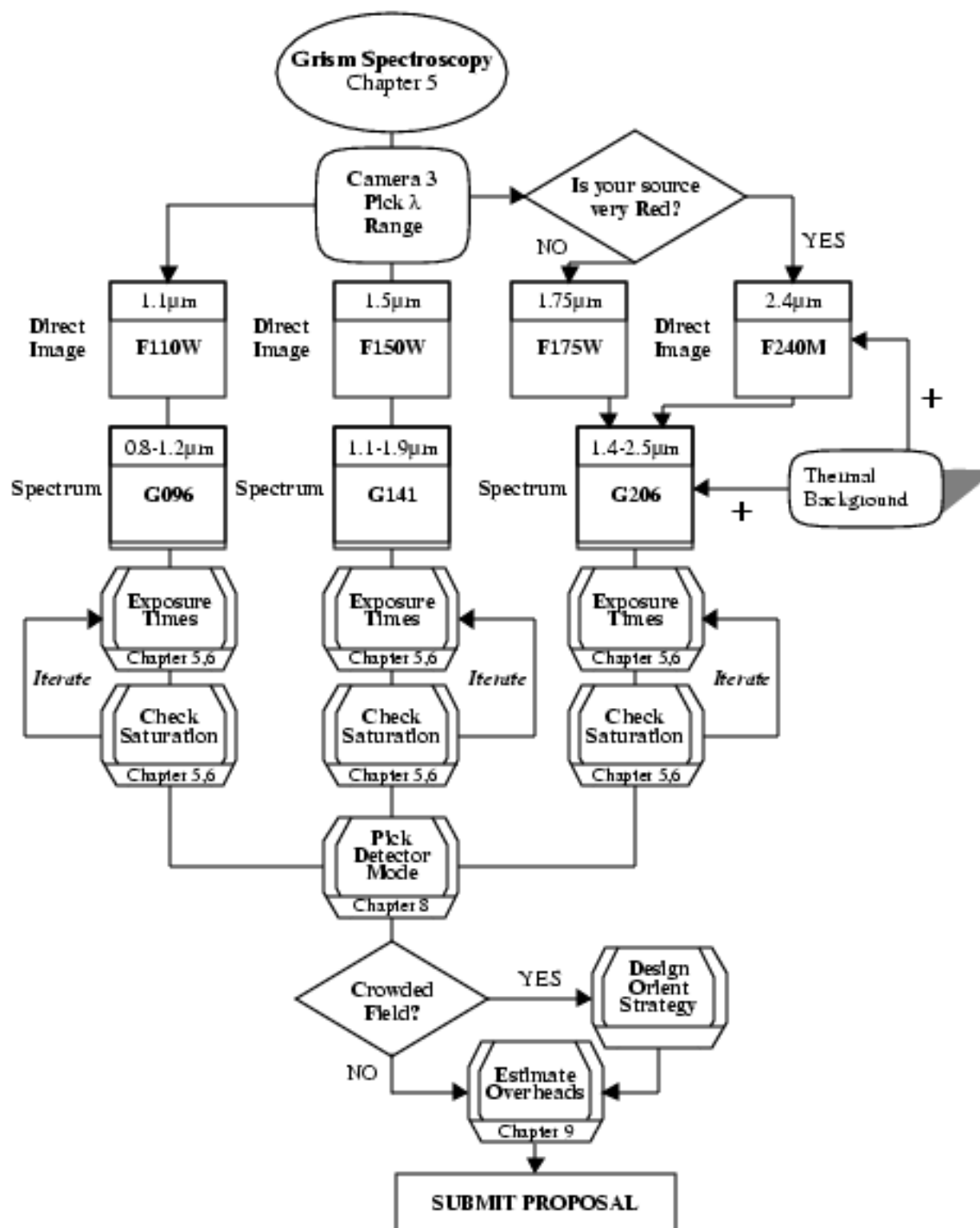
Sensitivity

Background radiation will be a greater concern for grisms than for imaging observations. Every pixel on the array will receive background radiation over the spectral bandpass of the particular grism, while the source spectrum will be dispersed over many pixels. Therefore, the ratio of the source to background flux will be much lower for the grisms than for the regular imaging mode filters. The expected detected background rate per pixel is shown in Table 5.3 below for the three grisms. The increase in the background flux for grism C is dramatic. Use grisms A and B when possible. Grism C is for the longer wavelengths only.

Table 5.3: Grism Background Radiation

Grism	Wavelength range microns	Background (e⁻/sec/pixel)	Background (Jansky/pix)
A	0.8-1.2	0.42	3.2×10^{-5}
B	1.1-1.9	1.6	9.5×10^{-5}
C	1.4-2.5	360	0.013

Figures 5.10 through 5.12 present the basic information for the three NICMOS grisms. Note that for Grism C, the large thermal background means that exposures can never be longer than about five minutes, even for faint sources, because the detector will be saturated by the background. As with other modes, observers should use the Exposure Time Calculator to estimate the signal-to-noise and exposure times for grism observations.

The ETC also provides a line correction factor curve. To use this, find the wavelength of your line and read off the correction factor ε_G from the graph. As described in Chapter 4 multiply the line flux by this factor and add to the continuum flux. The integration time may now be calculated from the sensitivity curve as if you had a pure continuum source. To use the sensitivity curves look up the integration time required for your source flux on the sensitivity curve for the signal to noise you want. Then go to the associated *exclusion zone* curve and check that you are not in the shaded areas. If you are, adjust your integration time appropriately until you are in the clear area. If you are to the left of the vertical dashed line then you must use bright object mode.

Grism A: G096

Table 5.4: Grism A: G096

Central (microns)	Mean (microns)	Peak (microns)	FWHM (microns)	Range	Max Tr (percent)
0.9673	0.9911	1.0010	0.4029	0.8–1.2	69.8
Continuum Filter F110W					
1.0998	1.1035	1.2035	0.5915	0.8–1.4	94.9

Figure 5.10: Grism A Throughput.
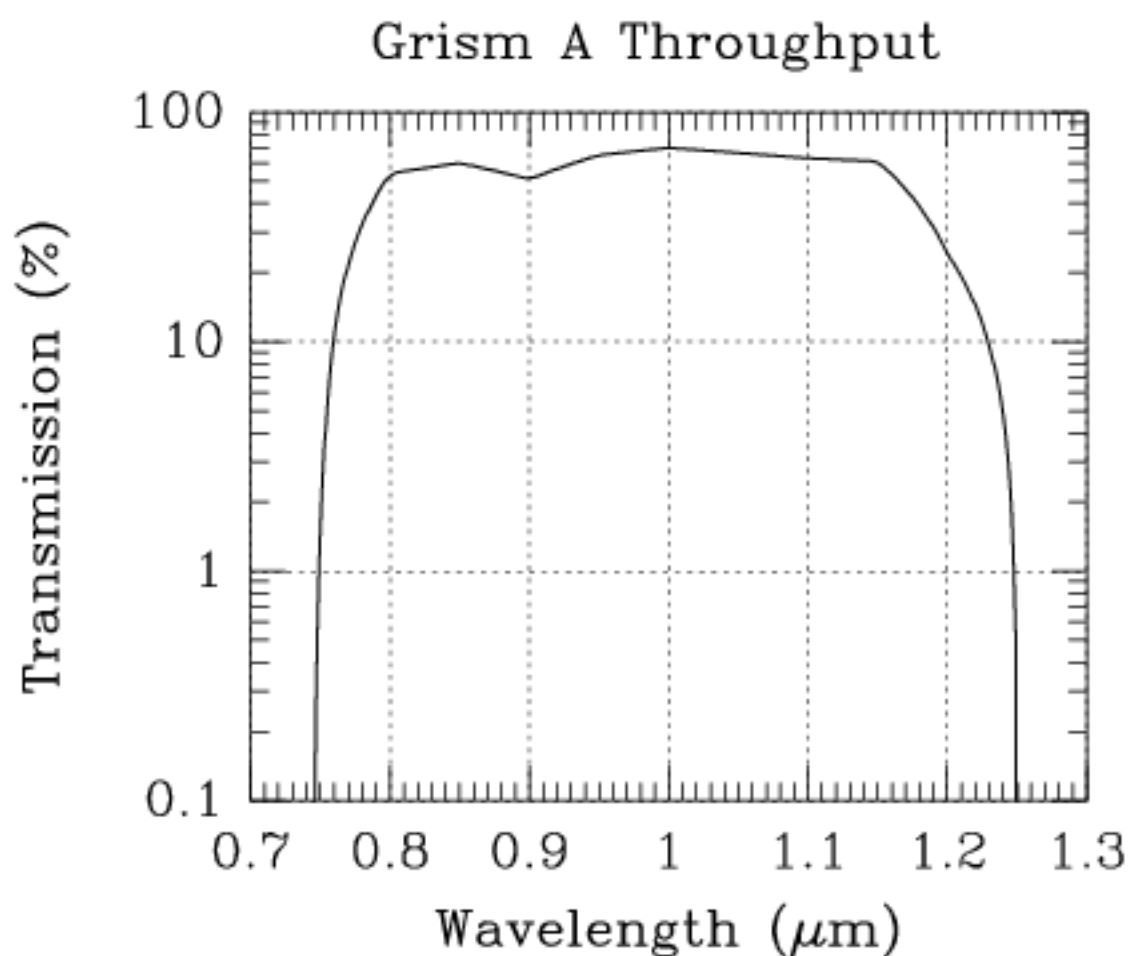
Grism B: G141

Thermal background is important.

Table 5.5: Grism B: G141

Central (microns)	Mean (microns)	Peak (microns)	FWHM (microns)	Range (microns)	Max Tr (percent)
1.414	1.5100	1.4020	0.7914	1.1–1.9	74.7
Continuum Filter F150W					
1.5035	1.5069	1.6355	0.8020	1.1–1.9	97.7

Figure 5.11: Grism B Throughput.

Grism B Throughput
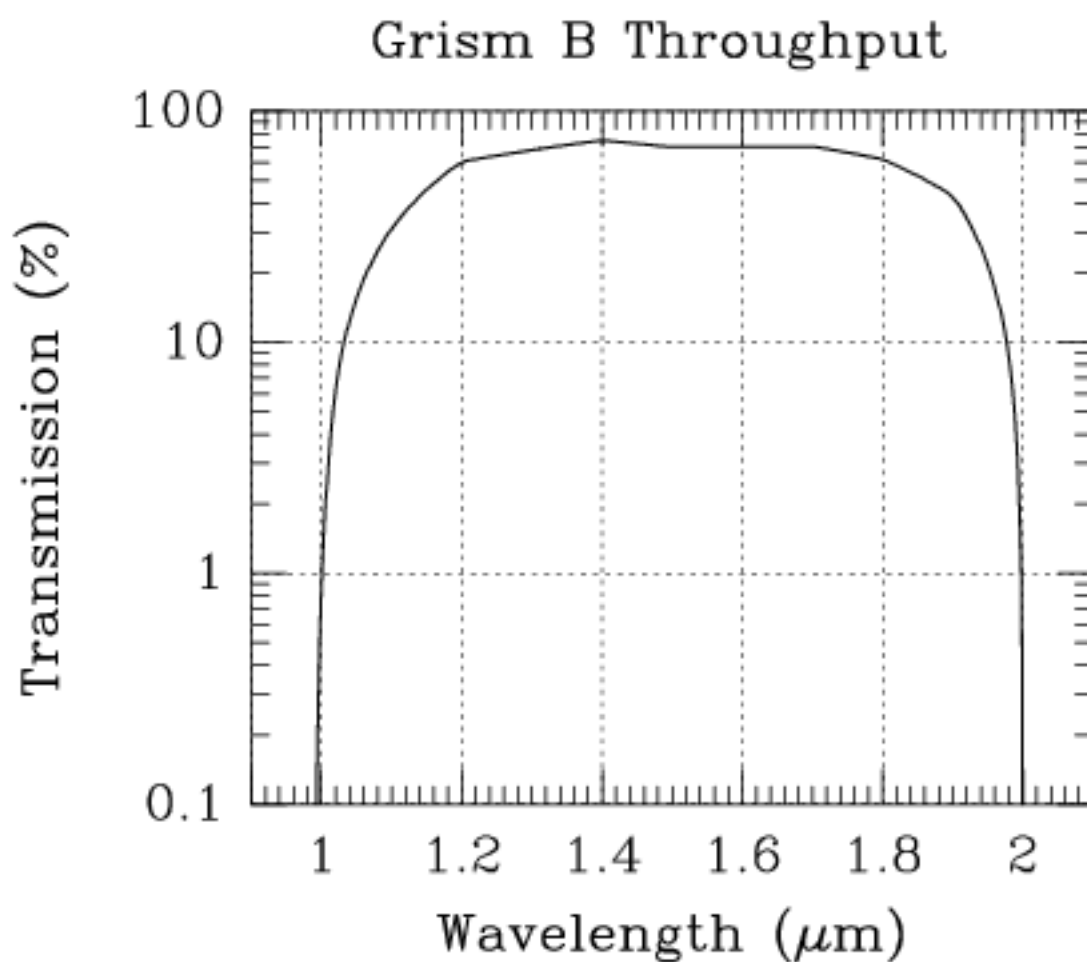
Grism C: G206

High thermal background. Use only for bright sources.

Table 5.8: Grism C: G206

Central (microns)	Mean (microns)	Peak (microns)	FWHM (microns)	Range (microns)	Max Tr (percent)
2.067	1.9523	2.0880	1.1575	1.4 - 2.5	73.4
Continuum Filters F175W, F240M					
1.7530	1.7508	1.9070	1.0940	1.2–2.3	96.6
2.3978	2.3977	2.3155	0.1975	2.3–2.5	92.4

Figure 5.12: The Grism C Throughput.
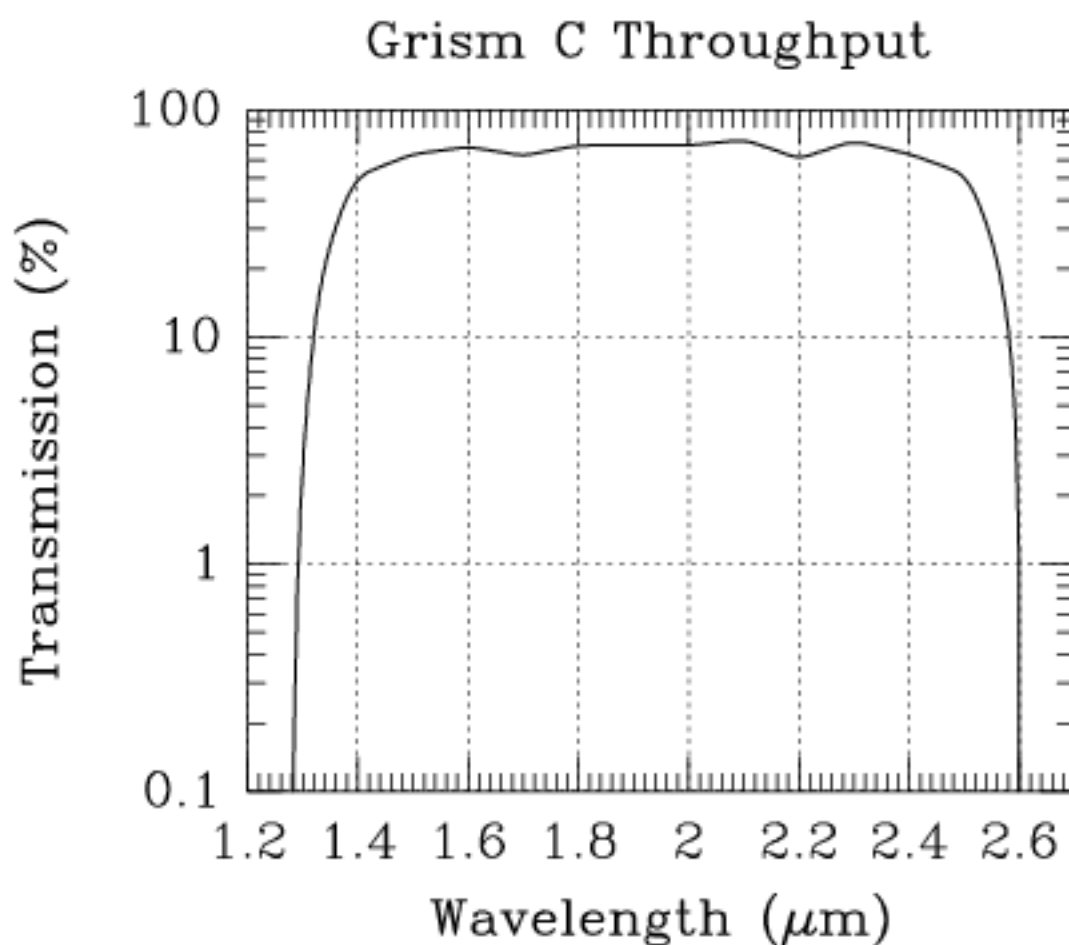
Grism Analysis Software

Software is being developed at the ST-ECF for the analysis of grism observations. Using this, the observer will be able to fully extract spectra of single objects from the images, including the disentanglement of overlapping spectra and extended sources. To obtain the best results it is recommended in fields with multiple or extended sources that grism images be obtained at more than one spacecraft roll angle (preferably 3 or more), and it is essential that the image spectrum pair be obtained as described. If the matching image is not obtained, reduction and analysis of the grism data may be very difficult.

Grism images can be calibrated in the regular way using Calnic A. Calnic A will perform all steps as for direct images with the exception of flatfielding. This step is skipped, and the quantum efficiency as a function of wavelength should be taken into account when extracting spectra. Software to extract spectra from calibrated grism images has been developed at the Space Telescope - European Coordinating Facility (ST-ECF). The programs are written in IDL, and a valid IDL license is necessary to run those programs. The software is available at http://ecf.hq.eso.org/nicmos/nicmos.html. There are two versions of the grism extraction software, the interactive version NICMOSlook and the pipeline program "Calnic C". For detailed documentation on the programs, consult the above WWW page or contact Wolfram Freudling (wfreudli@eso.org). The programs run both under IDL 4.x and IDL 5.0.

For grism spectroscopy of extended objects or crowded fields, observations of the same field with a variety of roll angles is advisable. Such data might be handled by extracting the spectra of a particular object from the image where there is the least amount of blending of the spectrum with other objects. A more promising procedure is to reconstruct a position-wavelength cube with a simultaneous deconvolution of all the grism images. Experimental software (again in IDL) has been developed at ST-ECF and further information is available at http://ecf.hq.eso.org/nicmos/nicmos.html.

Exposure Time Calculations

In this chapter we provide NICMOS-specific performance information needed to prepare a NICMOS Phase 1 proposal for Cycle 7-NICMOS. First, we discuss various parameters that affect performance, and the extent to which they are known. Next, we describe how to determine the system sensitivity. We then describe the ways in which you can determine the exposure time required for a given observation and the signal to noise that will be achieved; examples are provided. We describe several computer programs that will perform these calculations and which are available on the WWW. These programs may be used to calculate the sensitivity and exclusion curves for the NICMOS filters, polarizers, and grisms, discussed elsewhere in this Handbook. We also describe how to calculate signal to noise ratios and exposure times by hand for NICMOS.

Overview

At the time of writing, a final calibration of the throughput of NICMOS is not yet available. Observers should find the present calibration sufficient to prepare Phase 1 proposals but should consult the STScI NICMOS WWW pages for updated information when preparing Phase 11 proposals.

Instrumental Factors

Detectors

The detector properties which will affect the sensitivity are simply those familiar to ground-based optical and IR observers, namely dark current and read noise, and the detector quantum efficiency (DQE). Laboratory and preliminary on-orbit measurements have determined the read noise for the three NICMOS flight arrays to be ~35 electrons. The measured numbers are given in Table 7.1 on page 106.

Optics

NICMOS is a relatively simple instrument in layout, and thus contains a fairly small number of elements which affect the sensitivity. These are the filter transmission, the field of view (determined by the NICMOS optics external to the dewar, in combination with the HST mirrors), the reflectivities of the various external mirrors and the transmission of the dewar window.

The filter transmissions as functions of wavelength were measured in the laboratory, and the resulting curves are presented in Chapter 11. Some filters may have minor leaks outside the primary filter bandpass; the reality of these has not yet been established, and we assume here for the purposes of sensitivity calculations that the transmission is zero outside the primary bandpass.

NICMOS contains a total of seven mirrors external to the dewar, each of which reduces the signal received at the detector. The mirrors have protected silver coatings (except for the field divider assembly which has a gold coating) for maximum reflectivity, and have 98.5% reflectivity. The dewar window has a transmission of roughly 93%. Therefore, the combination of optical elements is expected to transmit ~84% of the incoming signal from the OTA.

The sensitivity will obviously be affected by the pixel field of view. The smaller the angular size of a pixel, the smaller the fraction of a given source that will illuminate the pixel. Finally, the optical efficiency will be degraded further by the reflectivities of the aluminum with MgF_2 overcoated HST primary and secondary mirrors. These are given as exactly one minus the emissivities.

Background Radiation

At long wavelengths the dominant effect limiting the NICMOS sensitivity will be the thermal background emission from the telescope. How large this will be depends on the areas of the primary and secondary mirror and their optical configuration, temperatures, and emissivities. We discussed the issue of thermal background and its stability in Chapter 3.

For the purposes of sensitivity calculations, we used the values listed in Tables 6.1 and 6.2 and assumed that the effects of debris on the mirrors can be ignored.

Table 6.1: Optical Efficiency

Optical Element	Efficiency
First bending mirror	0.985
Re-imaging mirror	0.985
Pupil mirror	0.985
Image mirror	0.985
First paraboloid	0.985
Second paraboloid	0.985
Bending mirror	0.985
Dewar window	0.93
Total	0.84

Table 6.2: HST Infrared and Optical Properties

Property	Assumed Value
Primary mirror collecting area	$38993 \ cm^2$
Primary mirror temperature	291 K
Primary mirror emissivity	0.048
Secondary mirror collecting area	$684.4 \ cm^2$
Secondary mirror pupil clear fraction	0.76
Secondary mirror temperature	288.5 K
Secondary mirror emissivity	0.048
Focal plane image scale	35.8 arcsec/cm
Back focal distance	640.6 cm

At shorter NICMOS wavelengths, sensitivities will be affected by the zodiacal background which is given by the equation in Chapter 3; the overall expected background is shown in Figure 3.6.

Background radiation will be a slightly worse problem in the case of Multi-Object Spectroscopy (MOS) than in the case of imaging observations. Every pixel on the array will always see the entire background radiation integrated over the grism bandpass. The expected detected background rate per pixel is shown in Table 5.3.

Calculating NICMOS Imaging Sensitivities

The sensitivity curves generated by the Exposure Time Calculator (described in Chapter 4) allow one to estimate the exposure times from a given source flux. In some situations it may be desirable to go through each step of the calculation. One example would be the case of a source with strong emission lines, where one wants to estimate the contribution of the line(s) to the signal. This could include the case of a strong emission line which happens to fall in the wing of a desired filter's bandpass. To facilitate such calculations, we provide in this section recipes for determining the signal to noise or exposure time by hand.

Signal to noise Calculation

The signal generated by a continuum source with a flux F_j [Jansky] falling on a pixel is:

$$C_c = F_j \gamma_{opt} \gamma_{det} \gamma_{filt} A_{prim} E \qquad (1)$$
$$= F_j \eta_c \; [e^-/\text{sec}]$$

where:

- γ_{opt} is the efficiency of the optics, including the HST mirrors and the NICMOS optics.

- γ_{det} is the detector quantum efficiency.

- γ_{filt} is the filter transmission.

- A_{prim} is the HST primary mirror collecting area.

- E is a constant given by:

$$E = 10^{-26}/(h\lambda) \qquad (2)$$

where h is Planck's constant and λ the wavelength.

The expression for C_c has to be integrated over the bandpass of the filter, since some of the terms vary significantly with wavelength. The value for η_c is listed for each filter in Tables 6.3, 6.4, and 6.5, so that the signal in e^-/sec can be estimated. It should be noted that to determine C_c more accurately, the source flux F should be included in the integral over the filter bandpass, since the source flux is bound to be a function of wavelength. This has been done, assuming a source effective temperature of 5,000K.

If an emission line falls in the bandpass of the filter, we need to take account of its effect on the signal (in some cases the emission line may generate almost all the detected signal). The line signal can be determined as:

$$C_l = L_{lj} \gamma_{opt} \gamma_{det,\lambda} \gamma_{filt,\lambda} A_{prim} E \qquad (3)$$
$$= \varepsilon_\lambda L_{lj} \; [e^-/\text{sec}]$$

where E is defined as before. However, on this occasion it is necessary to use a line flux l (in Wm^{-2}), and the detector quantum efficiency and filter transmission are determined for the wavelength λ of the emission line.

The factor ε_λ is plotted by the Exposure Time Calculator. Thus one only needs to pick the wavelength of interest, read off ε_λ, and multiply your flux, l_{lj} by this to get the line contribution to the flux in the filter. The maximum value of ε_λ, denoted as $\hat{\varepsilon}$, is also listed in Tables 6.3, 6.4, and 6.5. Note that for the grisms, where both lines and continuum will frequently be present, we have plotted ε_λ in units of $e^-/sec/Jansky$. Thus, in this case it is necessary to estimate the spectral flux density of any line emission in Janskys, which is done simply by using the line strengths and the spectral resolution of the grisms.

The total signal generated by the pixel is the sum of the continuum and line signals calculated above.

Next the background signal must be calculated. This is particularly important in the infrared, since *in some situations* the signal to noise in the final observation is determined largely by the photon noise in the background signal, rather than that in the source signal. At wavelengths longer than 1.6 microns in particular, the thermal background emission will very often be brighter than the target source, in many cases perhaps by several orders of magnitude. The expected background as a function of wavelength for each of the three NICMOS cameras is plotted in Figure 3.6. This has been used to derive the background signal which is listed for each filter in Table 6.3 to Table 6.5 in e^-/sec as B.

The final ingredients needed to calculate the signal to noise for the observation are the read noise N_r and dark current I_d. The read noise can be taken from Table 7.1. The dark current has not been very well determined at the time of writing, but we recommend that the upper limits listed in Table 7.1 should be adopted.

It is now possible to calculate the signal to noise ratio expected for an exposure of duration t seconds, where a number N_{read} of reads are taken before and after the integration. It is:

$$ SNR = \frac{C_s t}{\sqrt{(C_s + B + I_d)t + \dfrac{N_r^2}{N_{read}}}} \tag{4} $$

Where C_s, the count rate in e^-/sec, is the sum of C_c plus C_l.

It is important to note that in these equations, the flux to be entered (either F_j or l_{lj} or both) is *not* the total source flux, but the flux falling on a pixel. In the case of an extended source this can easily be worked out from the surface brightness and the size of the pixel. For a point source, it will be necessary to determine the fraction of the total flux which is contained within the area of one pixel and scale the source flux by this fraction. For Camera 1 in particular, this fraction may be quite small, and so will make a substantial difference to the outcome of the calculation.

The signal to noise ratio evaluated by a fit over the full PSF for point sources would, of course, be longer than this central pixel SNR; this discrepancy will be largest for the higher resolution cameras and of long wavelengths.

Exposure Time Calculation

The other situation frequently encountered is when the required signal to noise is known, and it is necessary to calculate from this the exposure time needed. In this case the same elements must be looked up as described above, and the required time can be calculated as:

$$t = \frac{(SNR)^2(C_s + B + I_d) + \sqrt{(SNR)^4(C_s + B + I_d)^2 + 4(SNR)^2 C_s^2 \frac{N_r^2}{N_{read}}}}{2C_s^2} \quad (5)$$

Table 6.3: Camera 1 Filter Sensitivity Parameters

Filter name	η_c [e⁻/sec/Jy]	$\hat{e}$ [e⁻/sec/(W/m²)]	B [e⁻/sec]
F090M	4.53×10^5	9.51×10^{17}	7.12×10^{-3}
F095N	3.02×10^4	7.66×10^{17}	4.53×10^{-4}
F097N	3.34×10^4	8.74×10^{17}	4.95×10^{-4}
F108N	4.23×10^4	1.39×10^{18}	5.83×10^{-4}
F110M	7.85×10^5	1.76×10^{18}	1.07×10^{-2}
F110W	2.09×10^6	2.25×10^{18}	2.89×10^{-2}
F113N	4.98×10^4	1.58×10^{18}	6.65×10^{-4}
F140W	3.40×10^6	5.28×10^{18}	4.71×10^{-2}
F145M	8.25×10^5	3.36×10^{18}	9.35×10^{-3}
F160W	1.87×10^6	5.26×10^{18}	2.70×10^{-2}
F164N	8.57×10^4	4.02×10^{18}	1.04×10^{-3}
F165M	9.39×10^5	5.01×10^{18}	1.29×10^{-2}
F166N	8.68×10^4	4.12×10^{18}	1.13×10^{-3}
F170M	1.01×10^6	5.48×10^{18}	1.86×10^{-2}
F187N	9.00×10^4	5.21×10^{18}	6.39×10^{-3}
F190N	9.30×10^4	5.65×10^{18}	8.54×10^{-3}
POL0S	1.34×10^6	1.44×10^{18}	3.68×10^2

Table 6.4: Camera 2 Filter Sensitivity Parameters

Filter Name	η_c [e⁻/sec/Jy]	$\mathcal{E}$ [e⁻/sec/(W/m²)]	B [e⁻/sec]
F110W	2.43×10^6	2.51×10^{18}	0.10
F160W	2.05×10^6	5.77×10^{18}	$9.03 \times 10\text{-}2$
F165M	1.04×10^6	5.53×10^{18}	$4.34 \times 10\text{-}2$
F171M	4.43×10^5	5.70×10^{18}	$2.39 \times 10\text{-}2$
F180M	4.19×10^5	6.03×10^{18}	$4.15 \times 10\text{-}2$
F187N	1.02×10^5	5.87×10^{18}	$2.20 \times 10\text{-}2$
F187W	1.13×10^6	6.02×10^{18}	0.32
F190N	1.04×10^5	6.41×10^{18}	$2.90 \times 10\text{-}2$
F204M	6.37×105	8.90×10^{18}	0.82
F205W	3.94×10^6	1.37×10^{19}	19.0
F207M	9.62×10^5	9.35×10^{18}	2.1
F212N	1.58×10^5	1.03×10^{19}	0.46
F215N	1.42×10^5	9.86×10^{19}	0.54
F216N	1.53×10^5	1.05×10^{19}	0.68
F222M	1.02×10^6	1.08×10^{19}	8.0
F237M	1.17×10^6	1.54×10^{19}	31.0
POL0L	1.21×10^6	9.71×10^{18}	1.91×10^{-2}

Table 6.5: Camera 3 Filter Sensitivity Parameters

Filter Name	η_c [e⁻/sec/Jy]	$\mathcal{E}$ [e⁻/sec/(W/m²)]	B [e⁻/sec]
F108N	4.49×10^4	1.46×10^{18}	1.34×10^{-2}
F110W	2.43×10^6	2.55×10^{18}	0.91
F113N	5.15×10^4	1.68×10^{18}	1.49×10^{-2}
F150W	3.96×10^6	6.15×10^{18}	1.8
F160W	2.12×10^6	6.02×10^{18}	0.66
F164N	9.66×10^4	4.59×10^{18}	2.55×10^{-2}
F166N	9.66×10^4	4.71×10^{18}	2.72×10^{-2}
F175W	6.21×10^6	1.28×10^{19}	83
F187N	1.06×10^5	6.06×10^{18}	0.16
F190N	1.08×10^5	6.62×10^{18}	0.21
F196N	1.16×10^5	6.99×10^{18}	0.47
F200N	1.27×10^5	7.62×10^{18}	0.74
F212N	1.62×10^5	1.08×10^{19}	3.4
F215N	1.49×10^5	1.03×10^{19}	4.0
F222M	1.08×10^6	1.16×10^{19}	59
F240M	1.57×10^6	1.60×10^{19}	3.68×10^{-2}

Software Tools

Rather than going through all the above calculations by hand for every source on an observing list, software tools can be used. The tools are available on the NICMOS World Wide Web page, and can be found by following the Software Tools link.

▽ These tools should be regarded as the official calibration of NICMOS for purposes of preparing Phase 1 observing proposals and should be used rather than the values presented above, if at all possible.

Filter Sensitivity Curves

The first of the tools available will calculate the flux required as a function of time to achieve a given signal to noise for any NICMOS filter. Two versions of this tool are available, one for point sources and one for extended sources.

Calculations are carried out on a grid of wavelengths across the bandpass of the chosen filter. At each wavelength we determine the filter transmission, detector quantum efficiency, optical efficiency of the NICMOS+HST system, and source flux. In the case of a point source we determine the fraction of the total source flux which is expected to land on the central pixel, assuming that the source lies directly in the center of a pixel, while for the extended source case we merely have to multiply the surface brightness by the pixel area. For a wide range of integration times we use the above data, plus the dark current, read noise and background radiation (both zodiacal and thermal backgrounds as discussed earlier in this chapter), to calculate the point source flux, or surface brightness, required to achieve a range of signal to noise ratios (in the current version of the software values of 10, 25, 50 and 100 are adopted).

Signal to Noise for a Source

For a particular source, with a known flux density or surface brightness, there are a pair of tools. These perform very similar calculations to those described above, with the output being signal to noise against time. Currently the source flux must be for the wavelength of the filter; eventually bells and whistles will be added so that you can enter the flux at one of the standard IR photometric bands (I, J, H or K).

Saturation and Detector Limitations

The signal to noise which can be achieved in a given time is one indication of how useful an observation is likely to be. However, there are two further pieces of information which are important to know, and which are not readily apparent from the mere knowledge of signal to noise: firstly, is the detector operating in its linear

response range, and secondly, what is limiting the signal to noise? A further pair of programs generate this information for each filter. These generate both the flux (or surface brightness, as appropriate) above which the observation is limited by photon noise (either from the source or the background) rather than detector noise, and the flux above which the observation enters the non-linear detector operation regime, which we refer to as saturated.

WWW Access to Imaging Tools

The tools described above can be accessed via the WWW pages already mentioned. To run the tools, you will have to first select whether you want to image point sources or extended sources, or obtain grism data. This choice will take you to another window where you will click on buttons to select the camera and filter, and then you will need to enter a number of reads, source color, temperature, and source flux (in Janskys). The latter is optional, and only used if you want to obtain signal to noise vs. time for a particular source. You can then click the "Submit simulation" button and you will be offered a set of outputs. All three of the tools described above are run simultaneously, so you can choose which of the types of output you want. The "input info" output reminds you what inputs were used and supplies warnings where necessary. "Get the tables" retrieves the ASCII output files generated by the code, and the "Get the plots" option retrieves a graphical display of the output, which you can save for later reference if desired.

Examples

▽ Note: these example use pre-launch calibration values and should *not* be relied upon for planning observations.

## Using Exposure Time and Signal to noise Calculators

In this section we describe how to use the programs found on STScI's NICMOS WWW pages, in order to determine the signal to noise for a particular source, or to determine the integration time needed to achieve a given signal to noise.

First time users of these tools should read the associated help discussion. Note that when using MULTIACCUM, NREAD should be left at its default value of 1, except when using the MIFxxx sequences when it should be set to 8.

Example 1: Signal to noise with Low Background

Here, the program has been used to model two sources being observed using Camera 1 through the F160W filter, see Figure 6.1. In the left panel we see the case of a 0.1 Jansky (H=10.0) source. For a source this bright, we see that whenever it is observed in any mode other than Bright Object Mode (i.e., integration times longer than about 0.2 seconds), the signal to noise obtained is always the same however many readouts are made at the beginning and end of the integration.

Figure 6.1: Signal to Noise with Low Background
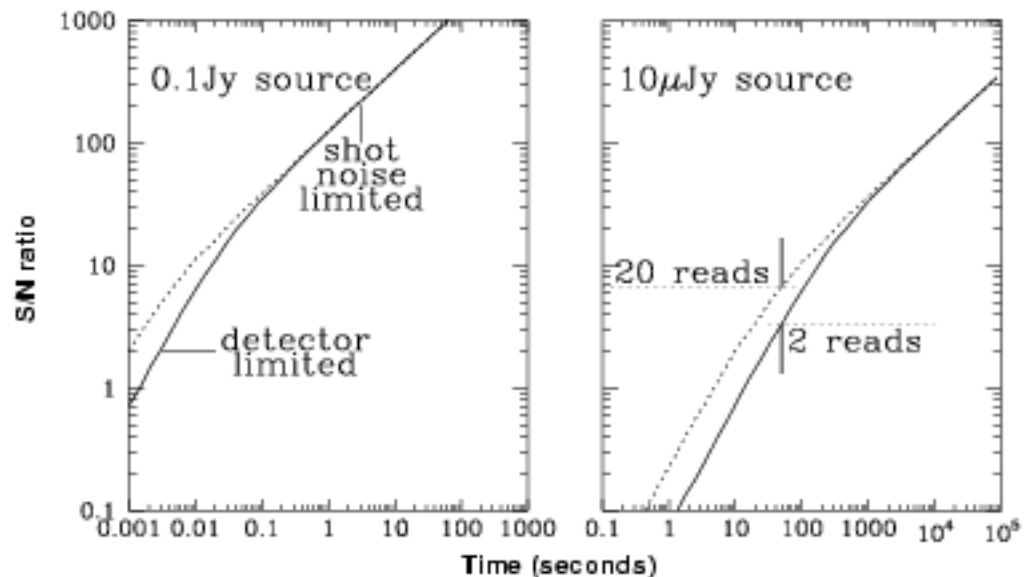
In these modes (ACCUM, or MULTIACCUM), the observation of the source in question is always photon-noise limited, and so the read noise of the detector is irrelevant, and the signal to noise increases roughly as the square root of the integration time. In the right panel is shown the case of a 10μ Jansky source (observed through the same filter). In this case, the number of readouts does have an effect on the signal to noise obtained for integration times less than about 1000 seconds. Where the signal to noise obtained is about 5 (integration times of a little less than a minute), increasing the number of readouts by a factor of ten can improve the signal to noise obtained by up to a factor of three or thereabouts. This example illustrates an important point: so long as the background is relatively faint, then if the signal to noise obtained is low, it is probably possible to improve it without increasing the integration time, by increasing the number of readouts. A balance should be sought between the integration time saved by doing this and any extra overhead incurred by making multiple readouts.

Example 2: Signal to noise with high background

Figure 6.2 shows what happens at longer wavelengths. Here we see two sources, with fluxes of 0.1 Jansky (K=9.5) and 100μ Janskys observed through the F237M filter with Camera 2. Here the background radiation is so bright that even

at very short exposure times the number of readouts makes little difference to the signal to noise obtained. For the 100μ Jy source, even when the signal to noise has dropped so low that the source is no longer detected, the number of readouts makes no difference. When the background is bright compared to the source, the observations will invariably be photon-noise limited, and so the only means of improving the signal to noise is to increase the integration time. Multiple initial and final reads are pointless in such cases.

Figure 6.2: Signal to noise with High Background
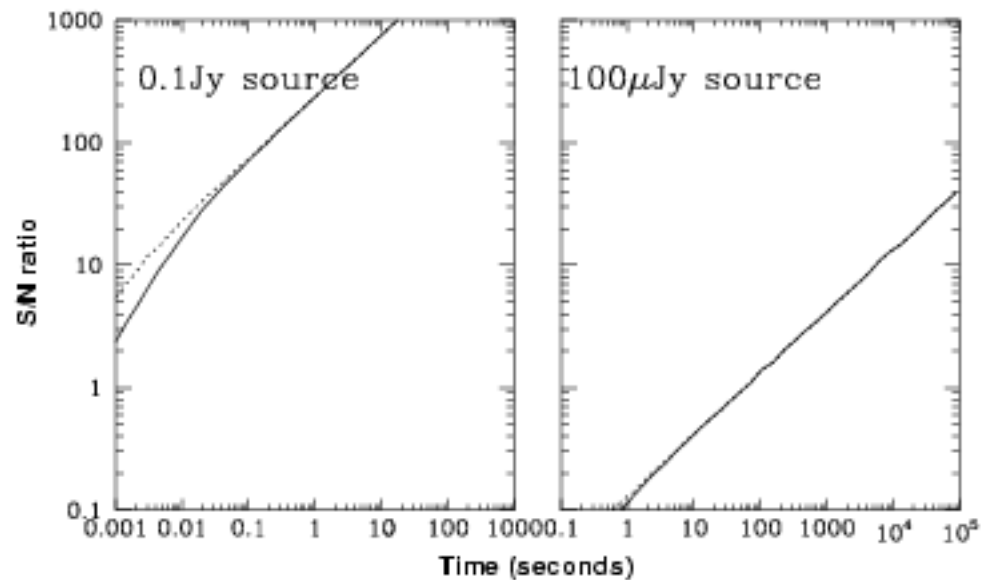
Example 3: Exposure Time Determination

Figure 6.3 illustrates the various parameters that are important in constructing a NICMOS observation, using output from the tools. We plot the flux required to obtain a signal to noise of 10, 25, 50 and 100 on a point source against integration time. Four cases are considered, and plotted in the Figure; these cases are identified as A, B, C, and D.

Figure 6.3: Effect of Parameters on NICMOS Observation
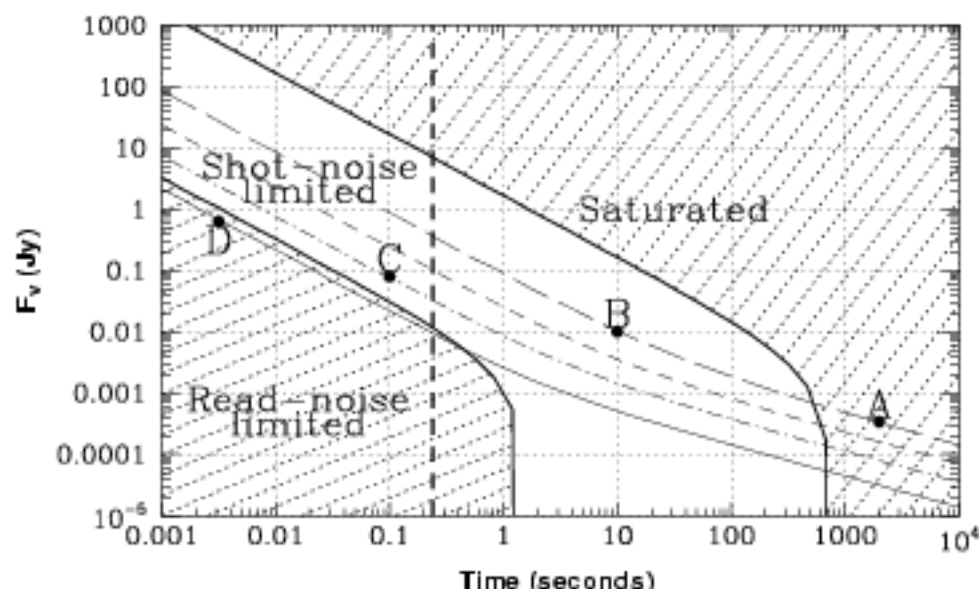
In case A, we see that we can obtain a signal to noise of 100 in an integration time of about 2000 seconds. However, the exclusion curves reveal that with such a long integration time the detector is saturated. This does not mean, however, that a signal to noise of 100 cannot be achieved for this source: it simply means that such a signal to noise cannot be achieved *in a single exposure*. Instead, to achieve such a high signal to noise it will be necessary to make a number of separate exposures (ACCUM or MULTIACCUM mode) and co-add the results. If the source of interest is actually fainter than this, and we merely needed to get a signal to noise of 100 on this bright target in order to get sufficient signal to noise on some nearby or surrounding fainter target, we could use MULTIACCUM mode, and repair the saturated core of this bright source.

Case B shows an observation which is optimal: this source can be observed to a signal to noise of 100 in a reasonable integration time (10 seconds), and there are no problems or complications.

Case C shows that it can actually be quicker to obtain *more* signal to noise. A signal to noise of 25 was deemed sufficient, but it transpires that for this source an integration time of 0.1 seconds is required for this signal to noise. This would require Bright Object mode, and to obtain a 0.1 second exposure for every pixel would require about 1600 seconds. However, by increasing the exposure time to about 0.6 seconds a signal to noise of about 90 is obtained, and this integration time is long enough that a standard MULTIACCUM exposure can be made.

Case D shows a source being observed in Bright Object mode, where a relatively short exposure obtains a signal to noise of 10, and the total integration time is a little less than a minute. In this case the signal to noise is dominated by the detector read-noise, however.

Example 4: Exposure Time Calculation for the Calibration Star P041-C

In this example we derive exposure times for the calibration star P041-C (see Table 15.4) for the purpose of characterizing the medium band filters F222M and F237M (CO band and continuum), and the narrow band filters F215N and F216N (Brγ and continuum) in Camera 2.

The K magnitude of P041-C is 10.56, corresponding to 0.037 Jansky at 2.2 microns. The star is a solar analog and we assume its color temperature to be 5800 K. The saturation diagrams produced for each filter by the WWW NICMOS exposure time calculator show that the source will saturate the two medium band filters after only 40 seconds of exposure, due to the high background which affects the 2 micron wavelength window. In the two narrow band filters, the saturation limit will be reached after an exposure of about 300 seconds. Since we want to remain well within the linear response regime of the detector, we choose exposure times which are a half of the saturation limit, namely, 20 seconds for the medium band filters and 150 seconds for the narrow band filters. With these times, the signal to noise ratio versus time diagram produced by the calculator indicates that SNR=280 in the F222M and F237M filters and SNR=315 in the F215N and F216N filters will be obtained. Such high signal to noise ratios are unlikely to be achievable, due to calibration limitations (such as flat field response and dark current); we expect, however, to be able to reach SNRs around 50–100.

Examples of Calculations by Hand

Example 1: Exposure Time for an Emission Line Source

We consider here the example of a diffuse Planetary Nebula with a diameter of 3.0 arcsecs, a Brγ emission line determined from the ground to have a strength of 10^{-13} W/m^2 and negligible continuum. The surface brightness of the nebula in the line is assumed to be uniform, and the observation will be made with Camera 2 in the F216N filter. We wish to obtain a signal to noise of 20 on each pixel. Two reads at the beginning and end of the exposure will be made.

First of all we determine that the surface brightness in the line is 1.5×10^{-14} W/m^2/arcsec^2. The size of a pixel in Camera 2 is 0.075 arcsec, and so the flux falling on a pixel is 8.3×10^{-17} W/m^2.

The signal generated by this line flux will be calculated using equation (3), in which l_{lj} is 8.3×10^{-17} W/m^2, as determined above. ε_λ is 9.5×10^{18} e$^-$/sec/(W/m^2), as determined by the ETC. We therefore determine the signal generated in the detector is $C_l = 2.0 \times 10^{-5} \times 0.62 \times 0.85 \times 4.16 \times 10^5 = 4.4$ e$^-$/sec.

Now to determine the exposure time needed we will use equation (5). C_l we have just determined, and C_c for this source is negligible. The background emission for this filter we find in Table 6.4 is 6.4 e$^-$/sec. At this point we note that the background emission is actually brighter than the source emission. Therefore, we will require a background image in order to remove the background from our image of the source. For a chopped observation, the time on source must equal the time on background. The ratio of the signals from source-plus-background to

background-only is 1.69. In this background limited observation the signal to noise will be determined by photon statistics in the signal: the detector noise will be more or less irrelevant. It is easy to show in this case that if we require a signal to noise SN_s on our background-subtracted image, we must obtain a signal to noise of $(SN_s{}^2x(1+1/1.69))^{0.5}$ on the image with the source in it, which in this case translates to a signal to noise of 25.2.

The dark current we take to be 0.1e⁻/sec, from Table 7.1. The read noise from Table 7.1 is 28e⁻ for this detector. The required signal to noise is 25.2. We can now use equation (5), and we find that the time required is 507 seconds. It must be borne in mind that this is only the on source time, and that another 507 seconds observation of the background will be required.

Example 2: Exposure Time for a Line Plus Continuum Source

In this example we consider the case of a galaxy which is to be observed with Camera 1 using the F095I1 and F097I1 filters. It is expected to have a uniform surface brightness of 0.2 Jansky/arcsec^2 in the continuum and $+2x10^{-15}$ W/m^2/arcsec^2 in the line. The redshift of the galaxy is 0.005. A signal to noise of 20 is required in the [SIII] line image after the continuum has been subtracted. The continuum spectral energy distribution is flat enough in this wavelength region that differences in continuum level between 0.95 and 0.97 microns can be ignored.

In order to generate the [SIII] line image, we will have to subtract the F097I1 image from the F095I1 image, assuming that the continuum at the two wavelengths is identical (for sources with very low line-to-continuum ratio, this assumption might be dangerous for the post-observation image analysis). We will assume for simplicity that these observations are all photon-noise limited, so that the signal to noise varies roughly as the square of integration time. The noise in the final line image will be the square root of the sum of the squares of the noise in the two observed images.

The continuum surface brightness is 0.2 Jansky/arcsec^2, and the constant η_c from Table 6.3 is 3.83×10^4 for the [SIII] continuum filter. The pixel surface area is 1.85×10^{-3} arcsec^2. Therefore the continuum signal in the F097I1 filter is C_c=0.2 x 3.83 x 10^4 x 1.85x10^{-3} = 14 e⁻/sec (from equation 1 on page 92).

In the line filter we have to consider the contributions both from the line and from the continuum. The continuum surface brightness is as used above, and the efficiency constant η_c is 3.45×10^4 from Table 6.3. This gives us a continuum signal of 0.2 x 3.45 x 10^4 x 1.85 x 10^{-3} = 13e⁻/sec. The line efficiency factor ε_λ is $+ x 10^{17}$ (e⁻/sec/(W/m^2)). Therefore, the signal generated by the line is C_l = $+2 \times 10^{-15}$ x$+$x 10^{17} x 1.85x10^{-3} = 3.1 e⁻/sec. Thus the combined signal in the F095I1 filter should be 16e⁻/sec.

The signal rates are roughly the same for the two images, so each will contribute roughly equal amounts of noise to the final image. (Note that if the continuum was much fainter than the line emission, the continuum image would contribute much less noise to the final result than the F095I1 image. If the item of interest is the resulting line image, it does not make sense to integrate for a long time to obtain good signal to noise on the continuum image, since it will not significantly affect the signal to noise in the final image. In our example here, both

images contribute similar amounts of noise to the result, and so it is equally important to obtain high signal to noise for both images.) Therefore the signal to noise required in each image is roughly $(16/31) \times 20 \times 2^{0.5}$, or 146.

For the F09511 filter, the background is 1.04×10^{-3} e-/sec (Table 6.3), the number of reads is 2, and the dark current is taken to be 0.1e-/sec as before. The required exposure time for this image is therefore roughly 1360 seconds. For the F09711 filter, the background is slightly higher, and the count rate slightly lower; the required exposure time turns out to be 1550 seconds. The two images thus require of order one orbit.

Finally, we should comment on two aspects of this proposal. First, the signal to noise being requested is very high. It is far from clear that the various calibration data needed will be of sufficiently high signal to noise to allow a signal to noise of 146 in the final product. In practice, a signal to noise of 100 is probably an impressive goal to aim for. Second, although the redshift of this galaxy is rather low, the line is on the edge of the filter curve. For sources with large redshifts, care is needed to check whether emission lines of interest fall into any of the available filters.

NICMOS Grism Sensitivity on the Web

As already mentioned, software tools are available on the NICMOS WWW pages to assist in the preparation of grism observations and proposals. These tools are exactly analogous to the tools previously described for imaging observations, and the same caveats apply. Since grism data will be difficult to interpret in the case of extended sources, these tools only deal with point sources.

Grism Sensitivity Curves

This tool is exactly analogous to the imaging tool described earlier. The same calculations are carried out in the same manner. The differences are that in this case the PSF is considered to be one dimensional only, and calculations must be carried out separately for various wavelengths inside the grism bandpass. In practice, we choose 3 wavelengths inside the grism bandpass, and carry out calculations at each of the three wavelengths for signal to noise ratios of 10 and 100. The results of this calculation were plotted in the previous section.

Signal to noise for a Particular Source

To obtain a signal to noise ratio for a particular source, with known flux density and color temperature, another tool is available. Currently the source flux must be for the central wavelength of the grism bandpass; eventually it will be possible to enter the flux at one of the standard IR photometric bands. The source currently is represented by a blackbody spectrum; eventually it may be possible to adopt a model atmosphere spectrum, or enter a user-supplied spectrum or a power-law continuum. The output from this code is time against wavelength for a set of signal to noise ratios (currently 10, 25, 50 and 100).

Saturation and Detector Limitations

Again, this tool is analogous to the corresponding image mode tool. It generates the fluxes required to saturate the detector and for the photon noise to

exceed the detector noise as a function of time. In principle this information should be calculated as a function of wavelength; however, since the sensitivity inside the grism passbands is only very weakly a function of wavelength, we carry out the calculations only for the central wavelength. Departures from this value will only be significant for wavelengths near the ends of the spectrum where the grism throughput is changing rapidly.

WWW Access to Grism Tools

If you select the grism spectra option, you will be offered choices almost identical to those for the imaging tools, except that now only one camera (Camera 3) is available.

NICMOS Detectors

NICMOS uses three 256 x 256 HgCdTe Rockwell arrays, one in each camera. We report on their measured detector quantum efficiency (DQE), read-noise, and dark current which have been determined at the unit test level prior to the 1996 thermal vacuum characterization. Other aspects of their expected performance are discussed here, including shading, linearity and saturation, cosmic ray susceptibility and flat fielding.

Physical Characteristics

Each detector array comprises 256 x 256 square pixels and is divided into 4 quadrants of 128 x 128 pixels, each of which is read out independently. The basic performance of the nominal flight detectors is summarized in Table 7.1. Typically, the read-noise is ~30e⁻/pixel, and the dark current << 0.1e⁻/sec/pixel. Only a few tens of bad pixels (i.e., very low response) were expected (but particulates—possibly paint flakes—have increased this number to ~100 per detector. The gain, ~5-6 e⁻/ADU, has been set so as to map the full useful dynamic range of the detectors into the 16-bit precision used for the output science images.

Detector Response Curves

Preliminary measurements of the wavelength-dependent detector quantum efficiencies, averaged over the detector, are shown in Figure 7.1.

Table 7.1: Flight Array Characteristics

Characteristics	Camera 1	Camera 2	Camera 3
Dark Current (e⁻/second)	<0.03	0.05	<0.03
Read Noise (e⁻)[a]	~30-35	~30-35	~30-35
Bad Pixels (including particles)	213 (.33%)	160 (0.24%)	139 (0.21%)
Conversion Gain (e⁻/ADU)	5.4	5.4	6.5
SATURATION (e⁻) (98% Linearity)	162,000	161,000	205,000
50% DQE Cutoff Wavelength (microns)	2.55	2.53	2.52

a. The quoted readout noise is the realized noise from a pair of readouts (i.e., the quadrature sum of a single initial and final readout). This number remains rather uncertain based on initial on-orbit tests.

Figure 7.1: DQE Versus Wavelength for Flight Arrays (solid line is NIC1, broken line NIC2, NIC3 is not plotted but is similar to the other two). Note that these curves reflect prelaunch measurements.
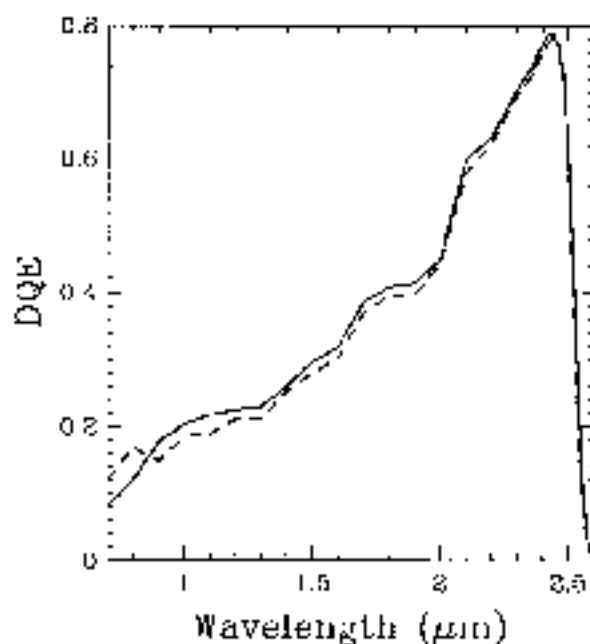
The fine details in these DQE curves should not be interpreted as detector features, as they may be artifacts introduced by the test set-up used to measure them. At the blue end, near 0.9 microns, the DQE is ~15%, and rises quasi-linearly up to a peak DQE ~80% at 2.4 microns, after which there is a rapid decrease to zero at 2.6 microns. The NICMOS arrays are blind to longer wavelength emission. When looking at these DQE curves, bear in mind that this is not the only criterion to be used in determining sensitivity in the near-IR. For

example, thermal emission from the telescope starts to be an issue beyond ~1.6 microns. The shot-noise on this bright background may degrade the signal to noise obtained at long wavelengths, negating the advantage offered by the increased DQE.

It is very important, especially for observations of very faint targets where the expected signal to noise is low, to note that the DQE presented here is only the average for the entire array. The flat field response described in detail later is non-uniform, and thus the DQE curves for individual pixels may be rather different.

The individual pixels in the NICMOS arrays are completely independent, and they do not suffer from the charge transfer effects present in CCDs, or from *bleeding* if the wells are filled due to over exposure. They do however have read-noise as well as their own special detector artifact, shading.

Detector Artifacts

Shading

The NICMOS arrays exhibit a noiseless signal gradient, a kind of pixel-dependent bias, orthogonal to the direction of primary clocking, called *shading*.

The shading effectively changes the bias level for the pixels as a function of time. The amplitude of the shading can be as large as several hundred electrons for some pixels under some circumstances. Through analysis of a considerable volume of on-orbit dark data, we have determined that for a given pixel the bias level introduced by the shading is dependent on the time since the last read of the pixel. Thus if the time between reads remains constant, the bias level introduced by the shading remains constant. For MULTIACCUM readout sequences where the time between readouts is increasing logarithmically, the bias level changes with each successive read, and thus the overall shading pattern evolves with readout. The first pixels to be read show the largest bias changes, and so the overall shading pattern is a DC offset which is roughly an exponential function of row number (it also varies along each row in a roughly exponential manner). The shading exhibits all the characteristics of a bias change, including lack of noise: the noise introduced by the shading is too small for us to measure.

We have calibrated the dependence of shading as a function of time between reads for each of the three NICMOS detectors using on-orbit darks, and are now able to use this information to construct "synthetic" dark current calibration reference files for all MULTIACCUM readout sequences. The accuracy of this calibration is good (a few percent for most readout times).

Amplifier Glow

Each quadrant of a NICMOS detector has its own readout amplifier, which is situated close to an exterior corner of the detector. When a readout is made, the amplifier injects a real signal into the detector, known as amplifier glow. This signal is largest closest to the corners of the detector where the amplifiers are situated, and falls rapidly towards the center of the detector. The signal is only present during a readout, but is repeated for each readout of a MULTIACCUM sequence. We have now calibrated the amplifier glow signal for each of the detectors; for each readout, the amplitude of the amplifier glow signal is of order one hundred electrons in the corners of the detector, and of order ten electrons close to the center. The signal is highly repeatable, and almost exactly linearly dependent on number of reads (however, there is some minor evidence that there may be a small non-linearity for reads made very close together in time; the amplitude of this non-linearity typically amounts to only a few electrons accumulated over an entire MULTIACCUM exposure in the brightest parts of the amplifier glow signal, however, so that our detection of this non-linearity is marginal). However, this is a real signal, and is subject to photon statistics, so it is a source of noise in NICMOS exposures. Thus, for the case of an ACCUM exposure with multiple and initial and final reads, although the multiple reads reduce the effective read noise of the observation, they also contribute extra photon noise via the amplifier glow, so that the gain in noise is in the end smaller than might be expected, and strongly dependent on location in the detector field of view (close to the corners the noise will actually increase). Similarly, making excessive numbers of reads in a MULTIACCUM exposure will add noise via the amplifier glow, so that the trade-off between improved Cosmic Ray rejection, reduced read noise, and increased photon noise in the final image is a complicated one.

Read-Noise

Each detector has four independent readout amplifiers, each of which reads a 128 x 128 quadrant. The four different readouts each generate very similar amounts of read noise to one another—this is illustrated in Figure 7.2, where the read noise distributions for the 1st and 4th quadrants of the Camera 1 array are compared. The distribution of read noise values for all the pixels in a given quadrant is relatively narrow (see Figure 7.2; a FWHM of 8 electrons is measured), so that there are very few very noisy pixels in these arrays (if the distribution were very broad, calculations of expected signal to noise values, which were critically dependent on the read noise, would be misleading).

Figure 7.2: Read Noise Characteristics for Two Quadrants on Camera 1 Detector
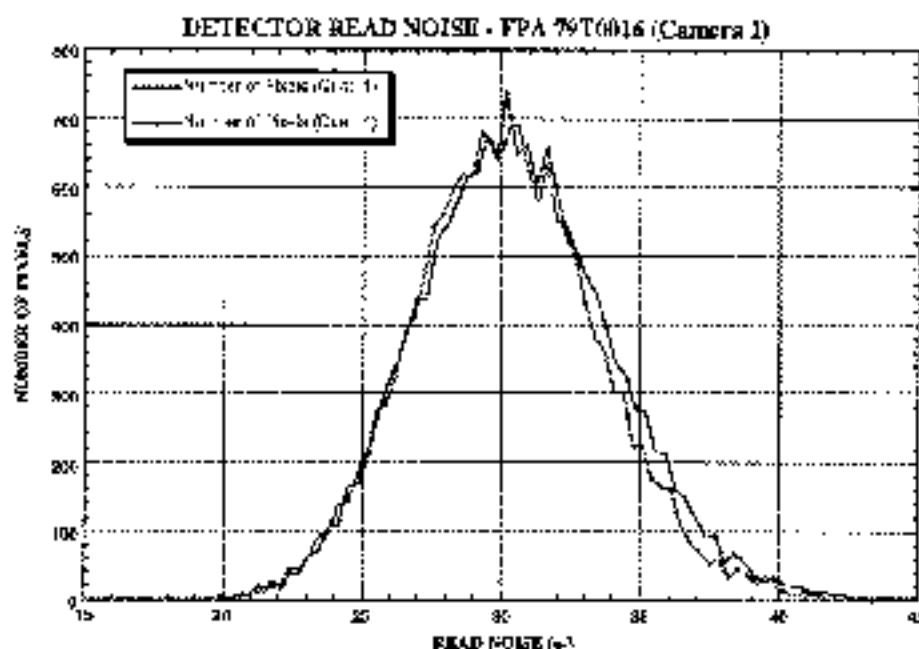
Linearity and Saturation

Ground-testing of NICMOS indicated that the detector response is slightly non-linear over most of the useful dynamic range. Saturation has been defined as when the response deviates by more than 5% from a linear fit: this is seen to occur for most pixels at about 90% of full well. We find that a deviation of more than 0.5% from linearity occurs at about 15% of full well. The response curve is well fit by a second order polynomial, which is used to correct observations in the calibration pipeline. At the time of this writing, on-orbit tests of the linearity are expected to be carried out shortly.

Effects of Overexposure of the NICMOS Detectors

Overexposure of the NICMOS detectors will not cause permanent harm and therefore NICMOS does not have bright object limitations. However, two artifacts result from exposures that overexpose one or more pixels:

- An afterimage with excess dark current persists for 10 minutes. Decay of this signal depends both upon elapsed time and, fairly strongly, upon the number of readouts performed (ongoing modifications to the "autoflush" procedure used between exposures may improve this situation). It is not unreasonable to expect signals of ~1 e⁻/second up to an hour following a severe exposure.

- Extremely bright targets can result in faint "phantom" images at the same pixel locations in the other three quadrants of the detector. (Each 256x256 pixel NICMOS detector consists of 4 128x128 quadrants).

Observers with targets expected to result in significant overexposure should examine the STScI NICMOS WWW pages for updates and consult with their STScI Contact Scientists during their Phase II proposal preparation.

Effect of Cosmic Rays

As with CCDs, cosmic ray hits will produce unwanted signal in the output images, but hot pixels are not expected to develop from such hits. The NICMOS arrays have been subjected to radiation doses much higher than expected in their entire lifetime in accelerator tests without sustaining any long-term damage or measurable depreciation in DQE. Hence, cosmic rays should have little impact on the long-term array performance in orbit.

On-orbit measurement of the distribution of cosmic rays shows 1.2 to 1.6 events/second/Camera for 5 sigma events. With a typical event generating a >=5 sigma event in ~2 pixels, this corresponds to 2 to 3 pixels/second/Camera. For a 2000 second integration, about 10% of the pixels in the detector will show cosmic ray events.

Therefore, the frequency of cosmic ray hits is large enough that we recommend the use of MULTIACCUM (or multiple ACCUM images) for all exposures longer than ~10 minutes, in order to filter out cosmic rays. MULTIACCUM provides a series of intermediate non-destructive reads as well as the final image (see Chapter 8). These intermediate reads can be used to identify cosmic ray hits, analogous to the use of CRSPLITs in WFPC2 or STIS observations. The calibration pipeline, described in Chapter 13, can identify and remove cosmic ray hits from MULTIACCUM observations.

Intra-Pixel Sensitivity Variations

As with many other modern array detectors, the sensitivity of the NICMOS detectors is lower near the edges of pixels then in their centers. It is as though there were very small regions of reduced sensitivity along the intra-pixel boundaries. This means that the response of a pixel to a source whose flux changes rapidly on a size scale comparable with or smaller than the pixel size will depend on where the center of the source lies with respect to the center of the pixel. Since the latter is not known a priori, this effect will introduce some uncertainty in the flux calibration for a point source. This uncertainty will be largest for Camera 3 at short wavelengths, for which the PSF is undersampled. We will try to measure the size of this effect on orbit, but we expect it to be no more than a few percent uncertainty for Camera 3.

Flat Field Response

Flat field frames taken with the NICMOS arrays show significant large-scale non-uniformity as well as pixel-to-pixel fluctuations. We shall correct these fluctuations in the normal way by flat fielding, which is an essential part of the calibration pipeline.

Characteristics of the Flat Fields

In conjunction with the NICMOS science team we carried out a number of flat field tests using a flight spare detector array, and report here on our results. (Detailed results are given in two technical reports: ISR 5 and 6, see the NICMOS WWW pages.) The flat field calibrations for the flight detectors themselves were performed in July 1996 during ground testing and calibration. A large program of sky and earth flats is presently starting on-orbit. Figure 7.3 shows the measured flat field response at a number of wavelengths. (We estimate that the likely uncertainties of the flat field response measurements are ~4%.) At 0.8 microns, the most sensitive areas on the array are > 2 times more sensitive than the mean, and the least sensitive areas < 1/2 as sensitive (i.e., there is variation by a factor of ~5 in the relative response across the array). This declines to a factor of ~3 at a wavelength of 2.2 microns, and at 2.5 microns the array is almost flat. To quantify the large scale variations we have binned the data into 10 x 10 pixel regions. Variations of almost a factor of 4 occur between the most and least sensitive regions in the array at intermediate wavelengths and this rises to a factor of eight at the shortest wavelengths.

In order to assess the amplitude of pixel-to-pixel variations in response, we generated a version of the flat field response smoothed by a 4 x 4 pixel kernel, then divided the original flat field response by this. The result is displayed in several ways in Figure 7.4, for a wavelength of 1.5 microns, and shows that the variations are essentially random with position on the array, and have a typical 1σ amplitude ~8% and that the pixel-to-pixel variations are independent of the global response.

Figure 7.3: Flat Field Response Images Using 10% Bandwidth Filters on a Flight Spare Array. Wavelengths used include (a) 0.8μm, (b) 1.5μm, (c) 2.1μm and (d) 2.5μm. The images have been normalized to the mean response for each wavelength. The contours and greyscale are linearly spaced in each image between normalized responses of 0.4 and 2.2. Significant areas of the array span this whole range at 0.8μm, while at 2.5μm the array is almost flat.
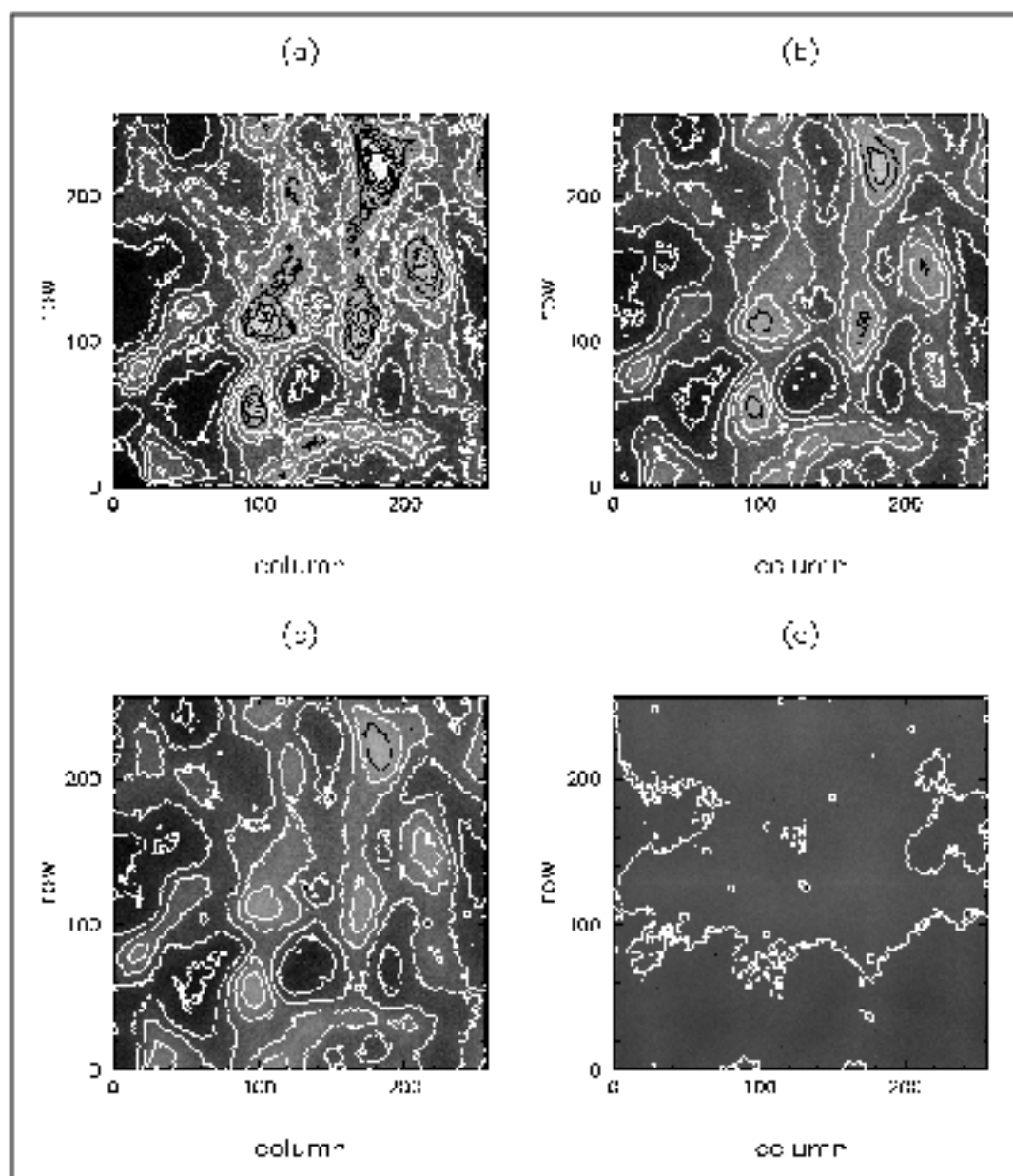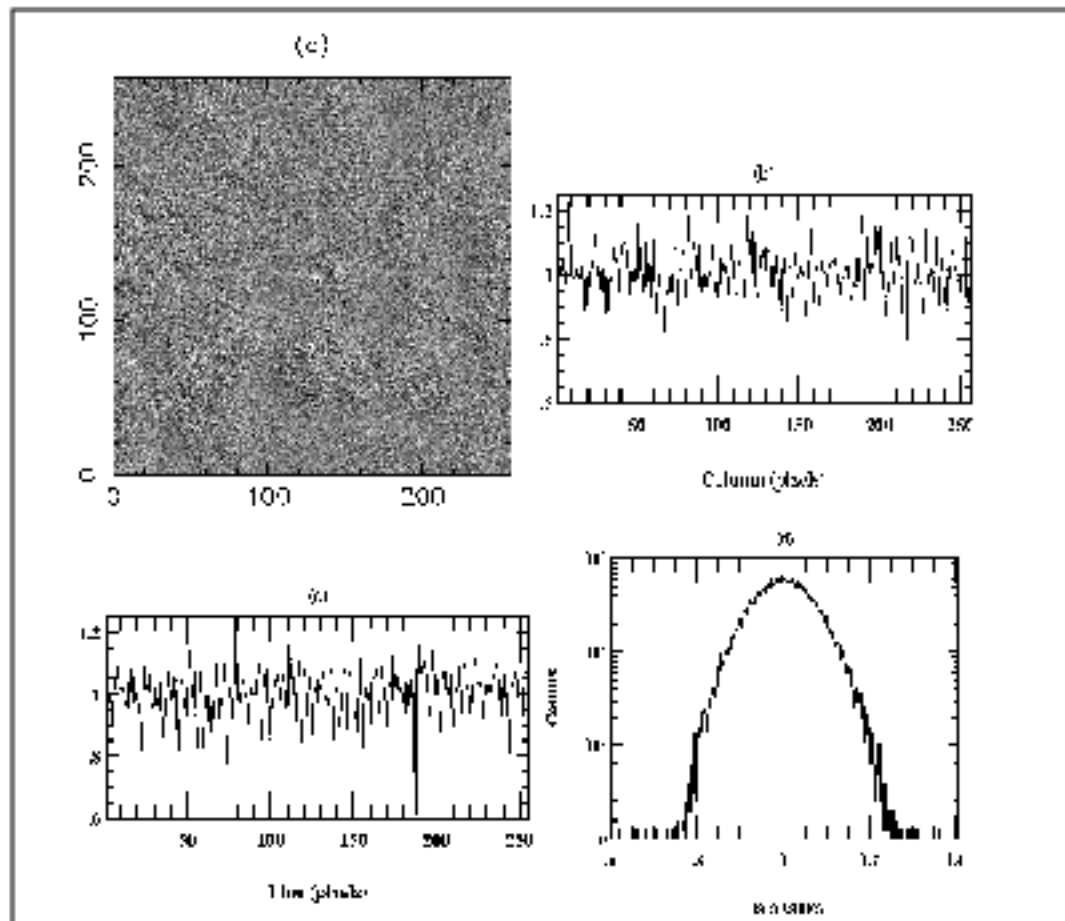
Figure 7.4: High Spatial Frequency Noise at 1.5μm. This was measured by dividing the image in Figure 7.3. (b) by a smoothed version of itself (see text). The grey-scale version in (a) is scaled between 0.9 and 1.1. Slices through the image are plotted in (b) along row 100 and in (c) along column 100. The distribution of data is plotted as a histogram in (d).

Wavelength Variations—Details

The size of the pixel-to-pixel sensitivity variations with wavelength is similar to that measured for spatial variations in the global flat field response. At 0.8 microns the standard deviation of the pixel-to-pixel sensitivity variations is ~11%, at 1.5 microns it is ~7%, at 2.1 microns ~6% and at 2.5 microns it is less than the uncertainties on our measurements. While it is difficult to define a single number which adequately quantifies the behavior of the flat field response over the entire array, the standard deviation plot in Figure 7.5 gives a reasonable representation of the general manner in which the flat field response varies with wavelength. Inspecting this figure we see that the patterns of variation in sensitivity with wavelength are rather similar on small and large scales.
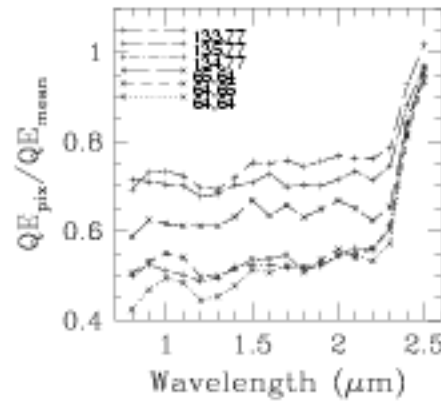
Figure 7.5: Amplitude of Flat Field Response Variations as a Function of Wavelength. The solid line shows the global flat field response, defined as the standard deviation of the individual pixel responses, while the dashed line shows the pixel-to-pixel variations. The two follow the same behavior very closely.
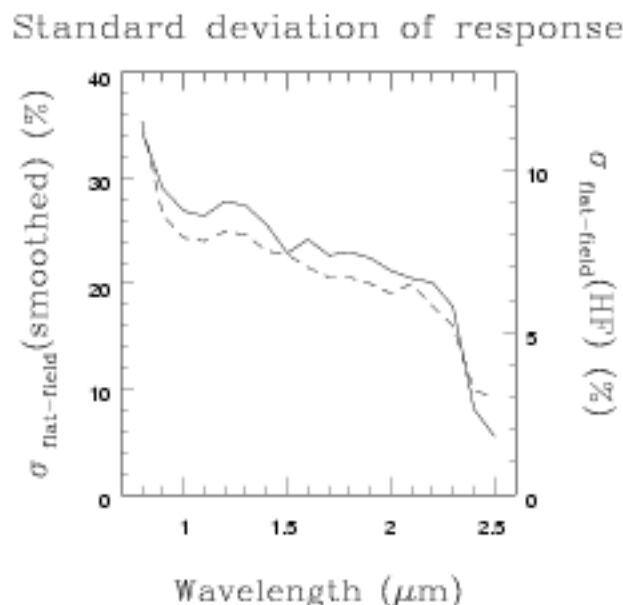

The relative response of four selected areas of three pixels is displayed in Figure 7.6. Each area plotted consists of adjacent pixels, either in a line or in an "L" shape. Two of the areas are from regions which were clearly of relatively high sensitivity, and the other two in regions of relatively low sensitivity. The ratio of the pixel sensitivity over the mean for the array at that wavelength is plotted against wavelength, using all of our 10% bandwidth measurements. The results show clearly that for many pixels, at wavelengths between 1.0 and 2.2 microns the variation in response changes fairly slowly, but that at a wavelength near 2.25 microns there is a turnover, past which the change with wavelength is dramatic.

Figure 7.6: Relative Response as a Function of Wavelength of Three-Pixel Groups. These diagrams basically show the response of a given pixel relative to the mean for the array at each wavelength, for groups of pixels in regions of low sensitivity (top panel) and high sensitivity (bottom panel). These figures show that the response flattens rapidly longward of 2.2 microns.
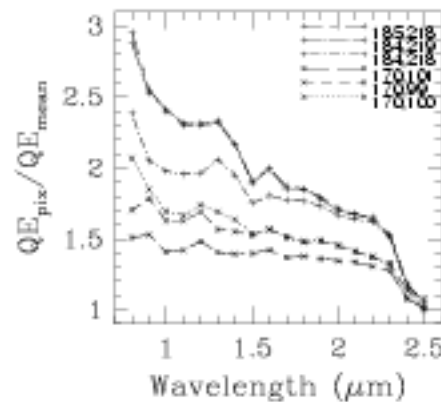
The rather dramatic change in the flat field response near 2.25 microns is likely to degrade the photometric accuracy of observations in the longest wavelength NICMOS filters. To estimate the magnitude of these effects we can make a number of comparisons of data in this wavelength region. First, we compare the broad band (K) flat field response with the 10% bandwidth 2.2 microns flat field response. The two flat field images differ by almost 10%, which emphasizes how rapidly the response is changing inside the K bandpass. Secondly, we have compared the flat field response images obtained using 2 filters: the 10% bandpass filter at 2.4 microns and the narrow bandpass filter at 2.415 microns. We find that they differ by about 4%, close to the uncertainties in the data. These results suggest that the change in the flat field response between 2.3 microns and 2.5 microns is more or less linear.

Overall, present indications are:

- The flat field response variations are large and wavelength dependent. The difference in response between the most and least sensitive areas is almost a factor of five at the shortest wavelengths and a factor of 1.1 at the longest wavelengths.

- The variation with wavelength is not linear, the largest variations occurring in small wavebands shortward of 1.1 microns and longward of 2.2 microns. The variations in response longward of about 2.2 microns are much more extreme than those shortward of 1.1 microns.

- The arrays exhibit wavelength dependent pixel-to-pixel response variations, ranging from an amplitude of order 10% at the shorter wavelengths to less than our measurement uncertainties at the longest wavelengths. The variation with wavelength of the pixel-to-pixel response variations is almost identical to the behavior of the global flat field response variations.

Despite these results, we expect to be able to flat field on-orbit astronomical data to high precision because the non-uniformities should be very stable with time.

Special Situations

Sources with Extreme Colors

We have carried out tests to establish the likely impact on photometric observations of sources of extreme colors induced by the wavelength-dependent flat field. For each filter, we used two sources with different colors assuming spectral energy distributions were black-body functions. The first case had a color temperature of 10,000K, and thus is typical of stellar photospheres and the resultant color is representative of the bluer of the sources that will be seen with NICMOS. (It is worth noting that for reflection nebulae illuminated by hot stars, a significantly bluer spectrum is often seen.) The second source had a color temperature of 700K which in ground-based terms corresponds to [J - K] = 5, a typical color encountered for embedded sources, such as Young Stellar Objects (YSOs). (Again, there are sources which are known to be redder. The Becklin-Neugebauer object, for example, has no published photometry at J, but has [H - K] = 4.1, and the massive YSO AFGL2591 has [J - K] = 6.0. YSOs with [J - K] = 7 are known, although not in large numbers.)

An example of a pair of the simulated spectra is shown Figure 7.7, for the F110W filter. In this filter an image of a very red source will be dominated by the flat field response in the 1.2 to 1.4 micron interval, while for a blue source the most important contribution will come from the 0.8 to 1.0 micron interval. The results of our study for the worst affected filters are shown in Table 7.2.

- Even for the broadest NICMOS filters the wavelength dependence of the flat field response generates only small photometric errors, typically less than 3% for sources of unknown color. Not surprisingly, the largest errors arise in the 3 broadband filters whose bandpasses include some part of the regions where the flat field response changes most rapidly.

- The same results hold true even for filters at the most extreme wavelengths (e.g., F090M, F222M and F240M) because of their small bandwidth.

- It will probably be difficult to obtain photometry to better than the limits shown in Table 7.2 for the F090M, F110W, F140W, F205W and F240M filters, and observers requiring higher accuracy should contact the Help Desk at STScI for guidance.

- These errors can probably be corrected if more accurate photometry is needed, by taking multi-wavelength observations and using an iterative correction technique.

- For observers requiring high precision photometry, these represent non-trivial limits beyond which it will not be possible to venture without obtaining multi-wavelength images. In order to obtain 1% precision using the F110W filter, for instance, observers should observe at a minimum of one other wavelength. The color information derived from the pair (or group) of images could then be used to construct a more appropriate flat field image, which could then be applied to improve the color information, and so on.

Figure 7.7: Detected Source Spectrum. These are for sources with color temperatures of 700K (solid line) and 10,000K (dashed line). It is easy to see that the detected image will be dominated by the flat field response in the 1.2-1.4μm region for a 700K source, while for a 10,000K source the detected image will be affected by the flat field response throughout the filter bandpass.
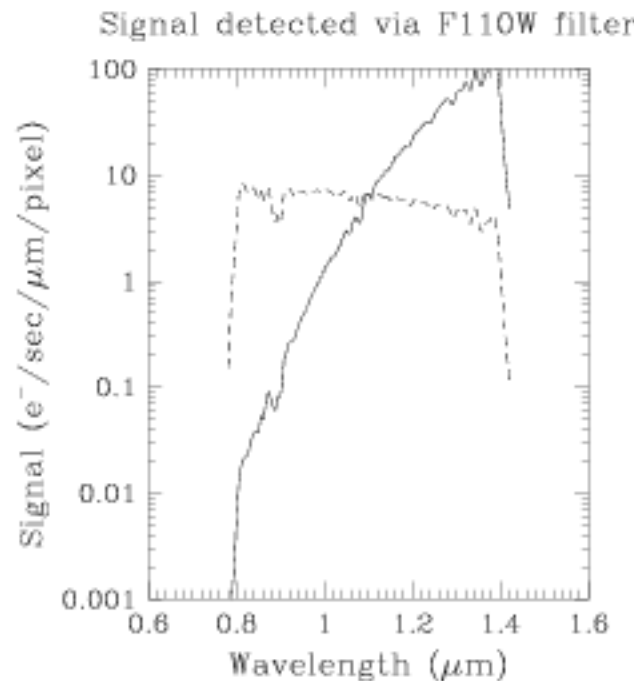

Signal detected via F110W filter

Table 7.2: Filters with Largest Photometric Errors for Sources of Extreme Color

Filter	10,000K model. Error (percent)	700K model. Error (percent)
F090M	<0.1	1.9
F110W	1.1	2.9
F140W	0.7	3.1
F160W	<0.1	0.3
F187W	<0.1	0.3
F205W	0.4	2.1
F222W	<0.1	0.1
F240M	1	0.9

Extended Sources with Extreme Spatial Color Variations

Our analysis has been limited to point sources, but some mention should be made of the situation for extended objects. A good example is the YSO AFGL2591. This has an extremely red core, whose [J - K] = 6 and which is entirely undetected optically. However, it also has a large IR nebula which is quite prominent at J and K, and in the red visual region, but much fainter at L, and which is probably a reflection nebulosity. Spatially, the nebula has highly variable color, some parts of it having fairly neutral or even slightly blue colors in the NICMOS waveband, while other parts are extremely red. Obtaining very accurate measurements of the color of such a source would again require the use of images at more than one wavelength and an iterative tool of the kind described earlier. A further example of this kind of complicated object is the prototypical post-AGB object CRL2688, the Cygnus Egg Nebula, which has an extremely blue bipolar reflection nebula surrounding an extremely red core. Techniques which require very accurate measurements of the surface brightness of extended objects, such as the brightness fluctuation technique for distant galaxies, will need to be applied with care given to the photometric uncertainties such as those discussed here.

Multi-Object Grism Spectroscopy

Flat fielding will be a potential limiting factor due to the combined effect of the source spectrum and sky background falling on individual pixels. Astronomical sources well above the background should be measurable. Spectra of very faint sources are likely to be severely modulated by the flat field.

Detector Readout Modes

The NICMOS flight software supports several detector readout modes which take advantage of the non-destructive read capabilities of the detectors to yield the optimum signal to noise for your science observations. These are described in detail in this chapter. In describing these we introduce the nomenclature used to command each of the modes in the Phase II proposal instructions. Finally we give recommendations about when to use of each of these readout modes.

▽   Nearly all observers should use the MULTIACCUM mode.

Introduction

NICMOS has four detector readout modes that may be used to take data. After observing time has been approved, the choices of readout mode can be selected by the observer when completing the Phase II proposal entry. However, a potential observer must understand the advantages and limitations of each of the readout modes in order to properly design their Phase I proposal. Since BRIGHTOBJ and RAMP are "available" modes (i.e., not fully supported by STScI), the necessity for

their use should be spelled out in the Phase 1 proposal. Efficiency is not a reason to use an "available" mode.

There are three supported readout options within this general framework:

1. Multiple-accumulate Mode.

2. Accumulate Mode.

3. Acquisition Mode.

The basic scientific rationale behind each of these modes, and a summary of their capabilities is outlined in Table 8.1, along with a recommendation regarding their use. The Phase II proposal instructions needed to identify the readout modes are given in brackets under the mode name.

Table 8.1: Readout Modes and their Functions

Mode	Use	Functionality	Recommendation
Accumulate (ACCUM)	Simplest observing mode Produces a single image May help ease data volume constraints	Can reduce noise by performing and averaging multiple initial and final readouts $t > 0.57$ seconds Limited to 173 tabular integration times, 32 of which may have matched dark current calibrations.	MULTIACCUM mode is preferred.
Multiple-Accumulate (MULTIACCUM)	Faint targets Large dynamic range Optimal image construction. Ground processing of cosmic rays and saturation. Long wavelength integrations	Multiple readouts at specific times during an integration $8590 > t > 0.215$ seconds Number of readouts ≤ 25	Suitable for most programs. Use whenever high dynamic range need e.g., source with bright core and faint extended emission or long integrations times.
Onboard Acquisition (ACQ)	Locate brightest source in a subarray and reposition telescope to place source behind coronographic spot	Two ACCUM exposures are obtained, combined with cosmic ray rejection, sources located, and centered.	Reasonably bright sources on uncrowded fields.
Bright Object (BRIGHTOBJ)	For bright targets which would saturate the arrays in the other modes with the shortest integration time allowed	reset/read/wait/read each pixel sequentially in a quadrant $t < 0.2$ seconds	When possible use a narrow filter with ACCUM instead
Ramp (RAMP)	Faint targets Large dynamic range Uncertain target flux On-board cosmic ray removal On-board saturation detection	Slope computation Reduces Data Volume Provides Variance and valid samples array $t > 50$ seconds number of readouts ≤ 50	MULTIACCUM superior. Only use this if data volume becomes an issue

▽ RAMP and BRIGHTOBJ modes are not supported for Cycle 7-NICMOS. See Appendix for a more detailed description of these modes.

Detector Resetting as a Shutter

It is important to remember that NICMOS *does not have a physical shutter mechanism*. Instead, the following sequence of operations are performed to obtain an exposure:

* *Array reset*: All pixels are set to zero—the bias level.

* *Array read*: The charge in each pixel is measured and stored in the on-board computer's memory. This happens as soon as practical after the array reset. In effect, a very short exposure image is stored in memory.

* *Integration*: NICMOS exposes for the period specified for the integration.

* *Array read*: The charge in each pixel is measured and stored in the on-board computer's memory.

Fast and Slow Readout Modes

The NICMOS detectors have two readout speeds: FAST and SLOW. The use of SLOW mode imposes a 3 second readout overhead which increases the minimum possible integration time (to slightly more than 3 seconds). When multiple readouts are obtained in ACCUM mode, the readout overhead becomes rather large (e.g., 30 seconds at the beginning and end of an exposure for NREAD=10 making 60 seconds the minimum exposure time).

▽ At this time we advise observers to use the FAST readout mode. No significant advantages results from using SLOW readout mode, and calibrations for that mode are not planned.

Accumulate Mode

The *Accumulate Readout Mode* (ACCUM) generates the simplest basic exposure. In its simplest incarnation, *two sample readout*, illustrated in Figure 8.1 it is analogous to a WFPC2 readout. This simple two sample readout strategy is the one to use for short integrations of relatively bright objects, and when you are observing in the background limited regime at long wavelengths. This section is therefore a good place to start to get familiar with the concepts inherent in the operation of the NICMOS arrays, including their *non-destructive readout*

capabilities. The allowed ACCUM mode integration times are restricted to 173 tabular values. Furthermore, as described on page 130, only a maximum of 32 of these will have matched dark calibration frames. (In Cycle 7 only a few times are being calibrated for ACCUM mode because few observers are using it.)

The first action of an ACCUM exposure is three passes through the detector *resetting* each of the pixels. The *reset* is immediately followed by a fourth pass through the detector *non-destructively reading* and storing the pixel values. This marks the beginning of the integration. The final action is a second non-destructive reading of the detector, which marks the end of the integration. *The returned image is the difference between the second and the first pass pixel values, and the integration time is defined as the time between the first and second read of the first pixel.* The minimum exposure time is ~ 0.6 sec, and the minimum time between successive exposures is ~ 8-12 seconds. It has the minimum time for output amplifier operation which minimizes the amplifier glow contribution to the image (see below). This method does not discriminate against cosmic ray events or check for saturation levels in the image onboard the spacecraft.

Figure 8.1: Basic NICMOS Readout—Simple Two-Sample Readout
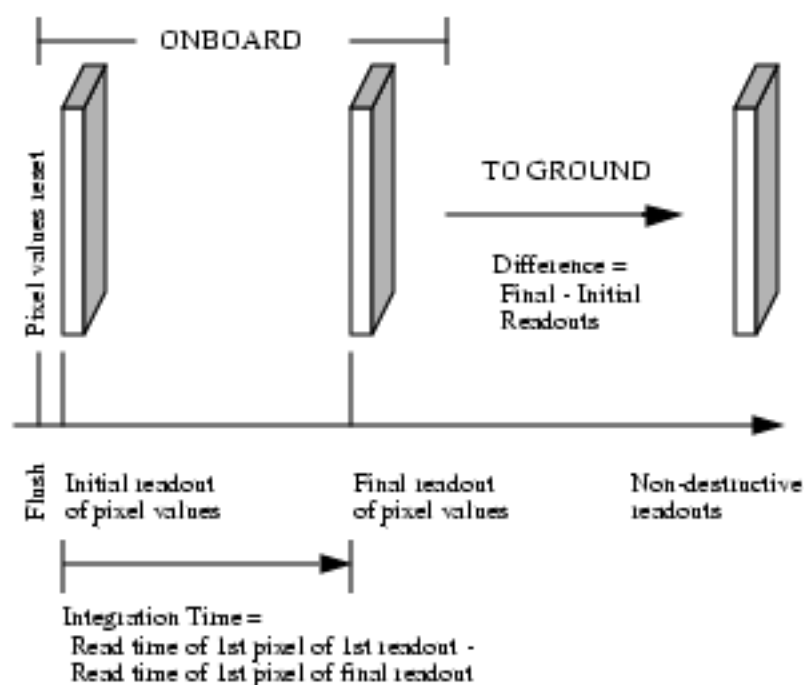
Flush time is 0.615s and is followed immediately by the Initial Readout.

Multiple Initial and Final Sample Readout

The observer has the option of requesting *multiple reads* in place of the single initial and final readouts in ACCUM mode. In this case after the detector array is reset it will be followed by 1–25 (specified by the NREAD parameter) reads of the initial pixel values which are averaged onboard to define the initial signal level.

After the exposure time has elapsed, the final pixel values are again read NREAD times and averaged onboard. The data downlinked is the difference between the initial and final average signal levels for each pixel. The integration time is defined as the time between the first read of the first pixel in the initial NREAD passes and the first read of the first pixel in the final NREAD passes. The use of multiple reads in ACCUM mode is illustrated in Figure 8.2 for the case of NREAD = 4.

▽ For Cycle 7 and Cycle 7-NICMOS only NREAD =1 or 9 is supported (any other values are considered "available"—unsupported—modes).

The advantage of this method is a reduction in the read noise associated with the initial and final reads, which can reduce the noise in intermediate time integrations on faint sources. In theory the read noise should be reduced by $1/(n)^{1/2}$ where n is the number of reads. For integrations where source photon noise or dark current noise exceeds the detector read noise the multiple readouts may not offer much advantage. This option puts a higher burden on the CPU and requires an additional time per readout of 0.3 seconds in FAST mode. This mode does not discriminate against cosmic ray events and does not check for saturation onboard the spacecraft. An effect known as amplifier glow, which adds extra signal and associated noise close to the corners of the array, is important when multiple readouts are made. Amplifier glow is an additive noise source. The photon noise added in the amplifier glow signal is large enough that for NREAD > 10 there is little further gain in noise, and the maximum improvement in effective read noise over a single initial and final read is about a factor of two.

Figure 8.2: ACCUM Mode with Four Initial and Final Readouts
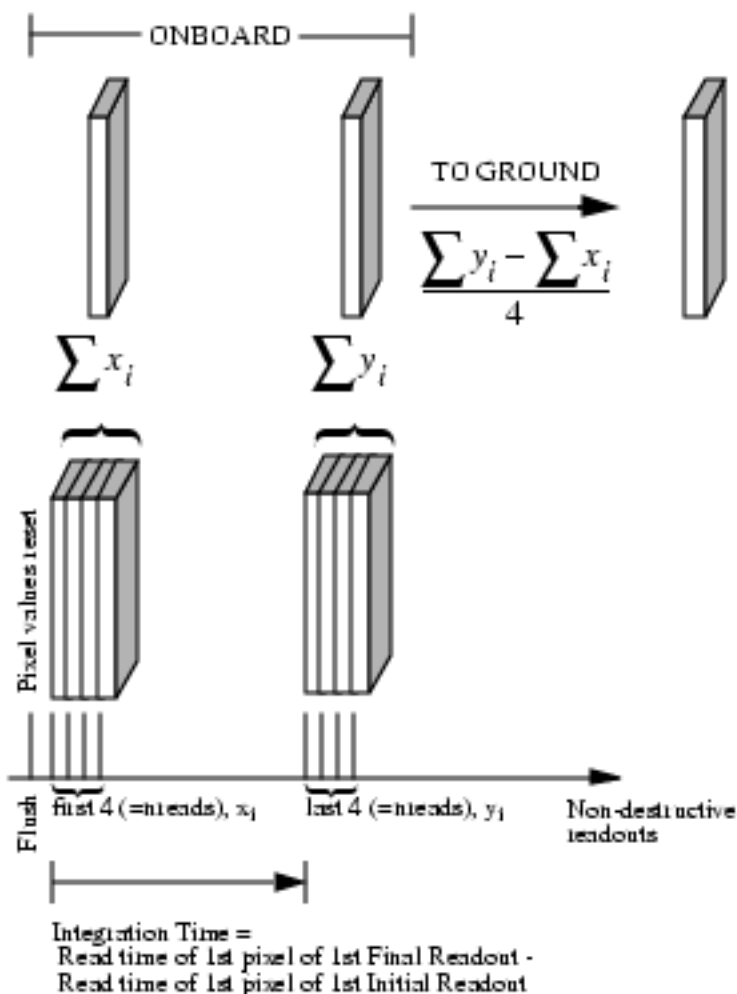
Multiple-Accumulate Mode

Normally a single integration on a target results in a single 256x256 image at the termination of the exposure. The non-destructive nature of the NICMOS readout offers more elaborate methods of using the instrument which aim to optimize the scientific content of the results. In particular it is possible to read-out images at intermediate stages of an integration and *return both these and the final image to the ground*. In this mode of operation, known as *Multiple-Accumulate* (MULTIACCUM), each intermediate readout can only consist of a single readout. The observer uses this capability by creating a list of times, specified by the SAMP-TIME parameters, at which the detector pixels are read out non-destructively creating images of various integration times. The choice of the times during the integration in which the observer can create these reads is very

flexible, for example they might be linearly spaced or logarithmically spaced. Linearly spaced exposures may be useful for very faint targets where cosmic ray filtering is important while logarithmically spaced exposures permit the observation of a very wide dynamic range. The process is shown schematically in Figure 8.3 for the case of logarithmically spaced intervals with NSAMP=4. In MULTIACCUM the detector reset is followed by a single read of the initial pixel values. Then a sequence of non-destructive array readouts are obtained at observer specified times. Up to 25 readouts can be specified spanning a total integration time from 0.203 seconds to 8590.0 seconds. The last read of the detector array ends the exposure and thus the last SAMP-TIME will be equal to the total exposure time. All of the readouts, including the initial readout, are stored and downlinked without any onboard processing. This is different to ACCUM mode as the initial read is also returned and no on board subtraction occurs. For N readouts, this mode requires the storage and transmission (downlink) of $N+1$ times as much data volume for ACCUM mode.

MULTIACCUM mode arguably provides the highest quality scientific data in return. The benefits of obtaining observations in MULTIACCUM mode fall into two areas.

- The dynamic range of the observation is greatly increased. Rather than being limited by the charge capacity of a NICMOS pixel (a few x 10^5 electrons), an observation's dynamic range is in principle limited by the product of the pixel capacity and the ratio of the longest and shortest exposures (8590.0 and 0.203 seconds). In practice, the PSF and internal stray light will probably be the limiting factors.

- An image can be reconstructed by processing of the stack of readouts to cope with the effects of cosmic ray particle events, as well as saturation.

MULTIACCUM provides the best choice for deep integrations or integrations on fields with objects of quite different brightness except when the signal is readnoise limited or the background signal is so bright that it requires the use of short exposures where the background of the telescope dominates the signal. *In the absence of compelling reasons, observers should use MULTIACCUM for all observations.*

Figure 8.3: Example MULTI-ACCUM with NSAMP = 4
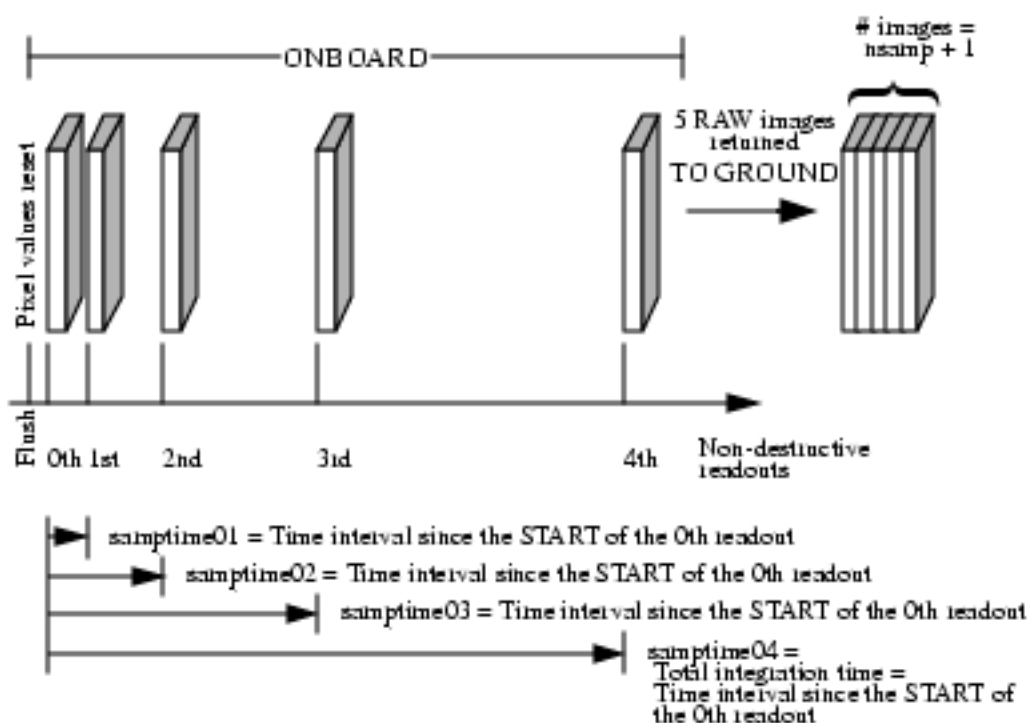
MULTIACCUM Predefined Sample Sequences (SAMP-SEQ)

While it is possible to specify MULTIACCUM observations with nearly any set of up to 25 readout times, such usage results in a requirement to send excessive volumes of commanding information up to HST. Accordingly, STScI and the NICMOS IDT defined a set of sequences which should cover nearly all applications of MULTIACCUM. These are defined in Table 8.2. The observer specifies the name of the sequence and the number of samples to be obtained. The SCAMRR and MCAMRR are to be used when the fastest temporal sampling is desired. The MIF sequences provide a combination of the ACCUM (with NREAD=8 to reduce noise) plus 9 intermediate samples for cosmic ray rejection and handling saturated sources. The SPARS64 and SPARS256 sequences have relatively few readouts and may be helpful when two or more cameras are operated in parallel (in particular they generally permit a second camera to operate in parallel with a minimal impact on the operation of the primary camera). The STEPx sequences all start with three rapid readouts and then are logarithmically spaced to provide a large dynamic range up to their defined time (e.g., STEP64 has log steps up to 64 seconds) and then revert to linear spacing.

Table 8.2: MULTIACCUM SAMP-SEQs

Sequence Name	Readout Times					Description
SCAMRR	0.203	0.406	0.609	0.812	1.015	Single camera faster possible operation
	1.218	1.421	1.624	1.827	2.030	
	2.233	2.436	2.639	2.842	3.045	
	3.248	3.451	3.654	3.857	4.060	
	4.263	4.466	4.669	4.872	5.075	
MCAMRR	0.303	0.606	0.909	1.212	1.515	Fastest possible operation with 2 or 3 cameras used in parallel
	1.818	2.121	2.424	2.727	3.030	
	3.333	3.636	3.939	4.242	4.545	
	4.848	5.151	5.454	5.757	6.060	
	6.363	6.666	6.969	7.272	7.575	
STEP1	0.303	0.606	0.995	1.993	2.991	Rapid reads up to 1 second then 1 second steps
	3.989	4.987	5.985	6.983	7.981	
	8.979	9.977	10.975	11.973	12.971	
	13.969	14.967	15.965	16.963	17.961	
	18.959	19.957	20.955	21.953	22.951	
STEP2	0.303	0.606	0.995	1.993	3.987	Rapid reads up to 2 seconds then 2 second steps
	5.981	7.975	9.969	11.963	13.957	
	15.951	17.945	19.939	21.933	23.927	
	25.921	27.915	29.909	31.903	33.897	
	35.891	37.885	39.879	41.873	43.867	
STEP8	0.303	0.606	0.995	1.993	3.987	Rapid reads up to 8 seconds then 8 second steps
	7.981	15.975	23.969	31.963	39.957	
	47.951	55.945	63.939	71.933	79.927	
	87.921	95.915	103.909	111.903	119.897	
	127.891	135.885	143.879	151.873	159.867	
STEP16	0.303	0.606	0.995	1.993	3.987	Rapid reads up to 16 seconds then 16 second steps
	7.981	15.975	31.969	47.963	63.957	
	79.951	95.945	111.939	127.933	143.927	
	159.921	175.915	191.909	207.903	223.897	
	239.891	255.885	271.879	287.873	303.867	
STEP32	0.303	0.606	0.995	1.993	3.987	Rapid reads up to 32 seconds then 32 second steps
	7.981	15.975	31.969	63.969	95.969	
	127.969	159.969	191.969	223.969	255.969	
	287.969	319.969	351.969	383.969	415.969	
	447.969	479.969	511.969	543.969	575.969	
STEP64	0.303	0.606	0.995	1.993	3.987	Rapid reads up to 64 seconds then 64 second steps
	7.981	15.975	31.969	63.969	127.967	
	191.965	255.963	319.961	383.959	447.957	
	511.955	575.953	639.951	703.949	767.947	
	831.945	895.943	959.941	1023.939	1087.937	
STEP128	0.303	0.606	0.995	1.993	3.987	Rapid reads up to 128 seconds then 128 second steps
	7.981	15.975	31.969	63.969	127.967	
	255.961	383.955	511.949	639.943	767.937	
	895.931	1023.925	1151.919	1279.913	1407.907	
	1535.901	1663.895	1791.889	1919.883	2047.877	
STEP256	0.303	0.606	0.995	1.993	3.987	Rapid reads up to 256 seconds then 256 second steps
	7.981	15.975	31.969	63.969	127.967	
	255.961	511.961	767.961	1023.961	1279.961	
	1535.961	1791.961	2047.961	2303.961	2559.961	
	2815.961	3071.961	3327.961	3583.961	3839.961	

Table 8.2: MULTIACCUM SAMP-SEQs (Continued)

Sequence Name	Readout Times					Description
MIF512	0.303	0.606	0.909	1.212	1.515	Eight rapid readout at start
	1.818	2.121	2.424	31.994	63.994	and end with 7 evenly spaced
	127.992	191.990	255.988	319.986	383.984	readouts over 512 seconds
	447.982	511.980	512.283	512.586	512.889	
	513.192	513.495	513.798	514.101	514.404	
MIF1024	0.303	0.606	0.909	1.212	1.515	Eight rapid readout at start
	1.818	2.121	2.424	63.999	127.997	and end with 7 evenly spaced
	255.991	383.985	511.979	639.973	767.967	readouts over 1024 seconds
	895.961	1023.955	1024.258	1024.561	1024.864	
	1025.167	1025.470	1025.773	1026.076	1026.379	
MIF2048	0.303	0.606	0.909	1.212	1.515	Eight rapid readout at start
	1.818	2.121	2.424	127.995	255.989	and end with 7 evenly spaced
	511.989	767.989	1023.989	1279.989	1535.989	readouts over 2048 seconds
	1791.989	2047.989	2048.292	2048.595	2048.898	
	2049.201	2049.504	2049.807	2050.110	2050.413	
MIF3072	0.303	0.606	0.909	1.212	1.515	Eight rapid readout at start
	1.818	2.121	2.424	127.995	255.989	and end with 7 evenly spaced
	639.988	1023.987	1407.986	1791.985	2175.984	readouts over 3072 seconds
	2559.983	3071.981	3072.284	3072.587	3072.890	
	3073.193	3073.496	3073.799	3074.102	3074.405	
SPARS64	0.303	0.606	63.994	127.992	191.990	Similar to STEP64 but
	255.988	319.986	383.984	447.982	511.980	without the rapid initial
	575.978	639.976	703.974	767.972	831.970	readouts
	895.968	959.966	1023.964	1087.962	1151.960	
	1215.958	1279.956	1343.954	1407.952	1471.950	
SPARS256	0.303	0.606	255.996	511.996	767.996	Similar to STEP256 but
	1023.996	1279.996	1535.996	1791.996	2047.996	without the rapid initial
	2303.996	2559.996	2815.996	3071.996	3327.996	readouts
	3583.996	3839.996	4095.996	4351.996	4607.996	
	4863.996	5119.996	5375.996	5631.996	5887.996	

Trade-offs Between ACCUM and MULTIACCUM

Given that there is so much more information present in a MULTIACCUM dataset than in an ACCUM dataset, it may seem obvious that MULTIACCUM should always be the preferred readout mode. In practise, the trade-off is not always so straightforward.

Because of the fixed read-out patterns available for use in MULTIACCUM mode (the SAMP-SEQs), in order to make an exposure of total integration time a minute or two, it is necessary in most modes to make a significant number of readouts. This leads to a significant volume of data to process. Additionally, the readouts are initially stored in a buffer in the NICMOS flight computer. A maximum of 100 readouts can be stored in this buffer, after which the contents of the buffer must be dumped to the Solid State Recorder. A full dump of 100 reads takes almost three minutes. At the time of writing, this process cannot occur in parallel with other

NICMOS observations, which means that for every 100 images obtained, nearly three minutes of overhead time are incurred. Obviously, for programs requiring many exposures of only a few minutes' duration, if MULTIACCUM readout mode is used this can lead to very large overheads. ACCUM mode, on the other hand, yields only a single image in memory for each exposure, and so is much less expensive in overheads. Efforts are underway to reduce this overhead time, by making it possible to schedule buffer dumps in parallel with exposing the detectors in some circumstances, but this effort is not yet complete. ACCUM mode may thus appear attractive for programs requiring many exposures. Finally, because almost all MULTIACCUM exposures will consist of many readouts (typically ten or more), the amplifier glow signal, and the resulting photon noise, will be quite significant. In ACCUM mode on the other hand, it is possible to adopt just two reads (one initial and one final), greatly reducing the amplifier glow signal. This may be advantageous in cases where the background and target are very faint (e.g., narrowband line images).

There are a variety of disadvantages to ACCUM mode. First, the ability which is present in a MULTIACCUM exposure to filter out CR hits which occur during the exposure is lost. We find for NICMOS that typically between 2 and 4 pixels are hit per second per camera by CRs: most of these are low energy and so can be filtered out of a MULTIACCUM exposure by the calnica software. In ACCUM mode the process of CR removal requires separate exposures, and is a time consuming piece of post-processing as it is for WFPC2. Second, the ability to detect pixel saturation, which again is done automatically for MULTIACCUM observations by calnica, can in some circumstances be lost in ACCUM mode. The reason for this is that the time elapsed between the first read for each pixel and the reset immediately prior to the read is approximately 0.2 seconds. During this time, pixels exposed to a bright target will accumulate significant signal, which is then present in the first read. When this is subtracted on-board in ACCUM mode, all the charge accumulated in the time between reset and read will be subtracted. If the pixel has saturated during the exposure, the difference between initial and final reads will be less than the expected saturation value for the pixel, and thus it may be impossible to recognise that the pixel as saturated. Thus in the case of bright targets, erroneous signal levels may be recorded in ACCUM mode. Third, in ACCUM mode, even if pixel saturation is detected, it is not possible to repair the data obtained in the saturated pixel. In MULTIACCUM mode, pixels which have saturated can be repaired by using the results of previous, unsaturated reads during the same exposure. Finally, because of the many advantages of MULTIACCUM over ACCUM, during Cycle 7 rather few observers are using ACCUM mode. As a result, the quality of the calibration of dark current for ACCUM mode is likely to be significantly lower than that for MULTIACCUM.

In conclusion, in cases where a multitude of short duration exposures must be made per orbit, or where there is very low background and a desire to minimise the amplifier glow contribution to the noise, ACCUM may possibly (but not necessarily) be a good choice. In all other cases it is likely that MULTIACCUM will yield the best results, and we recommend that all observers attempt to use MULTIACCUM.

Read Times and Dark Current Calibration in ACCUM Mode

Because of the effects of shading, and the possibility that the underlying dark current may vary with time since reset, the removal of dark current (for calibration purposes, we implicitly assume shading and amplifier glow is a part of the time variable "dark current") from data is more complicated than for many other instruments. The most accurate way to remove the dark current from any observation is a measurement of the dark current with an identical integration time. This would also apply to every individual read-out in a MULTIACCUM observation. Of course, this would be prohibitively expensive in on-orbit calibration time. Instead, we have adopted two strategies. First, for ACCUM observations we will make dark current calibration observations for a set of 8 exposure times for a single initial and final read (listed below) and 14 exposure times for 9 initial and final reads. As for WFPC2, only a certain set of exposure times are allowed in ACCUM mode (173 times are specified currently, ranging from 0.57 seconds to 3600 seconds), and in Phase II proposals any user selected exposure time will be rounded down to the nearest available option from the 173 available times. If you select one of the times listed below (this list will be published with the Phase II Proposal Instructions), then the calibration database used by the calibration pipeline software will contain dark current calibration files which are an exact match to your exposure times. On the other hand, if you must use any other one of the 173 allowed exposure times in ACCUM mode, the calibration pipeline will interpolate between the various files in the database to determine the dark current for your exposure time. Based on our current understanding, we expect this to be a very accurate technique, and to be limited by the signal to noise in the dark observations rather than by the interpolation accuracy. For MULTIACCUM mode, dark calibrations will be made to match each of the 16 SAMP-SEQs. Finally, we note that SLOW readout mode is not supported and no calibration of this mode will be provided by STScI.

Acquisition Mode

Images obtained using the coronograph in Camera 2 may be taken using any of the detector read-out modes. An ACQ mode observation performs an autonomous on-board acquisition (mode 2 acquisition) for subsequent coronograph images.

In this mode the target is first acquired in the Coronographic Acquisition Aperture (see Figure 5.1). The ACQ mode image is now obtained, with an integration time specified by the observer, which should be long enough to determine the centroid of the target image accurately. An ACQ mode exposure actually results in two images. Each image is analogous to an ACCUM mode image (i.e., it has a single reset and read before and after each integration period). The two images are flat fielded and corrected for the "shading" effect (see Chapter 3) using the on-board NICMOS computer, and then compared in order to filter out

Table 8.3: Preliminary Exposure Times with Dark Current Calibration

Time (seconds) (NREAD=1)	Time (seconds) (NREAD=9)
1.071	9.939
2.038	12.075
4.963	15.157
9.715	18.339
25.714	22.533
58.142	30.274
110.246	44.969
229.680	62.702
	88.335
	114.806
	163.642
	234.240
	365.156
	485.148

any CR hits. The brightest object common to both images and located inside the coronographic acquisition aperture is found. This object is assumed to be the desired target. A simple (and of undemonstrated reliability for anything other than a point or circular source) algorithm is now used to determine the position of the centroid of this source, and the telescope is moved such that this position is centered in the coronographic hole. The expected accuracy of this procedure for point sources is better than one quarter of a Camera 2 pixel (i.e., 0.019 arcsec), assuming all cosmic rays are successfully removed on-board. The instrument is now ready to acquire more data, and the ACQ mode procedure finished.

Problems to beware of in the ACQ process include cosmic rays and coronograph centering accuracy. It is expected, as mentioned above, that the target should be centered behind the hole with an accuracy of better than one quarter of a pixel. How much better remains to be seen. Observers should note that in order to compare library PSFs with coronographic images for the purposes of determining source extensions or morphology, an accuracy of one quarter of a pixel may not be sufficient at long wavelengths. The two separate images obtained in ACQ mode will filter out most cosmic rays in short exposures, but if an ACQ mode exposure longer than about 10 minutes (i.e., 5 minutes for each of the CRSPLIT images) is required, observers should seriously consider a REUSE TARGET OFFSET or INT-ACQ observation, because the probability of a CR hit not being filtered out on-board becomes larger the longer the exposure. In this case it is likely that the acquisition procedure will fail because the brightest source will be a CR hit, and the intended target will not be hidden behind the coronograph during the

subsequent integrations. If the target is bright enough to saturate the detector during the ACQ mode exposure, this is likely to cause poor centering. A failed or unsatisfactory acquisition will probably cause the subsequently acquired images to be useless to the observer. Our initial on-orbit experience suggests that an onboard acquisition is unlikely to succeed for targets with an H magnitude brighter than roughly 4, but this number will be refined with further experience.

▽ The coronographic mode acquisition capability was being characterized during the period this Handbook was revised. An update on its performance will be placed on the STScI NICMOS WWW page on 1 August 1997.

The data which are returned to the ground will be formatted as a hybrid between ACCUM and MULTIACCUM mode data. The two individual images will each be returned (not flat fielded or reduced in any way) to the ground, and will be reduced in the calibration pipeline exactly as if they were two separate ACCUM mode images. However, they are stored in a single FITS data file, similar to a 2-read MULTIACCUM observation, except that there will be no zeroth read returned to the ground.

NICMOS Science Data

One of the major differences the user will find compared to existing instruments on-board HST is that NICMOS (and STIS) data delivered to the observer contains not only the images obtained, but also have variance and quality arrays for each of them. On a pixel by pixel basis these give the statistical uncertainty in the data, and flags identifying any abnormalities in the data respectively. In the case of RAMP mode, as we describe in the Appendix, the variance array is created on board. For the other three modes of operation, these arrays are constructed in the analysis in the ground processing systems (pipelines). For NICMOS data there will be an integration time and a number of valid samples images for each dataset. All the data the user will see will contain all five of these components for each image in a dataset.

See Chapter 13 for a detailed discussion of the NICMOS data products.

Overheads and Orbit Time Determination

In this chapter we describe the overheads associated with NICMOS observations and give examples of how to determine the number of orbits that your program will require.

Overview

Once you have determined the set of science exposures and any additional target acquisition or calibration exposures you may require for your science program, you are ready to determine the total number of orbits to request. Generally, this is a straightforward exercise involving tallying up the overheads on the individual exposures and on the selected pattern (see Chapter 10), packing the exposure and overhead times into individual orbits, and tallying up the results to determine your total orbit request. This process may need to be iterated, in order to seek the most efficient use of the orbit time.

We refer you to the CP/Phase 1 Proposal Instructions for information on the Observatory policies and practices with respect to orbit time requests and for the orbit determination work sheets. Below, we provide a summary of the NICMOS specific overheads, and give several examples to illustrate how to calculate your orbit requirements for Phase 1 Proposals.

NICMOS Exposure Overheads

Estimates of the overheads on exposures are summarized in Table 9.1. All numbers given are preliminary, approximate, rounded where appropriate to the nearest half minute and do not attempt to differentiate in detail the overheads for different NICMOS modes and configurations. They are subject to change prior to the actual scheduling of Cycle 7-NICMOS proposals (i.e., prior to Phase II). They represent our current best predictions. These overhead times are to be used (in conjunction with the actual exposure time and the Cycle 7-NICMOS Phase 1 Proposal Instructions) to estimate the total time in orbits for your Cycle 7-NICMOS proposal time request. After your HST proposal is accepted, you will be asked to submit a Phase II proposal to allow scheduling of your approved observations. At that time you will be presented with actual, up to date overheads by the scheduling software. Allowing sufficient time for overhead in your Phase 1 proposal is important; additional time to cover unplanned overhead will not be granted later.

We note the following important points.

- *Generic (Observatory Level) Overheads*:

  - The first time you acquire an object you must include the overhead for the guide star acquisition.

  - In subsequent contiguous orbits you must include the overhead for the guide star re-acquisition; if you are observing in the continuous viewing zone (CVZ, see the CP/Phase 1 Proposal Instructions), no guide star *re-acquisitions* are required.

  - The re-acquisitions can be assumed to be accurate to ≤ 10 milli-arcsecs; thus additional target acquisitions or peakups are not needed following a re-acquisition.

  - Time must be allowed for each deliberate movement of the telescope; e.g., if you are performing a target acquisition exposure on a nearby star and then offsetting to your target or if you are taking a series of exposures in which you move the target relative to the camera, you must allow time for the moves.

- *NICMOS Specific Overheads*:

  - The 12 second set-up time at the beginning of each orbit or at each different telescope pointing is inclusive of the filter selection. There is no additional set-up time for new telescope pointings due to dithering or chopping with the same instrument configuration.

  - Overheads are operating-mode dependent. In particular, the overhead for the BRIGHTOBJ mode is particularly onerous, since this mode resets and reads each pixel, one pixel at a time.

  - The target acquisition overhead of 98 seconds for coronography needs to be accounted for the first time an object is acquired under the coronographic spot. No re-acquisition is required for observing the same target in different filters, or from one orbit to the next.

- Overhead times for changing cameras are equal to the slew time for the physical distance between the centers of the cameras in arcsecs + 10 seconds. In addition, the observer must include 12 seconds for set-up which includes filter selection.

- The amount of time required to chop depends on the chop throw, and whether an on-target guide star re-acquisition is desired. The telescope can maintain lock on the guide stars if the chop throw is smaller than 2 arcminutes. If it is larger, then the observer can choose to maintain pointing through the gyros (drop-to-gyro) or re-acquire the guide stars (3 minute overhead per re-acquisition—note that this is not the 6-minute orbit re-acquisition) every time the telescope goes back to the target; with the first option the pointing uncertainty is about 1 milliarcsec/second due to telescope drift. The drop-to-gyro option can be adopted for background pointings, where telescope drift is not a concern.

- In most cases, the data management overhead of 3 minutes will be hidden inside the orbit occultation time. However, if a total of (summed over the three cameras) 100 or more read-outs occur within the visibility period of one orbit, the observer must include 3 minutes overhead every 100 read-outs.

Table 9.1: NICMOS Overheads

Action	Overhead
Generic (Observatory Level)	
Guide star acquisition	Initial acquisition 7.1 minutes re-acquisitions on subsequent orbits = 5.3 minutes per orbit
Spacecraft POSTARG moves	for offsets less than 1 arcminute and more than 10 arcsecs = 1 minute, for offsets between 10 arcsecs and 1 arcsec = 0.5 minute; for offsets less than 1 arcsec in size = 20 seconds
Slew of x arcsecs to new target within an orbit (slew < 2 arcmin, same guide stars)	(x + 20) seconds
Type 2 Slew to new target within an orbit (slew > 2 arcmin, new guide stars)	<1 degree slew: 2.5 min. + 9 min. guide star acq. 1 degree < slew <10 degrees: 5.0 min. + 9 min. guide star acq. 10 degrees < slew <100 degrees: 13 min. + 9 min. guide star acq.
Provisional NICMOS Specific Overheads	
Set-up at beginning of each orbit or at each different telescope pointing - always required. (other than dither/chop maneuvering)	18 seconds
Filter change	18 seconds
Exposure overheads: ACCUM MULTIACCUM BRIGHTOBJ	 (28 + NREAD x 0.705) seconds in FAST readout 27 seconds (exptime x 16384 + 10) seconds
Target acquisition (for coronography)	110 + 2 * exptime seconds (includes slew)

Table 9.1: NICMOS Overheads (Continued)

Action	Overhead
Change of camera: from 2 to 3 or vice versa from 1 to 2 or vice versa from 1 to 3 or vice versa	64 seconds + 216 seconds for set-up 38 seconds + 52 seconds for set-up 59 seconds + 221 seconds for set-up
Dithering/Chopping of x arcsecs (< 2 arcmin)	$(x + 20)$ seconds
Chopping of x arcsec (> 2 arcmin, using drop-to-gyro)	$(x + 31)$ seconds
Chopping of x arcsec (> 2 arcmin, with guide star re-acquisition)	$(x + 31)$ seconds + 6.4 minutes for each guide star re-acq
Data management (for every 100 read-outs within an orbit)	3 minutes

Orbit Use Determination

The easiest way to learn how to compute total orbit time requests is to work through a few examples. We provide below seven examples of how to use the information in Table 9.1 to determine your orbit requirements. The overhead examples cover the following cases:

- Example 1: Coronographic observation, with the TWO-CHOP pattern.

- Example 2: Polarimetric observation, with the FOUR-CHOP pattern.

- Example 3: Emission-line mapping of an extended object, with the SQUARE-WAVE-DITH pattern.

- Example 4: General observation with switch of camera and pattern.

- Example 5: Mapping of an extended object with the SPIRAL-DITH-CHOP pattern.

Unless otherwise specified, we assume in the examples that the target declination is 50 degrees, which implies that its visibility period during one orbit is 56 minutes (see the Phase 1 Proposal Instructions).

Example 1: A Two-Chop Pattern Using Multi-Accum and the Coronograph

The proposed science is to observe the extended nebulosity around an IR-bright source at $\lambda = 2.1$ microns. Since the source would saturate the cameras, the observer decides to hide it behind the coronographic spot in NIC2. Coronographic observations require an onboard acquisition of the target under the coronographic spot (see Chapter 5). The two acquisition exposures, which are needed to locate the target in the Camera 2 field of view are assumed here to require 10 seconds integration each in the selected filter (F207M for this observation). The total overhead for reading the two images, calculating the

positions of the target and the coronograph spot, and moving the target under the spot is 170 seconds. The long wavelength observations are affected by non-negligible background, and the observer chooses the TWO-CHOP pattern with a chopping throw of 19 arcsec for background subtraction. The overhead for slewing between the target and each of the two backgrounds is 36 seconds, and the same guide stars can be maintained for such small slews (Table 9.1). The sequence for the TWO-CHOP pattern is: target-background-target-background, with the two background fields positioned on opposite sides of the target (see Chapter 10).

The observer wishes to use the F207M filter in MULTIACCUM mode for the observation, and wants exposure times of 15 minutes at each pointing, for a total exposure time target+background of 60 (i.e., 15 x 4) minutes, half of which is spent on the target. A good sequence for this time would be STEP64 with NSAMP=22, a total time per exposure of 896 seconds. The orbit requirements are summarized in Table 9.2 below:

Table 9.2: Orbit Determination for Example 1

Action	Time (minutes)	Explanation
Orbit 1		
Initial Guide Star Acquisition	7.1	Needed at start of observation of new target
Target Acquisition (under the coronographic spot)	2.8	121 seconds overheads 10 seconds for first acquisition exposure 10 seconds for second acquisition exposure 29 seconds slew to coronagraph
Science exposure, NIC2 F207M	15.4	896 seconds exposure time on target 27 seconds for MULTIACCUM overhead
Science exposure, NIC2 F207M	16.0	36 seconds chopping slew 896 seconds exposure time on background 27 seconds for MULTIACCUM overhead
Orbit 2		
Guide star re-acquisition	5.3	Start of new orbit
Science exposure, NIC2 F207M	15.4	896 seconds exposure time on target 27 seconds for MULTIACCUM overhead
Science exposure, NIC2 F207M	16.0	36 seconds chopping slew 896 seconds exposure time on background 27 seconds for MULTIACCUM overhead

Te total time spent on the target is (7.1+2.7+15.4+16.0) = 41.2 minutes, with a visibility period of 56 minutes. Thus, the third and fourth exposures in the F207M filter must be done during the second orbit, following the guide star re-acquisition and the instrument set-up, since NICMOS exposures cannot be paused across orbits, and the third exposure would not fit in what remains of the first visibility window. The user requests two orbits to accomplish the proposed science observation. (The observer should develop their program by including additional

exposures through the same or other appropriate filters to make more efficient use of what is left of the orbits).

Example 2: Polarization Observations Using a Chop Pattern and MULTI-ACCUM

Polarimetric observations at long wavelengths will be obtained for target A. The NIC1 filters POL0S, POL120S, and POL240S will provide information on the three Stokes parameters. The observer requires exposure times of 20 minutes in each polarizer, in MULTIACCUM mode. A good sequence for this time would be STEP128 with NSAMP=19, a total time per exposure of 1280 seconds.

The declination of the source is 30 degrees, so the visibility period during one orbit is 53 minutes. The orbit requirement is summarized in Table 9.3 below.

Table 9.3: Orbit Determination for Example 2

Action	Time (minutes)	Explanation
Orbit 1		
Initial Guide Star Acquisition	7.1	Needed at start of observation of new target
Science exposure, NIC1 POL0S	21.8	1280 seconds exposure time on target 27 seconds for MULTIACCUM overhead
Science exposure, NIC1 POL120S	21.8	1280 seconds exposure time on target 27 seconds for MULTIACCUM overhead
Orbit 2		
Guide Star re-acquisition	5.3	Start of new orbit
Science exposure, NIC1 POL240S	21.8	1208 seconds exposure time on target 27 seconds for MULTIACCUM overhead

Example 3: Making a Map using SQUARE-WAVE-DITH

The proposer wants to map an extended region in the light of [FeII] (λ 1.644 microns). The choice is to use the F164N (line) and F166N (continuum) filters of NIC1, MULTIACCUM mode, and the SQUARE-WAVE-DITH pattern. The selected dithering step is 4 arcsec, with a total of 3 positions. The slewing overhead between each position will be 26 seconds. The requested exposure time at each position is 10 minutes in each filter, implying that the exposure time for the observation is: T = (10 x 2 x 3) = 60 minutes, exclusive of overheads. The

orbit requirements are summarized in Table 9.4. A good sequence for this time would be STEP128 with NSAMP=14, a total time per exposure of 640 seconds.

Table 9.4: Orbit Determination for Example 3

Action	Time (minutes)	Explanation
Orbit 1		
Initial Guide Star Acquisition	7.1	Needed at start of observation of new target
Science exposure, NIC1 F164N	11.2	640 seconds exposure time on position # 1 27 seconds for MULTIACCUM overhead
Science exposure, NIC1 F164N	11.5	27 seconds for dither 640 seconds exposure time on position # 2 27 seconds for MULTIACCUM overhead
Science exposure, NIC1 F164N	11.5	25 seconds dither 640 seconds exposure time on position # 3 27 seconds for MULTIACCUM overhead
Science exposure, NIC1 F166N	11.5	640 seconds exposure time on position # 1 27 seconds for MULTIACCUM overhead 25 seconds dither
Orbit 2		
Guide Star re-acquisition	5.3	Start of new orbit
Science exposure, NIC1 F166N	11.1	640 seconds exposure time on position # 2 27 seconds for MULTIACCUM overhead
Science exposure, NIC1 F166N	11.5	25 seconds for dither 640 seconds exposure time on position # 3 27 seconds for MULTIACCUM overhead

Example 4: Changing Cameras and Pattern

The proposed science is to observe a target taking:

- Exposures in the NIC1 F108N filter, using the MULTIACCUM mode and the XSTRIP-DITH pattern, with 5 arcsecs dithering step and 4 positions; the exposure time is T=900 seconds at each position. A good sequence for this time would be STEP64 with NSAMP=22, a total time per exposure of 896 seconds.

- Exposures in the NIC2 F205W filter, using the ACCUM mode with NREAD=1. The TWO-CHOP pattern with chopping throw of 150 arcsecs and guide star re-acquisition on the target (see Example 1) is selected to remove the background. The exposure time is T=250 seconds at each pointing, implying a total on-source exposure time of 500 seconds. The closest TPG time is 251.188 seconds and 0.598 seconds must be added to get 251.786 seconds total exposure time. Table 9.5 lists the orbit requirements.

Table 9.5: Orbit Determination for Example 4

Action	Time (minutes)	Explanation
Orbit 1		
Initial Guide Star Acquisition	7.1	Needed at start of observation of new target
Science exposure, NIC1 F110M	15.4	896 seconds exposure time on position # 1 27 seconds for MULTIACCUM overhead
Science exposure, NIC1 F110M	15.8	26 seconds for dither 896 seconds exposure time on position # 2 27 seconds for MULTIACCUM overhead
Orbit 2		
Science exposure, NIC1 F110M	15.4	26 seconds dither 896 seconds exposure time on position # 3 27 seconds for MULTIACCUM overhead
Guide Star re-acquisition	5.3	Start of new orbit
Science exposure, NIC1 F110M	15.8	26 seconds dither 896 seconds exposure time on position # 4 27 seconds for MULTIACCUM overhead
Science exposure, NIC2 F205W	6.2	(39+51) seconds for camera change + set-up 252 seconds exposure on target 31 seconds ACCUM overhead
Science exposure, NIC2 F205W	5.9	74 seconds chop 252 seconds exposure on background # 1 29 seconds ACCUM overhead
Orbit 3		
Guide Star re-acquisition	5.3	Start of new orbit
Science exposure, NIC2 F205W	4.7	252 seconds exposure on target 29 seconds ACCUM overhead
Science exposure, NIC2 F205W	5.9	74 seconds chop 252 seconds exposure time on background # 2 29 seconds ACCUM overhead

After the initial guide star acquisition and the instrument set-up of 12 seconds, the first science exposure of 896 seconds in the first filter (F110M) is obtained on the first pointing (position #1). The telescope slew to reach position #2 requires 26 seconds, and the exposure in the F110M filter is repeated up to the forth position. For the second part of the observation, the switch from NIC1 to NIC2 requires 90 seconds. The on-target exposure time requested in the F205W filter is T=500 seconds, split between the two target visits of the TWO-CHOP pattern. After the first exposure on the target and after the camera read-out, the telescope slews to the background in 74 seconds. The subsequent slew, back onto the target, is followed by a guide star re-acquisition of 6 minutes. The sequence continues, alternating target and background, until the pattern is completed.

Example 5: Another Example of Mapping

The observer wants to map an extended object, for instance a galaxy, with NIC2 and the F187W filter. The wavelength chosen is long enough that the observation may be affected by background emission, and the SPIRAL-DITH-CHOP is selected for background removal. The dithering step is set equal to the size of NIC2, 19.2 arcsec, and the chopping throw is set to 180 arcsec. The SPIRAL-DITH-CHOP pattern will start at the center of the target and move outward. The galaxy has a bright core and relatively faint extended emission, so MULTIACCUM mode will be used. The proposed exposure time is 3 minutes per pointing, and the galaxy will be covered with 9 different pointings. A good sequence for this time would be STEP32 with NSAMP=13, a total time per exposure of 192 seconds. The orbit requirements are summarized in Table 9.6.

Table 9.6: Orbit Determination for Example 5

Action	Time (minutes)	Explanation
Orbit 1		
Initial Guide Star Acquisition	7.1	Needed at start of observation of new target
Science exposure, NIC2 F187W	3.7	192 seconds exposure time on target position # 1 27 seconds for MULTIACCUM overhead
Science exposure, NIC2 F187W	5.0	78 seconds chop 192 seconds exposure time on background # 1 27 seconds for MULTIACCUM overhead
Science exposure, NIC2 F187W	11.2	72 seconds chop 383 seconds guide star re-acquisition 192 seconds exposure time on target position # 2 27 seconds for MULTIACCUM overhead
Science exposure, NIC2 F187W	5.0	78 seconds chop 192 seconds exposure time on background # 2 27 seconds for MULTIACCUM overhead
Science exposure, NIC2 F187W	11.3	76 seconds chop 383 seconds guide star re-acquisition 192 seconds exposure time on target position # 3 27 seconds for MULTIACCUM overhead
Orbit 2		
Guide Star re-acquisition	5.3	Start of new orbit
Science exposure, NIC2 F187W	5.0	77 seconds chop 192 seconds exposure time on background # 3 27 seconds for MULTIACCUM overhead
Science exposure, NIC2 F187W	3.7	192 seconds exposure time on target position # 4 27 seconds for MULTIACCUM overhead
DUMP buffer	1.0	Partial buffer dump
Science exposure, NIC2 F187W	5.0	78 seconds chop 192 seconds exposure time on background # 4 27 seconds for MULTIACCUM overhead

Table 9.6: Orbit Determination for Example 5 (Continued)

Action	Time (minutes)	Explanation
Science exposure, NIC2 F187W	11.4	80 seconds chop 383 seconds guide star re-acquisition 192 seconds exposure time on target position # 5 27 seconds for MULTIACCUM overhead
Science exposure, NIC2 F187W	5.0	77 seconds chop 192 seconds exposure time on background # 5 27 seconds for MULTIACCUM read out
Guide Star re-acquisition	5.3	Start of new orbit
Science exposure, NIC2 F187W	11.3	76 seconds chop 383 seconds guide star reacq 192 seconds exposure time on background # 6 27 seconds for MULTIACCUM overhead
Science exposure, NIC2 F187W	5.0	77 seconds chop 192 seconds exposure time on background # 6 27 seconds for MULTIACCUM overhead

Orbit 3

Action	Time (minutes)	Explanation
Science exposure, NIC2 F187W	3.7	192 seconds exposure time on target position # 7 27 seconds for MULTIACCUM overhead
Science exposure, NIC2 F187W	5.0	77 seconds chop 192 seconds exposure time on background # 7 27 seconds for MULTIACCUM read out
DUMP buffer	1.3	Partial buffer dump
Science exposure, NIC2 F187W	11.2	72 seconds chop 383 seconds guide star re-acquisition 192 seconds exposure time on target position # 8 27 seconds for MULTIACCUM overhead
Science exposure, NIC2 F187W	5.0	77 seconds chop 192 seconds exposure time on background # 8 27 seconds for MULTIACCUM read out
Science exposure, NIC2 F187W	11.2	72 seconds chop 383 seconds guide star reacq 192 seconds exposure time on background # 9 27 seconds for MULTIACCUM overhead
Science exposure, NIC2 F187W	5.0	77 seconds chop 192 seconds exposure time on target position # 9 27 seconds for MULTIACCUM overhead

The size of the chop is determined by the distance between the pointings; the time for the slew between the target and the background is always 77 seconds, while that for the slew between the background and the target is about 72 seconds. Note that guide star reacquisitions at the start of a visibility period can hide some time in occultation. Thus the observer is charged more time (383 s) for reacquisitions that occur during a visibility period.

PART 3

Supporting Material

The chapters in this part present more detailed material in support of the Users Guide. Included are a description of observing techniques for measuring the background and mapping extended targets; the detailed sensitivity information for each imaging filter; and some reference material on infrared flux units and lists of infrared lines.

Techniques for Dithering, Background Measurement and Mosaicing

In this chapter we deal with techniques for small scale motions to remove localized detector non-uniformities, mapping areas larger than the size of the field of view of the NICMOS cameras, and the issue of removing the thermal background of the telescope. Special procedures have been created to enable you to perform these operations.

Introduction

Multiple exposures with small offsets in the pointing of the telescope are usually necessary or recommended for NICMOS observations. We distinguish three particular circumstances which may require small offsets:

- **Dithering** to permit the removal of dead or non-calibrated pixels (i.e., non-correctable) on the detectors.

- Dithering or **chopping** to measure the background associated with an astronomical source.

- **Mosaicing** to image a source larger than the NICMOS field of view.

The techniques described in this chapter may be used to accomplish any one or any combination of these goals.

The early SMOV results show that the background is considerably fainter than was expected prior to the deployment of NICMOS (see Chapter 3). While only a preliminary analysis of the SMOV data has been completed, it appears that the thermal background is spatially uniform with variations no larger than a few percent across the field of view of NIC3. Temporal variations on orbit timescales with <10% amplitude have been observed and more significant variations cannot yet be excluded. The description of the thermal background in Chapters 3 and 6 and the Exposure Time Calculator provide a basis for estimating the relative contributions of source and background. It is strongly advised that provision for direct measurement of the background be included in proposals whenever the background is significant relative to the source(s) of interest. While the frequency of such measurements is presently difficult to define, at least once per orbit should suffice when the background is not overly critical to an observation and more frequent measurements should be planned when the background must be measured to high accuracy.

▽ All observations at wavelengths beyond 1.6 microns should at least consider the potential need for background measurements.

Background images will be obtained by offsetting the telescope from the target to point to an "empty" region of the sky. The ability to routinely offset the telescope pointing will then be a fundamental operational requirement for NICMOS. To make it easier to plan observations beyond 1.6 microns, a set of pre-defined observing *patterns* was built; these patterns combine exposures taken at different telescope pointings into an *association*. A *pattern* is a set of images of the same astronomical target obtained at pointings offset from each other, for the purpose, for instance, of creating background images. The *associations* of exposures are created for the purpose of processing simultaneously all the images from a single pattern. In addition to background subtraction at long NICMOS wavelengths, the *patterns* will be useful for creating *maps* of extended targets at any wavelength.

Two distinct type of telescope motion are defined:

- *Dither*: Individual motions are limited to no more than 40 arcsecs. These are intended to be used to perform small dithers, to measure backgrounds for compact sources, and to accomplish sequences of overlapping exposures for the construction of mosaics. Such sequences will be assembled into a single final image by the calibration pipeline.

- *Chop*: Motions up to 1800 arcsecs are permitted. These are intended for the measurement of the background at one or more locations significantly removed from the target pointing. Each non-contiguous background pointing will be assembled into its own final image in addition to the target pointing by the calibration pipeline.

Telescope motions involve overheads for physically moving the telescope and, if necessary, for re-acquiring the guide stars. Therefore, significant time overheads may be incurred by observations which need background subtraction or propose to map extended regions of the sky. A careful estimate of the overheads associated with a specific observation or set of observations is necessary to evaluate the number of orbits required (see Chapter 9).

Chopping and Dithering Strategies

The most efficient strategy for removing the background from a science exposure strongly depends on the nature of the target and of the science to be accomplished. In general two types of targets can be defined: compact and extended.

Compact Objects

For compact objects, such as point sources, background subtraction can be achieved by moving the target across the camera field of view (see Figure 10.1). A dither pattern, which involves movements of a few arcsecs from one exposure to the next, can then be used. This is an efficient way to build background images, since the target is present in each exposure, and a background image can be created from the stacking and filtering of all exposures.

Figure 10.1: Dithering.
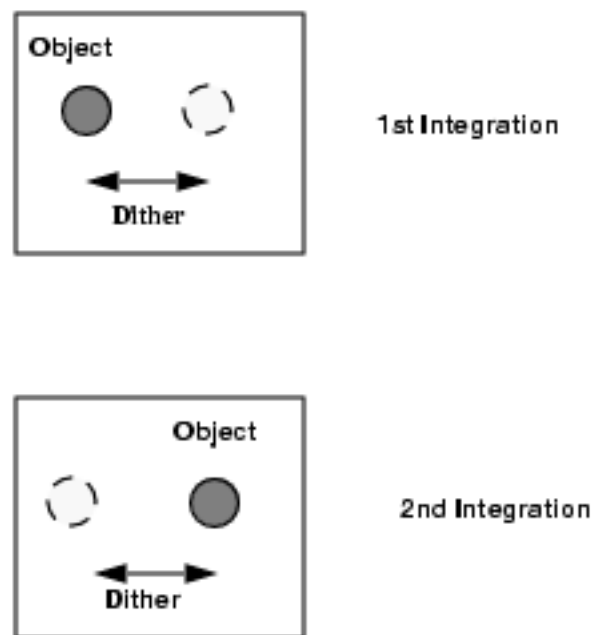
Extended Objects

For an extended object which occupies a significant portion of the NICMOS field of view, the dithering technique does not apply to building background images. In this case, offsets to an adjacent field (chopping), chosen to be at least one camera field away in an arbitrary direction, are necessary. By offsetting in different directions a stacked and filtered sky can be created which removes the effect of contaminating objects in the offset fields (see Figure 10.2). As in the case of compact objects, these offsets might be quite small, but for large galaxies for example, they may need to be over considerable distances. The user will have the ability to specify the offset values and directions and their number in the Phase II instructions.

Figure 10.2: Chopping
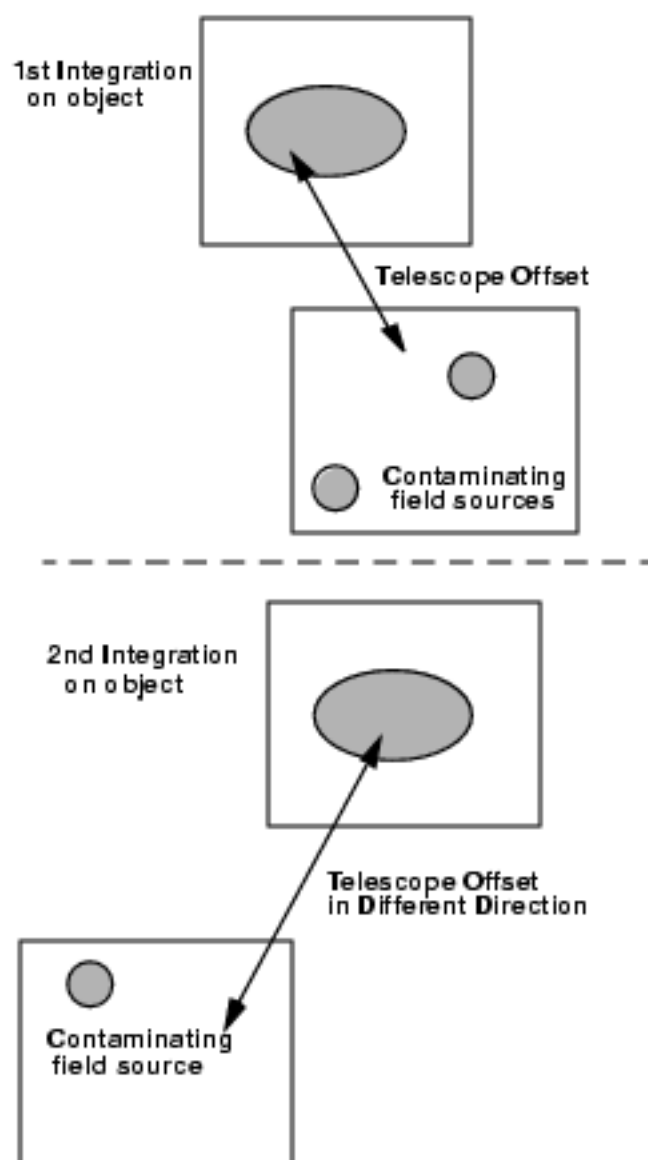
Chopping and Dithering Patterns

There are a set of 11 pre-designed patterns available for NICMOS observations. They include: 4 dither patterns, 4 chop patterns, and 3 dither-chop patterns. For each of these, the observer will be able to specify, during the Phase II Proposal submission, the total number of positions desired (2 to 40), the dither size (0 to 40 arcsecs), the chop size (0 to 1800 arcsecs), and the orientation of the pattern on the sky. The option POS-TARG will be still available for offsetting the telescope and creating custom-design patterns, but there are a number of advantages in using the pre-designed patterns:

- They simplify the specification of complex observations in the Phase II proposal.

- All the observations pertaining to a pattern result in one association and are simultaneously calibrated and combined in the data calibration pipeline, including background calibration, cosmic ray removal, and flat field averaging. Observations obtained with POSTARG do not result in associations, and will have to be combined manually by the observer.

- They permit the observation of a mosaic with a fixed position angle without fixing spacecraft roll, which increases the number of opportunities to schedule the observations.

Multiple exposures may be obtained at each position by the use of the number-of-iterations (NEXP) optional parameter. This may be useful for cosmic ray removal.

The 11 patterns are listed in Table 10.1, together with applicable parameters, such as the allowed values for the number of steps in the pattern (Num_Pos), for the dither size and for the chop size. In addition, the figure number where the pattern is graphically shown is given in column 5 of Table 10.1. Offset sizes and number of steps in a pattern affect the amount of overhead time required to perform an observation (see Chapter 9). The effects of dithering or chopping on an astronomical image are shown in a set of examples in the next section.

Table 10.1: NICMOS Pre-designed Observing Patterns and Parameters

Pattern Name	Num. Pos.	Dither Size	Chop Size	See Figure
NONE (default)	NA	NA	NA	
SPIRAL-DITH	2-40	0.0-40.0	NA	Figure 10.3
SQUARE-WAVE-DITH	2-40	0.0-40.0	NA	Figure 10.3
XSTRIP-DITH	2-40	0.0-40.0	NA	Figure 10.3
YSTRIP-DITH	2-40	0.0-40.0	NA	Figure 10.3
ONE-CHOP	2-40	NA	0.0-1800.0	Figure 10.4
TWO-CHOP	2-40	NA	0.0-1800.0	Figure 10.4
FOUR-CHOP	2-40	NA	0.0-1800.0	Figure 10.4
EIGHT-CHOP	2-40	NA	0.0-1800.0	Figure 10.4
SPIRAL-DITH-CHOP	2-40	0.0-40.0	0.0-1800.0	Figure 10.5
XSTRIP-DITH-CHOP	2-40	0.0-40.0	0.0-1800.0	Figure 10.5
YSTRIP-DITH-CHOP	2-40	0.0-40.0	0.0-1800.0	Figure 10.5

Dither Patterns

The dither patterns are recommended for the background subtraction from observations of point sources (beyond 1.6 microns), for the construction of mosaics (maps) of regions of the sky, and for the reduction of flat field uncertainties. The four dither patterns are called SPIRAL-DITH, SQUARE-WAVE-DITH, XSTRIP-DITH, and YSTRIP-DITH. Most of the names are self-explanatory: the SPIRAL-DITH pattern produces a spiral around the first pointing; the SQUARE-WAVE-DITH pattern covers extended regions by moving along a square-wave shape; the XSTRIP-DITH and the YSTRIP-DITH patterns map a strip of the sky along the x and y directions of the detector (as defined in Figure 4.23). The difference between the XSTRIP-DITH and the YSTRIP-DITH patterns is that the first moves by default along the grism dispersion axis, while the second moves orthogonal to the grism dispersion axis. The four patterns are illustrated below:

Figure 10.3: Dither Patterns

SPIRAL-DITH

$5 \leftarrow 4 \leftarrow 3$
$6 \quad 1 \rightarrow 2 \quad 11$
$7 \rightarrow 8 \rightarrow 9 \rightarrow 10$

YSTRIP-DITH

6
5
4
3
2
1

SQUARE-WAVE-DITH

$2 \rightarrow 3 \quad 6 \rightarrow 7$
$1 \quad 4 \rightarrow 5 \quad 8 \rightarrow 9$

XSTRIP-DITH

$1 \rightarrow 2 \rightarrow 3 \rightarrow 4 \rightarrow 5 \rightarrow 6 \rightarrow$
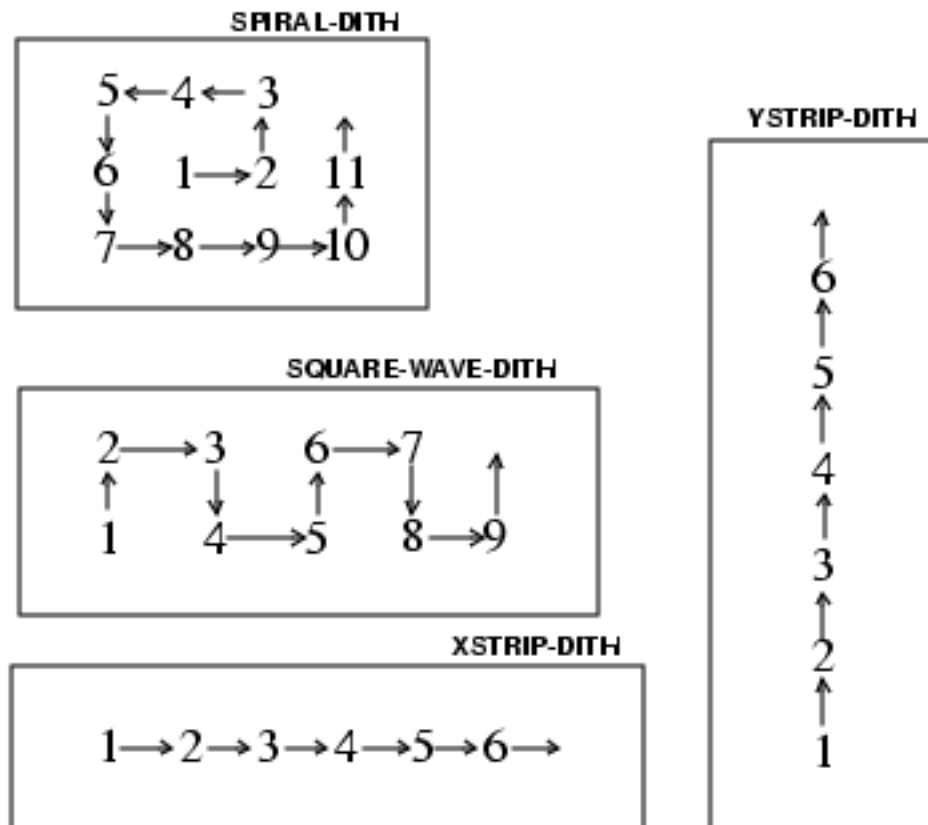
Chop Patterns

The chop patterns are recommended for measuring the background adjacent to extended targets. For each chop pattern, half of the exposures are taken on the target (position 1). The names of the chop patterns are: ONE-CHOP, TWO-CHOP, FOUR-CHOP, and EIGHT-CHOP. The ONE-CHOP pattern produces one image of the target and one image of the background. the TWO-CHOP pattern produces one image (with two exposures) of the target and two background images, with the background fields positioned on opposite sides of the target. The two other patterns increase the number of target-background pairs to four and eight, respectively. A large number of background images may be required if they contain a large number of contaminating sources or if the background is highly structured. The four chop patterns are shown in the figure below:

Figure 10.4: Chop Patterns

ONE-CHOP

$$1 \longleftrightarrow 2$$

TWO-CHOP

$$4 \longleftrightarrow 1 \longleftrightarrow 2$$

FOUR-CHOP

EIGHT-CHOP
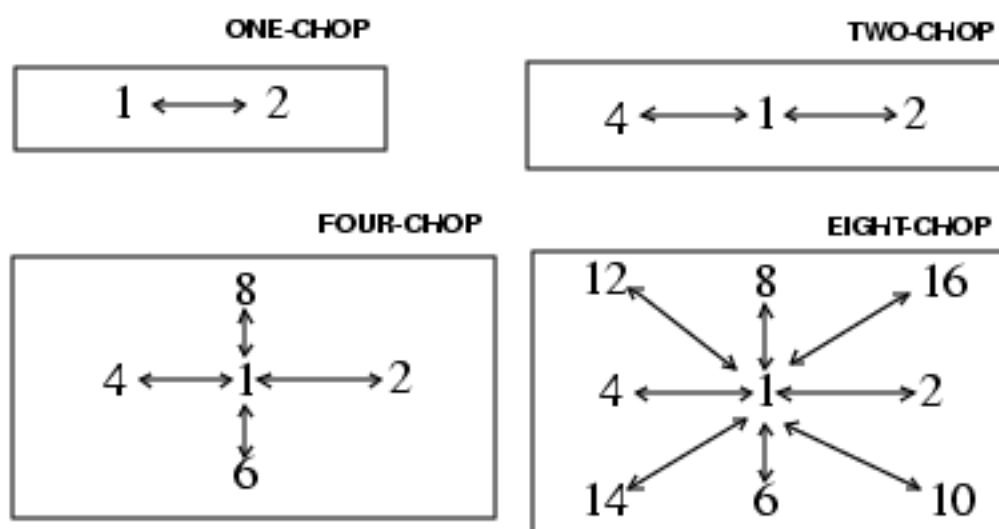
Combined Patterns

The combined patterns permit dithering interleaved with chops to measure the background. They are recommended for simultaneous mapping and background subtraction during observations of extended targets, beyond 1.6 microns. Three combined patterns are implemented: SPIRAL-DITH-CHOP, XSTRIP-DITH-CHOP, and YSTRIP-DITH-CHOP. Their characteristics are analogous to the dither patterns SPIRAL-DITH, XSTRIP-DITH, and YSTRIP-DITH, respectively, with the addition that each dither step is coupled with a background image obtained by chopping. The three combined patterns are shown in Figure 10.5.

Figure 10.5: Combined Patterns

SPIRAL-DITH-CHOP

XSTRIP-DITH-CHOP

YSTRIP-DITH-CHOP
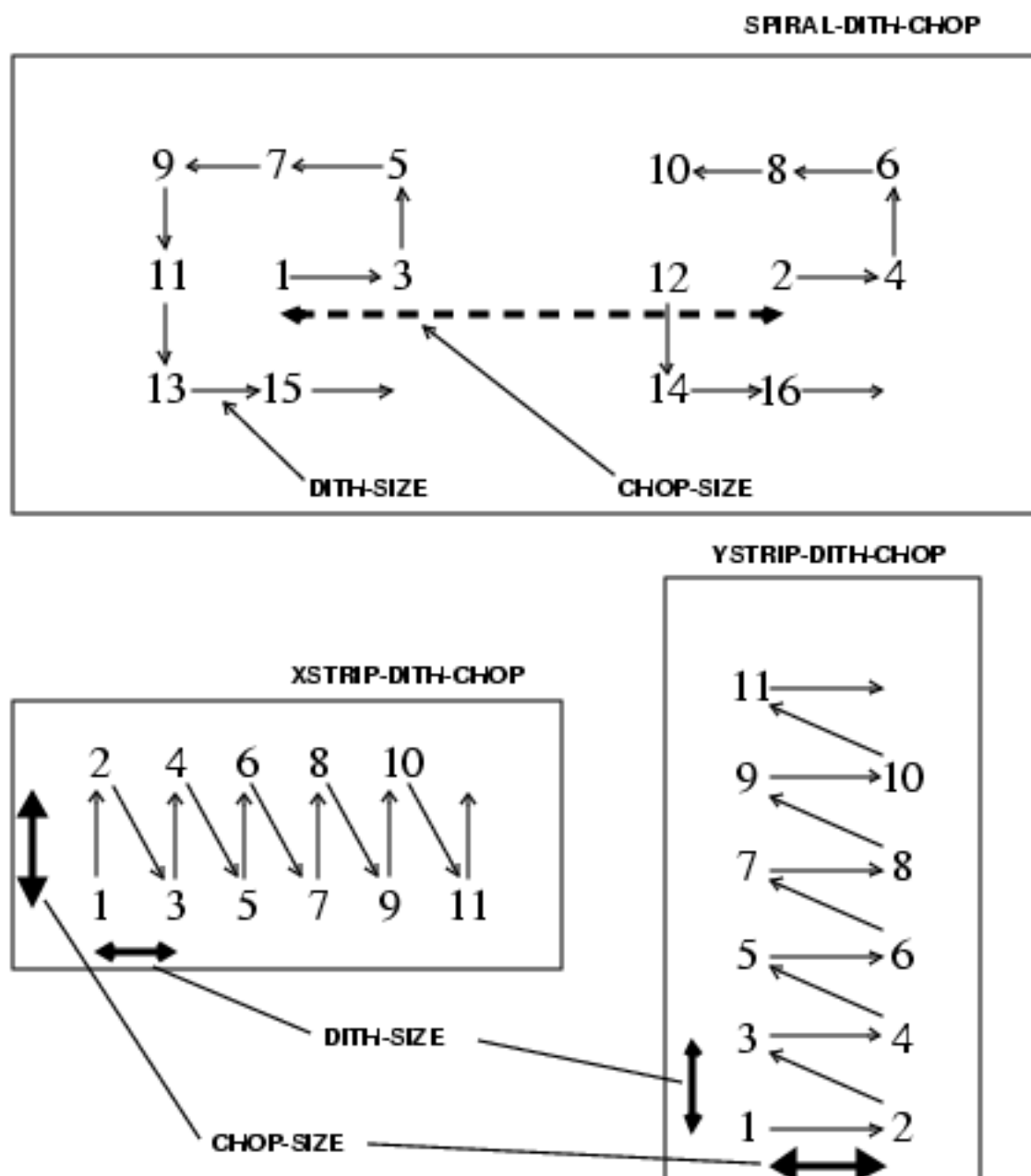
Examples

The next few pages show a few selected examples of how the patterns work on astronomical observations.

Figure 10.6: Square Wave Dither
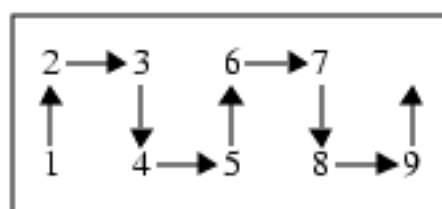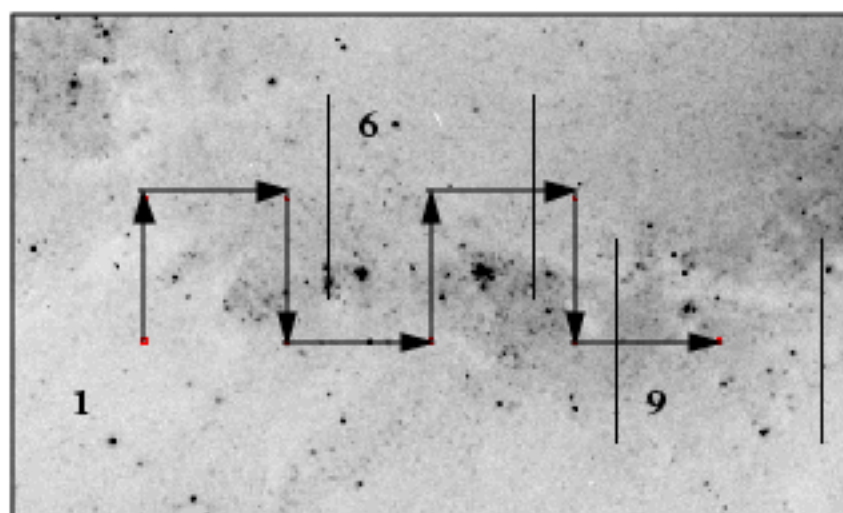
Images Taken:
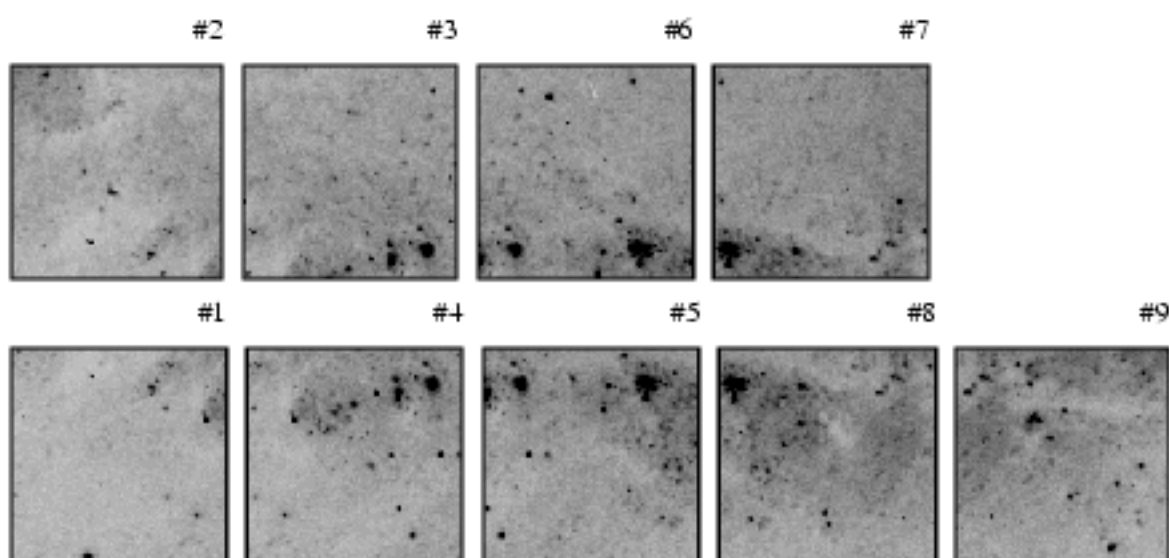
Figure 10.7: Two-Chop Pattern
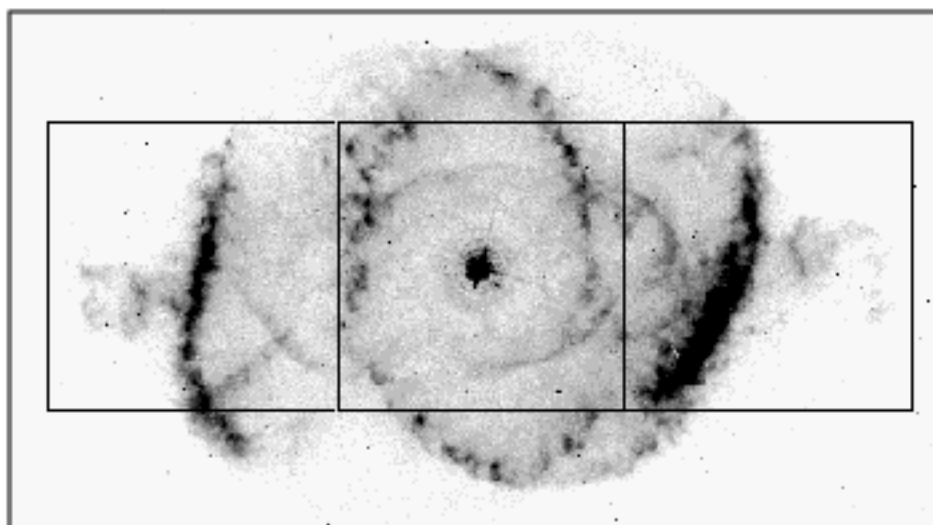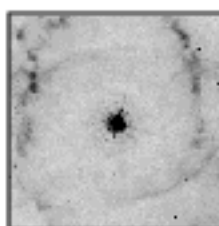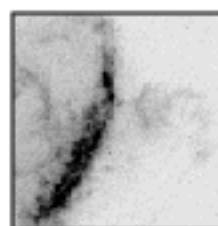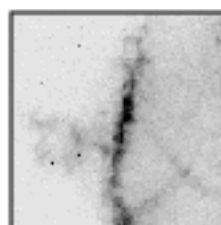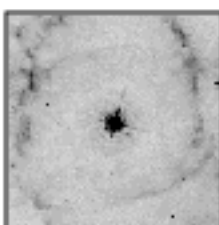
Images Taken:

Figure 10.8: Four-Chop Pattern
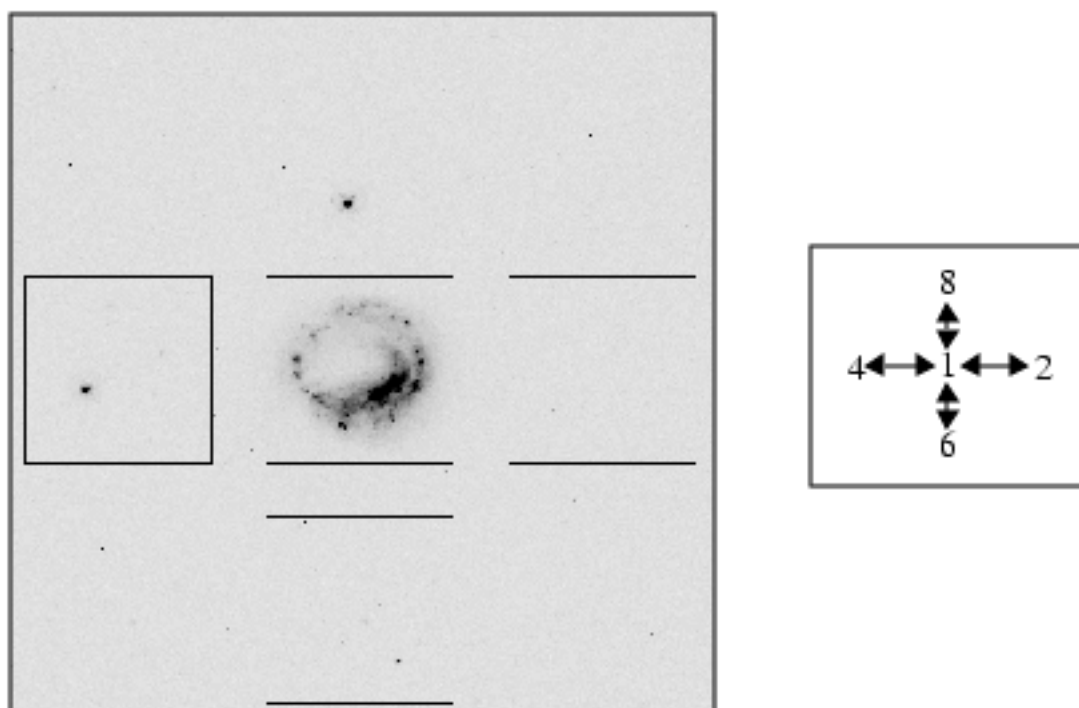
Images Taken:
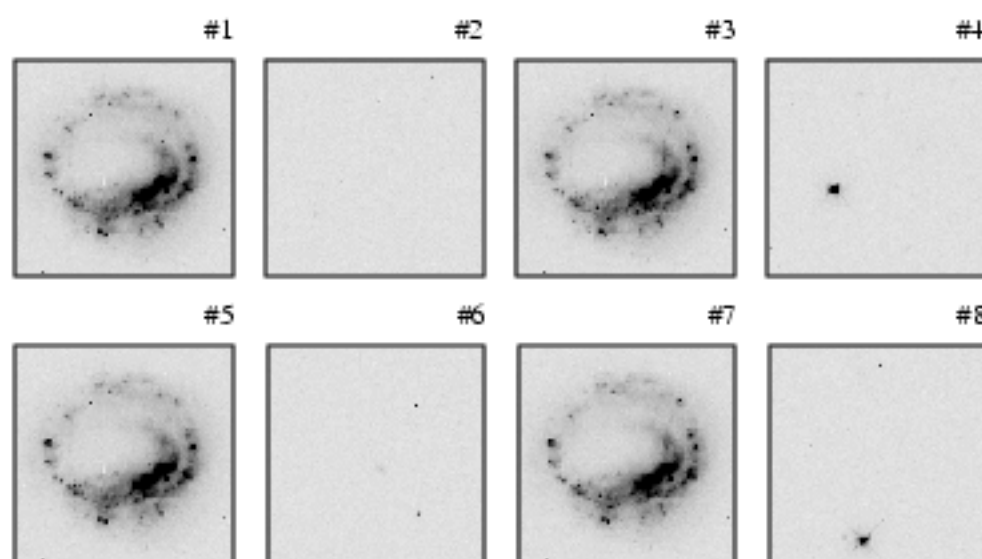
Figure 10.9: Spiral-Dith-Chop Pattern
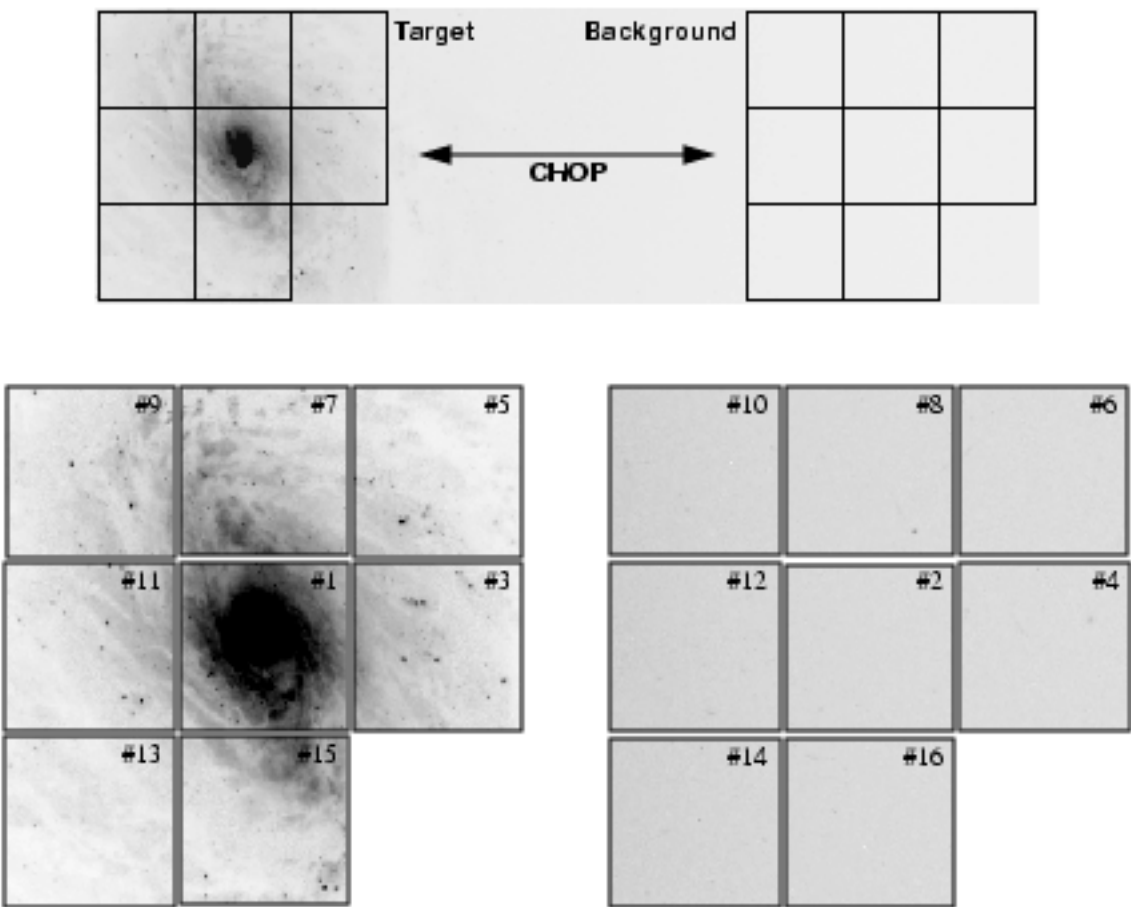
Sequence of Frames

Orienting Patterns

Observations will often require that patterns are executed with specific position angles (PA) on the sky. For instance an observer may need to map an elongated region with PA=*n* degrees on the sky, using the SQUARE-WAVE-DITH pattern. Since the use of the ORIENT special requirement usually constrains the scheduling opportunities for a target (and may result in the unavailability of suitable guide stars), NICMOS implements an optional parameter called PATTERN-ORIENT (see next section). With this parameter, the orientation of the pattern on the sky can be set independently of the orientation of the three NICMOS detectors (and vice-versa). If a specific orientation of the detectors is also required, then the observatory level special requirement ORIENT must be set together with PATTERN-ORIENT.

The default value for PATTERN-ORIENT is DETECTOR, and the pattern motions are in the NICMOS (x-y) focal plane orientation, i.e., rotated 225 degrees from the U3 axis. The orientation of the patterns on the sky is then determined by the orientation of the telescope with the ORIENT special requirement. Other values for the PATTERN-ORIENT parameter are given by the standard convention for PA, from 0.0 to 360.0, North through East. For example, the XSTRIP-DITH pattern with PATTERN-ORIENT=0 will track from East to West on the sky (the +Y, vertical in the preceding figure, axis is pointing North), and with PATTERN-ORIENT=45 from Southeast to Northwest. The YSTRIP-DITH pattern with PATTERN-ORIENT=0 will track from South to North.

Phase II Proposal Instructions for Patterns

▽ We discuss the Phase II instructions for patterns in this section in order to illustrate the options available, however, this is *not* an exhaustive description and is *not* the appropriate reference to use when preparing a Phase II proposal. At that stage you should refer to the Institute's Phase II Proposal Instructions, which contain a complete and up-to-date guide.

This section is not crucial for preparing the Phase I proposal, but it may be relevant to know beforehand which parameters will be available, and what values these parameters can have. One, and only one, pattern may be defined on an individual exposure logsheet line. A pattern may only be specified on the *prime* NICMOS camera. The motions between each exposure are carried out by expanding the pattern into a sequence of individual exposures separated by POSTARG operations. Only a single filter may be used within a pattern (i.e. only one filter may be specified on a Phase II exposure logsheet line).

The set of exposures resulting from a pattern is called an association. A number of optional parameters are implemented for associations, and are listed below.

These patterns may also be used with motions of the Field Offset Mirror. While the FOM is "available" (i.e., not supported) for Cycle 7-NICMOS, observations requiring very rapid small offsets may benefit from its use and observers can discuss this with their Contact Scientist during the Phase II proposal process.

Parameters

- PATTERN=NONE (default) or Pattern_Name   (see Table 10.1).

- NUM-POS = 2 to 40   (number of steps in dither or chop pattern to perform).

- DITH-SIZE = 0.0 to 40.0   (size of *each* step in arcsecs).

- CHOP-SIZE = 0.0 to 1800.0   (size of *each* step in arcsecs).

- OFFSET=SAM (default),   (use SAMs; gyros for large moves with re-acquire); SAM-NO-REACQ,   (use SAMs; do not attempt to re-acquire guide stars); SAM-NO-GYRO,   (use SAMs; must use same or new guide stars).

- PATTERN-ORIENT-DETECTOR (default),   (move in detector X-Y system) 0.0 - 360.0 degrees from PA=0 increasing to East (Note that this does *not* constrain telescope roll; use existing ORIENT requirement).

Types of Motions

The OFFSET parameter defines which type of telescope motion will be performed during a pattern, in order to dither or chop. Telescope motions fall into three categories:

- Small angle motions (SAMs) where FGS Fine Lock guiding is maintained. Such SAMs are typically limited to < 2 arcmins from the point of the initial guide star acquisition. This is the practical limit of the radial extent of the pattern. Often it will be smaller due to guide star availability.

- SAMs without FGS guiding (i.e., GYRO HOLD pointing control). These are necessary for larger motions (> 2 arcmins). The telescope will drift at a rate of 1 to 2 milli-arcsecs per second of time (elapsed time—*not* exposure time).

- SAMs with RE-ACQuisitions at each return to the target position. This can be used to chop between a target and an offset background measurement pointing (which would be observed with GYRO HOLD pointing control).

The available options for OFFSET are:

- SAM, the default, will use guide stars whenever possible. If a motion, or the sequence of motions, moves the telescope sufficiently from the original position that guide stars are no longer available then exposures will be obtained using GYRO HOLD. If a subsequent motion returns the telescope to a point where the original guide stars become available then it will RE-ACQuire the guide stars. This incurs an overhead of ~3 minutes for each RE-ACQuisition.

- SAM-NO-REACQ will use guide stars (FGS Fine Lock) until the *first* instance in the pattern when guide stars become unavailable. The remainder of the pattern will be executed using GYRO HOLD pointing control.

- SAM-NO-GYRO will use guide stars for all exposures. If guide stars are not available, the observation cannot be scheduled.

CHAPTER 11
Imaging Reference Material

This chapter provides the sensitivity information for the imaging filters, ordered by camera and increasing central wavelength. See Chapter 4 for a detailed description of the the figures in this chapter. The corresponding information for the grism and polarizer elements is provided in the same format in Chapter 5.

Camera 1, Filter F090M

Central wavelength(μm)	Mean Wavelength(μm)	Peak Wavelength (μm)	FWHM (μm)	Range (μm)	MaxTr %	Pixel Fraction
0.9003	0.8970	0.9175	0.1885	0.8 - 1.0	79.64	0.150

Figure 11.1: Camera 1, Filter F090M
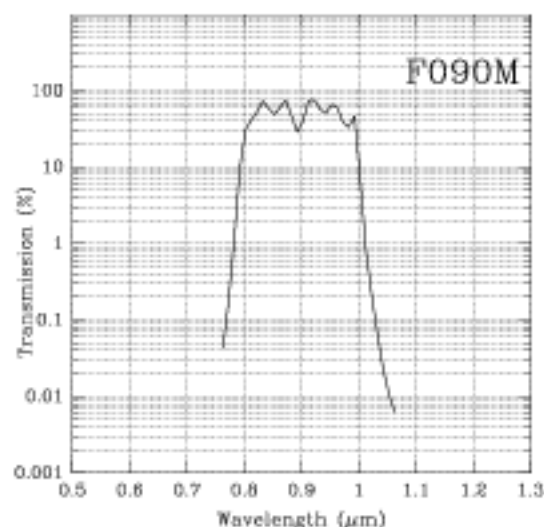
Camera 1, Filter F095N

[S III] Line

Central wavelength (μm)	Mean wavelength (μm)	Peak wavelength (μm)	FWHM (μm)	Range (μm)	MaxTr %	Pixel Fraction
0.9538	0.9536	0.9508	0.0088	1%	66.31	0.136

Figure 11.2: Camera 1, Filter F095M
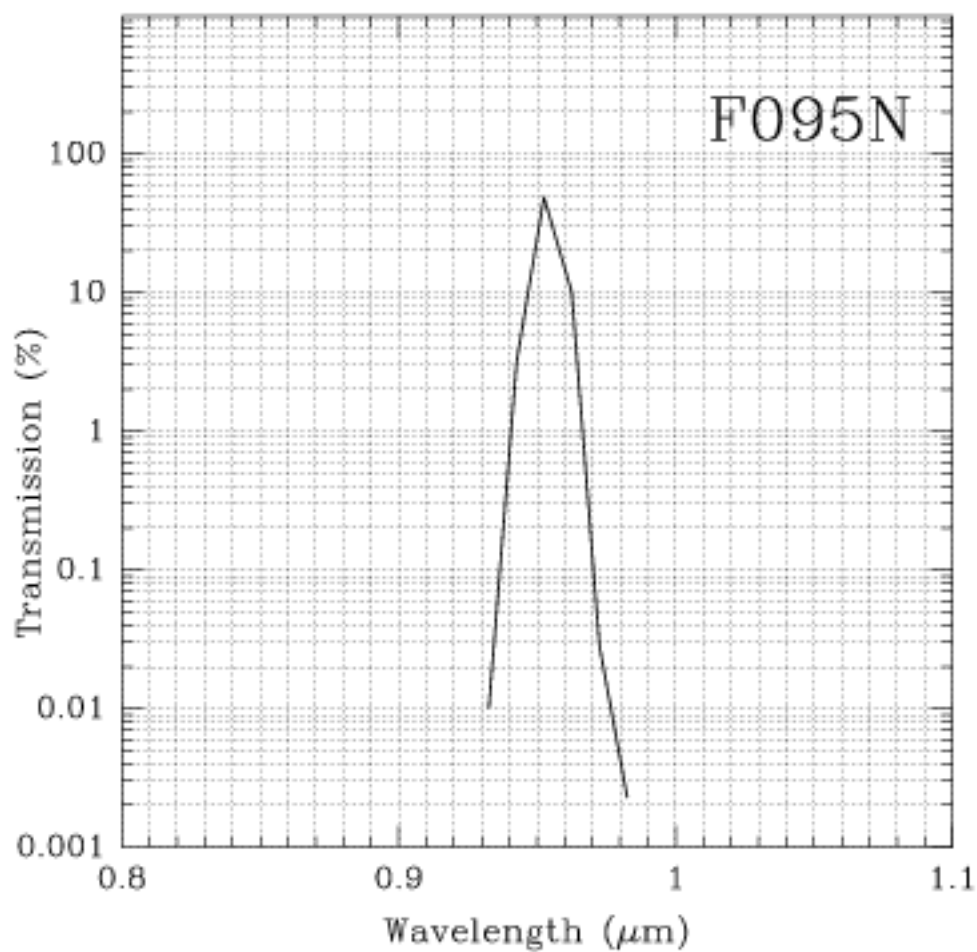
Camera 1, Filter F097N

[SIII] Continuum

Central wavelength (µm)	Mean wavelength (µm)	Peak wavelength (µm)	FWHM (µm)	Range (µm)	MaxTr %	Pixel Fraction
0.9717	0.9715	0.9740	0.0094	1%	73.51	0.131

Figure 11.3: Camera 1, Filter F097N
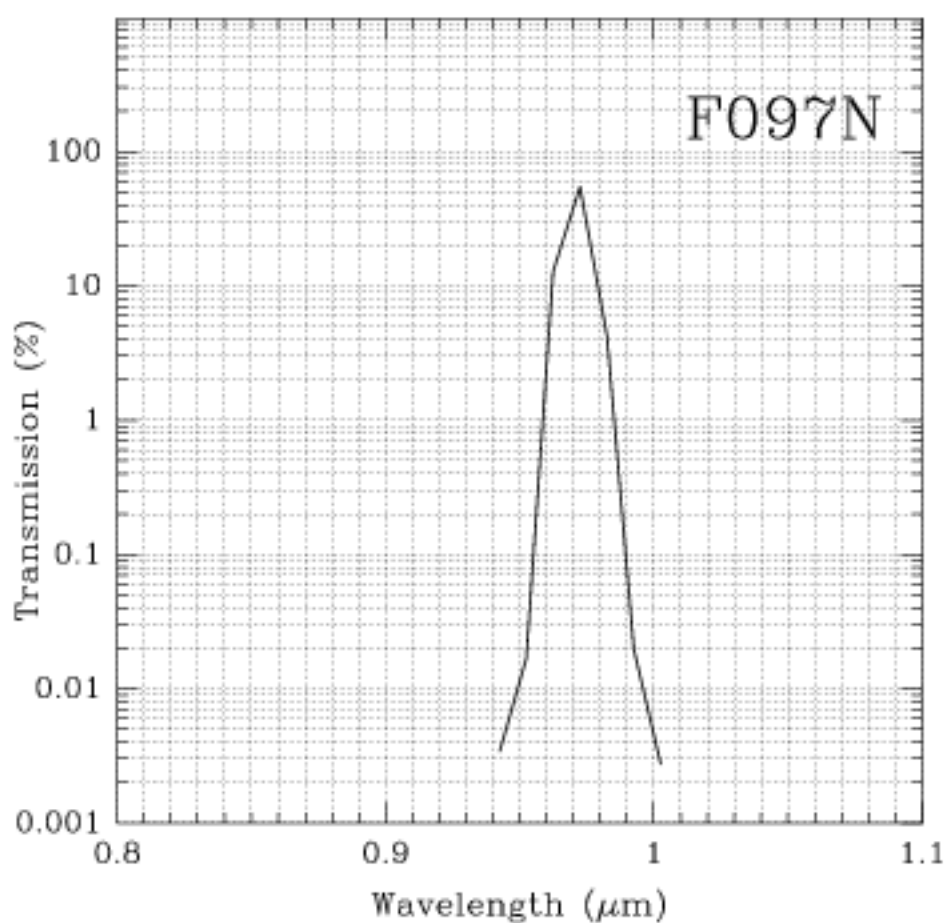
Camera 1, Filter F108N

Hel Line

Filter F108N is also available in Camera 3.

Central wavelength (μm)	Mean wavelength (μm)	Peak wavelength (μm)	FWHM (μm)	Range (μm)	MaxTr %	Pixel Fraction
1.0817	1.0816	1.0790	0.0094	1%	81.94	0.111

Figure 11.4: Camera 1, Filter F108N
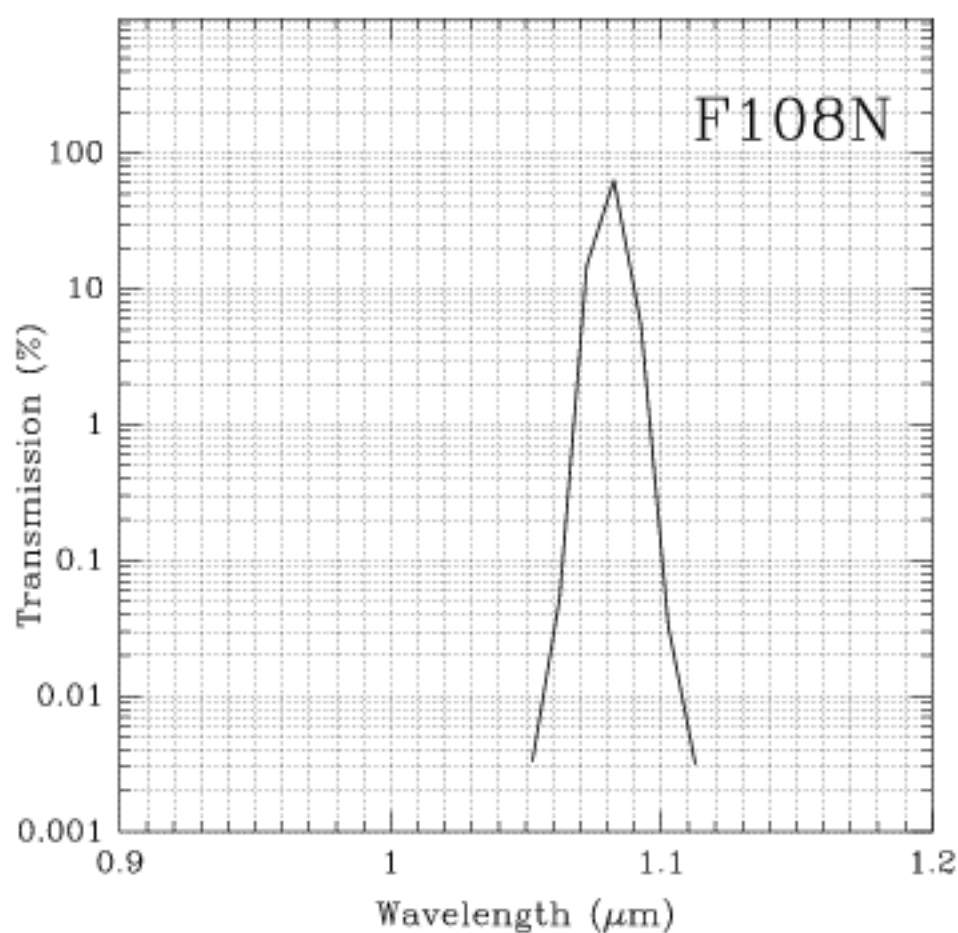
Camera 1, Filter F110M

Note: Camera 1 also has a broader F110W filter.

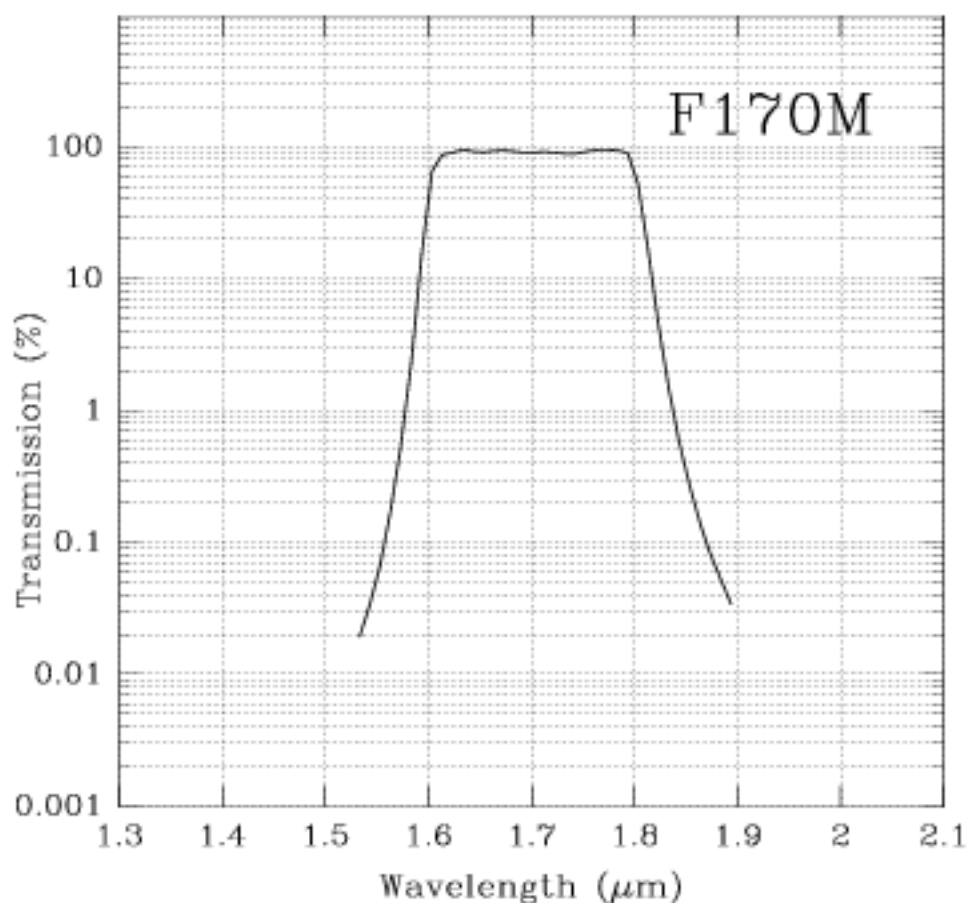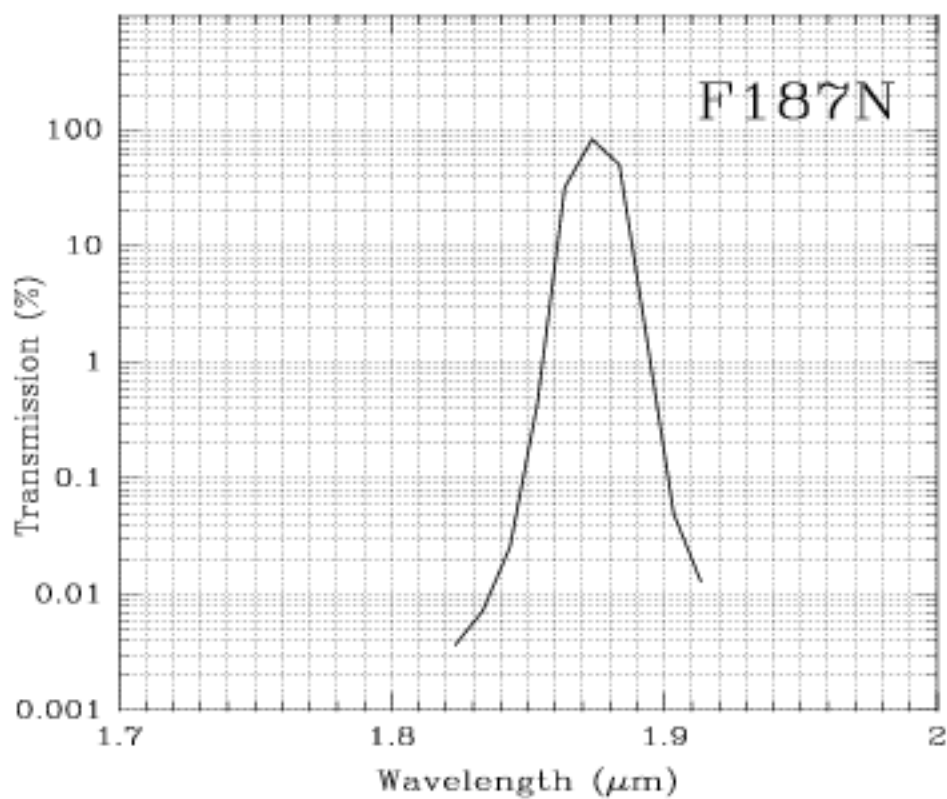| Central Wavelength (μm)	Mean Wavelength (μm)	Peak Wavelength (μm)	FWHM (μm)	Range (μm)	MaxTr %	Pixel Fraction
1.1013	1.1003	1.1295	0.1995	1.0-1.2	90.49	0.108

Figure 11.5: Camera 1, Filter F110M
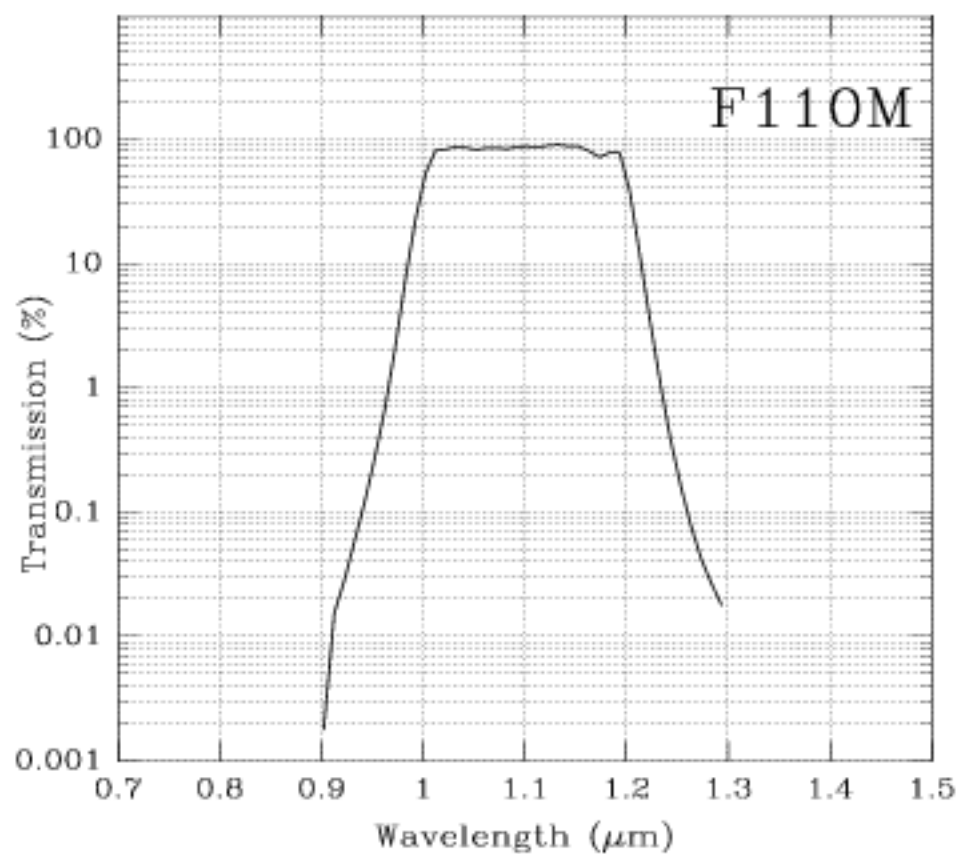
Camera 1, Filter F110W

This filter is also available on Cameras 2 and 3.

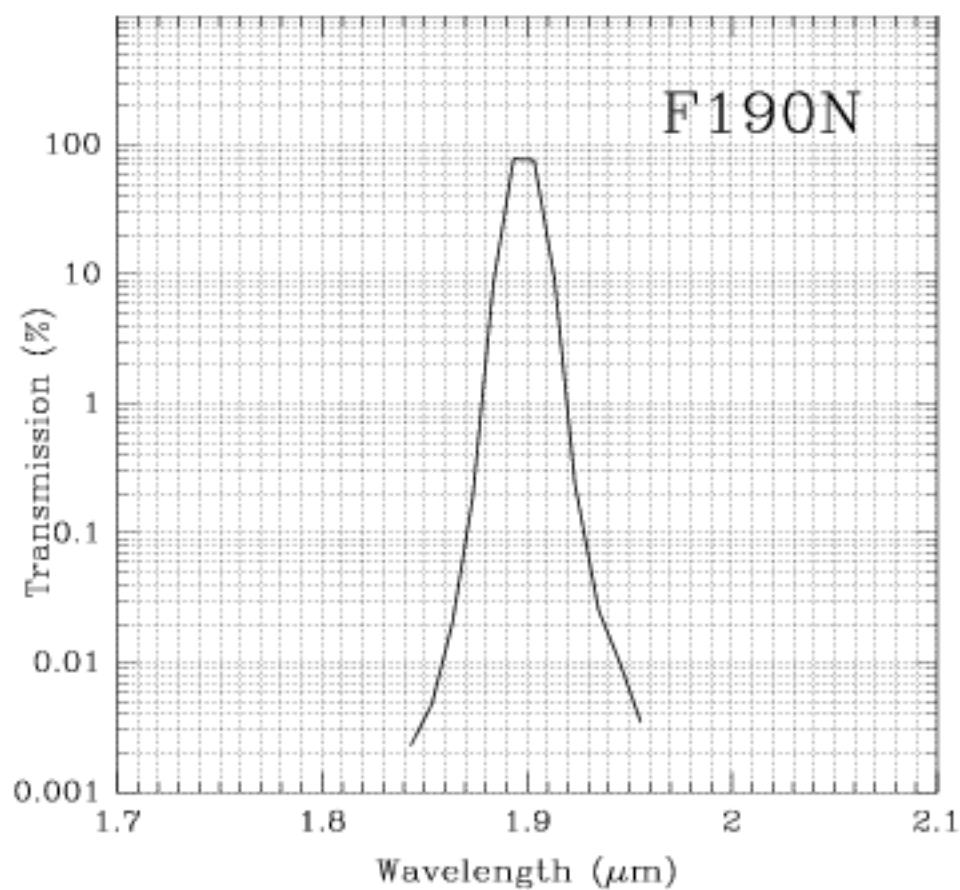| Central wavelength (μm)	Mean wavelength (μm)	Peak wavelength (μm)	FWHM (μm)	Range (μm)	MaxTr %	Pixel Fraction
1.0985	1.1022	1.2760	0.5920	0.8-1.35	95.11	0.113

Figure 11.6: Camera 1, Filter F110W
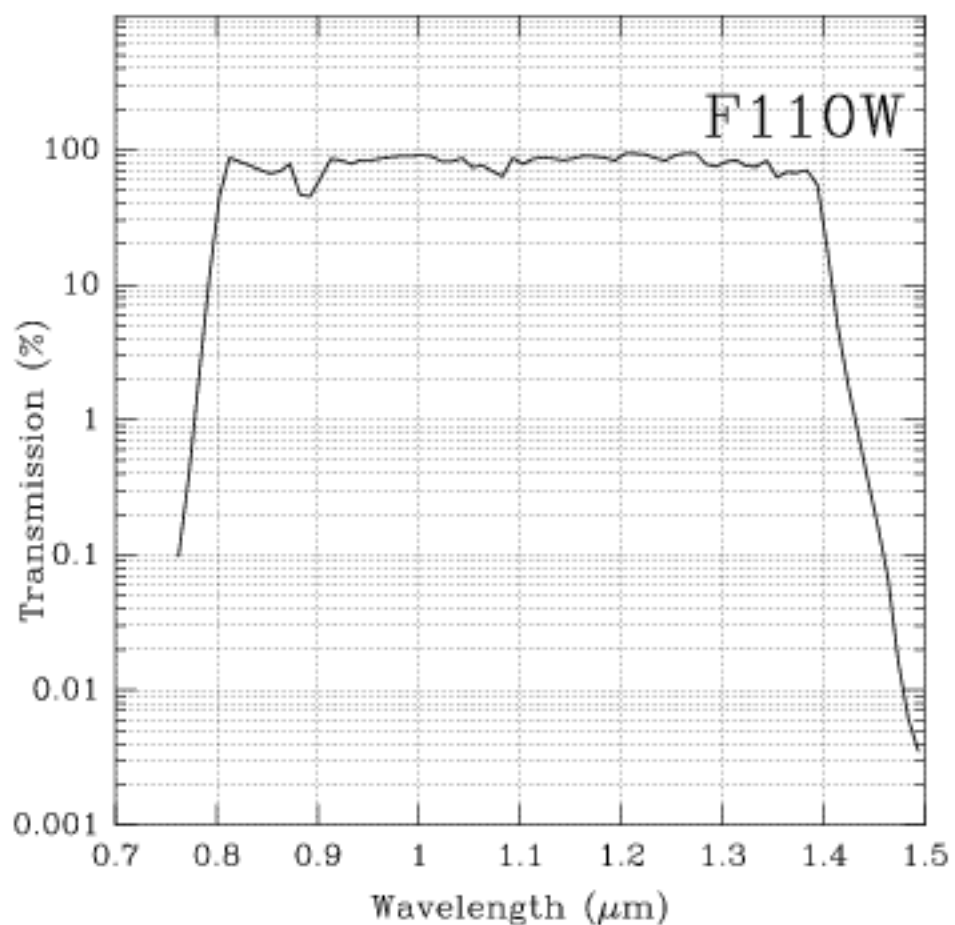
Camera 1, Filter F113N

Hel Continuum

This filter is also available on Camera 3.

Central wavelength (μm)	Mean wavelength (μm)	Peak wavelength (μm)	FWHM (μm)	Range (μm)	MaxTr %	Pixel Fraction
1.1297	1.1298	1.1312	0.0110	1%	86.24	0.102

Figure 11.7: Camera 1, Filter F113N
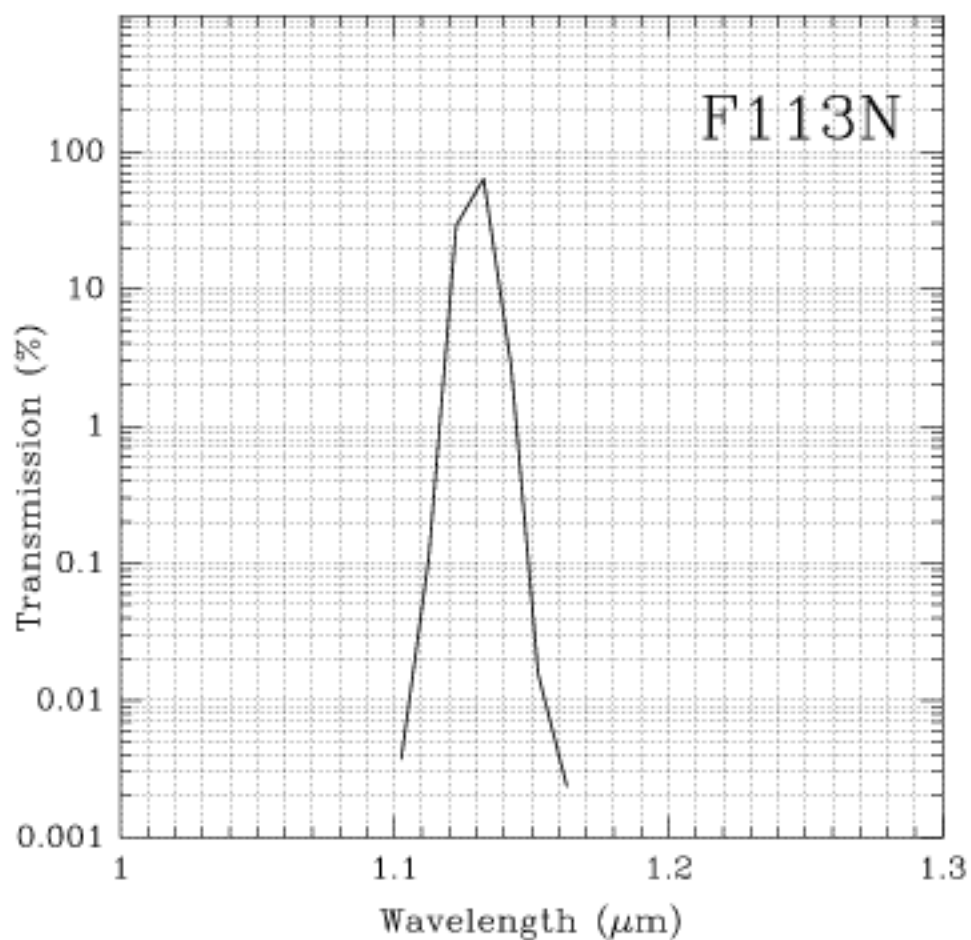
Camera 1, Filter F140W

Central wavelength (µm)	Mean wavelength (µm)	Peak wavelength (µm)	FWHM (µm)	Range (µm)	MaxTr %	Pixel Fraction
1.3973	1.3993	1.2240	0.7965	0.8-1.8	95.50	0.0766

Figure 11.8: Camera 1, Filter F140W
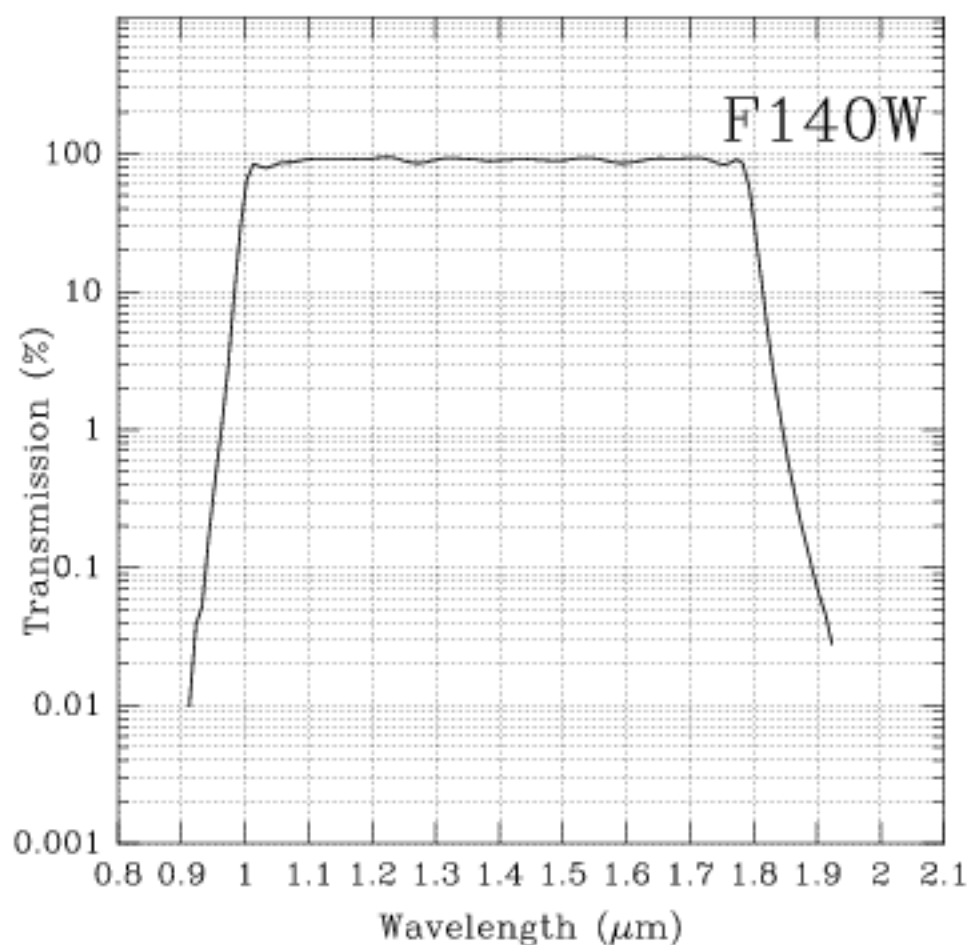
Camera 1, Filter F145M

H_2O Band

Central wavelength (μm)	Mean wavelength (μm)	Peak wavelength (μm)	FWHM (μm)	Range (μm)	MaxTr %	Pixel Fraction
1.4513	1.4524	1.5100	0.1965	1.35-1.55	94.03	0.0640

Figure 11.9: Camera 1, Filter F145M
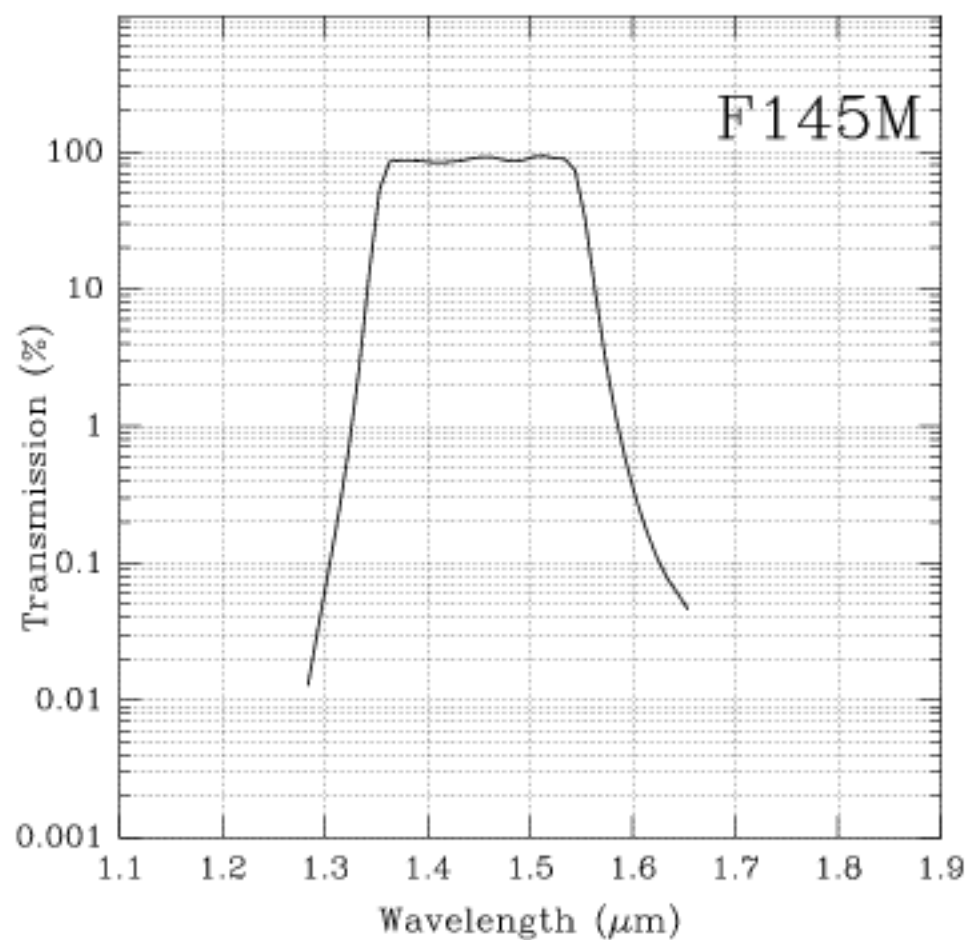
Camera 1, Filter F160W

Minimum background.
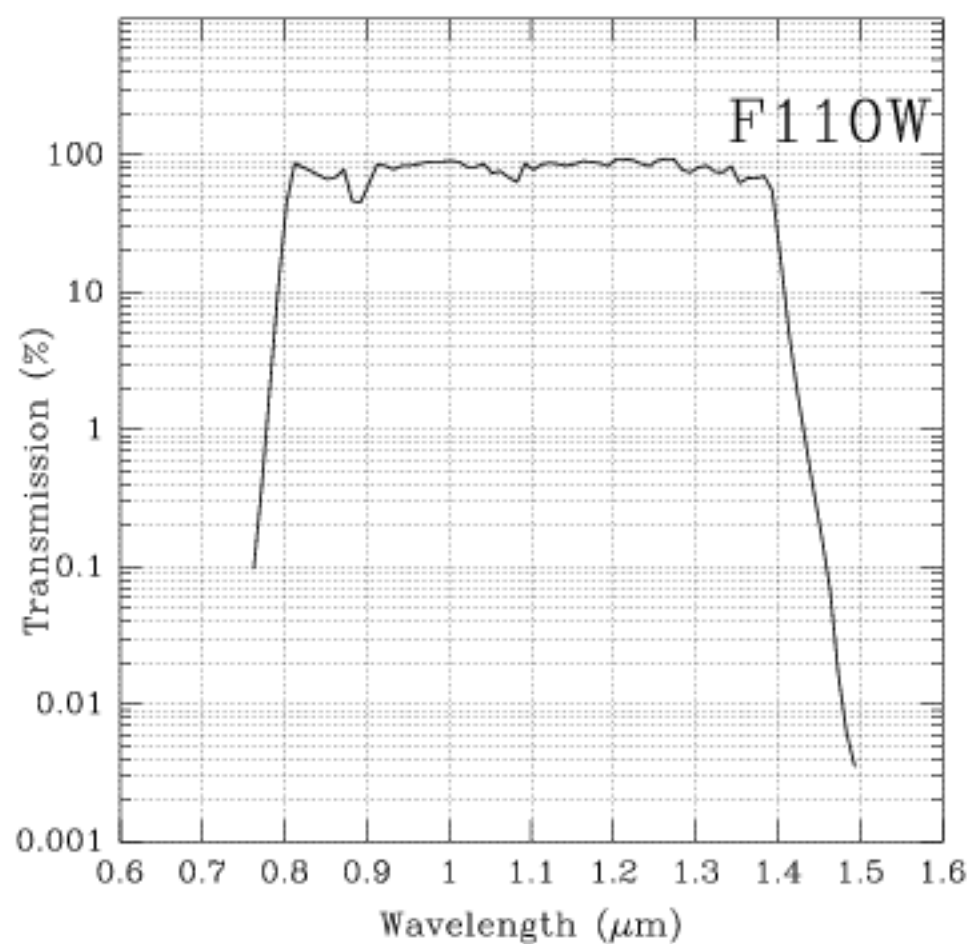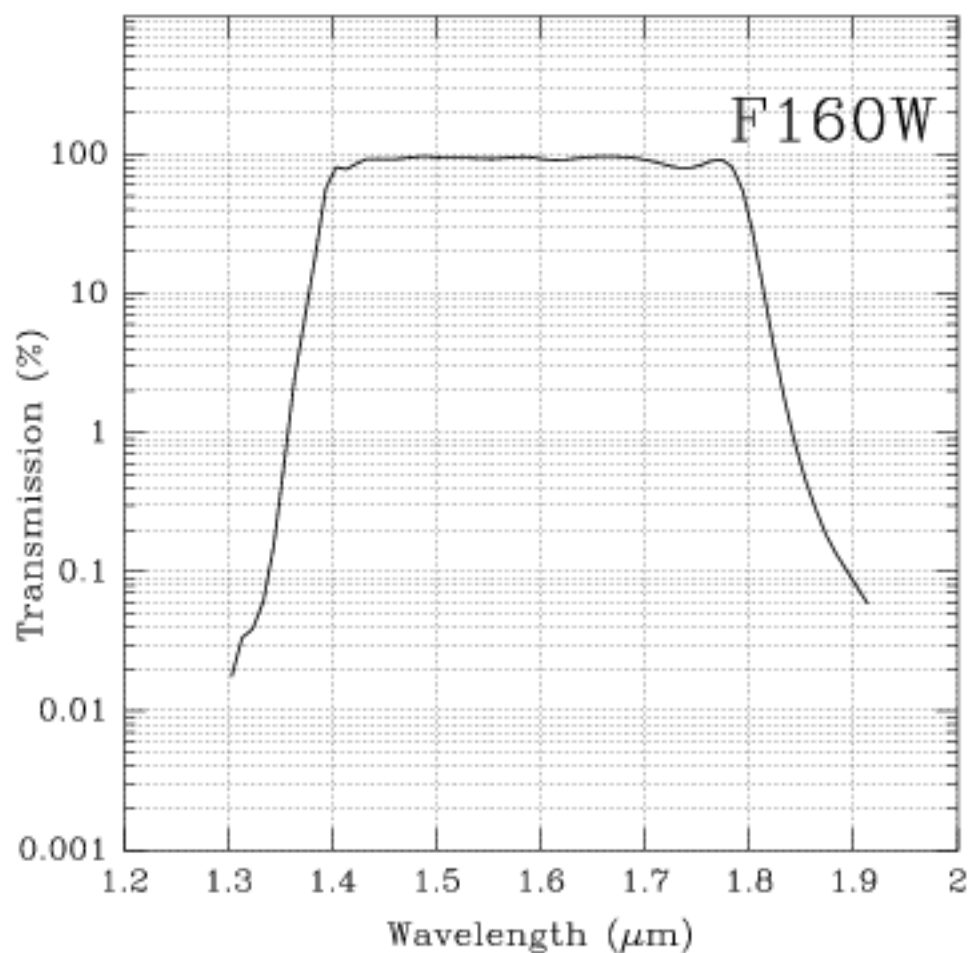
This filter is also available on Cameras 2 and 3.

Central wavelength (μm)	Mean wavelength (μm)	Peak wavelength (μm)	FWHM (μm)	Range (μm)	MaxTr %	Pixel Fraction
1.5960	1.5947	1.5830	0.4000	1.35-1.75	96.37	0.0562

Figure 11.10: Camera 1, Filter F160W
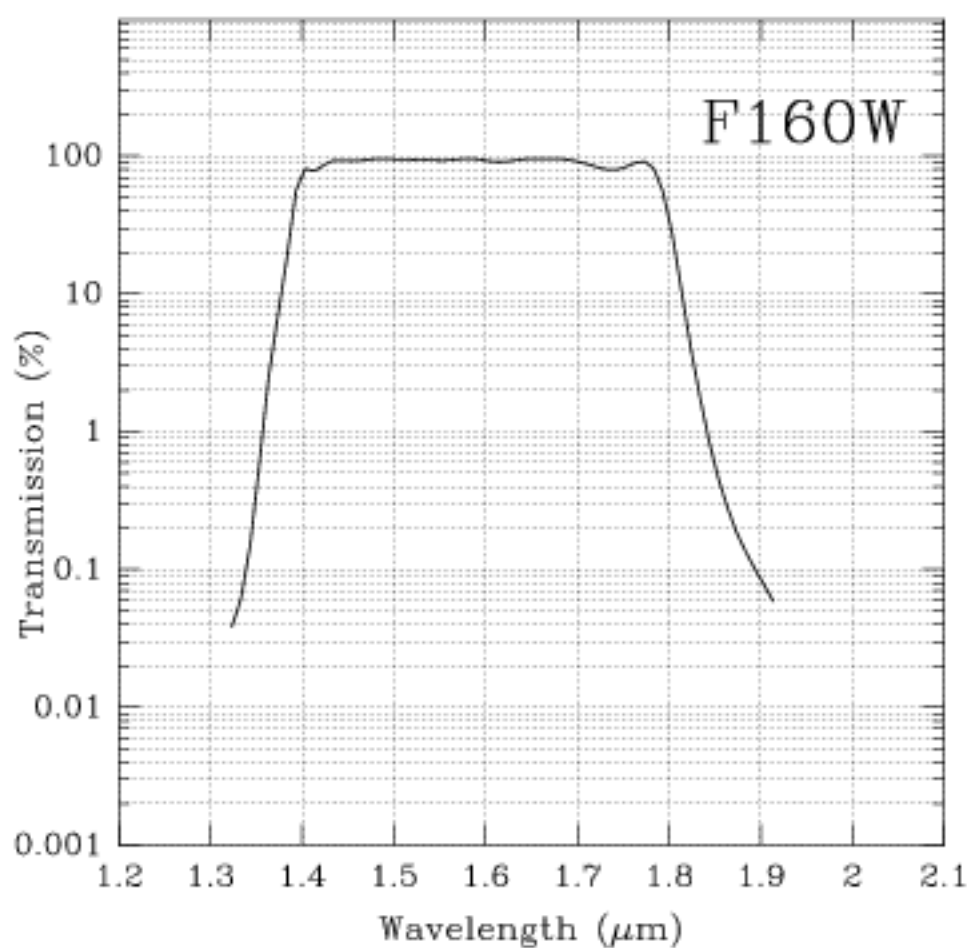
Camera 1, Filter F164N

[FeII] Line
This filter is also available on Camera 3.

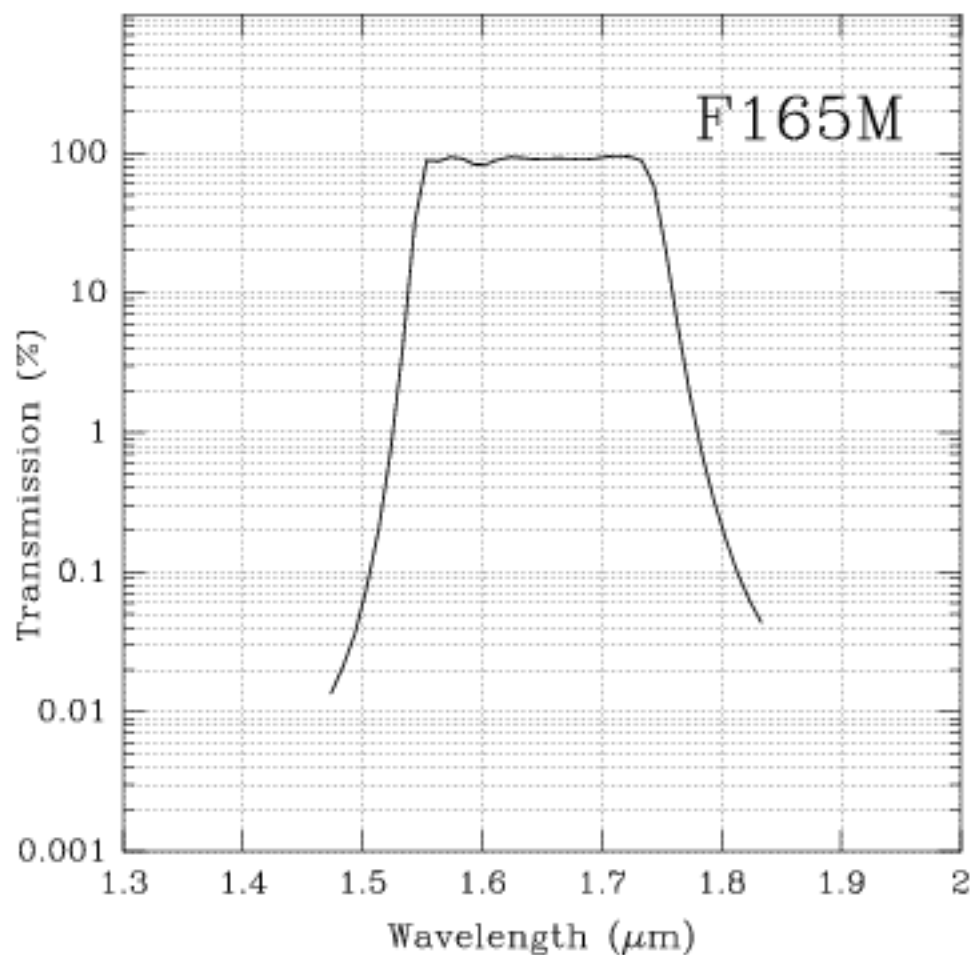| Central wavelength (μm)	Mean wavelength (μm)	Peak wavelength (μm)	FWHM (μm)	Range (μm)	MaxTr %	Pixel Fraction
1.6353	1.6354	1.6378	0.0166	1%	93.41	0.0534

Figure 11.11: Camera 1, Filter F164N
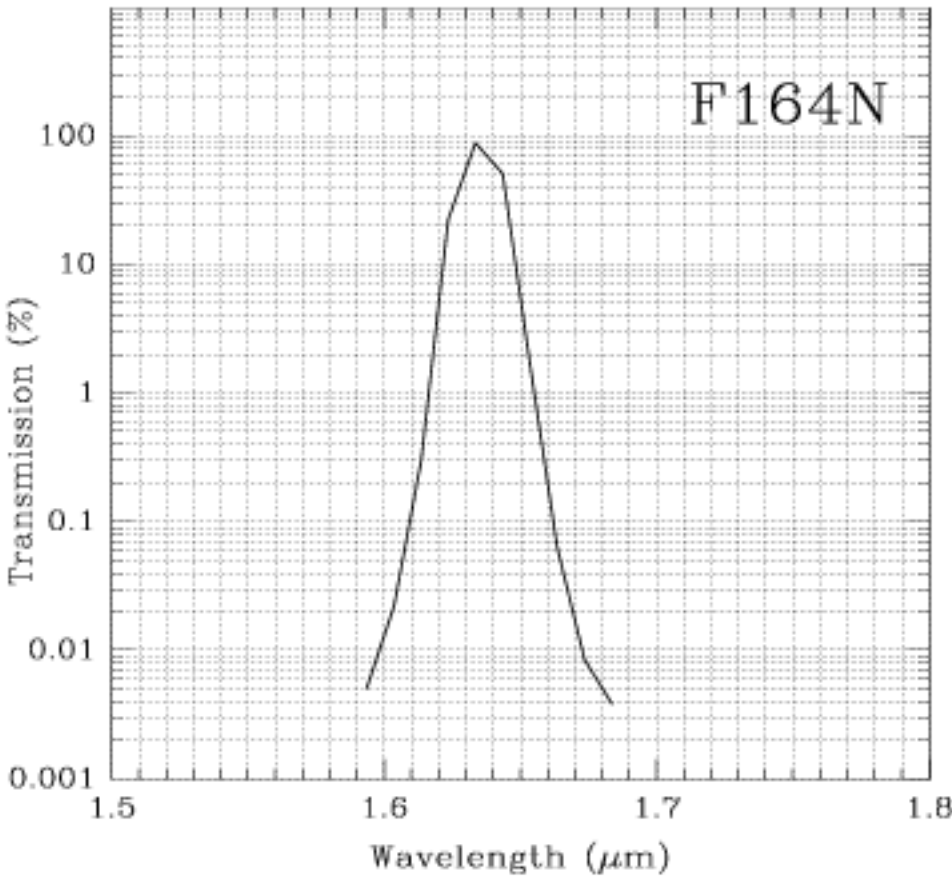
Camera 1, Filter F165M

H$_2$O Continuum

This filter is also available on Camera 2.

Central wavelength (μm)	Mean wavelength (μm)	Peak wavelength (μm)	FWHM (μm)	Range (μm)	MaxTr %	Pixel Fraction
1.6438	1.6446	1.5735	0.1985	1.55-1.75	94.78	0.0521

Figure 11.12: Camera 1, F165M
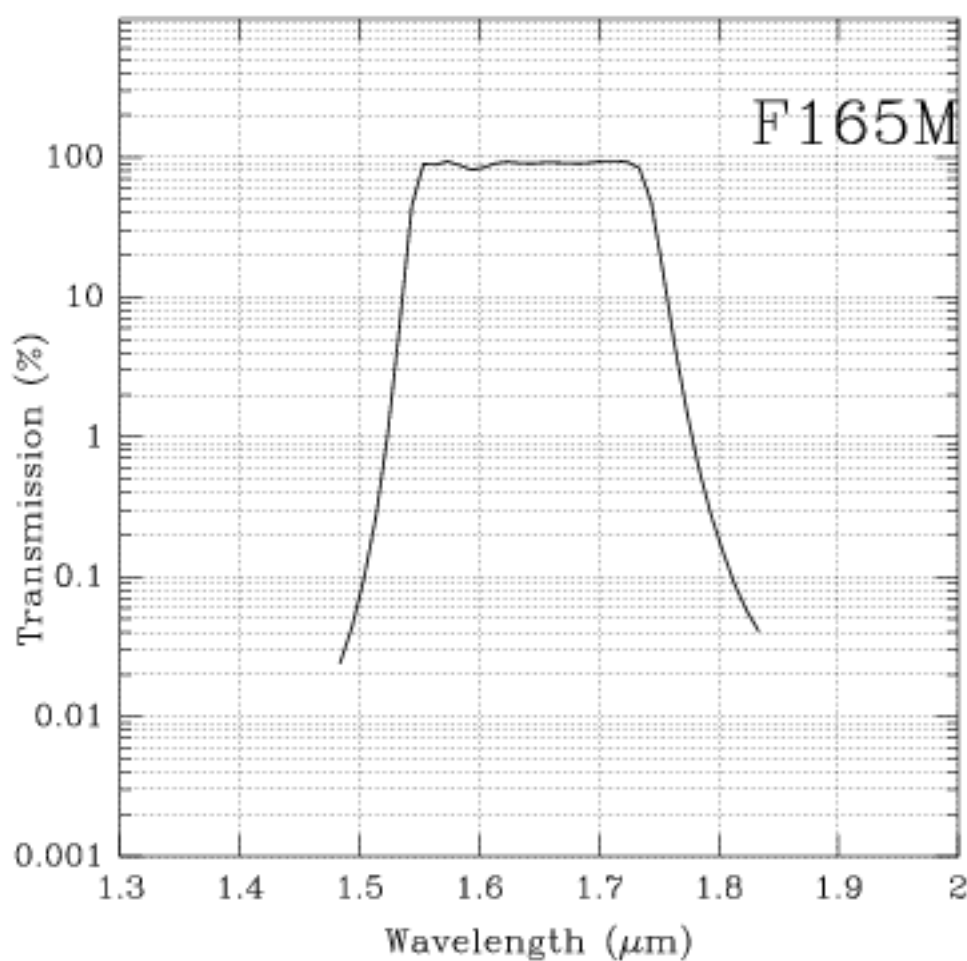
Camera 1, Filter F166N

[FeII] Continuum

This filter is also available on Camera 3.

Central wavelength (μm)	Mean wavelength (μm)	Peak wavelength (μm)	FWHM (μm)	Range (μm)	MaxTr %	Pixel Fraction
1.6606	1.6606	1.6622	0.0168	1%	90.12	0.0505

Figure 11.13: Camera 1, Filter F166N
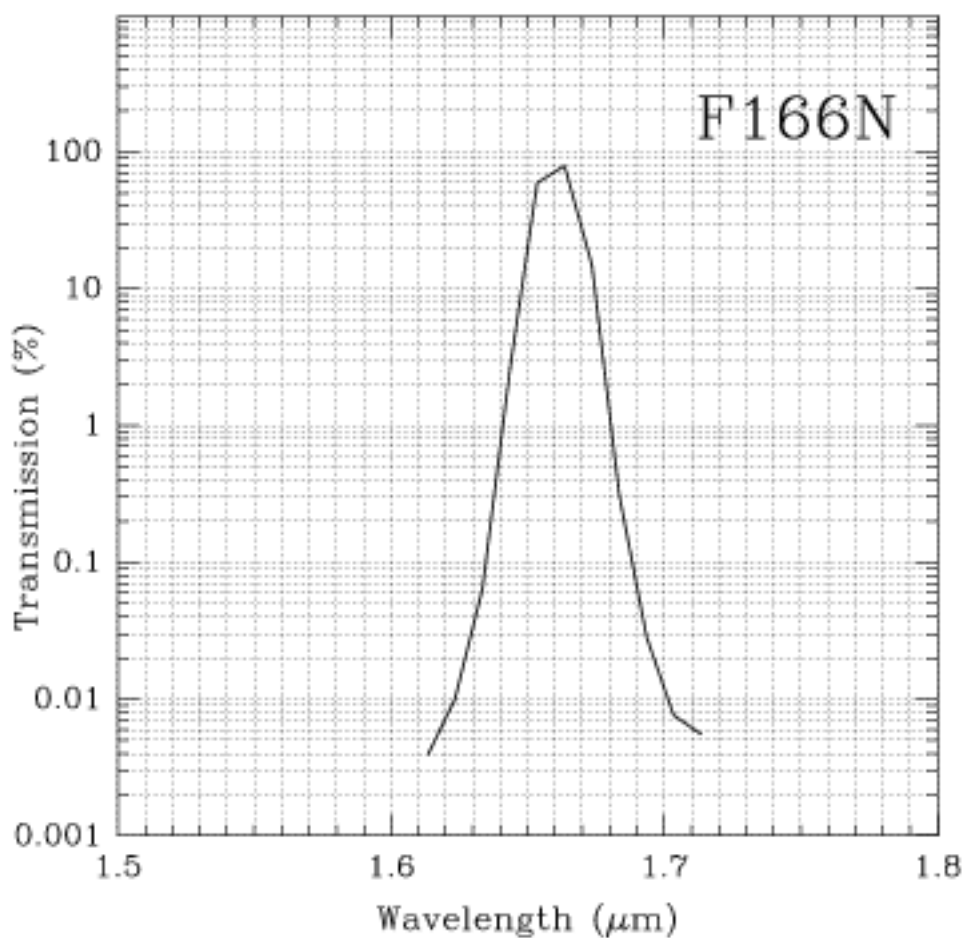
Camera 1, Filter F170M

This filter is also available on Camera 2.

Central wavelength (μm)	Mean wavelength (μm)	Peak wavelength (μm)	FWHM (μm)	Range (μm)	MaxTr %	Pixel Fraction
1.7025	1.7032	1.6330	0.2030	1.6-1.8	95.55	0.0481

Figure 11.14: Camera 1, Filter F170M

Camera 1, Filter F187N

Paschen α

This filter is also available on Camera 2 and 3.

Central wavelength (μm)	Mean wavelength (μm)	Peak wavelength (μm)	FWHM (μm)	Range (μm)	MaxTr %	Pixel Fraction
1.875	1.8748	1.8756	0.0188	1%	88.93	0.0411

Figure 11.15: Camera 1, Filter F187N
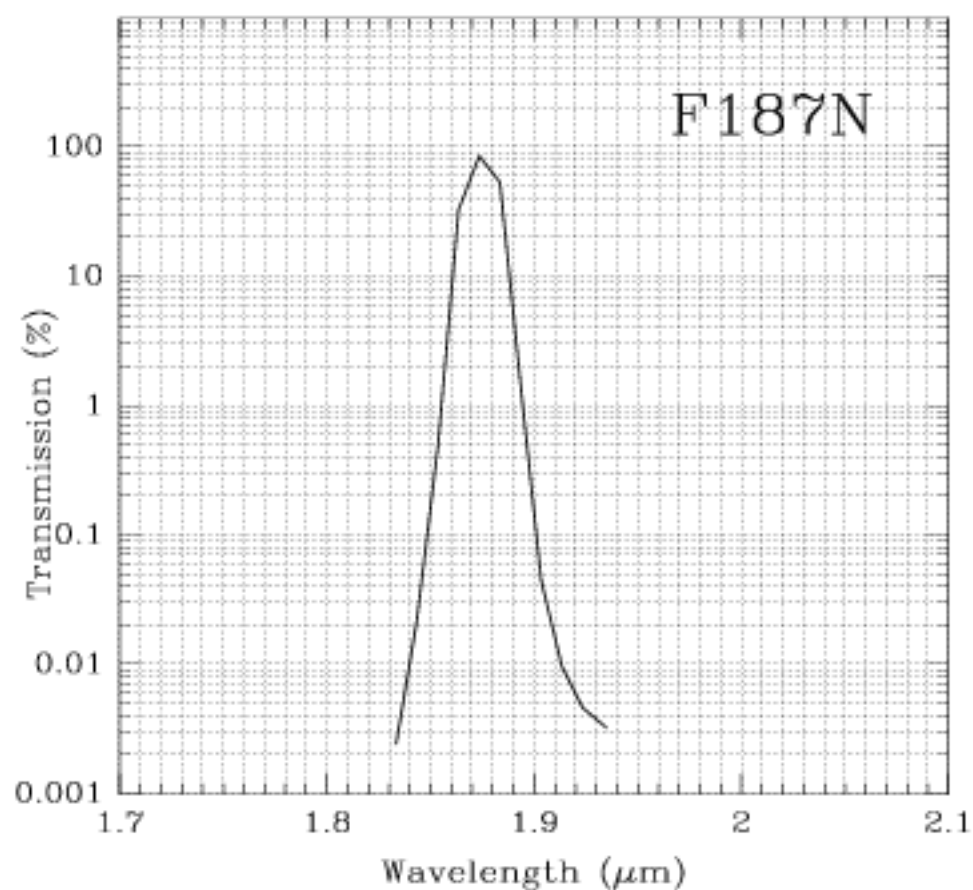
Camera 1, Filter F190N

Paschen α continuum

This filter is also available on Cameras 2 and 3.

Central wavelength (μm)	Mean wavelength (μm)	Peak wavelength (μm)	FWHM (μm)	Range (μm)	MaxTr %	Pixel Fraction
1.8987	1.8986	1.8942	0.0174	1%	93.05	0.0401

Figure 11.16: Camera 1, Filter F190N

Camera 2, Filter F110W

This filter is also available on Cameras 1 and 3.

Central wavelength (µm)	Mean wavelength (µm)	Peak wavelength (µm)	FWHM (µm)	Range (µm)	MaxTr %	Pixel Fraction
1.0998	1.1035	1.2035	0.5915	0.8-1.4	94.90	0.288

Figure 11.17: Camera 2, Filter F110W

Camera 2, Filter F160W

Minimum background

This filter is also available on Cameras 1 and 3.

Central wavelength (μm)	Mean wavelength (μm)	Peak wavelength (μm)	FWHM (μm)	Range (μm)	MaxTr %	Pixel Fraction
1.5940	1.5931	1.5820	0.4030	1.4-1.8	96.59	0.159

Figure 11.18: Camera 2, Filter F160W

Camera 2, Filter F165M

Planetary continuum

This filter is also available on Camera 1.

Central wavelength (μm)	Mean wavelength (μm)	Peak wavelength (μm)	FWHM (μm)	Range (μm)	MaxTr %	Pixel Fraction
1.6463	1.6473	1.5540	0.1985	1.55-1.75	95.36	0.149

Figure 11.19: Camera 2, Filter F165M

Camera 2, Filter F171M

HCO$_2$ and C$_2$ continuum

Central wavelength (μm)	Mean wavelength (μm)	Peak wavelength (μm)	FWHM (μm)	Range (μm)	MaxTr %	Pixel Fraction
1.7206	1.7209	1.7224	0.0712	1.68-1.75	95.15	0.138

Figure 11.20: Camera 2, Filter F171M
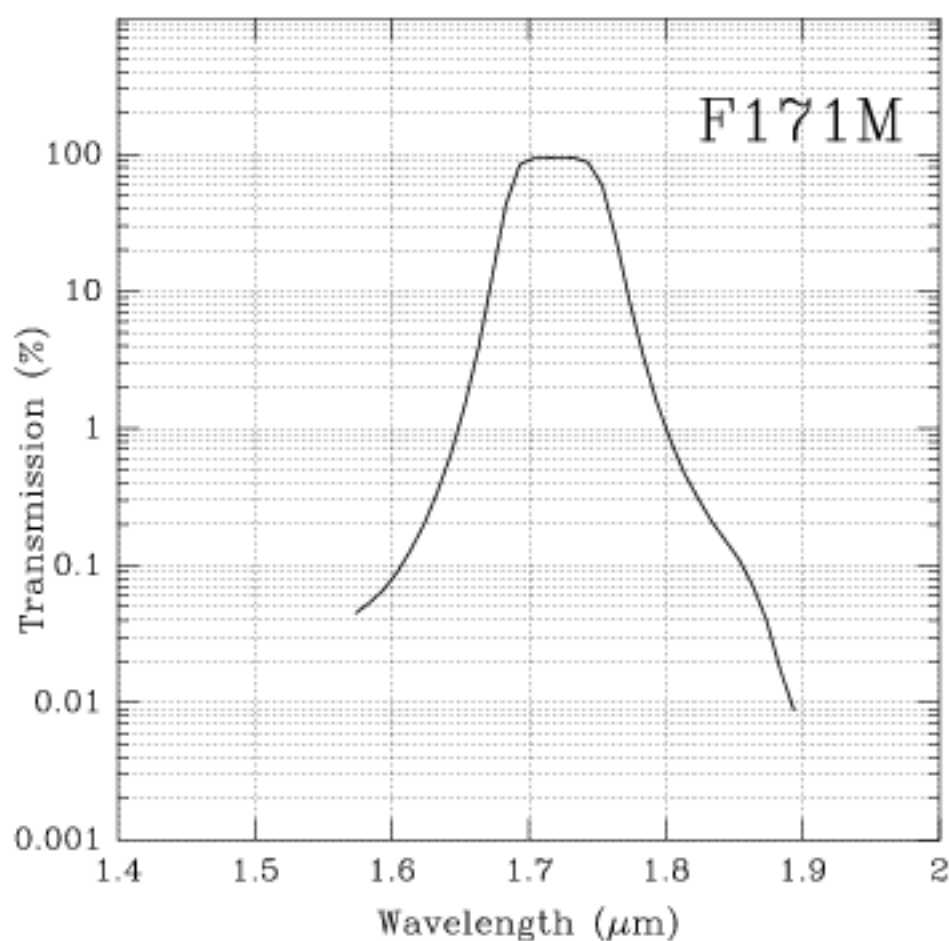
Camera 2, Filter F180M

HCO$_2$ and C$_2$

Thermal background important

Central wavelength (µm)	Mean wavelength (µm)	Peak wavelength (µm)	FWHM (µm)	Range (µm)	MaxTr %	Pixel Fraction
1.7968	1.7971	1.8108	0.0684	1.765-1.835	93.40	0.128

Figure 11.21: Camera 2, Filter F180M
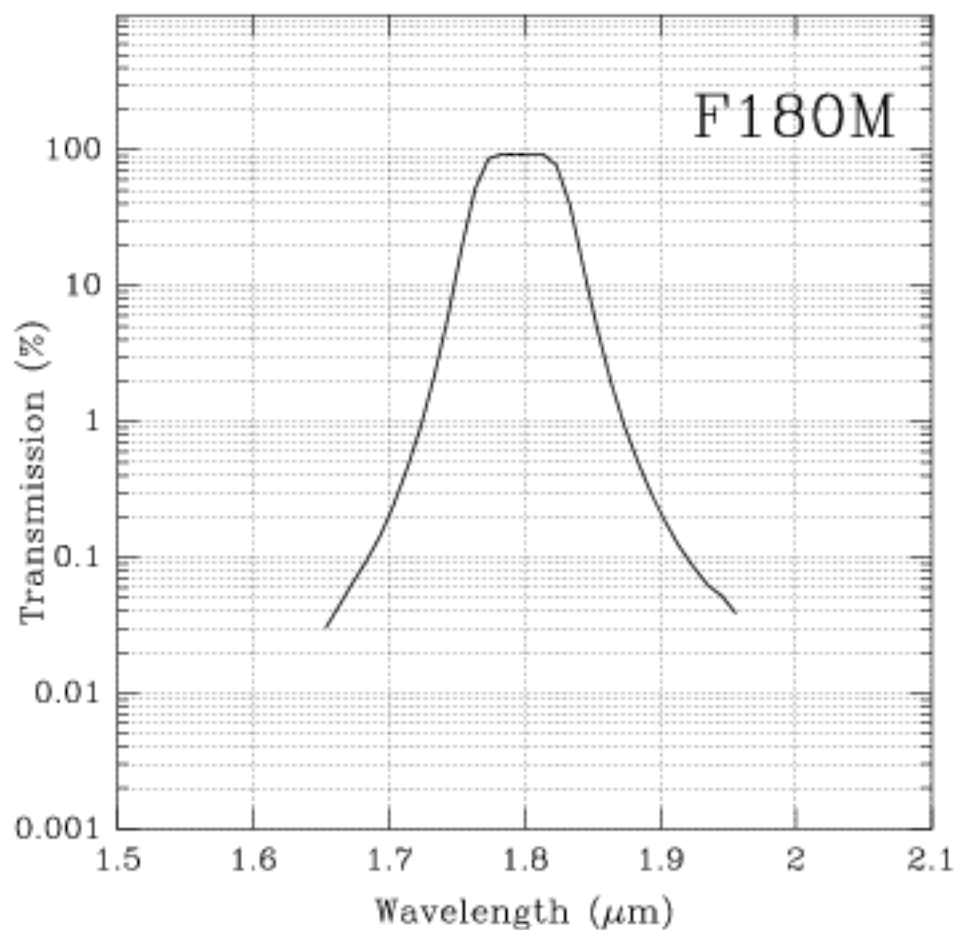
Camera 2, Filter F187N

Paschen α
Also available on Cameras 1 and 3.

Central wavelength (μm)	Mean wavelength (μm)	Peak wavelength (μm)	FWHM (μm)	Range (μm)	MaxTr %	Pixel Fraction
1.8740	1.8738	1.8746	0.0192	1%	88.91	0.119

Figure 11.22: Camera 2, Filter F187N

Camera 2, Filter F187W

Thermal background important.

Central wavelength (µm)	Mean wavelength (µm)	Peak wavelength (µm)	FWHM (µm)	Range (µm)	MaxTr %	Pixel Fraction
1.8722	1.8708	1.8930	0.2436	1.75-2.35	87.97	0.117

Figure 11.23: Camera 2, Filter F187W
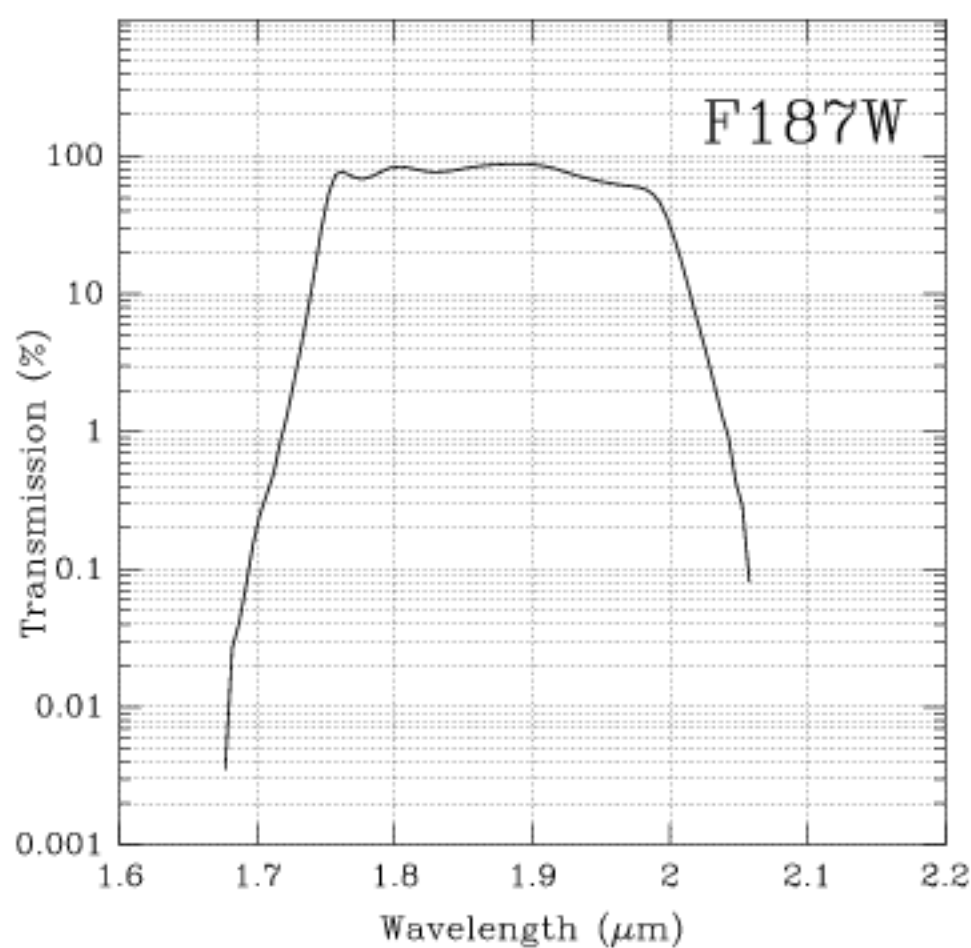
Camera 2, Filter F190N

Paschen α continuum

Also available on Cameras 1 and 3.

Central wavelength (μm)	Mean wavelength (μm)	Peak wavelength (μm)	FWHM (μm)	Range (μm)	MaxTr %	Pixel Fraction
1.9005	1.9003	1.9004	0.0174	1%	93.22	0.116

Figure 11.24: Camera 2, Filter F190N
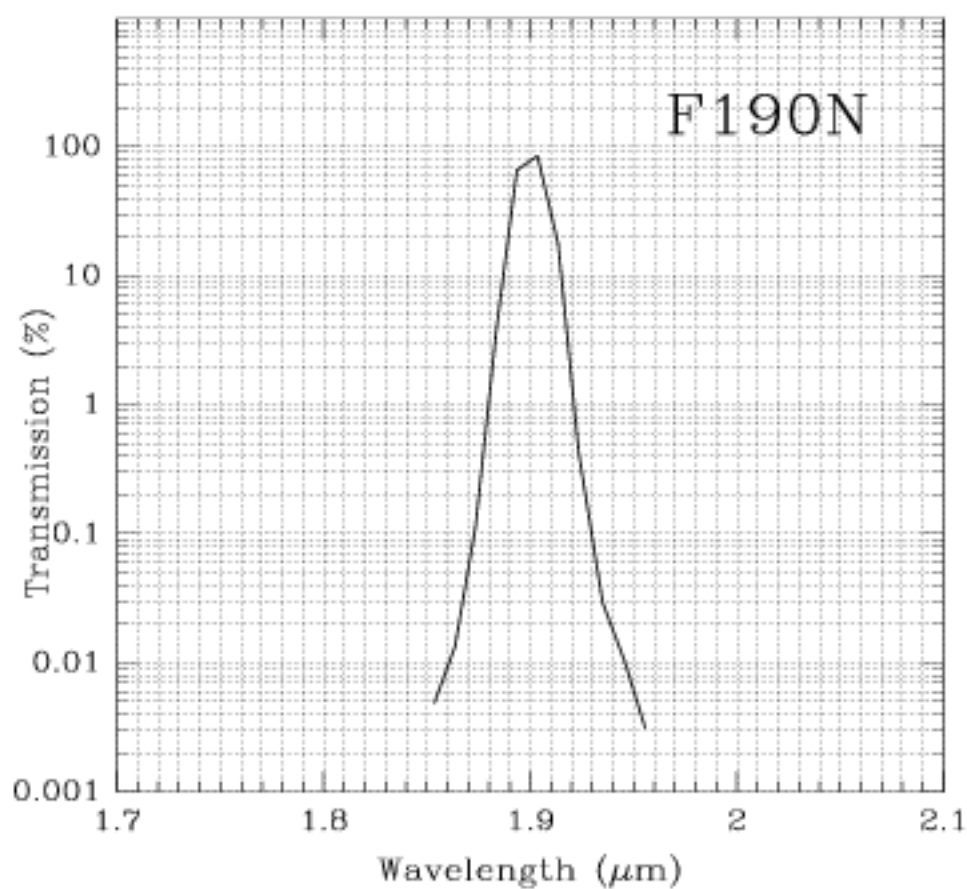
Camera 2, Filter F204M

Methane band

Thermal background important.

Central wavelength (μm)	Mean wavelength (μm)	Peak wavelength (μm)	FWHM (μm)	Range (μm)	MaxTr %	Pixel Fraction
2.0313	2.0327	2.0342	0.105	1.99-2.09	91.77	0.104

Figure 11.25: Camera 2, Filter F204M
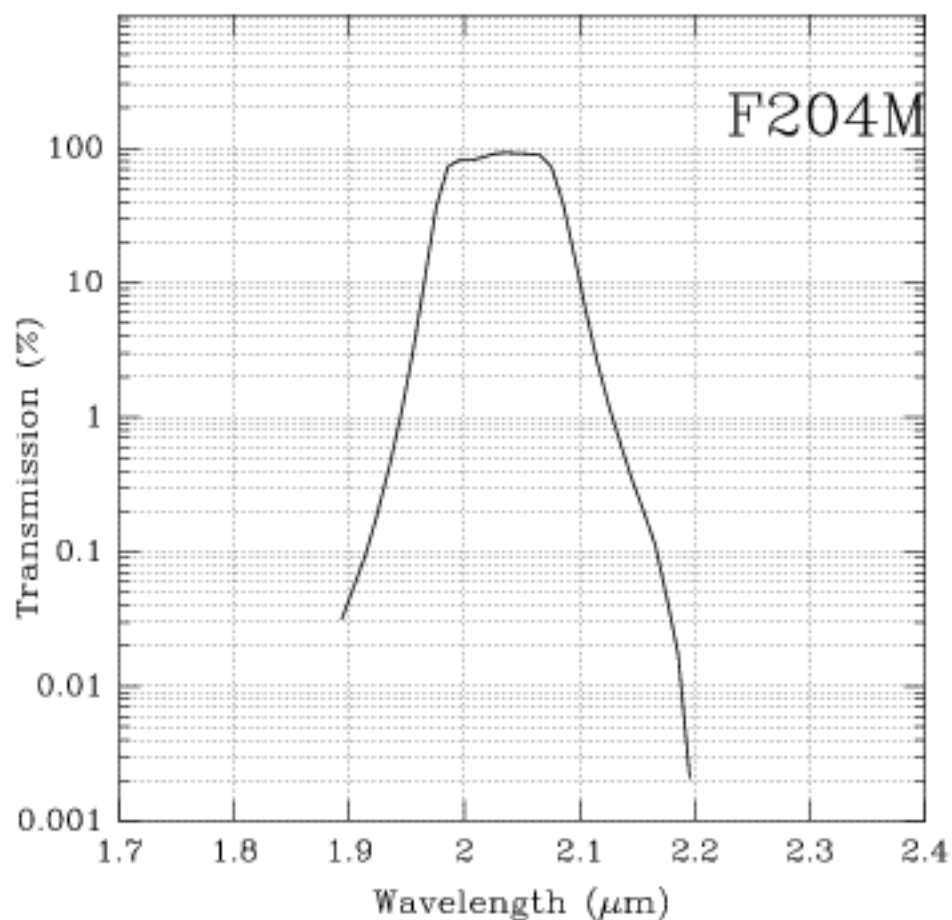
Camera 2, Filter F205W

Thermal background important.

Central wavelength (μm)	Mean wavelength (μm)	Peak wavelength (μm)	FWHM (μm)	Range (μm)	MaxTr %	Pixel Fraction
2.0428	2.0406	1.9560	0.6125	1.75-2.0	98.14	0.107

Figure 11.26: Camera 2, Filter F205W
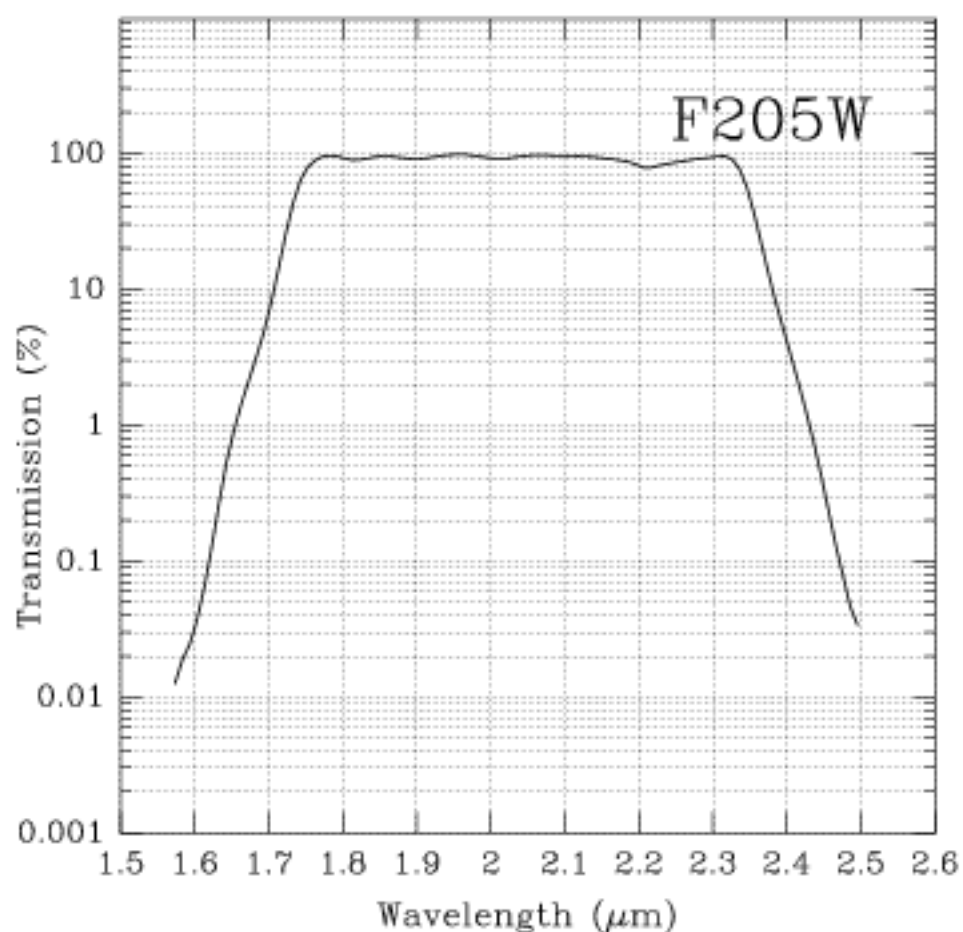
Camera 2, Filter F207M

Thermal background important.

Central wavelength (μm)	Mean wavelength (μm)	Peak wavelength (μm)	FWHM (μm)	Range (μm)	MaxTr %	Pixel Fraction
2.0827	2.0786	2.0252	0.1522	2.0-2.15	96.40	0.0976

Figure 11.27: Camera 2, Filter F207M
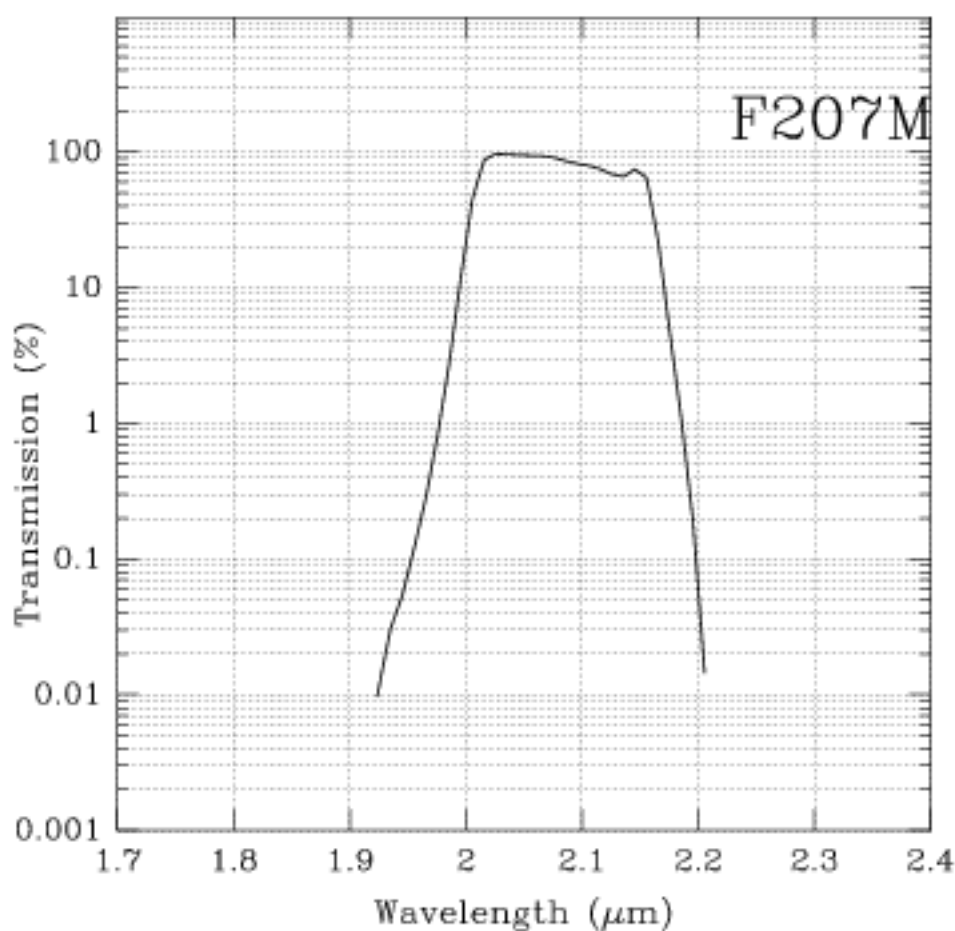
# Camera 2, Filter F212N

H$_2$ line

Also available on Camera 3.

Thermal background important.

Central wavelength (µm)	Mean wavelength (µm)	Peak wavelength (µm)	FWHM (µm)	Range (µm)	MaxTr %	Pixel Fraction
2.1211	2.1213	2.1228	0.0206	1%	90.90	0.0953

Figure 11.28: Camera 2, Filter F212N
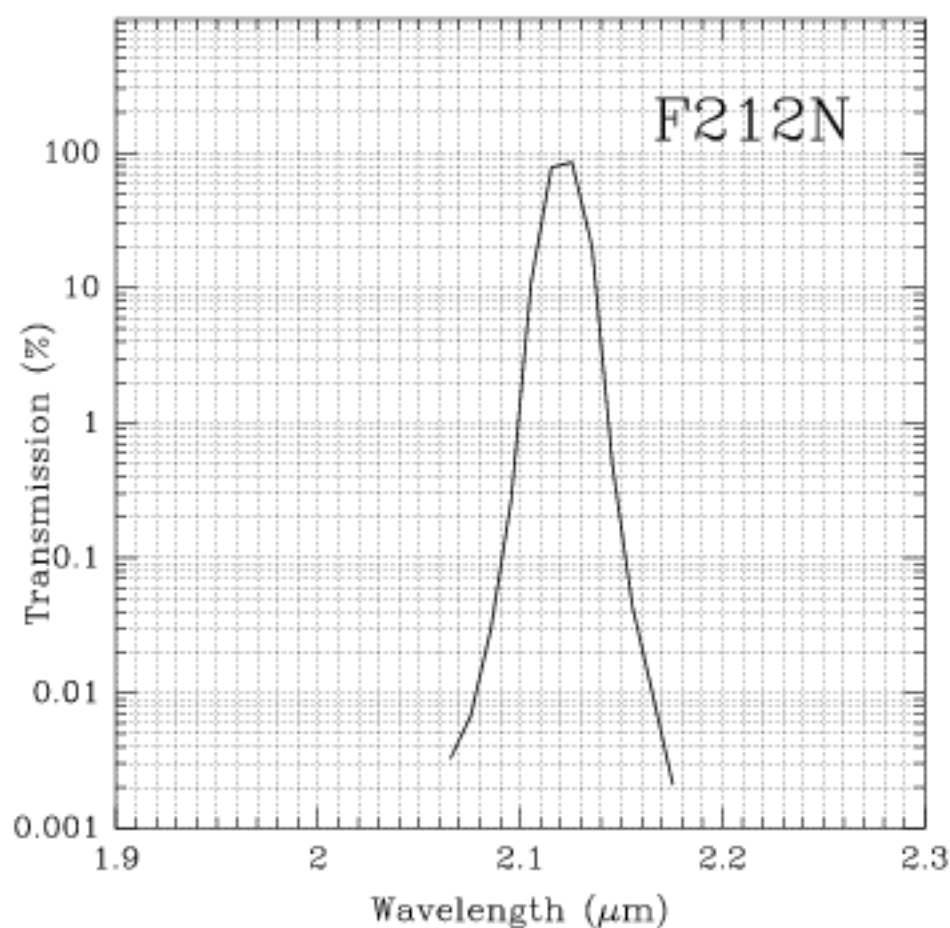
Camera 2, Filter F215N

H$_2$ + Brackett γ continuum

Thermal background important

Central wavelength (µm)	Mean wavelength (µm)	Peak wavelength (µm)	FWHM (µm)	Range (µm)	MaxTr %	Pixel Fraction
2.1488	2.1487	2.1562	0.0200	1%	85.91	0.0933

Figure 11.29: Camera 2, Filter F215N
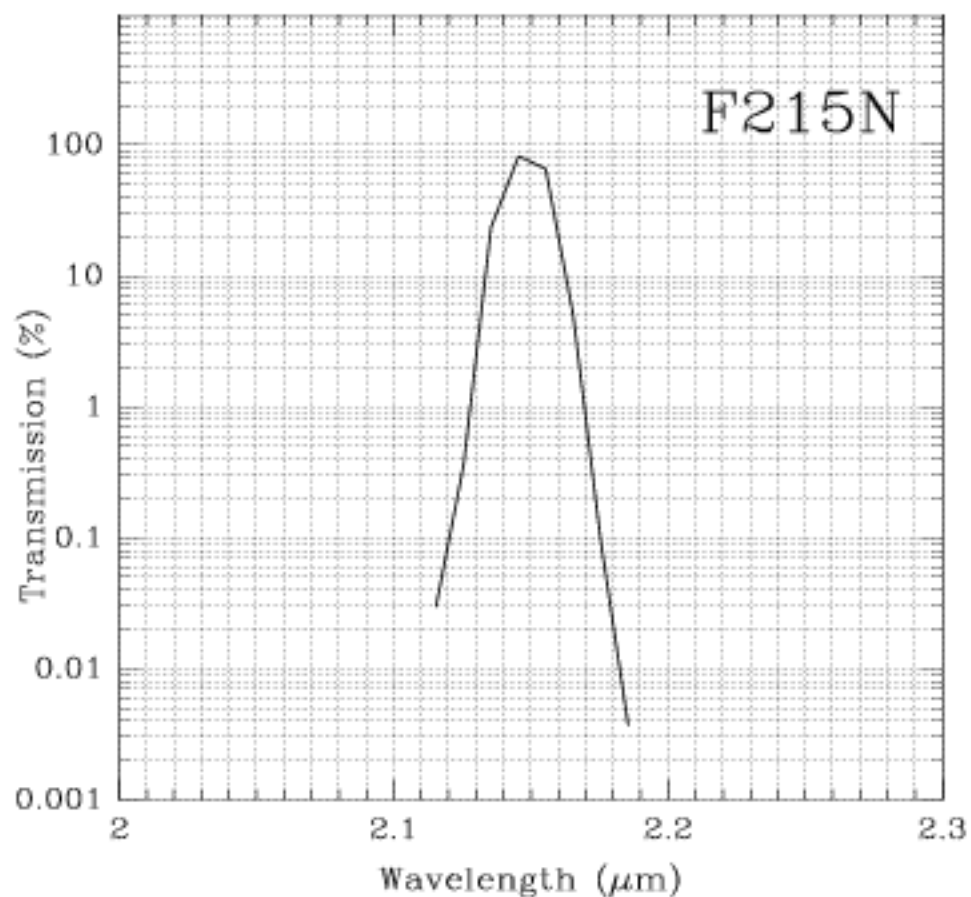
Camera 2, Filter F216N

Brackett γ line

Thermal background important.

Central wavelength (µm)	Mean wavelength (µm)	Peak wavelength (µm)	FWHM (µm)	Range (µm)	MaxTr %	Pixel Fraction
2.1642	2.1641	2.1668	0.0208	1%	90.07	0.0915

Figure 11.30: Camera 2, Filter F216N
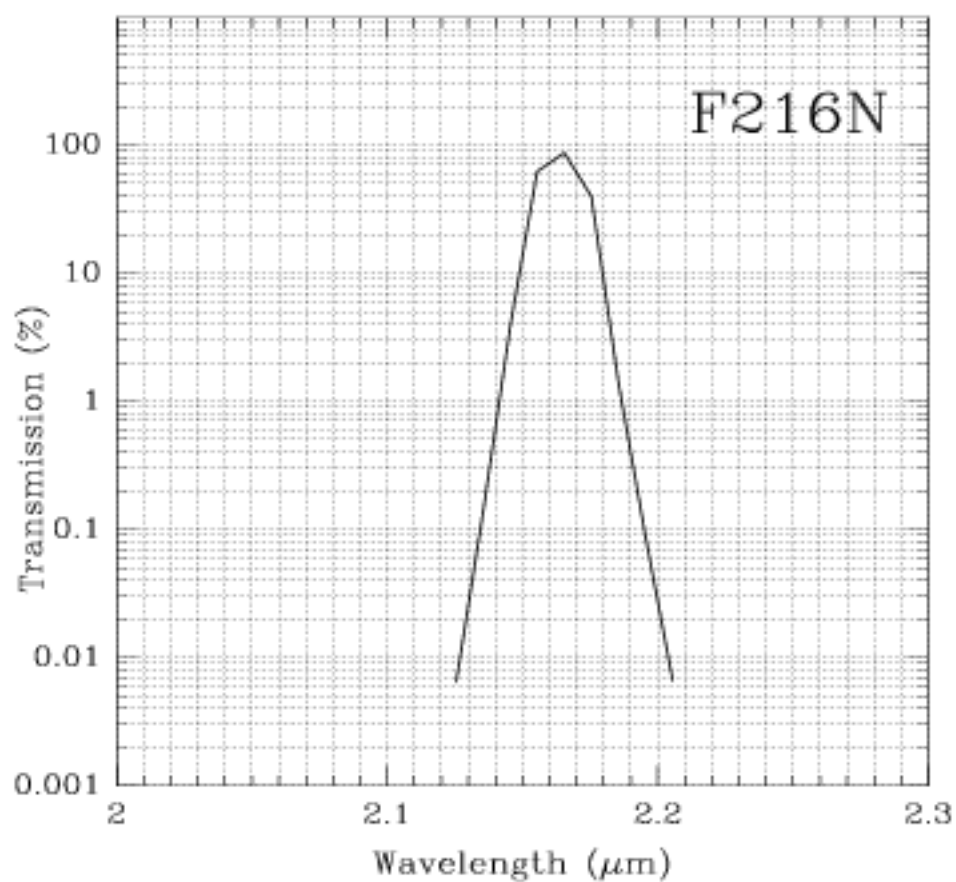
Camera 2, Filter F222M

CO continuum

Also available on Camera 3.

Thermal background important.

Central wavelength (μm)	Mean wavelength (μm)	Peak wavelength (μm)	FWHM (μm)	Range (μm)	MaxTr %	Pixel Fraction
2.2160	2.2164	2.1804	0.1432	2.15-2.3	89.90	0.0881

Figure 11.31: Camera 2, Filter F222M
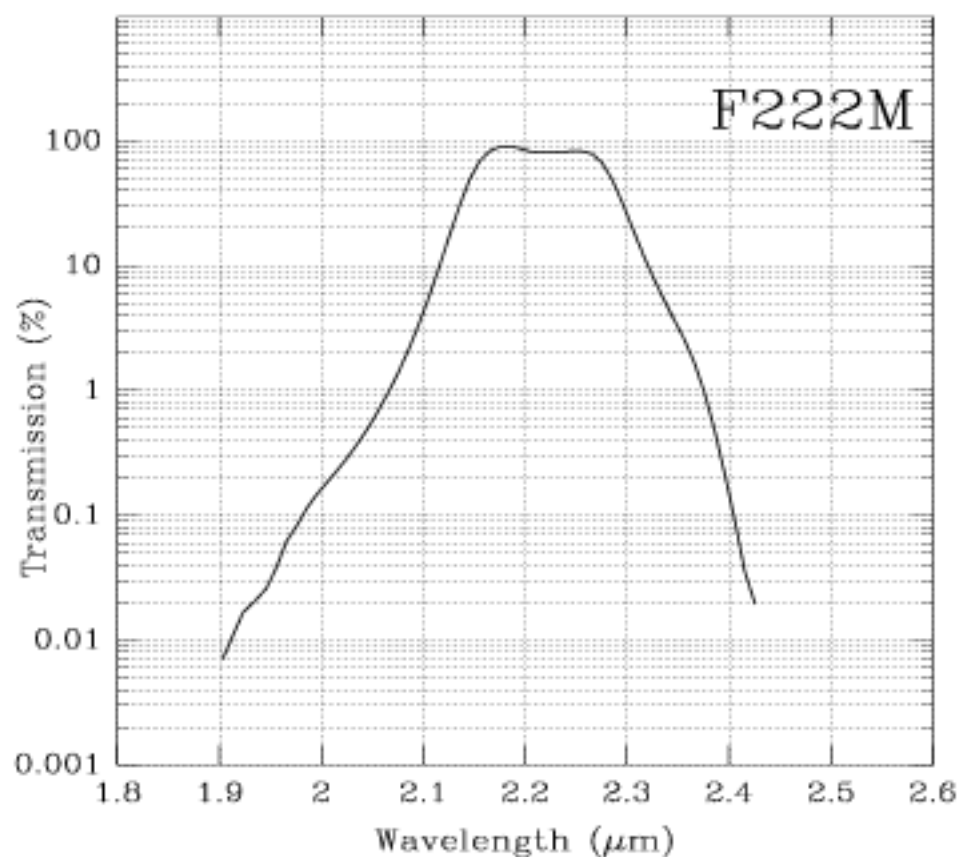
Camera 2, Filter F237M

CO

Also available on Camera 3 as F240M.

Thermal background important.

Central wavelength (μm)	Mean wavelength (μm)	Peak wavelength (μm)	FWHM (μm)	Range (μm)	MaxTr %	Pixel Fraction
2.3677	2.3694	2.3852	0.1546	2.3-2.45	92.38	0.0797

Figure 11.32: Camera 2, Filter F237M
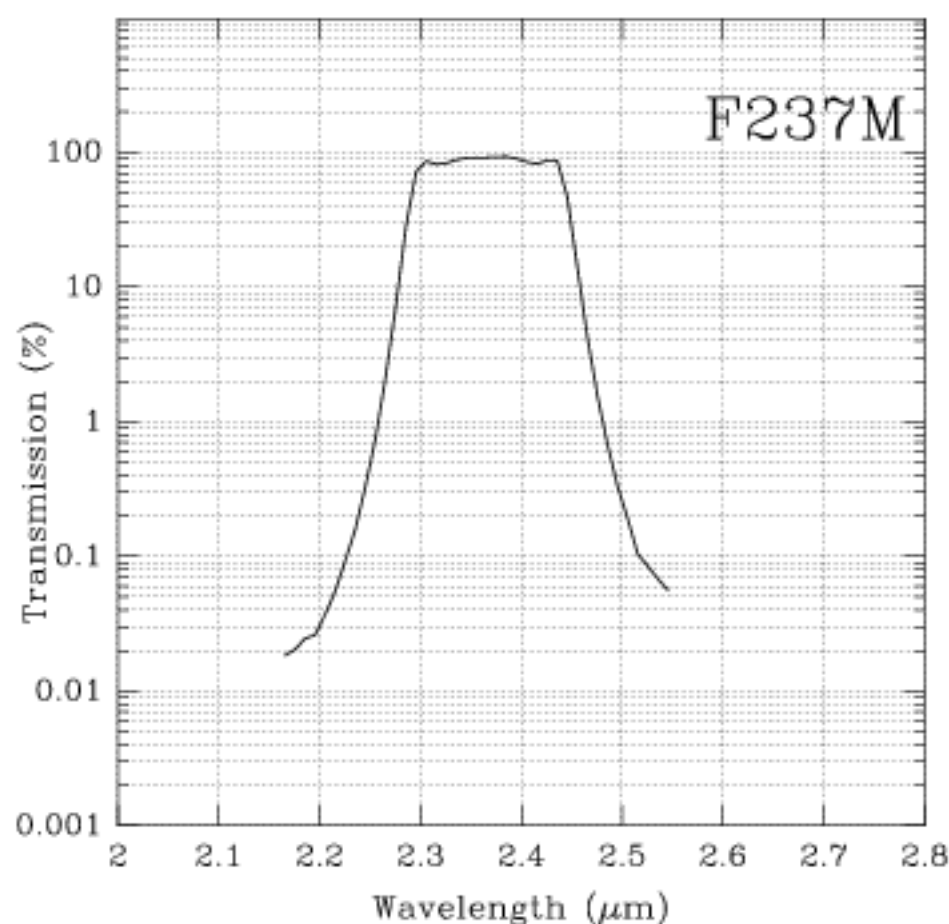
Camera 3, Filter F108N

Hel line

Also available on Camera 1.

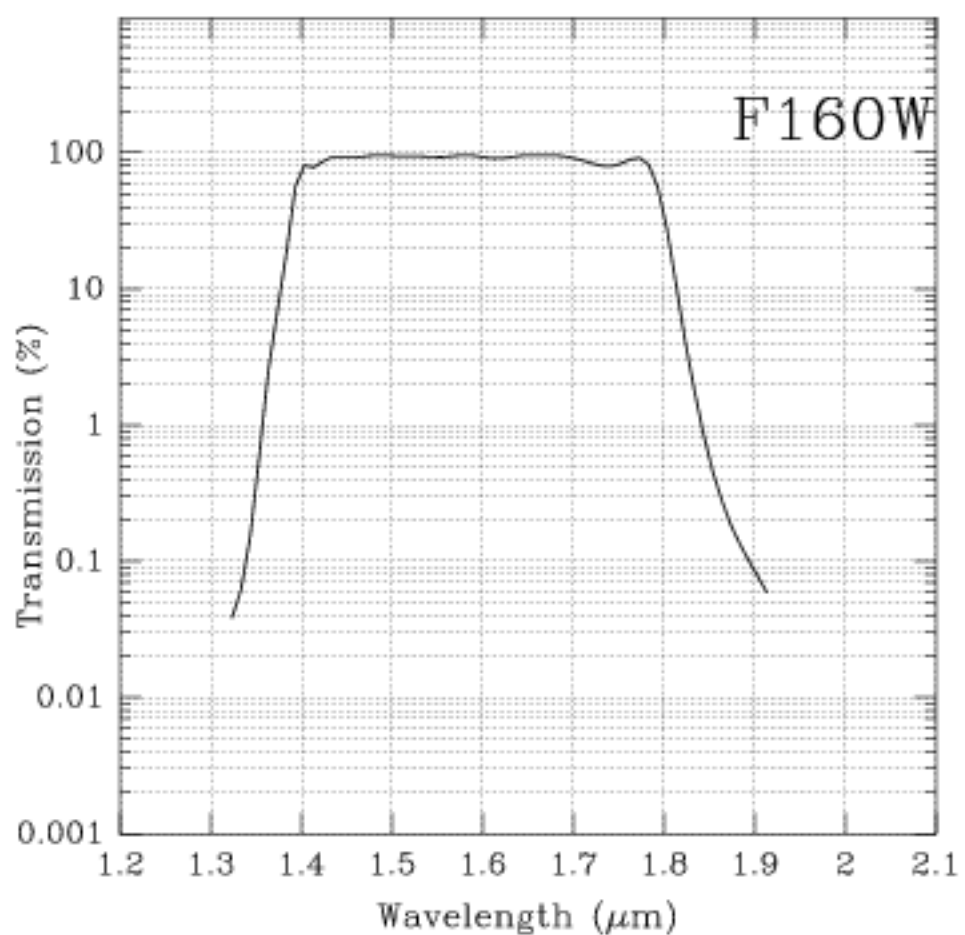| Central wavelength (μm)	Mean wavelength (μm)	Peak wavelength (μm)	FWHM (μm)	Range (μm)	MaxTr %	Pixel Fraction
1.0800	1.0799	1.0776	0.0096	1%	75.82	0.582

Figure 11.33: Camera 3, Filter F108N
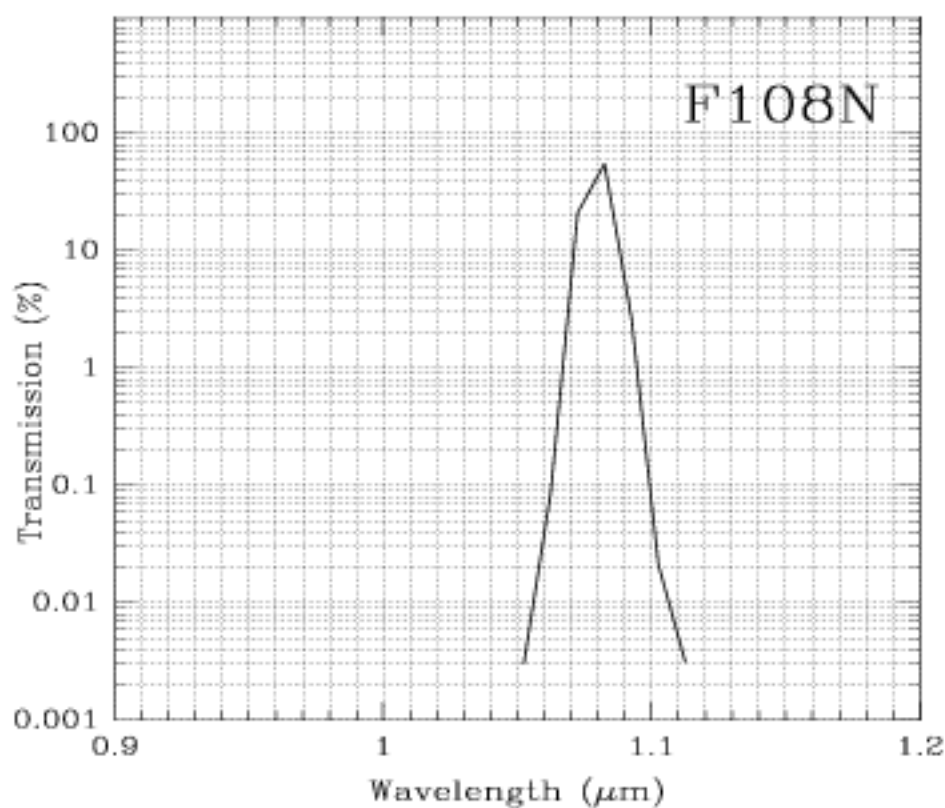
Camera 3, Filter F110W

Also available on Cameras 1 and 2.

Central wavelength (μm)	Mean wavelength (μm)	Peak wavelength (μm)	FWHM (μm)	Range (μm)	MaxTr %	Pixel fraction
1.0998	1.1035	1.2035	0.5915	0.8-1.4	94.90	0.590

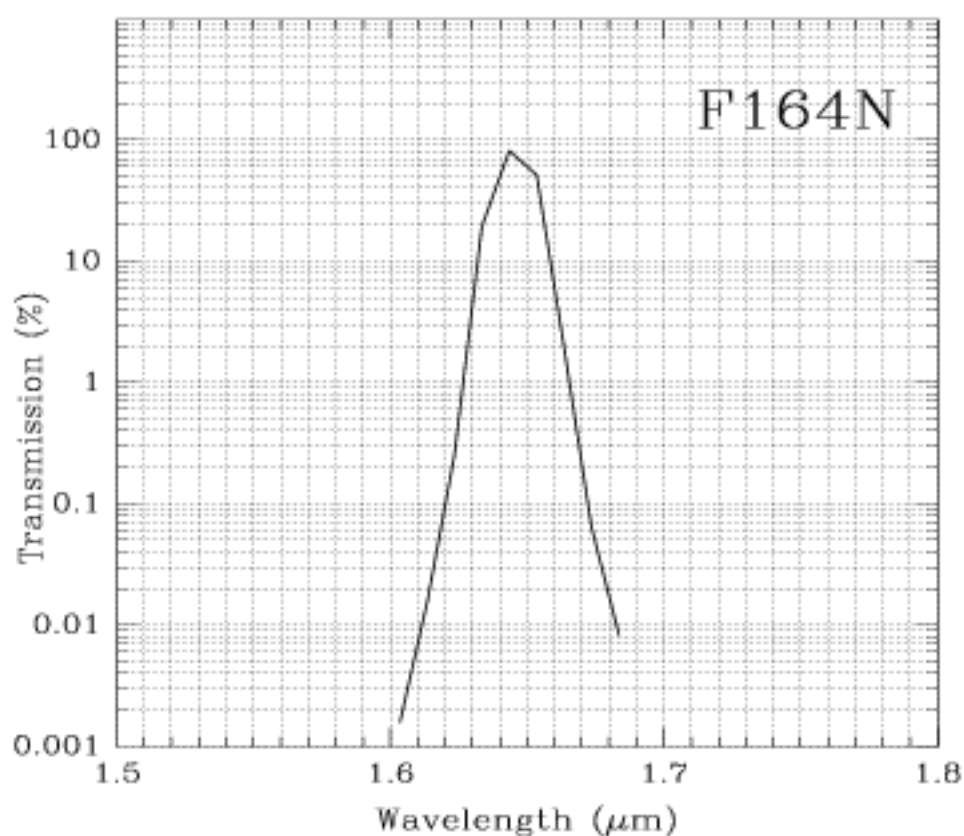Figure 11.34: Transmission Curve for F110W
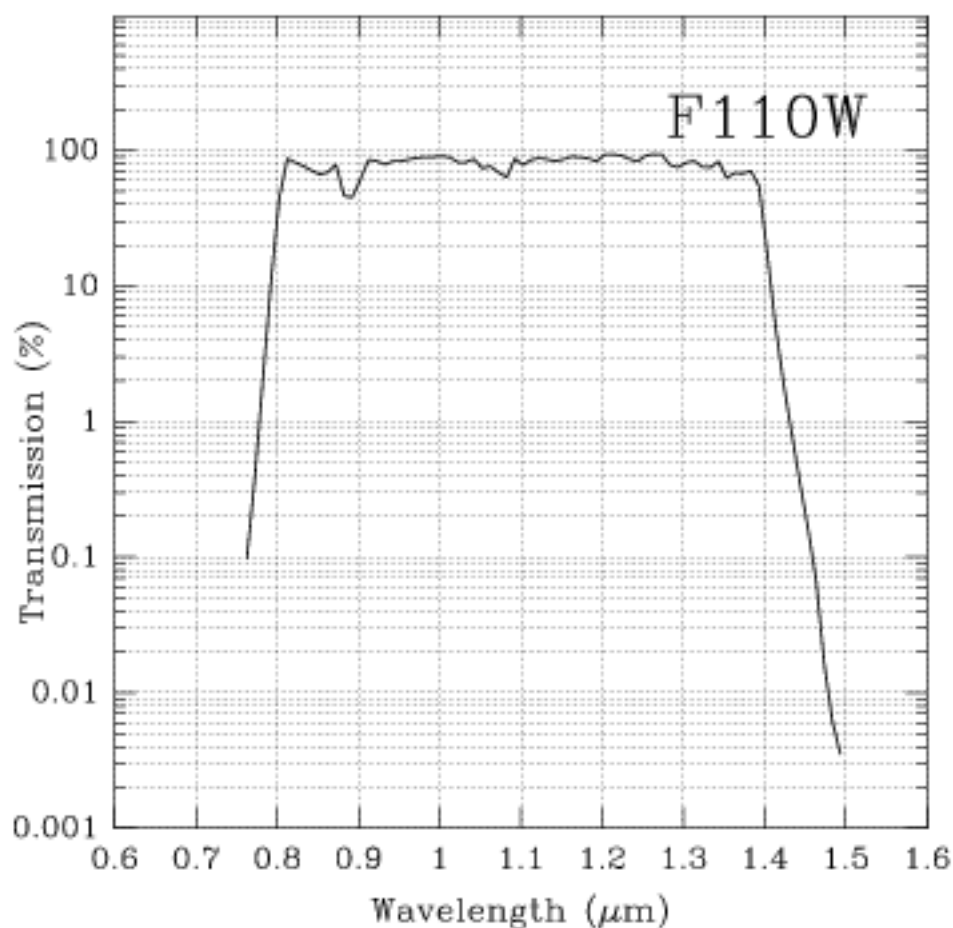
Camera 3, Filter F113N

HeI continuum

Also available on Camera 1.

Central wavelength (μm)	Mean wavelength (μm)	Peak wavelength (μm)	FWHM (μm)	Range (μm)	MaxTr %	Pixel Fraction
1.1283	1.1283	1.1316	0.0110	1%	84.81	0.579

Figure 11.35: Camera 3, Filter F113N
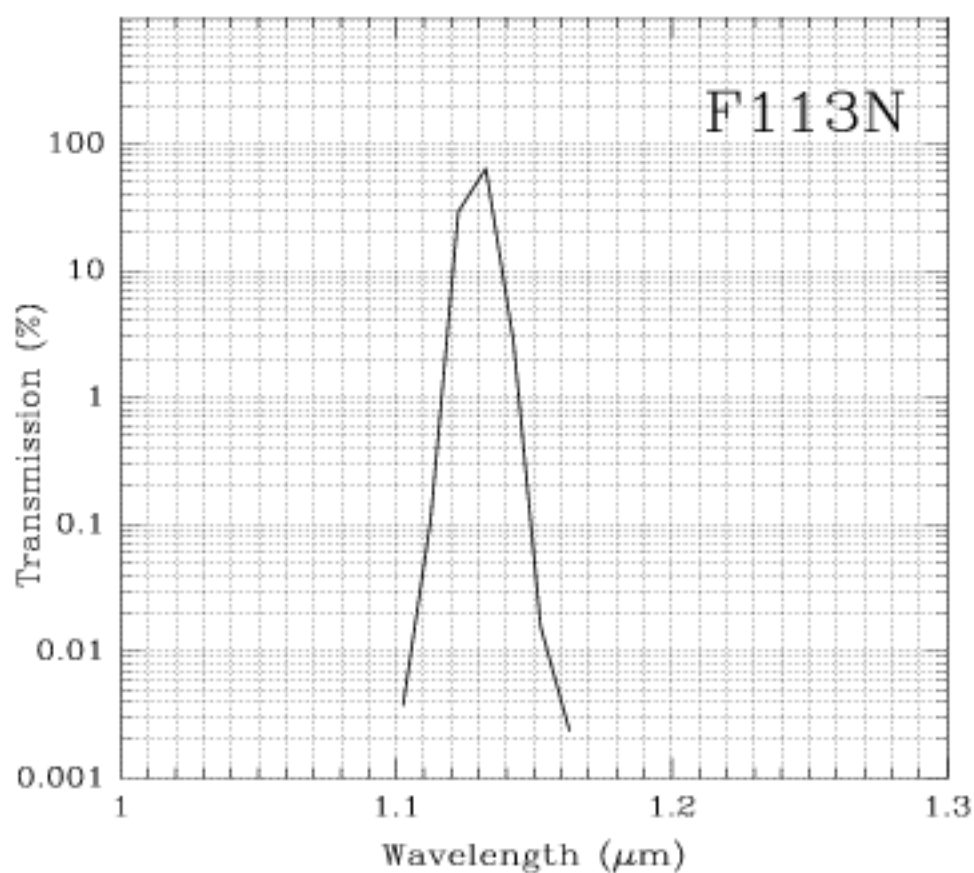
Camera 3, Filter F150W

Grism B continuum

Thermal background important.

Central wavelength (μm)	Mean wavelength (μm)	Peak wavelength (μm)	FWHM (μm)	Range (μm)	MaxTr %	Pixel fraction
1.5035	1.5069	1.6355	0.8020	1.1-1.9	97.67	0.534

Figure 11.36: Camera 3, Filter F150W
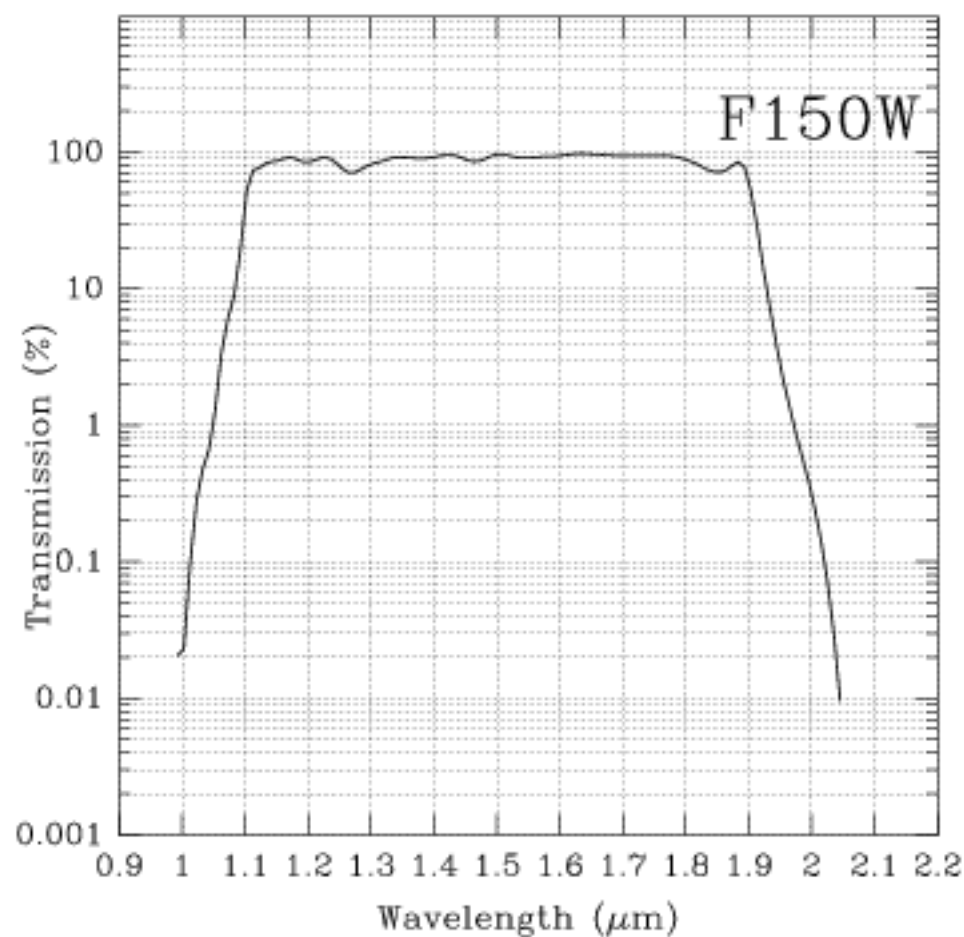
Camera 3, Filter F160W

Minimum background

Also available on Cameras 1 and 2.

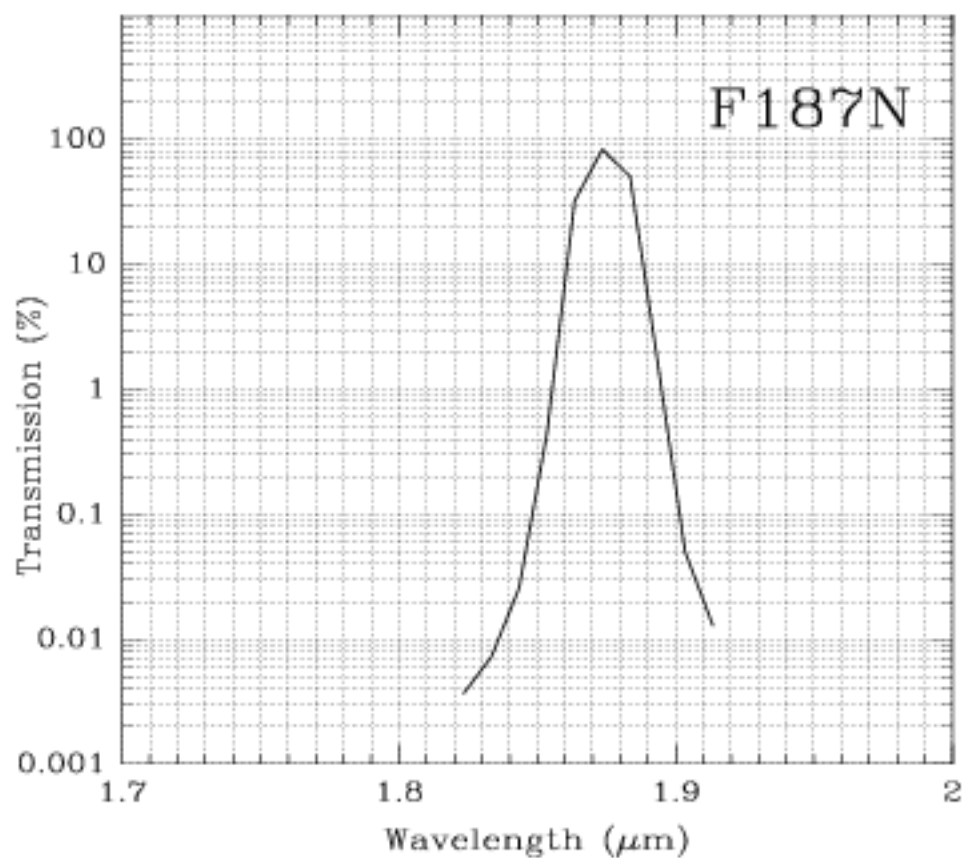| Central wavelength (µm)	Mean wavelength (µm)	Peak wavelength (µm)	FWHM (µm)	Range (µm)	MaxTr %	Pixel fraction
1.5940	1.5931	1.5820	0.4030	1.4-1.8	96.59	0.524

Figure 11.37: Camera 3, Filter F160W

Camera 3, Filter F164N

[FeII] line
Also available on Camera 1.

Central wavelength (μm)	Mean wavelength (μm)	Peak wavelength (μm)	FWHM (μm)	Range (μm)	MaxTr %	Pixel Fraction
1.646	1.6460	1.6476	0.0170	1%	86.27	0.523

Figure 11.38: Camera 3, Filter F164N

Camera 3, Filter F166N

[FeII] continuum

Also available in Camera 1.

Central wavelength (μm)	Mean wavelength (μm)	Peak wavelength (μm)	FWHM (μm)	Range (μm)	MaxTr %	Pixel Fraction
1.6582	1.6582	1.6602	0.0164	1%	87.24	0.513

Figure 11.39: Camera 3, Filter F166N
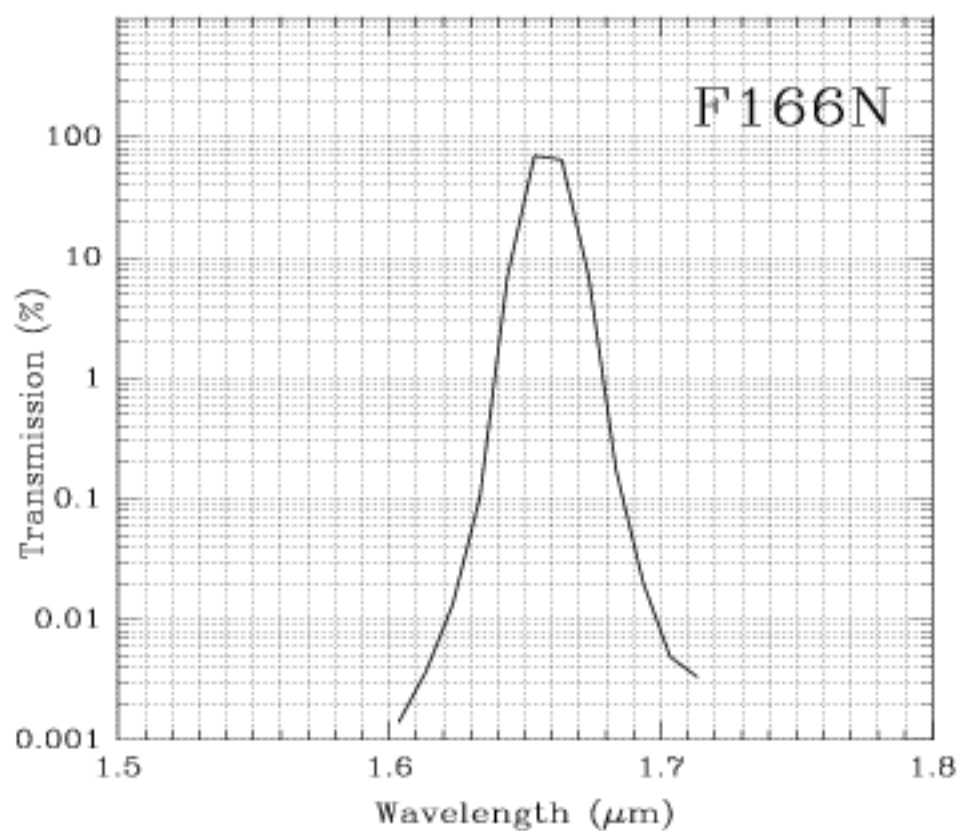
Camera 3, Filter F175W

Also available on Cameras 2 and 3.

Thermal background important.

Central wavelength (μm)	Mean wavelength (μm)	Peak wavelength (μm)	FWHM (μm)	Range (μm)	MaxTr %	Pixel fraction
1.7530	1.7508	1.9070	1.0940	1.2-2.3	96.58	0.486

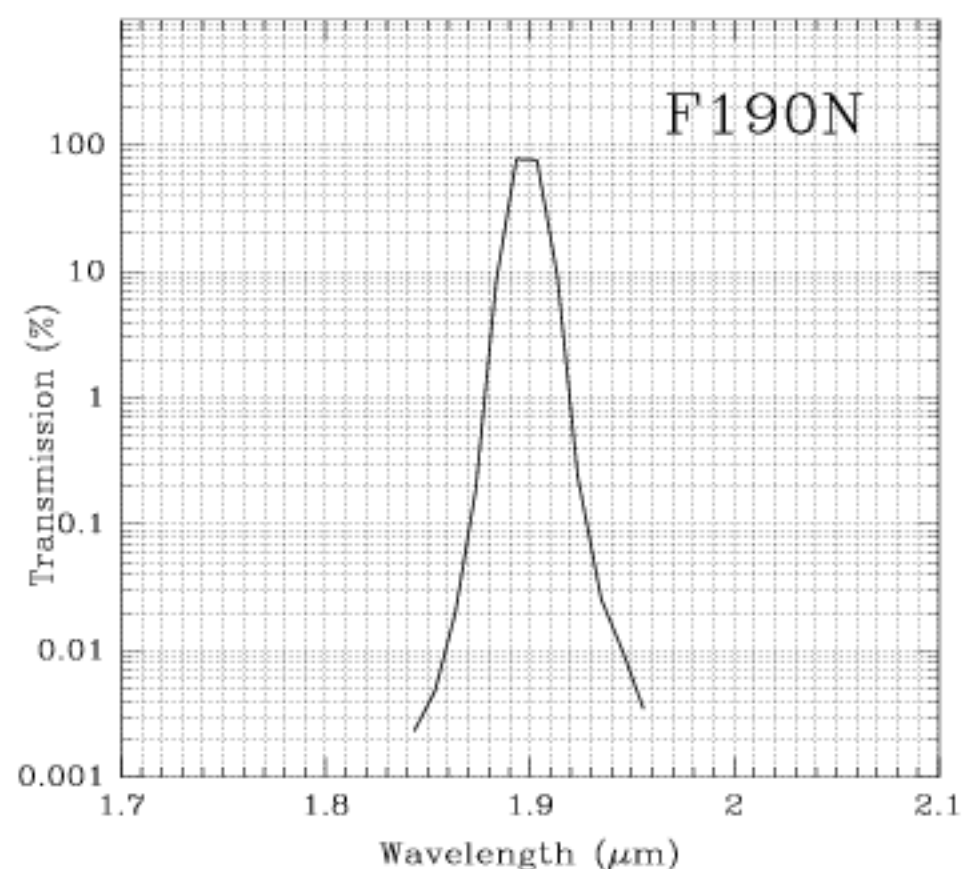Figure 11.40: Camera 3, Filter F175W
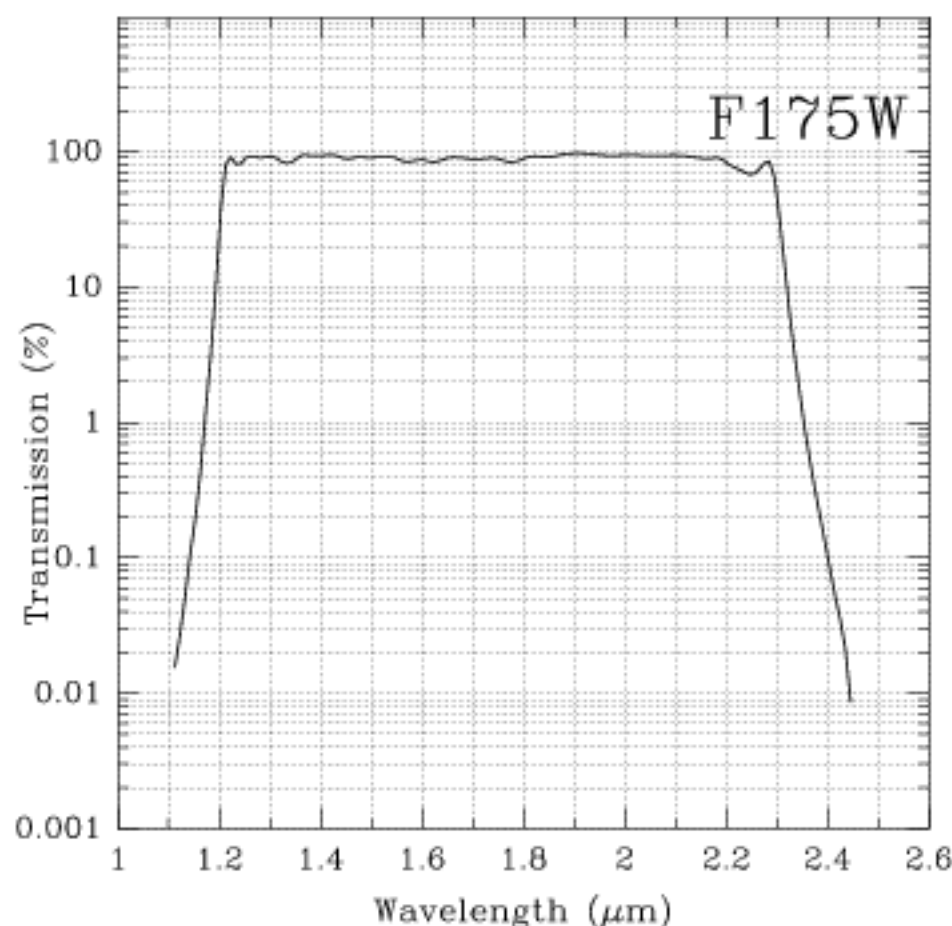
Camera 3, Filter F187N

Paschen α line

Also available on Cameras 1 and 2.

Central wavelength (µm)	Mean wavelength (µm)	Peak wavelength (µm)	FWHM (µm)	Range	MaxTr %	Pixel fraction
1.8740	1.8738	1.8746	0.0192	1%	88.91	0.471

Figure 11.41: Camera 3, Filter F187N

Camera 3, Filter F190N

Paschen α continuum

Also available on Cameras 1 and 2.

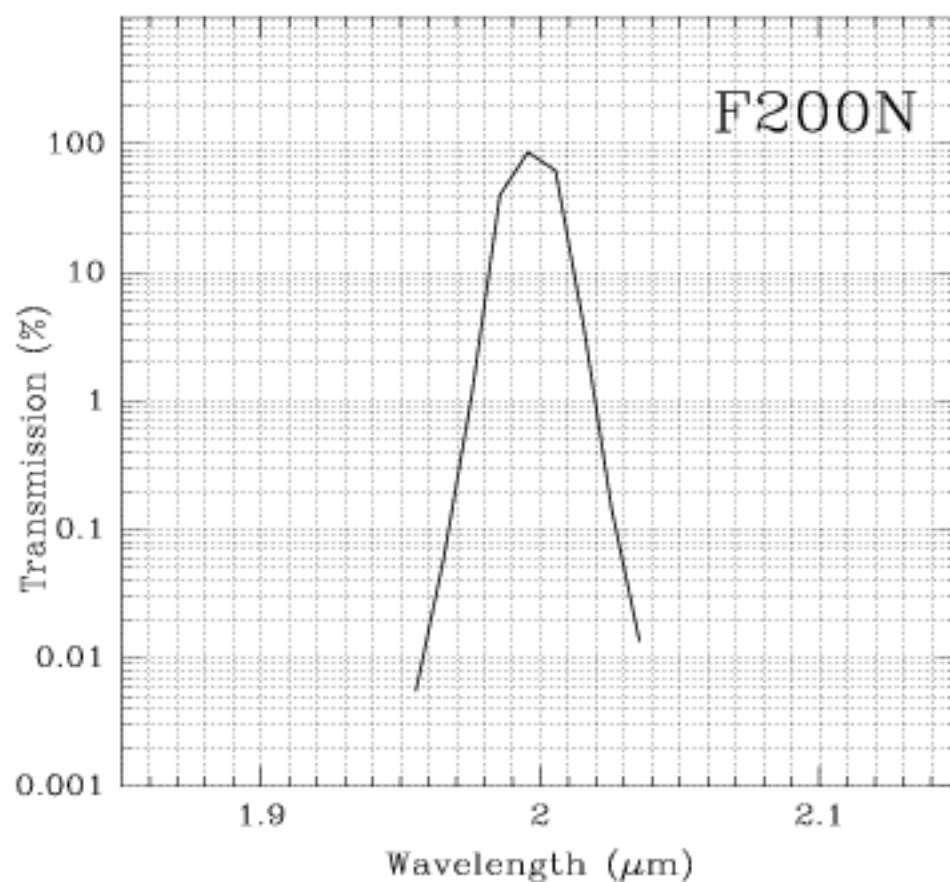| Central wavelength (μm)	Mean wavelength (μm)	Peak wavelength (μm)	FWHM (μm)	Range (μm)	MaxTr %	Pixel Fraction
1.9005	1.9003	1.9004	0.0174	1%	93.22	0.466

Figure 11.42: Camera 3, Filter F190N

Camera 3, Filter F196N

[SiVI]

Thermal background important.

Central wavelength (μm)	Mean wavelength (μm)	Peak wavelength (μm)	FWHM (μm)	Range	MaxTr %	Pixel fraction
1.9641	1.9639	1.9698	0.0186	1%	93.74	0.450

Figure 11.43: Camera 3, Filter F196N
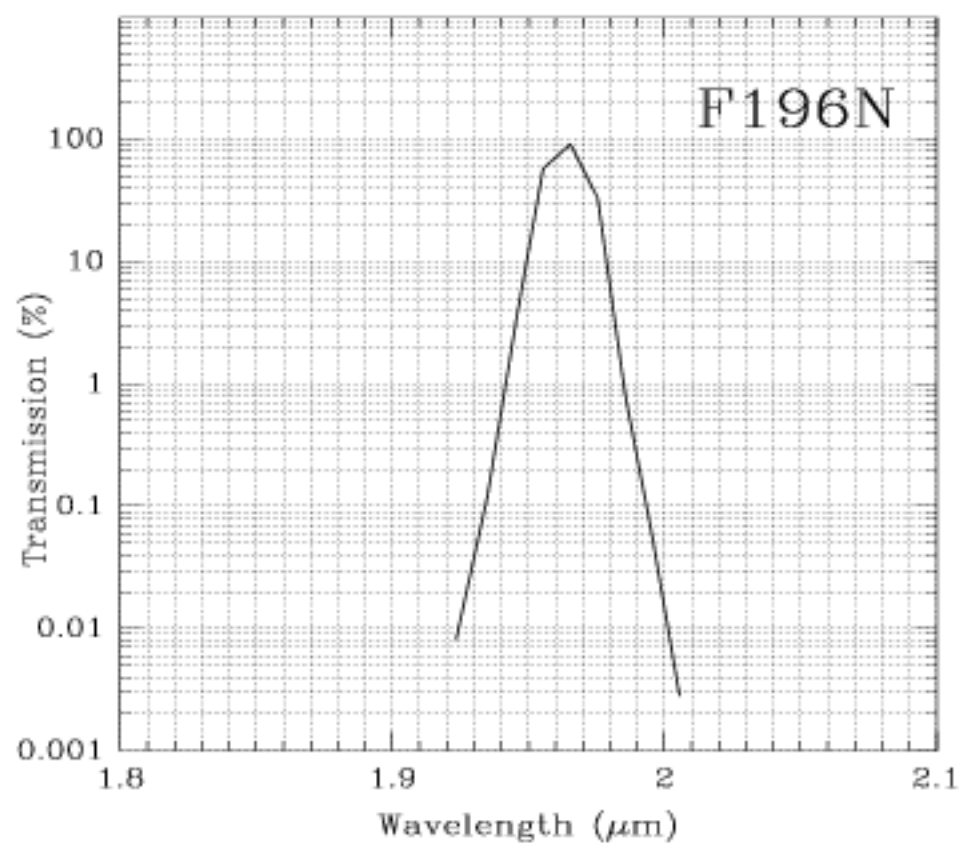
Camera 3, Filter F200N

[SiVI] continuum

Thermal background important.

Central wavelength (μm)	Mean wavelength (μm)	Peak wavelength (μm)	FWHM (μm)	Range (μm)	MaxTr %	Pixel Fraction
1.9973	1.9974	1.9996	0.0206	1%	91.75	0.445

Figure 11.44: Camera 3, Filter F200N
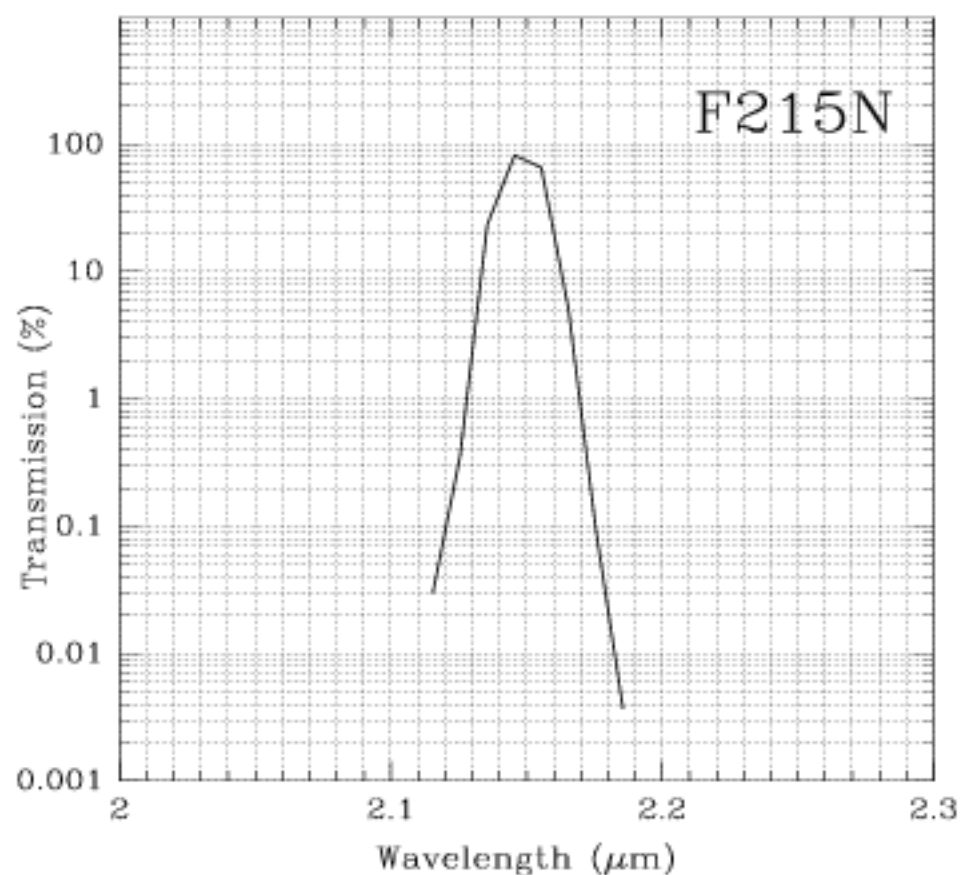
Camera 3, Filter F212N

H$_2$ line
Also available in Camera 2.

Thermal background important.

Central wavelength (µm)	Mean wavelength (µm)	Peak wavelength (µm)	FWHM (µm)	Range	MaxTr %	Pixel fraction
2.1211	2.1213	2.1228	0.0206	1%	90.90	0.418

Figure 11.45: Camera 3, Filter F212N
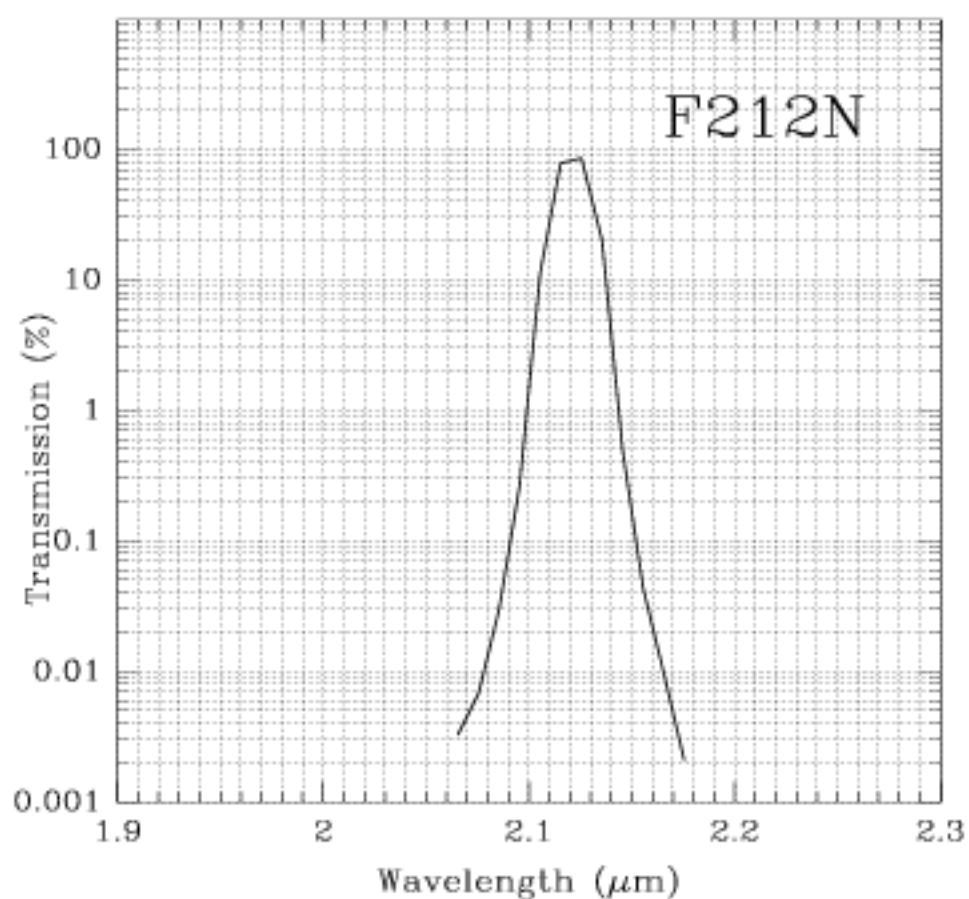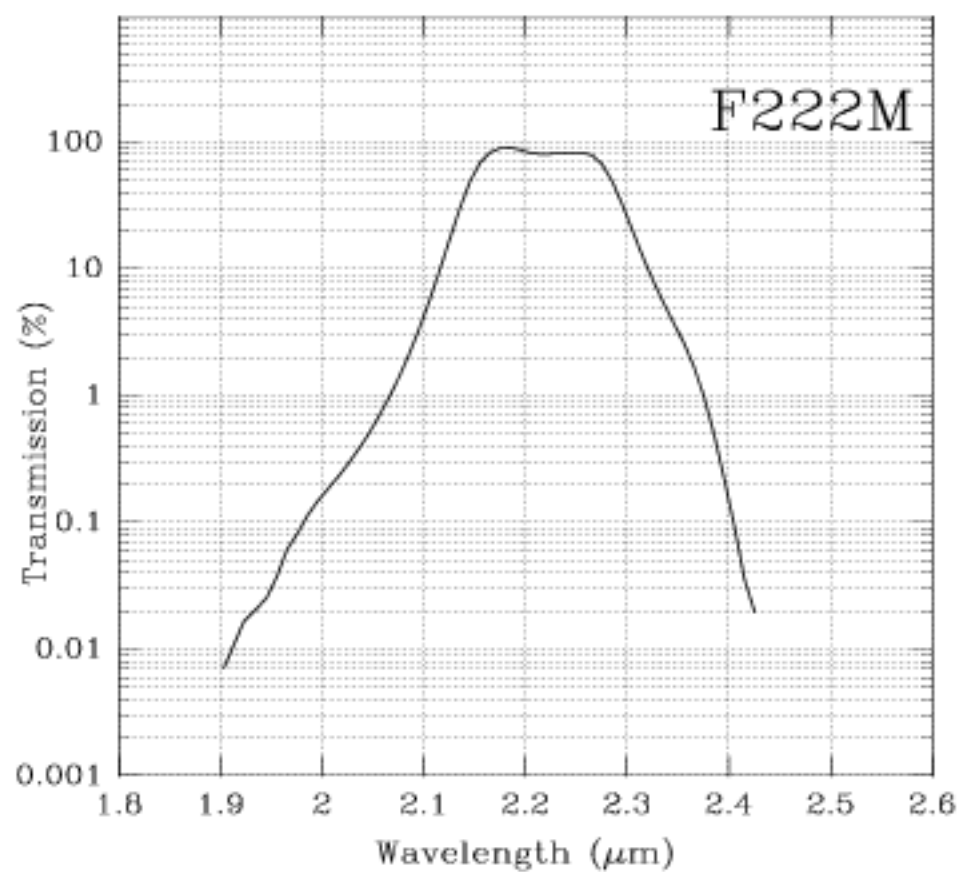
Camera 3, Filter F215N

H$_2$ continuum

Also available in Camera 2.

Thermal background important.

Central wavelength (µm)	Mean wavelength (µm)	Peak wavelength (µm)	FWHM (µm)	Range (µm)	MaxTr %	Pixel Fraction
2.1488	2.1487	2.1562	0.0200	1%	85.91	0.413

Figure 11.46: Camera 3, Filter F215N

Camera 3, Filter F222M

CO continuum

Also available on Camera 2.

Thermal background important.

| Central wavelength (µm)	Mean wavelength (µm)	Peak wavelength (µm)	FWHM (µm)	Range (µm)	MaxTr %	Pixel Fraction
2.216	2.216	2.18	0.1432	2.15-2.3	89.9	0.397

Figure 11.47: Camera 3, Filter F222M

Camera 3, Filter F240M

CO band
Thermal background important.

Central wavelength (µm)	Mean wavelength (µm)	Peak wavelength (µm)	FWHM (µm)	Range (µm)	MaxTr %	Pixel Fraction
2.3978	2.3977	2.3155	0.1975	2.3-2.5	92.43	0.363

Figure 11.48: Camera 3, Filter F240M
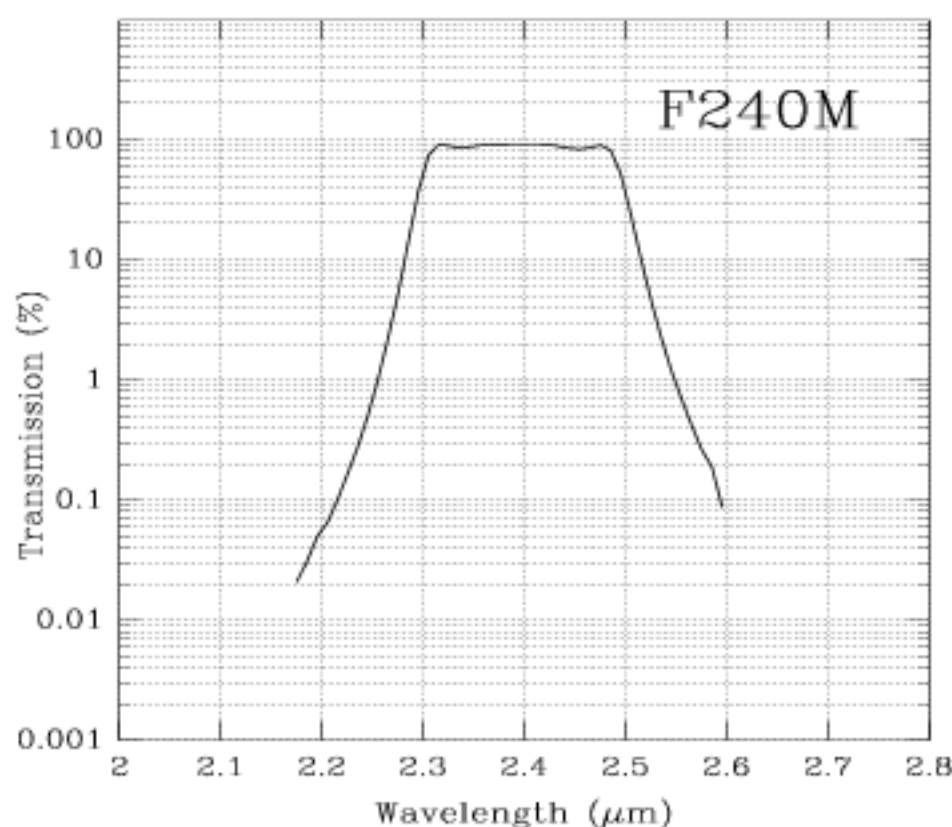
Flux Units and
Line Lists

In this chapter we provide a variety of background material that may be useful when preparing proposals. This material includes a discussion of the flux and surface brightness units often used in the infrared, which may not be familiar to some users, plus a large compilation of spectral lines that may be encountered in the infrared, and which are either in the NICMOS waveband or which are related to lines which are.

Infrared Flux Units

In the infrared, as in the optical, the means of reporting source brightnesses and the units employed have varied considerably. In recent years, however, magnitude systems have been used less frequently, and the most popular unit for expressing brightnesses, both for point source fluxes and surface brightnesses, is steadily becoming the Jansky. We have adopted the Jansky as the standard flux unit for NICMOS in our documentation and in observer-oriented software. Here we provide some simple formulae and tables to facilitate the conversion from other units into Jy.

Background

Infrared astronomy really began in the 1960s, when the vast majority of astronomy was still carried out in the visual region. Flux measurements were routinely reported in the UBV magnitude system, and to attempt to integrate IR astronomy into this system, Johnson (Ap.J., **134**, 69) defined the first IR magnitude system. This involved four new photometric bands, the J, K, L and M bands which were centered on wavelengths of 1.3, 2.2, 3.6 and 5.0 microns. These bands were defined not only by the filter bandpasses, but also by the wavebands of the 'windows' of high transmission through the atmosphere. In this system, all measurements were referred to the Sun, which was assumed to be a G2V star with an effective temperature of 5785K, and was taken to have a V-K color of roughly +2.2. From his own measurements in this system, Johnson determined Vega to have a K magnitude of +0.02 and K-L=+0.04.

Until the early 1980s IR astronomical observations were restricted to spectra or single channel photometry, and most photometry was reported in systems at least loosely based on Johnson's system, though with the addition of a new band at 1.6 microns known as the H band and the development of two bands in place of the one formerly defined by Johnson as the L band, a new definition of the L band centered on 3.4 microns, and a rather narrower band known as L' centered on 3.74 microns.

As the new science of infrared astronomy rapidly expanded its wavelength coverage, many new photometric bands were adopted, both for ground-based observations and for use by the many balloon- and rocket-borne observations and surveys. The differing constraints presented by these different environments for IR telescopes resulted in systems with disappointingly little commonality or overlap, and today the IR astronomer is left with a plethora of different systems to work with.

The IRAS survey results, which were published in 1986, presented observations made photometrically in four bands in the mid- and far-infrared, and mid-infrared spectra, and all were presented in units of Janskys, rather than defining yet another new magnitude system. Since then, IR data from many sites around the world have been increasingly commonly presented in Janskys (Jy), or in Jy/arcsec^2 in the case of surface brightness data (although IRAS maps are often presented in the rather grandiloquent units of MJy/steradian).

Ground-based mid-IR photometry is usually carried out using the N and Q photometric bands, which are themselves defined more by the atmospheric transmission than by any purely scientific regard. IRAS, freed of the constraints imposed by the atmosphere, adopted its own 12 micron and 25 micron bands, which were extremely broad and therefore offered high sensitivity. Similarly, NICMOS, being above the atmosphere, is not forced to adopt filter bandpasses (See Chapter 4) like those used at ground-based observatories, but instead has filters constrained purely by the anticipated scientific demands. Thus in practice NICMOS does not have filters matched to any of the standard ground-based photometric bands.

Units for NICMOS

In order to facilitate proposal preparation by observers, STScI is making available a number of computer programs to assist with signal to noise ratio and integration time calculations. Given the multitude of units and systems that have been used for IR photometry (magnitudes, Janskys, $Wm^{-2}\mu m^{-1}$, $Wcm^{-2}\mu m^{-1}$, erg $sec^{-1}cm^{-2}\mu m^{-1}$) and for surface brightness measurements (Janskys $arcsec^{-2}$, MJy $steradian^{-1}$, magnitudes $arcsec^{-2}$), presenting these data to observers could become somewhat cumbersome. Additionally, given the lack of any *standard* IR filters (as explained above), in order to express brightnesses in magnitudes we would have to adopt our own NICMOS magnitude system, and observers would have to transform ground-based photometry into the NICMOS bands. We have therefore adopted a single standard set of flux units, Janskys for all photometry and spectroscopy, and Janksys $arcsec^{-2}$ for all surface brightness measurements in all NICMOS documentation and observer-oriented software. The NICMOS calibration pipeline software delivers results calibrated in Janskys $arcsec^{-2}$, as well as the more familiar HST unit of erg $s^{-1}cm^{-2}Å^{-1}$.

We are aware that some observers do not routinely use these units, and therefore below we give a set of simple formulae to use to convert between systems, and some conversion tables. In the future we will also make available, via the World Wide Web, software to perform conversions between different systems and units.

Formulae

Converting Between F_ν and F_λ

One Jansky (Jy) is defined as $10^{-26}Wm^{-2}Hz^{-1}$, so it is a unit of measurement of the spectral flux density, F_ν.

For F_ν in Jy, use the following formula:

$$F_\lambda = \beta F_\nu / \lambda^2,$$

where λ is the wavelength in microns (μm), and β is a constant chosen from Table 12.1 and depending on the units of F_λ. (This is simply derived, using the fact that $d\nu/d\lambda = c/\lambda^2$.)

Table 12.1: Constants for Converting F_λ and F_ν

F_λ measured in	β
$Wm^{-2}\mu m^{-1}$	3×10^{-12}
$Wcm^{-2}\mu m^{-1}$	3×10^{-16}
$erg\,sec^{-1}\,cm^{-2}\,\mu m^{-1}$	3×10^{-9}
$erg\,sec^{-1}\,cm^{-2}\,Å^{-1}$	3×10^{-13}

Remember that $1\,W = 10^7\,erg\,sec^{-1}$, and $1\mu m = 10^4 Å$.

Conversion Between Fluxes and Magnitudes

The spectral flux density F_ν can be calculated from its magnitude as

$$F_\nu = 10^{-m/2.5} F_o$$

where m is the magnitude and F_o the zero-point flux for the given photometric band. We list the central wavelengths and zero-point fluxes for the more commonly encountered photometric bands below in Table 12.2. The CIT system was originally based on Beckwith et al (1976, Ap.J., **208**, 390); the UKIRT system is in fact based on the original CIT system, but with adjustments made largely owing to different filter bandpasses. It should be noted that for a given photometric band there will be small differences in the effective wavelength and zero-point flux from one observatory to another, and for astronomical objects with radically different colors, so these figures can only be treated as approximate.

Table 12.2: Effective Wavelengths and Zero-points for Photometric Bands

Band	λ [μm]	F_o [Jy] (CIT)	F_o [Jy] (UKIRT)
V	0.56	3540	3540
R	0.70	2870	-
I	0.90	2250	-
J	1.25	1670	1600
H	1.65	980	1020
K	2.2	620	657
L	3.4	280	290
L'	3.74	-	252
M	4.8	150	163
N	10.1	37	39.8
Q	20.0	10	10.4

Conversion Between Surface Brightness Units

Surface brightnesses are generally measured in Janskys arcsec^{-2}, MJy steradian^{-1} or magnitudes arcsec^{-2}. If you have a surface brightness S_v in MJy steradian^{-1}, then you can use:

S_v[Jy arcsec^{-2}] = S_v[MJy ster^{-1}] x 0.084616.

If you have S_v in magnitudes arcsec^{-2}, you can simply use the formula and zero-points as given in the previous section for point sources.

Look-up Tables and Software

In this section we provide look-up tables to facilitate rapid, approximate conversion between the different systems mentioned in the preceding section.

For both integrated source fluxes and surface brightnesses, we provide tables of conversions between systems at the wavelengths of the four commonly used photometric bands which cover the NICMOS operating waveband of 0.8–2.5 microns. To carry out some of the conversions described here, simple programs are available on the NICMOS World Wide Web pages at STScI. We are adopting here the CIT system defined in Table 12.2.

By using Table 12.3 it is possible to estimate the CIT magnitude corresponding to any flux in Jy, by using the property that multiplying or dividing the flux by one hundred adds or subtracts five magnitudes.

Table 12.3: F_γ to Magnitude Conversion

F_γ [Jy]	I	J	H	K
10.0	5.88	5.56	4.98	4.48
8.0	6.12	5.80	5.22	4.72
6.0	6.44	6.11	5.53	5.04
5.0	6.63	6.31	5.73	5.23
4.0	6.88	6.55	5.97	5.48
3.0	7.19	6.86	6.29	5.79
2.5	7.39	7.06	6.48	5.99
2.0	7.63	7.30	6.73	6.23
1.5	7.94	7.62	7.04	6.54
1.25	8.14	7.81	7.24	6.74
1.0	8.38	8.06	7.48	6.98
0.8	8.62	8.30	7.72	7.22
0.6	8.94	8.61	8.03	7.54
0.5	9.13	8.81	8.23	7.73
0.4	9.38	9.05	8.47	7.98
0.3	9.69	9.36	8.79	8.29
0.25	9.89	9.57	8.98	8.49
0.2	10.13	9.8	9.23	8.73
0.15	10.44	10.12	9.54	9.04
0.125	10.64	10.31	9.74	9.24
0.1	10.88	10.56	9.98	9.48

Table 12.4: I- Band Flux Conversion

F_ν [Jy]	I [mag]	F_λ [$Wm^{-2}\mu m^{-1}$]	F_λ [$W\,cm^{-2}\mu m^{-1}$]	F_λ [$erg\,s^{-1}\,cm^{-2}\,\text{Å}^{-1}$]
2250	0.0	8.32×10^{-9}	8.32×10^{-13}	8.32×10^{-10}
894	1.0	3.312×10^{-9}	3.312×10^{-13}	3.312×10^{-10}
356	2.0	1.319×10^{-9}	1.319×10^{-13}	1.319×10^{-10}
142	3.0	5.25×10^{-10}	5.25×10^{-14}	5.25×10^{-11}
56.4	4.0	2.09×10^{-10}	2.09×10^{-14}	2.09×10^{-11}
22.5	5.0	8.32×10^{-11}	8.32×10^{-15}	8.32×10^{-12}
8.94	6.0	3.312×10^{-11}	3.312×10^{-15}	3.312×10^{-12}
3.56	7.0	1.319×10^{-11}	1.319×10^{-15}	1.319×10^{-12}
1.42	8.0	5.25×10^{-12}	5.25×10^{-16}	5.25×10^{-13}
0.564	9.0	2.09×10^{-12}	2.09×10^{-16}	2.09×10^{-13}
0.225	10.0	8.32×10^{-13}	8.32×10^{-17}	8.32×10^{-14}
0.0894	11.0	3.312×10^{-13}	3.312×10^{-17}	3.312×10^{-14}
0.0356	12.0	1.319×10^{-13}	1.319×10^{-17}	1.319×10^{-14}
0.0142	13.0	5.25×10^{-14}	5.25×10^{-18}	5.25×10^{-15}
0.00564	14.0	2.09×10^{-14}	2.09×10^{-18}	2.09×10^{-15}
0.00225	15.0	8.32×10^{-15}	8.32×10^{-19}	8.32×10^{-16}
8.94×10^{-4}	16.0	3.312×10^{-15}	3.312×10^{-19}	3.312×10^{-16}
3.56×10^{-4}	17.0	1.319×10^{-15}	1.319×10^{-19}	1.319×10^{-16}
1.42×10^{-4}	18.0	5.25×10^{-16}	5.25×10^{-20}	5.25×10^{-17}
5.64×10^{-5}	19.0	2.09×10^{-16}	2.09×10^{-20}	2.09×10^{-17}
2.25×10^{-5}	20.0	8.32×10^{-17}	8.32×10^{-21}	8.32×10^{-18}
8.94×10^{-6}	21.0	3.312×10^{-17}	3.312×10^{-21}	3.312×10^{-18}
3.56×10^{-6}	22.0	1.319×10^{-17}	1.319×10^{-21}	1.319×10^{-18}
1.42×10^{-6}	23.0	5.25×10^{-18}	5.25×10^{-22}	5.25×10^{-19}
5.64×10^{-7}	24.0	2.09×10^{-18}	2.09×10^{-22}	2.09×10^{-19}
2.25×10^{-7}	25.0	8.32×10^{-19}	8.32×10^{-23}	8.32×10^{-20}
8.94×10^{-8}	26.0	3.312×10^{-19}	3.312×10^{-23}	3.312×10^{-20}

Table 12.5: J-band Flux Conversion

F_ν [Jy]	J [mag]	F_λ [Wm^{-2}μm^{-1}]	F_λ [Wcm^{-2}μm^{-1}]	F_λ [erg cm^{-2}s^{-1}Å^{-1}]
1670	0.0	3.21×10^{-9}	3.21×10^{-13}	3.21×10^{-10}
665	1.0	1.28×10^{-9}	1.28×10^{-13}	1.28×10^{-10}
265	2.0	5.08×10^{-10}	5.08×10^{-14}	5.08×10^{-11}
106	3.0	2.02×10^{-10}	2.02×10^{-14}	2.02×10^{-11}
42.0	4.0	8.06×10^{-11}	8.06×10^{-15}	8.06×10^{-12}
16.7	5.0	3.21×10^{-11}	3.21×10^{-15}	3.21×10^{-12}
6.65	6.0	1.28×10^{-11}	1.28×10^{-15}	1.28×10^{-12}
2.65	7.0	5.08×10^{-12}	5.08×10^{-16}	5.08×10^{-13}
1.06	8.0	2.02×10^{-12}	2.02×10^{-16}	2.02×10^{-13}
0.420	9.0	8.06×10^{-13}	8.06×10^{-17}	8.06×10^{-14}
0.167	10.0	3.21×10^{-13}	3.21×10^{-17}	3.21×10^{-14}
0.0665	11.0	1.28×10^{-13}	1.28×10^{-17}	1.28×10^{-14}
0.0265	12.0	5.08×10^{-14}	5.08×10^{-18}	5.08×10^{-15}
0.0106	13.0	2.02×10^{-14}	2.02×10^{-18}	2.02×10^{-15}
0.00420	14.0	8.06×10^{-15}	8.06×10^{-19}	8.06×10^{-16}
0.00167	15.0	3.21×10^{-15}	3.21×10^{-19}	3.21×10^{-16}
6.65×10^{-4}	16.0	1.28×10^{-15}	1.28×10^{-19}	1.28×10^{-16}
2.65×10^{-4}	17.0	5.08×10^{-16}	5.08×10^{-20}	5.08×10^{-17}
1.06×10^{-4}	18.0	2.02×10^{-16}	2.02×10^{-20}	2.02×10^{-17}
4.20×10^{-5}	19.0	8.06×10^{-17}	8.06×10^{-21}	8.06×10^{-18}
1.67×10^{-5}	20.0	3.21×10^{-17}	3.21×10^{-21}	3.21×10^{-18}
6.65×10^{-6}	21.0	1.28×10^{-17}	1.28×10^{-21}	1.28×10^{-18}
2.65×10^{-6}	22.0	5.08×10^{-18}	5.08×10^{-22}	5.08×10^{-19}
1.06×10^{-6}	23.0	2.02×10^{-18}	2.02×10^{-22}	2.02×10^{-19}
4.20×10^{-7}	24.0	8.06×10^{-19}	8.06×10^{-23}	8.06×10^{-20}
1.67×10^{-7}	25.0	3.21×10^{-19}	3.21×10^{-23}	3.21×10^{-20}
6.65×10^{-8}	26.0	1.28×10^{-19}	1.28×10^{-23}	1.28×10^{-20}

Table 12.6: H-band Flux Conversion

F_ν [Jy]	H [mag]	F_λ [Wm$^{-2}\mu$m^{-1}]	F_λ [Wcm$^{-2}\mu$m^{-1}]	F_λ [erg s^{-1}cm^{-2}Å^{-1}]
980	0.0	1.08×10^{-9}	1.08×10^{-13}	1.08×10^{-10}
390	1.0	4.3×10^{-10}	4.3×10^{-14}	4.3×10^{-11}
155	2.0	1.712×10^{-10}	1.712×10^{-14}	1.712×10^{-11}
61.8	3.0	6.814×10^{-11}	6.814×10^{-15}	6.814×10^{-12}
24.6	4.0	2.713×10^{-11}	2.713×10^{-15}	2.713×10^{-12}
9.8	5.0	1.08×10^{-11}	1.08×10^{-15}	1.08×10^{-12}
3.9	6.0	4.3×10^{-12}	4.3×10^{-16}	4.3×10^{-13}
1.55	7.0	1.712×10^{-12}	1.712×10^{-16}	1.712×10^{-13}
0.618	8.0	6.814×10^{-13}	6.814×10^{-17}	6.814×10^{-14}
0.246	9.0	2.713×10^{-13}	2.713×10^{-17}	2.713×10^{-14}
0.098	10.0	1.08×10^{-13}	1.08×10^{-17}	1.08×10^{-14}
0.039	11.0	4.3×10^{-14}	4.3×10^{-18}	4.3×10^{-15}
0.0155	12.0	1.712×10^{-14}	1.712×10^{-18}	1.712×10^{-15}
0.00618	13.0	6.814×10^{-15}	6.814×10^{-19}	6.814×10^{-16}
0.00246	14.0	2.713×10^{-15}	2.713×10^{-19}	2.713×10^{-16}
9.8×10^{-4}	15.0	1.08×10^{-15}	1.08×10^{-19}	1.08×10^{-16}
3.9×10^{-4}	16.0	4.3×10^{-16}	4.3×10^{-20}	4.3×10^{-17}
1.55×10^{-4}	17.0	1.712×10^{-16}	1.712×10^{-20}	1.712×10^{-17}
6.18×10^{-5}	18.0	6.814×10^{-17}	6.814×10^{-21}	6.814×10^{-18}
2.46×10^{-5}	19.0	2.713×10^{-17}	2.713×10^{-21}	2.713×10^{-18}
9.8×10^{-6}	20.0	1.08×10^{-17}	1.08×10^{-21}	1.08×10^{-18}
3.9×10^{-6}	21.0	4.3×10^{-18}	4.3×10^{-22}	4.3×10^{-19}
1.55×10^{-6}	22.0	1.712×10^{-18}	1.712×10^{-22}	1.712×10^{-19}
6.18×10^{-7}	23.0	6.814×10^{-19}	6.814×10^{-23}	6.814×10^{-20}
2.46×10^{-7}	24.0	2.713×10^{-19}	2.713×10^{-23}	2.713×10^{-20}
9.8×10^{-8}	25.0	1.08×10^{-19}	1.08×10^{-23}	1.08×10^{-20}
3.9×10^{-8}	26.0	4.3×10^{-20}	4.3×10^{-24}	4.3×10^{-21}

Table 12.7: K-band Flux Conversion

F_ν [Jy]	K [mag]	F_λ [Wm^{-2}μm^{-1}]	F_λ [Wcm^{-2}μm^{-1}]	F_λ [erg s^{-1}cm^{-2}Å^{-1}]
620	0.0	3.84×10^{-10}	3.84×10^{-14}	3.84×10^{-11}
247	1.0	1.53×10^{-10}	1.53×10^{-14}	1.53×10^{-11}
98.3	2.0	6.09×10^{-11}	6.09×10^{-15}	6.09×10^{-12}
39.1	3.0	2.43×10^{-11}	2.43×10^{-15}	2.43×10^{-12}
15.6	4.0	9.66×10^{-12}	9.66×10^{-16}	9.66×10^{-13}
6.20	5.0	3.84×10^{-12}	3.84×10^{-16}	3.84×10^{-13}
2.47	6.0	1.53×10^{-12}	1.53×10^{-16}	1.53×10^{-13}
0.983	7.0	6.09×10^{-13}	6.09×10^{-17}	6.09×10^{-14}
0.391	8.0	2.43×10^{-13}	2.43×10^{-17}	2.43×10^{-14}
0.156	9.0	9.66×10^{-14}	9.66×10^{-18}	9.66×10^{-15}
0.0620	10.0	3.84×10^{-14}	3.84×10^{-18}	3.84×10^{-15}
0.0247	11.0	1.53×10^{-14}	1.53×10^{-18}	1.53×10^{-15}
0.00983	12.0	6.09×10^{-15}	6.09×10^{-19}	6.09×10^{-16}
0.00391	13.0	2.43×10^{-15}	2.43×10^{-19}	2.43×10^{-16}
0.00156	14.0	9.66×10^{-16}	9.66×10^{-20}	9.66×10^{-17}
6.20×10^{-4}	15.0	3.84×10^{-16}	3.84×10^{-20}	3.84×10^{-17}
2.47×10^{-4}	16.0	1.53×10^{-16}	1.53×10^{-20}	1.53×10^{-17}
9.83×10^{-5}	17.0	6.09×10^{-17}	6.09×10^{-21}	6.09×10^{-18}
3.91×10^{-5}	18.0	2.43×10^{-17}	2.43×10^{-21}	2.43×10^{-18}
1.56×10^{-5}	19.0	9.66×10^{-18}	9.66×10^{-22}	9.66×10^{-19}
6.20×10^{-6}	20.0	3.84×10^{-18}	3.84×10^{-22}	3.84×10^{-19}
2.47×10^{-6}	21.0	1.53×10^{-18}	1.53×10^{-22}	1.53×10^{-19}
9.83×10^{-7}	22.0	6.09×10^{-19}	6.09×10^{-23}	6.09×10^{-20}
3.91×10^{-7}	23.0	2.43×10^{-19}	2.43×10^{-23}	2.43×10^{-20}
1.56×10^{-7}	24.0	9.66×10^{-20}	9.66×10^{-24}	9.66×10^{-21}
6.20×10^{-8}	25.0	3.84×10^{-20}	3.84×10^{-24}	3.84×10^{-21}
2.47×10^{-8}	26.0	1.53×10^{-20}	1.53×10^{-24}	1.53×10^{-21}

Table 12.8: Surface Brightness Conversion

mag arcsec^{-2}	I-Band		J-Band		H-Band		K-Band	
	Jy arcsec^{-2}	MJy steradian^{-1}	Jy arcsec^{-2}	MJy steradian^{-1}	Jy arcsec^{-2}	MJy steradian^{-1}	Jy arcsec^{-2}	MJy steradian^{-1}
0.0	2250	2.66×10^4	1670	1.97×10^4	980	1.16×10^4	620	7320
1.0	894	1.06×10^4	665	7860	390	4610	247	2930
2.0	356	4210	265	3130	155	1830	98.3	1160
3.0	142	1680	106	1250	61.8	730	39.1	462
4.0	56.4	667	42.0	496	24.6	291	15.6	184
5.0	22.5	266	16.7	197	9.8	116	6.20	732
6.0	8.94	106	6.65	78.6	3.9	46.1	2.47	29.3
7.0	3.56	42.1	2.65	31.3	1.55	18.3	0.983	11.6
8.0	1.42	16.8	1.06	12.5	0.618	7.3	0.391	4.62
9.0	0.564	6.67	0.420	4.96	0.246	2.91	0.156	1.84
10.0	0.225	2.66	0.167	1.97	0.098	1.16	0.0620	0.732
11.0	0.0894	1.06	0.0665	0.786	0.039	0.461	0.0247	0.293
12.0	0.0356	0.421	0.0265	0.313	0.0155	0.183	0.00983	0.116
13.0	0.0142	0.168	0.0106	0.125	0.00618	0.073	0.00391	0.0462
14.0	0.00564	0.0667	0.00420	0.0496	0.00246	0.0291	0.00156	0.0184
15.0	0.00225	0.0266	0.00167	0.0197	9.8×10^{-4}	0.0116	6.20×10^{-4}	0.00732
16.0	8.94×10^{-4}	0.0106	6.65×10^{-4}	0.00786	3.9×10^{-4}	0.00461	2.47×10^{-4}	0.00293
17.0	3.56×10^{-4}	0.00421	2.65×10^{-4}	0.00313	1.55×10^{-4}	0.00183	9.83×10^{-5}	0.00116
18.0	1.42×10^{-4}	0.00168	1.06×10^{-4}	0.00125	6.18×10^{-5}	7.3×10^{-4}	3.91×10^{-5}	4.62×10^{-4}
19.0	5.64×10^{-5}	6.67×10^{-4}	4.20×10^{-5}	4.96×10^{-4}	2.46×10^{-5}	2.91×10^{-4}	1.56×10^{-5}	1.84×10^{-4}
20.0	2.25×10^{-5}	2.66×10^{-4}	1.67×10^{-5}	1.97×10^{-4}	9.8×10^{-6}	1.16×10^{-4}	6.20×10^{-6}	7.32×10^{-5}
21.0	8.94×10^{-6}	1.06×10^{-4}	6.65×10^{-6}	7.86×10^{-5}	3.9×10^{-6}	4.61×10^{-5}	2.47×10^{-6}	2.93×10^{-5}
22.0	3.56×10^{-6}	4.21×10^{-5}	2.65×10^{-6}	3.13×10^{-5}	1.55×10^{-6}	1.83×10^{-5}	9.83×10^{-7}	1.16×10^{-5}
23.0	1.42×10^{-6}	1.68×10^{-5}	1.06×10^{-6}	1.25×10^{-5}	6.18×10^{-7}	7.3×10^{-6}	3.91×10^{-7}	4.62×10^{-6}
24.0	5.64×10^{-7}	6.67×10^{-6}	4.20×10^{-7}	4.96×10^{-6}	2.46×10^{-7}	2.91×10^{-6}	1.56×10^{-7}	1.84×10^{-6}
25.0	2.25×10^{-7}	2.66×10^{-6}	1.67×10^{-7}	1.97×10^{-6}	9.8×10^{-8}	1.16×10^{-6}	6.20×10^{-8}	7.32×10^{-7}
26.0	8.94×10^{-8}	1.06×10^{-6}	6.65×10^{-8}	7.86×10^{-7}	3.9×10^{-8}	4.61×10^{-7}	2.47×10^{-8}	2.93×10^{-7}

Examples

1. Given a source with a flux of 0.9mJy at 1350Å, convert this flux to erg $s^{-1}cm^{-2}Å^{-1}$. From section 3, Table 12.1, we see that the conversion constant β is 3×10^{-13} and the wavelength is 1350Å = 0.135μm. Thus:

$$F_\lambda = 3 \times 10^{-13} \times 9 \times 10^{-4} / 0.135^2 = 1.48 \times 10^{-14} \text{erg s}^{-1}cm^{-2}Å^{-1}$$

2. Given a V magnitude of 15.6, and knowledge that V-K=2.5 in the UKIRT system, estimate the flux in Jy at K. Since V-K=2.5 we know that K=13.1. From Table 12.2, the zero-point flux in the UKIRT system for K is 657Jy. Thus the 2.2μm flux is:

$$F_V = 10^{-13.1/2.5} \times 657 = 3.8 \times 10^{-3} Jy$$

3. Given a surface brightness of 21.1 magnitudes $arcsec^{-2}$ at J, convert this into Jy $arcsec^{-2}$ and into MJy $steradian^{-1}$. Taking the zero-point for the J band from Table 12.2, we determine that the surface brightness is:

$$10^{-21.1/2.5} \times 1670 = 6.06 \times 10^{-6} Jy \; arcsec^{-2}, \text{ or } 6.06 \times 10^{-6}/0.084616 =$$
$$7.17 \times 10^{-5} MJy \; ster^{-1}$$

4. Given a flux at 0.9μm of 2.3×10^{-7}Jy, estimate the l magnitude. 2.3×10^{-7}Jy is less than 2.3×10^{-1}Jy by three powers of a hundred, or 15 magnitudes. From Table 12.3 we see that 0.25Jy is equivalent to an l-band magnitude of 9.89. Thus 2.3×10^{-7} is roughly 15 magnitudes fainter than this, or of order l=24.9.

Infrared Line Lists

We present here lists of some of the more important atomic and molecular lines in the infrared. It is by no means exhaustive.

Table 12.9: Recombination Lines of Atomic Hydrogen: Paschen Series[a]

Transition $(N_u - N_l)$	Vacuum Wavelength (microns)	Vacuum Frequency (cm^{-1})	I/I(Hbeta) $T_e=N_e=10^4$
4-3	1.8756	5531.55	0.332
5-3	1.2822	7799.33	0.162
6-3	1.0941	9139.8	0.0901
7-3	1.0052	9948.1	

a. Intensities from Hummer & Storey, MNRAS 224, 801.

Table 12.10: Recombination Lines of Atomic Hydrogen: Brackett Series

Transition (N_U-N_l)	Vacuum Wavelength (microns)	Frequency (cm^{-1})	I/I(Hβ) T_e=10^4
5-4	4.5225	2467.765	0.0777
6-4	2.6259	3808.25	
7-4	2.1661	4616.61	0.0275
8-4	1.9451	5141.14	0.0181
9-4	1.8181	5500.8	0.0126
10-4	1.7367	5758.1	0.00909
11-4	1.6811	5948.45	0.00679
12-4	1.6412	6093.22	0.00521
13-4	1.6114	6205.9	0.00409
14-4	1.5885	6295.3	0.00327
15-4	1.5705	6367.4	0.00266
16-4	1.5561	6426.4	0.00220
17-4	1.5443	6475.3	0.00184
18-4	1.5346	6516.3	0.00156
19-4	1.5265	6551.0	0.00133
20-4	1.5196	6580.7	0.00116
series limit	1.459	6855.	

Table 12.11: HeI and HeII Lines

ID	Transition	λ(μm)
HeI	7F-3D,3Fo-3D	1.0031
HeI	7F-3D,1Fo-1D	1.0034
HeII	14-6	1.0049
HeII	5-4	1.0133
HeI	6D-3P,3dD-3Po	1.0314
HeII	13-6	1.0422
HeI	6S-3P,3S-3Po	1.0668
HeI	2P-2S,3Po-3S,GU=3	1.0832
HeI	2P-2S,3Po-3P,GU=1	1.0832
HeI	2P-2S,3Po-3S,GU=5	1.0833

Table 12.11: HeI and HeII Lines

ID	Transition	λ(μm)
HeI	2P-2S,3Po-3S,GU=9	1.0833
HeI	6P-3D,1Po-1d	1.0905
HeI	6F-3D,3Fo-3D	1.0916
HeI	6F-3D,1Fo-1D	1.0920
HeII	12-6	1.0938
HeI	6P-3D,3Po-3D	1.0997
HeI	5P-3S,1Po-1S	1.1016
HeI	6D-3P,1D-1Po	1.1048
HeII	7LIMIT	1.1164
HeI	6S-3P,1S-1Po	1.1229
HeII	7-5	1.1628
HeII	11-6	1.1677
HeI	5D-3P,3D-3Po	1.1972
HeII	21-7	1.2256
HeII	22-7	1.2418
HeI	4P-3S,3Po-3S	1.2531
HeII	20-7	1.2719
HeI	5P-3D,1Po-1D	1.2759
HeI	5F-3D,3Fo-3D	1.2789
HeII	10-6	1.2817
HeI	5S-3P,3S-3Po	1.2850
HeII	19-7	1.2914
HeI	5D-3P,1D-1Po	1.2971
HeI	5F-3D,1Fo-1D	1.2976
HeI	5P-3D,3Po-3D	1.2988
HeII	18-7	1.3150
HeI	5S-3P,1S-1Po	1.3415
HeII	17-7	1.3442
HeII	15-7	1.4273
HeII	8LIMIT	1.4578
HeII	9-6	1.4765

Table 12.11: HeI and HeII Lines

ID	Transition	$\lambda(\mu m)$
HeII	14-7	1.4882
HeI	4P-3S,1Po-1S	1.5088
HeII	13-7	1.5719
HeII	25-8	1.6241
HeII	24-8	1.6400
HeII	23-8	1.6584
HeII	22-8	1.6799
HeII	12-7	1.6926
HeI	4D-3P,3D-3Po	1.7007
HeII	21-8	1.7053
HeII	20-8	1.7355
HeII	19-8	1.7717
HeII	18-8	1.8167
HeII	9LIMIT	1.8450
HeI	4P-3D,1Po-1D	1.8561
HeII	6-5	1.8639
HeI	4F-3D,3Fo-3D	1.8691
HeI	4F-3D,1Fo-1d	1.8702
HeII	17-8	1.8725
HeII	8-6	1.8753
HeII	11-7	1.8770
HeI	8S-4P,3S-3Po	1.9068
HeI	4D-3P,1D-1Po	1.9094
HeI	4P-3D,3Po-3D	1.9548
HeII	15-8	2.0379
HeI	6P-4S,3Po-3S	2.0430
HeI	2P-2S,1Po-1S	2.0587
HeI	4S-3P,3S-3Po	2.1126
HeI	3pP-4sS	2.1132
HeI	4S-3P,1S-1Po	2.1138
HeII	25-9	2.1195

Table 12.11: HeI and HeII Lines

ID	Transition	λ (μm)
HeII	24-9	2.1469
HeI	7S-4P,3S-3Po	2.1500
HeI	7F-4D,3Fo-3D	2.1614
HeI	4dD-7fF	2.1617
HeI	7F-4D,1Fo-1D	2.1623
HeII	14-8	2.1653
HeI	4-7	2.166
HeII	23-9	2.1786
HeI	7D-4P,1D-1Po	2.1847
HeII	10-7	2.1891
HeII	22-9	2.2155
HeI	7S-4P,1S-1Po	2.2290
HeII	21-9	2.2601
HeII	10LIMIT	2.2778
HeI	6P-4S,1Po-1S	2.3069
HeII	20-9	2.314
HeII	13-8	2.348
HeII	19-9	2.3788
HeII	18-9	2.4606
HeI	6D-4P,3D-3Po	2.4734

Table 12.12: CO Vibration-rotation Band-heads[a]

	$^{12}C^{16}O$ Vacuum Wavelength (microns)	Frequency (cm^{-1})	$^{13}C^{16}O$ Vacuum Wavelength (microns)	Frequency (cm^{-1})
2-0	2.2935	4360.1	2.3448	4264.7
3-1	2.3227	4305.4	2.3739	4212.4
4-2	2.3535	4250.8	2.4037	4160.3
5-3	2.3829	4196.5	2.4341	4108.3
6-4	2.4142	4142.2	2.4652	4056.4
7-5	2.4461	4088.2	2.4971	4004.7

Table 12.12: CO Vibration-rotation Band-heads[a] (Continued)

	$^{12}C^{16}O$ Vacuum Wavelength (microns)	Frequency (cm^{-1})	$^{13}C^{16}O$ Vacuum Wavelength (microns)	Frequency (cm^{-1})
8-6	2.4787	4034.3		
9-7	2.5122	3980.5		
3-0	1.5582	6417.8		
4-1	1.5780	6337.2		
5-2	1.5982	6257.2		
6-3	1.6187	6177.7		
7-4	1.6397	6098.8		
8-5	1.6610	6020.5		

a. All of the delta v = 2 bandheads occur near J=50.

Table 12.13: Important H_2 Lines[a]

Line Name		Wavel (μm)	Freq (cm^{-1})	g(J)	Eupper (K)	A (10e^{-7}s)	LTE I(line)/I(1-0S(1))			
							1000K	2000K	3000K	4000K
1-0	S(0)	2.2235	4497.41	5	6471	2.53	0.27	0.21	0.19	0.19
1-0	S(1)	2.1218	4712.91	21	6956	3.47	1.00	1.00	1.00	1.00
1-0	S(2)	2.0338	4917.01	9	7584	3.98	0.27	0.37	0.42	0.44
1-0	S(3)	1.9576	5108.40	33	8365	4.21	0.51	1.02	1.29	1.45
1-0	S(4)	1.8920	5282.52	13	9286	4.19	0.082	0.26	0.39	0.47
1-0	S(5)	1.8358	5447.25	45	10341	3.96	0.096	0.52	0.91	1.21
1-0	S(6)	1.7880	5592.9	17	11522	3.54	0.010	0.10	0.21	0.31
1-0	S(7)	1.7480	5720.8	57	12817	2.98	0.008	0.15	0.40	0.65
1-0	S(8)	1.7147	5831.9	21	14221	2.34	0.001	0.022	0.074	0.14
1-0	S(9)	1.6877	5925.1	69	15722	1.68	0.025	0.11	0.22	
1-0	S(10)	1.6665	6000.0	25	17311	1.05	0.003	0.015	0.034	
1-0	S(11)	1.6504	6059.0	81	18979	0.53	0.002	0.014	0.037	
1-0	Q(1)	2.4066	4155.25	9	6149	4.29	1.05	0.70	0.61	0.57
1-0	Q(2)	2.4134	4143.47	5	6471	3.03	0.30	0.23	0.22	0.21
1-0	Q(3)	2.4237	4125.87	21	6956	2.78	0.70	0.70	0.70	0.70
1-0	Q(4)	2.4375	4112.57	9	7586	2.65	0.15	0.21	0.23	0.24

Table 12.13: Important H_2 Lines[a] (Continued)

Line Name		Wavel (μm)	Freq (cm^{-1})	g(J)	Eupper (K)	A (10e^{-7}s)	LTE I(line)/I(1-0S(1))			
							1000K	2000K	3000K	4000K
1-0	Q(5)	2.4548	4073.72	33	8365	2.55	0.24	0.49	0.62	0.70
1-0	Q(6)	2.4756	4039.5	13	9286	2.45	0.036	0.12	0.17	0.21
1-0	Q(7)	2.5001	3999.9	45	10341	2.34	0.042	0.11	0.40	0.53
3-2	S(0)	2.5014	3997.73	5	17387	3.88	0.001	0.007	0.016	
3-2	S(1)	2.3864	4190.33	21	17818	5.14	0.006	0.035	0.087	
3-2	S(2)	2.2870	4372.49	9	18386	5.63	0.002	0.014	0.037	
3-2	S(3)	2.2014	4542.57	33	19086	5.63	0.006	0.043	0.12	
3-2	S(4)	2.1280	4699.32	13	19912	5.22	0.001	0.012	0.036	
3-2	S(5)	2.0656	4841.3	45	20856	4.50	0.003	0.023	0.088	
3-2	S(6)	2.0130	4967.7	17	21911	3.57	0.006	0.021		
3-2	S(7)	1.9692	5078.1	57	23069	2.54	0.001	0.010	0.038	
4-3	S(3)	2.3446	4265.4	21						
4-3	S(4)	2.2668	4411.5	9						
4-3	S(5)	2.201	4543.5	33						
5-4	S(5)	2.3555	4245.4	45						
5-4	S(7)	2.2510	4442.5	57						
2-0	S(0)	1.2383	8075.3	5	12095	1.27	0.001	0.012	0.028	0.043
2-0	S(1)	1.1622	8604.2	21	12550	1.90	0.004	0.061	0.15	0.23
2-0	S(2)	1.1382	8785.5	9	13150	2.38	0.001	0.025	0.070	0.12
2-0	S(3)	1.1175	8948.6	33	13890	2.77	0.002	0.074	0.24	0.43
2-0	S(4)	1.0998	9092.4	13	14764	3.07	0.021	0.078	0.15	
2-0	S(5)	1.0851	9215.5	45	15763	3.28	0.001	0.048	0.21	0.44
2-9	Q(1)	1.2383	8075.3	9	11789	1.94	0.003	0.037	0.082	0.12
2-0	Q(2)	1.2419	8051.9	5	12095	1.38	0.001	0.012	0.029	0.045
2-0	Q(3)	1.2473	8017.2	21	12550	1.29	0.002	0.039	0.098	0.24
2-0	Q(4)	1.2545	7971.1	9	13150	1.27	0.001	0.012	0.033	0.056
2-0	Q(5)	1.2636	7913.3	33	13890	1.23	0.001	0.024	0.093	0.17
2-0	O(2)	1.2932	7732.6	1	11635	3.47	0.001	0.008	0.016	0.024
2-0	O(3)	1.3354	7488.3	9	11789	1.61	0.003	0.028	0.063	0.094
2-0	O(4)	1.3817	7237.5	5	12095	1.03	0.001	0.008	0.020	0.030

Table 12.13: Important H$_2$ Lines[a] (Continued)

Line Name		Wavel (µm)	Freq (cm^{-1})	g(J)	Eupper (K)	A (10e^{-7}s)	LTE I(line)/I(1-0S(1))			
							1000K	2000K	3000K	4000K
2-0	O(5)	1.4322	6982.5	21	12550	0.698	0.001	0.018	0.046	0.074

a. Energy levels calculated using Dabrowski & Herzberg, Can J Phys 62, 1639 (1984). Einstein coefficients from Turner et al. ApJ Suppl 35, 281 (1977).

PART 4

Calibration

The chapters in this part describe the calibration of NICMOS. These chapters include an overview of the calibration pipeline process; the expected accuracies for data taken in Cycle 7; and the present plans for calibrating and verifying the instrument's performance.

Calibration Pipeline

This chapter describes the pipeline calibration system developed at STScI. This system provides observers with NICMOS data after various instrumental signatures are removed, conversions to flux units are performed, and patterns of exposures are combined. Several enhancements to the HST ground system have been made to support NICMOS, including the concept of associations of datasets and an improved file format for data storage and distribution. A detailed description of the analysis of HST data in general and NICMOS data in particular will be found in the next release of the *HST Data Handbook*.

Overview and New Features

All data taken with NICMOS are automatically processed and calibrated by a suite of software programs known as the *pipeline*. The purpose of pipeline processing is to provide data products to observers and the HST Data Archive in a form suitable for most scientific analyses. Pipeline processing is also applied to engineering data, calibration data, and calibration software.

The basic sequence of steps in the STScI pipeline system (also known as OPUS) is:

1. Assemble data received from HST into datasets.

2. Perform a standard level of calibration of the science data.

3. Store both the uncalibrated and calibrated datasets in the Archive and populate the Archive database catalog to support StarView queries.

The pipeline must also handle exceptions (e.g., incomplete data) and perform a general data evaluation and quality control step. Final delivery of data to

observers is accomplished by the data distribution mechanisms of the Archive system.

The calibration step has several goals:

- Remove the known instrumental signatures (e.g., flat field and dark current).

- Correct linear and physical units (e.g., gain and flux calibration).

- Flag degraded or suspect data values and provide estimates of the statistical uncertainties of each pixel.

While a calibration pipeline may not be able to provide the optimal calibration for a specific observation (which may, in fact, not become available until some time after the data were obtained and calibrated), the goal is to provide data calibrated to a level suitable for initial evaluation and analysis for all users. Further, observers frequently require a detailed understanding of the calibrations applied to their data and the ability to repeat, often with improved calibration products, the calibration process at their home institution. To support this last goal, the calibration software is available within the STSDAS system and the calibration reference files (e.g., flat fields) are available from the HST Archive via StarView.

Associations

To improve the utility of the pipeline processing for the second generation science instruments—NICMOS and STIS—several significant changes have been make to the structure of the calibration pipeline. The largest of these changes has been to enable the combination of multiple observations during the calibration process. This permits the pipeline to both generate a combined product and to use calibrations obtained contemporaneously with the science observations. This capability is designed to support the cosmic ray event removal, mosaicing, and background subtraction for NICMOS observations. As discussed in Chapter 10, mechanisms exist for compactly requesting such observations in the Phase II proposal.

Concept

The basic element in the HST ground system has historically been the *exposure*. The first generation HST science instruments are commanded to generate single exposures, which result from a recognizably distinct sequence of commands to the instrument. This creates a flow of data which is assembled into a single *dataset*. Each dataset is given a unique 9 character identifier (an *IPPPSSOOT* in STScI terminology) and is processed by the pipeline, calibrated, and archived separately from all other datasets.

An illustrative (partial) counter example to this procedure is the WFPC2 CRSPLIT proposal instruction. This results in two WFPC2 exposures from a single line on the exposure logsheet (the way in which observers specify commands for HST). However, the HST ground system treats a CRSPLIT as two distinct exposures which are commanded, processed, calibrated, and archived

separately. The pipeline does not combine these two images (datasets) to create the single image without cosmic ray events *which was the observer's original intention*. Presently, the observers (and any future archival researchers) are left to perform this task on their own.

The second generation instruments present many instances in which the combination of data from two or more exposures is necessary to create a scientifically useful data product. Both NICMOS and STIS will need to combine exposures to remove cosmic rays and to improve flat fielding (by dithering or *stepping*). For NICMOS, the HST thermal background is expected to have significant temporal variations. Multiple exposures (dithered for small targets and offset onto blank sky—chopped—for larger targets) will be necessary to measure and remove this background. While this has been standard practice for ground based infrared observations and is the basis of essentially all existing infrared data reduction schemes, it is a new paradigm for the HST ground system.

Usage

Associations exist to simplify the use of HST data by observers. This starts from the proposal phase, continues with a more complete calibration process than would be possible without associations, carries into the archiving and retrieval of associated data, and includes the use of HST data by observers within the STSDAS system.

An association is a set of one or more exposures along with an association table and, optionally, one or more products. We define the following terms:

- An *exposure* is the atomic unit of HST data.

- A *dataset* is a collection of files having a common rootname (first 9 characters).

- A *product* is a dataset derived from one or more exposures.

The first generation instruments all have a one-to-one correspondence between exposures and datasets. They do not have products. NICMOS and STIS use the association structure as a meta-dataset. Further, they use the information in multiple exposures during the calibration process to create products.

From a high level, an association is a means of identifying a set of exposures as belonging together and being, in some sense, dependent upon one another. The association concept permits these exposures to be calibrated, archived, retrieved, and reprocessed (within OPUS or STSDAS) as a set rather than as individual objects. In one sense, this is a book-keeping operation which is being transferred from the observer to the HST data pipeline and archive.

Associations are defined by optional parameters on a single exposure logsheet line. That is, there is a one-to-one correspondence between proposal logsheet lines and associations (although it is possible to have exposures which are not in associations).

Observers may obtain one or more exposures at each of one or more positions on the sky using the NICMOS proposal grammar. Typically usage will be:

- To obtain a sequence of slightly offset exposures (dithering) to improve the flat fielding, avoid bad pixels and cosmic rays, and, for sufficiently compact targets, to remove the background illumination.

- Mapping of targets larger than the NICMOS detector's field of view.

- To obtain a sequence of observations in which the telescope is chopped between the target and one or more offset regions of (hopefully blank) sky.

A set of pre-defined patterns are provided in the proposal instructions for these types of observations or a combination of both types. The Institute ground system will expand the observer's single line request into multiple exposures each with its own identifying name (1PPPSSOOT) and populate the necessary database relations to describe this association for the OPUS system.

Re-engineering

For the second generation science instruments several other modifications to the pipeline system have been made. The format of the data products from the pipeline has been changed from the GEIS (Generic Edited Information Set) files used previously to FITS (Flexible Image Transport System) files with image extensions. The IRAF/STSDAS system has been modified to operate directly on these files. Each NICMOS image is expressed as a set of five image extensions representing the image, its variance, a bit encoded data quality map, the number of valid samples at each pixel, and the integration time at each pixel. This structure is used at all stages of the calibration process which permits the re-execution of selected elements of the pipeline without starting from the initial point. Third, the calibration code itself is now written in the C programing language (rather than IRAF's SPP language). An interface between the data files and a set of NICMOS specific data structures (called HSTIO) has also been written. These changes should greatly simplify the modification of the pipeline code by users and the development of new NICMOS specific data processing tasks.

NICMOS Pipeline

The NICMOS calibration task is divided into two stages: **calnica**, which is used for every individual exposure, and **calnicb**, which is used after **calnica** on those exposures which comprise an association.

Static Calibrations—calnica

The first calibration stage, **calnica**, (Figure 13.1) performs those calibrations which can be done to a single exposure using the configuration information from its telemetry and the Calibration Data Base. The calibrations used in this stage are obtained from the Calibration Data Base. Such calibrations are derived from the calibration program (see Chapter 15) and typically change on time scales of

months. This is analogous to the WFPC2 calibration process (**calwp2**). **Calnica** performs the following steps:

- Flag known bad pixels in the data quality array.

- Calculate a noise model for each pixel.

- Subtract the bias level.

- Correct for non-linearity.

- Scale (when necessary) and subtract the dark image.

- Flat field to bring each pixel to a common gain.

- Convert the image data to count rate units.

- Calculate various image statistics (e.g., median).

- Store the photometric calibration in image header keywords.

- Correct for cosmic ray events and pixel saturation (in MULTIACCUM data).

- Calculate estimates of the background.

- Analyze the internal engineering telemetry for potential problems with the observation.

Figure 13.1: Conceptual calnica Pipeline
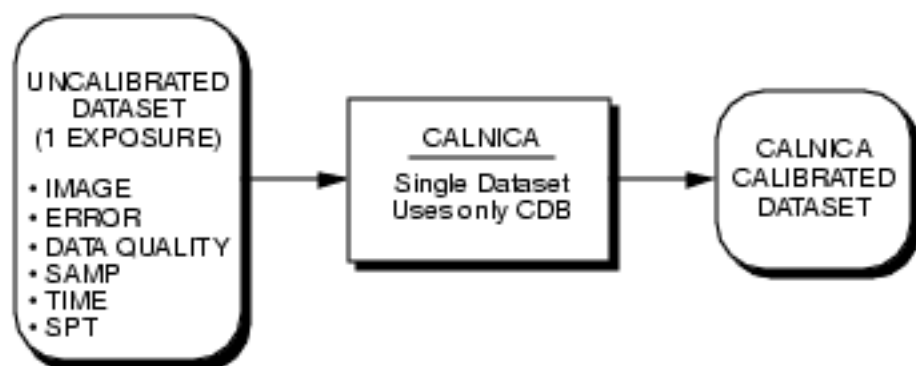
Observers will be given both the uncalibrated (raw) data and the processed data for each exposure. For MULTIACCUM observations, partially calibrated data for each readout will be generated (which excludes the cosmic ray and saturation corrections) in addition to a final single image.

To recalibrate NICMOS data, you will need the **calnica** software (soon to be included in the STSDAS distribution) and the necessary calibration reference files (available from the HST Data Archive using StarView).

The data processing flow chart for normal imaging and spectroscopic images is shown in Figure 13.2.

Figure 13.2: Calibration Steps of the calnica Pipeline

Input Files	Processing Steps	Keyword Switches	Calibrated Output Files

Raw Science Images RAW, SPT

Subtract ADC Bias Level — BIASCORR

Subtract M-ACCUM Zero-Read — ZOFFCORR

MASKFILE → Mask Bad Pixels — MASKCORR

NOISFILE → Compute Statistical Errors — NOISCALC

NLINFILE → Linearity Correction — NLINCORR

DARKFILE → Dark Current Subtraction — DARKCORR

FLATFILE → Flat Field Correction — FLATCORR

Convert to Count Rates — UNITCORR

PHOTTAB → Photometric Calibration — PHOTCORR

Cosmic Ray Identification — CRIDCALC

IMA

BACKTAB → Predict Background — BACKCALC

User Warnings

CAL

Contemporaneous Observations—calnicb

While previously it has been possible to execute multiple exposures from a single proposal logsheet line (e.g., WFPC2, CR-SPLIT, and NEXP=*n* constructs), this capability has been significantly expanded to support new requirements of the second generation science instruments. Typical examples include the removal of cosmic rays, the construction of a mosaic image, and the subtraction of the sky background from a sequence of on-target and off-target observations. These observations are distinguished by the fact that their calibration and processing depends upon other observations obtained *at the same time*.

The **calnicb** part of the pipeline carries out the calibration and merging of associated data frames, each of which has first been processed by **calnica**. In the case shown in Figure 13.3, the associated set has 3 individual datasets that are combined into one merged and calibrated dataset.

Figure 13.3: Conceptual calnicb Pipeline
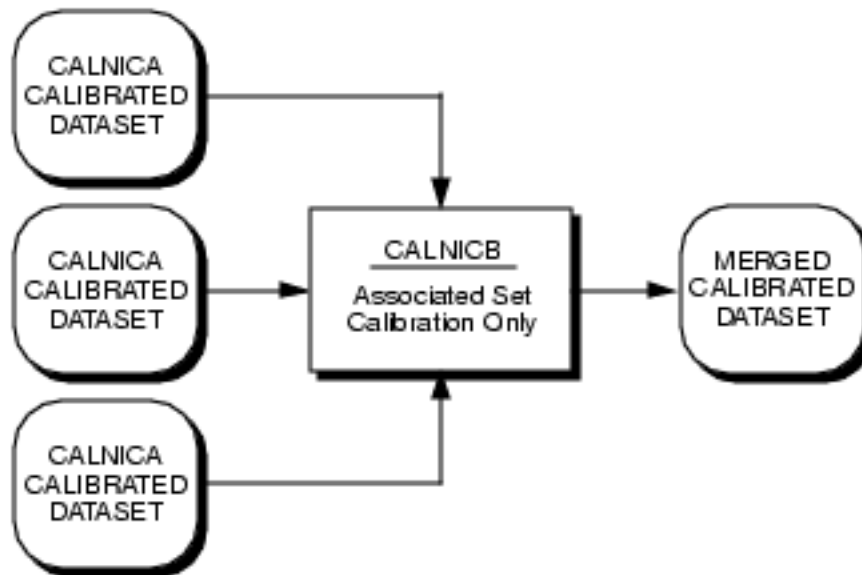
We refer to these sets of exposures as associations. The **calnicb** task operates on an entire association, and produces one or more products from that set (Figure 13.3). In the case of dither patterns, **calnicb** reads from the headers of the individual exposure files what the telescope offsets were. It then identifies sources in the images, and, starting with the telescope pointing information from the headers as an initial guess, determines what the pointings actually were. It then combines the images into a final mosaic, rejecting from the output any Cosmic Rays that had not been detected in the individual exposures when they were processed by calnica. The **calnicb** code uses all the data quality information generated by calnica to avoid propagating identified Cosmic Rays, bad pixels, or saturated pixels, into the output mosaic. In the case of chopped images, if multiple images were obtained at each chop position, calnicb generates a mosaic for each background position and outputs each of those; it then combines each of the

background images to generate a background for the target position, and removes this background from the mosaic it has generated for the target position, and then outputs the result of this operation as the final, background subtracted mosaiced image of the target. When **calnicb** is calculating the offsets between images, it starts with the telescope pointing information as its first guess. If it is unable to match the various images by adjusting this pointing information by more than some limit, the code reverts to using the pointing information alone, on the assumption that there are no sources bright enough to detect in the individual images, or that there are instrumental artifacts which are confusing the offset calculation, or that the telescope suffered a loss of guide star lock during one or more of the exposures resulting in a potentially very large offset being introduced. To date, we have found that all of these things happen very rarely indeed.

NICMOS Data Products

Standard NICMOS Dataset Structure

NICMOS data are represented by five arrays for each readout. These arrays contain the:

- Science image.

- Error array.

- Quality flags array.

- Samples array.

- Integration time array.

Each downlinked readout is always represented by these five arrays (Figure 13.4). Multiple readouts in the same dataset (e.g., MULTIACCUM data) are represented by repeated sets of these five arrays (Figure 13.5). It is expected that compact FITS representations will be available to store arrays in which all elements have the same value.

In the basic NICMOS data format, shown in Figure 13.4, each readout is represented by 5 arrays, each as a separate extension in the FITS container file. Any of the five arrays may be accessed by specifying its extension number: for example to access the data quality flags, specify the third extension.

Figure 13.4: Data Format for ACCUM, RAMP, BRIGHTOBJ and ACQ Modes
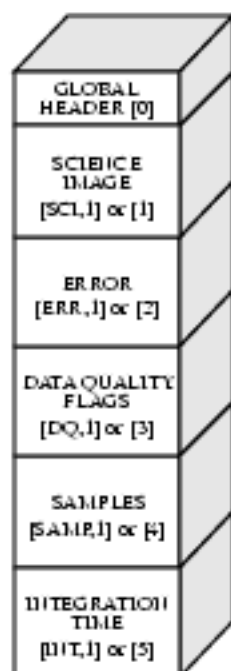
Science Image

The science image contains the information recorded by the NICMOS camera. The data may be represented as counts (i.e., data numbers) or as count rates (i.e., data numbers per second). Generally the latter is desirable since it is easier to interpret in mosaiced datasets and corresponds closely to flux.

Error Array

The error array contains an estimate of the statistics error at each pixel. It is expressed as a real number of standard deviations. This is a calculated quantity based on a model of the instrument and its environment.

Quality Flags Array

The quality flags array provides 16 independent flags for each pixel. Each flag has a true (set) or false (unset) state and is encoded as a bit in a 16 bit (short integer) word. Users are advised that this word should *not* be interpreted as an integer.

Samples Array

The samples array is used for one of two purposes:

- For data where multiple samples of the array were obtained during the integration, the samples array denotes the number of samples for each pixel in the corresponding science image.

- When multiple integrations are combined to produce a single image, the samples array will contain the number of samples retained at each pixel. Note that this implies that the original number of samples information is not propagated forward into combined images.

Integration Time Array

The integration time array contains the total integration time at each pixel. While initially a simple parameter in some observing modes, combining datasets into composite mosaics and using the information obtained by multiple non-destructive readouts during an integration requires us to keep track of the actual exposure time for each pixel. This array is useful for simple conversions between counts and count rates.

The MULTIACCUM mode (Figure 13.5) produces multiple images. The file structure for such a dataset consists of a lattice of the 5 image arrays which are created for each readout, as shown in Figure 13.5.

Figure 13.5: MULTIACCUM Data Format
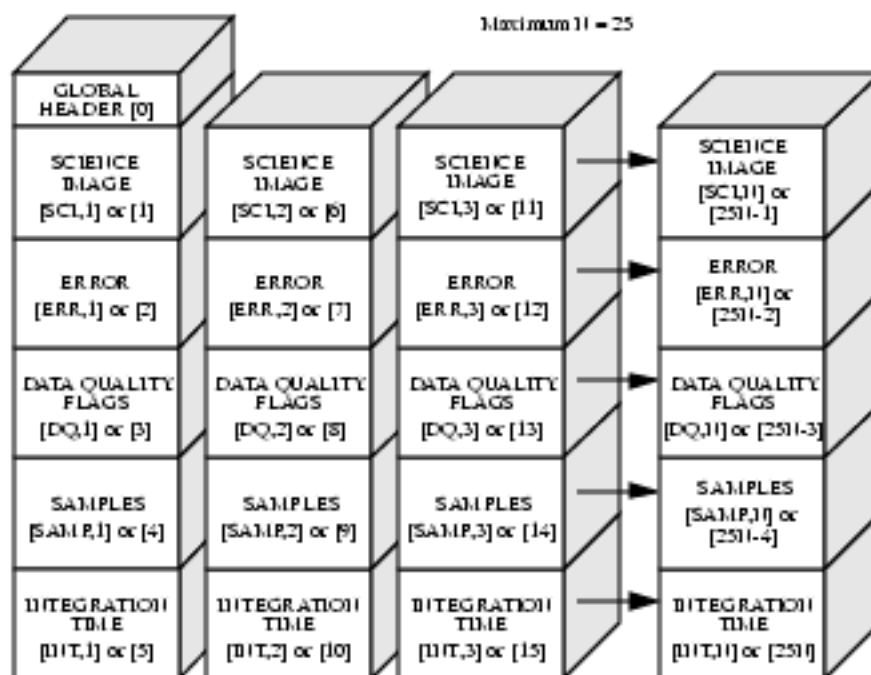
IRAF Access

Backwards Compatibility

This data structure will be implemented so that the *default* array is the most meaningful science image array. For example, if you request IRAF to display a dataset, the first science image array would be displayed. Access to the other arrays within a dataset will be via element numbers (1–5; mod 5 for datasets containing multiple readouts) or via a standardized naming convention (see Figure

13.4 and Figure 13.5). It is a critical requirement that existing IRAF tasks be able to access any array in a NICMOS dataset.

FITS File Format

The physical format of NICMOS datasets will be FITS with image extensions. Data will both be delivered to observers and used within IRAF and STSDAS in this format. A modified version of the IRAF kernel has been developed at STScI to support this data format directly. This permits the use of NICMOS data without conversion (i.e., the **strfits** task is not necessary). This will be distributed with the STSDAS system before Cycle 7.

CHAPTER 14

Expected Calibration Accuracies

This chapter describes the expected accuracies which should be reached in the calibration of NICMOS during Cycle 7 and Cycle 7-NICMOS.

Expected Accuracies

Remarks

In Table 14.1 we list a provisional summary of our calibration goals for Cycle 7 and Cycle 7-NICMOS. These goals will be achieved through the analysis of data obtained both from the ground testing, on-orbit during the Servicing Mission Orbital Verification (SMOV) phase, and the Cycle 7 calibration program (see Chapter 15). Observers may, and should, plan on NICMOS achieving these levels of performance. While higher levels of performance may indeed by possible (and even achieved) in Cycle 7, observers should not depend upon NICMOS being calibrated better than defined here. Science programs which require superior calibrations should request and justify additional observing time to reach the necessary calibration accuracy.

Areas of Significant Uncertainty

The present knowledge of photometric calibration does not yet permit a definitive projection of the ultimate accuracies which may be obtainable with

NICMOS. We have adopted fairly conservative estimates for the achievable photometric (and, consequently, polarimetric) accuracies. Areas of uncertainty include the quality of the transformations, the long term stability of NICMOS, and (for a small portion of each Camera's field of view) the effects of vignetting.

Perforce our existing calibration data for Camera 3 have been obtained with it out of focus and therefore the estimates for its in-focus performance remain extrapolations.

The astrometric performance of NICMOS is not yet well understood. There appears to be continuing motions occurring within the dewar and the optical bench holding the detectors (which is located inside of the dewar). Additional data may become available as part of the August 1, 1997 STScI NICMOS WWW update on the coronographs performance.

Provisional Cycle 7 Calibration Goals

Table 14.1: Summary of Cycle 7 Calibration Goals

Attribute	Accuracy	Limiting Factor/Notes
Detector dark current and shading	<10 DN	All MULTIACCUM sequences will have good calibrations. A small subset of the available ACCUM mode exposure times will have a direct calibration.
Flat fields	1% (Cameras 1,2) 2% Camera 3	Color dependence may limit flats in some cases. The low spatial frequency may only be reliable to ≤ 3%.
Photometry	5-10% photometric zero point 2% relative over FOV 2% stability	Photometric systems Intrapixel effects Filter leaks on red sources
PSF and focus	Maintained within 1 mm	Breathing and dewar motion are approximately equal effects.
Coronographic PSF	.019 arcsec positioning	Hole and detector are not at a common focus
Polarization	~1% relative intensity 3-5% polarization accuracy	Photometric performance Ghosts/polarizing efficiency
GRISM wavelength calibration	.01 μm	Limited by centroiding of target for wavelength zero point determination.
GRISM photometric calibration	20–30% absolute and relative	Expected accuracy over central 80% of spectral range. Grism C flat field may not achieve this performance.
Astrometry	0.2% plate scale 0.1" to FGS frame	Uncertain due to continued focal plane motions

Calibration Plans

This Chapter describes the current state of the NICMOS calibration performed during SLTV, SMOV, and that planned for Cycle 7.

Introduction

The calibrations available during Cycle 7 and Cycle 7-NICMOS will be based on three distinct calibration activities. First, NICMOS has been extensively tested on the ground. These tests included a limited amount of calibration, particularly during the System Level Thermal Vacuum (SLTV) testing. Second, we are presently completing a period following the installation of NICMOS into HST for testing and initial calibration. This activity is known as the Servicing Mission Observatory Verification (SMOV). Finally, the routine Cycle 7 calibration program is now getting underway.

It is important to distinguish between the various goals of these calibration activities. SLTV was intended to demonstrate the proper functioning of the Scientific Instrument (SI) and to obtain, to the extent possible, an initial calibration of a subset of its capabilities. SMOV is intended to demonstrate that the instrument is functioning as expected, based on the SLTV experience, to characterize those parameters not measurable during SLTV (e.g., the thermal background generated by the HST optics), to establish necessary operation parameters (e.g. plate scale), and to begin the calibration of NICMOS. In many cases the complete calibration will be conducted during Cycle 7 with SMOV being used to demonstrate that the planned calibrations are in fact feasible. This

approach is designed to enable the acquisition of science observations at the earliest possible date, even if the best possible calibrations do not become available until some time later. This contributes to the efficiency with which HST can be operated and maximizes the total number of NICMOS observations over its cryogen limited lifetime.

Thermal Vacuum Test

The NICMOS System Level Thermal Vacuum test program (SLTV) was conducted at Ball Aerospace in three stages between June and December 1996. The primary purpose of this activity was the validation of the operation of the assembled instrument in an environment nearly identical to HST's. This included testing the thermal performance of the instrument, demonstrating proper operation of all commandable operating modes, exercising all mechanisms, and testing safing procedures. It also included characterization of the detector performance (e.g., read noise and dark current). Of particular importance to the overall calibration program, flat fields using the flight optics and detectors were obtained in each filter.

Enough calibrations were obtained from SLTV to provide a partial load of the Calibration Data Base at STScI. These calibrations are available to users (via the HST Data Archive) and are used by STScI in the routine data processing calibration pipeline. Clearly, some of these calibrations will require updating from on-orbit observations before they are of much scientific utility (e.g., the photometric zero points).

The existance of the dewar anomoly described in Chapter 3 was a major factor in the conduct of the SLTV program. Both validation of the extended range PAM mechanism and efforts to limit the stresses within the dewar were accomplished.

Servicing Mission Observatory Verification

The baseline SMOV plan for NICMOS consisted of the 22 activities as listed in Table 15.1. Some of these (e.g., 1 through 6) test specific components of the instruments while others characterize its performance within the HST environment (e.g., 7, 8, 17, and 22). Activities 12 and 13 align the NICMOS fore-optics; activities 9, 10, 11, and 21 enable the use of the coronograph in Camera 2; activities 15 and 20 characterize the detectors; and activities 18 and 19 establish the initial photometric calibration.

Tests to agressively monitor focus and to explore the trade off between performing coronographic observations with the NIC2 detector or the coronographic hole (on the field divider) in focus were added during SMOV. Further, a number of Early Release Observations of scientifically interesting targets were obtained to communicate the capabilities of NICMOS to the

astronomical community and the public. These observations are (or, in the case of some EROs will soon be) in the public domain and can be easily located in the HST archive under the starview "general" screen field "Proposal Type" equal to "SM2/NIC".

Cycle 7 Calibration Program

As a consequence of the NIC3 defocus, the Cycle 7 calibration plan at the time this handbook is being written, contains mainly the calibration of the NIC1 and NIC2 cameras and will execute a limited calibration program for NIC3. A summary of the calibration programs included in the Cycle 7 calibration plan is found in Table 15.2.

The Cycle 7 calibration plan consists of routine monitoring and special calibration programs as well as of contingency calibration programs that will be executed only in the event the cameras show large physical displacements. NIC3 specific calibration programs are also included in the calibration plan. These programs will be executed when scientific observations with NIC3 are enabled.

A revision of this calibration plan will be undertaken by the end of the 1997, after we gain experience during the first 5-6 months of Cycle 7 and after the evolution of NICMOS is better known. A postscript version of the report fully describing NICMOS calibration activities for Cycle 7 is available on the NICMOS WEB page:

`http://www.stsci.edu/ftp/instrument_news/NICMOS/nicmos_doc.html`

The calibration programs may each be examined by using the ID number and the HST Program and Schedule Information Page:

`http://presto.stsci.edu/public/propinfo.html`

.

Table 15.1: Planned NICMOS SMOV Activities

Activity	Title	Demonstrates or Calibrates
1	NICMOS to Hold Mode	Basic operation of computer and HST interfaces.
2	NICMOS Internal Parallel Test	Demonstrate absence of interference due to parallel operation of camera and filter wheels.
3	NICMOS Memory Load and Dump Test	Test memory and code in internal computer.
4	NICMOS Field Offset Mechanism Test	Test and characterize operation and optical performance of the Field Offset Mirror.
5	NICMOS Filter Wheel Mechanisms Test	Verify operation and correct location of each position on each filter wheel.
6	NICMOS SAA Contour Test	Characterize effects of radiation on NICMOS electronics and detector performance; determine optimal SAA limits.
7	NICMOS Dewar Heaters Setpoint Adjustment	Establish optimal external dewar temperature.
8	NICMOS Transfer Function Test	Set optimal detector DC offset voltages.
9	NICMOS Target Acquisition Test	Demonstrate Mode 2 (autonomous) acquisitions.
10	NICMOS to FGS Astrometric Calibration	Establish the locations of the NICMOS detectors within the FGS coordinate system.
11	NICMOS Plate Scale and Astrometric Calibration	Determine plate scales, relative field rotations, and field distortions for each camera.
12	NICMOS Coarse Optical Alignment	Initial focus and tip/tilt adjustment of the Pupil alignment mirror based on modeled images.
13	NICMOS Fine Optical Alignment	Optimal positioning of the PAM based on grid of small PAM motions.
14	NICMOS Point Spread Function Characterization	Characterization of the imaging performance of NICMOS and initial set of PSF observations.
15	NICMOS Persistence Test	Characterize the effect of severe overexposure of the NICMOS detectors.
16	NICMOS Intflat Transfer and Stability Test	Demonstration of flat fielding capability and stability monitoring. Bootstrap of SLTV flat fields.
17	NICMOS HST Thermal Background Test	Characterization of HST generated thermal background over a broad range of situations.
18	NICMOS Absolute Photometry Test	Standard star observations across NICMOS wavelength range. Updates SLTV throughput calibration.
19	NICMOS Differential Photometry Test	Inter-camera photometric precision and stability test obtained from observations of a star at 25 positions.
20	NICMOS Detector Noise and Dark Characterization	Characterization of detector noise and dark current. Verification of stability since SLTV.
21	Coronograph Verification	Optical characterization of coronographic stray light rejection and PSF of the obscured star.
22	Limb Avoidance Determination	Determination of the appropriate bright and dark earth limb angle restrictions for normal and low-background NICMOS observations.

Table 15.2: NICMOS Cycle 7 Calibration Plan

ID	Proposal Title	Frequency	Execution	Estimated Time (orbits)		Accuracy	Comments
				"External"	"Internal"		
	Routine Monitoring Programs						
7703-10/7596	MULTIACCUM Darks	1 1-4 weeks	Jan. 97		186	10 DN	Data in all three cameras
7689/7775	Earth Flats	continuous			540	2%	NIC1&2; NIC3 reduced program
7690	Internal Lamp Flats	1-4 weeks		44		1%	NIC1&2
7607	Photometric Monitoring	1-4 weeks		40		2%	NIC1&2; NIC3 reduced program
7608	Focus Monitoring	2-4 weeks		114		1 mm	Data and analysis for NIC1&2&3
	Special Calibration Programs						
7688	ACCUM Darks	1	Sept. 97		33	10 ADU	Data in all three cameras
7691	Photometric Zero Point	1	Aug. 97	12	2	5-10%	NIC1&2
7692	Polarizers	1	Sept. 97	12	2	1%	NIC1&2
7693	Pupil Transfer Function	1	Sept. 97	15		1%	NIC1&2; NIC3 on hold
7611	Thermal Background	1+(cont.)	Jun.-Jul. 97		20+(80)	n/a	Data and analysis for NIC2&3
	Contingency Calibration Programs						
7609	NICMOS to FGS Astrometry	TBD	TBD	1xTBD		0.1"	On hold; data in three cameras
7610	Plate Scale Calibration	TBD	TBD	4xTBD		0.2%	On hold; data in three cameras
7694	Coronograph Stability Verification	1	TBD	4		n/a	On hold until further notice
	NIC3 Specific Calibration Programs						
7695	GRISM Wavelength Calibration	1	TBD	3		0.01 μm	On hold until further notice
7696	GRISM Absolute Sensitivity	1	TBD	6		20-30%	On hold until further notice
	TOTAL TIME (including all executions)			250+5xTBD	821+(80)		

Detector Performance

All three detectors will be characterized to the same extent. High quality darks will be obtained for all requested MULTIACCUM sequences during June and early July 1997 (proposals ID 7703 to 7710). Changes in the detectors performance will be monitored with a monthly periodicity (proposal ID 7596). Darks will also be obtained for a limited subset of ACCUM exposure times (proposal ID 7688). Other ACCUM exposure times will require interpolated dark current subtraction that may be less satisfactory.

Flat Fields

High quality internal lamp flat-fields for all NIC1 and NIC2 polarizers, broad- and medium-band filters will be obtained in July 1997 (proposal ID 7690). The temporal evolution of the pixel-to-pixel response as a function of camera and wavelength will be monitored once a month using a subset of NIC1 and NIC2 filters. No data will be taken for NIC3 filters until the camera is back into PAM focus range, or close enough to enable NIC3 science observations.

Earth flat-fields will be obtained throughout the Cycle 7 for the complete set of NIC1 and NIC2 narrow-band filters as well as for a few NIC3 filters (proposal IDs 7689 and 7775). Data in a few medium-band filters will also be obtained to characterize the OTA illumination patterns.

Additional measurements aimed at the detection and modelling of any spurious large scale structure in the flat-fields will be obtained (proposal ID 7693). Since flat-fields will be obtained by illuminating the detectors with a bright diffuse source (i.e., internal lamps or Earth), these spurious structures could be introduced by the possible leaks of NICMOS cold mask when illuminated by these diffuse sources.

Photometry

A preliminary photometric calibration of NICMOS filters, based on a limited set of observations, has been achieved during SMOV. Photometric observations of standard stars will be obtained in all NIC1 and NIC2 filters as part of the Cycle 7 calibration plan (proposal ID 7691). Images of two HST absolute standards, one white dwarf (G191-B2B) and one solar analog (P330E) will be obtained as part of this program. The spectral and photometric characteristcis of G191-B2B and P330E are fully described in Bohlin, Colina & Finley (1995) and in Colina & Bohlin (1997), respectively. In addition, images of a bright red star (OPH-S1) will be obtained to measure possible red-leaks in the filters, in particular the narrow filters at the short wavelength range of NICMOS.

We plan to observe a small number of very red stars (final targets to be determined) as part of this calibration program. These data will be installed in the Archive and made public immediately after the observations are executed, to enable the users to do photometric transformations between the HST system and any other photometric system.

The photometric stability of NIC1 and NIC2 cameras as a function of time and wavelength will be monitored once a month with observations of a standard star in a subset of filters covering the entire wavelength range of NICMOS (proposal ID 7607). The photometric stability of NIC3 camera will be monitored with observations in the filters F110W and F160W.

Thermal Background

The absolute level and stability of the thermal background as seen by the NICMOS cameras has already been measured as part of the SMOV program. The Cycle 7 calibration program will extend the SMOV program with images obtained in NIC2/F237M and NIC3/F222M filters (proposal ID 7611). Images will be taken during June and July 1997 as pointed parallel observations to map possible changes in the thermal backgorund as a result of temperature changes in HST optics. An extended program is on hold and would only be executed if additional measurements are required to fully characterize the stability of the thermal background.

Polarizers

The instrumental polarization and zero position angle of NIC1 and NIC2 polarizers will be measured by taking images of two bright near-infrared polarized standards HDE283812 and CHA-DC-F7. The photometric and polarization characteristics of these two standards are found in Whittet et al. (1992). Changes in the polarization as a function of position within the chip will also be measured by moving one of the polarized targets in a spiral pattern across the chip. Additional images of the HST unpolarized standards HD64299 and BD+32d3739 will also be taken. The photometric and polarization properties of these two standards are found in Turnshek et al. (1990).

No characterization of the polarizers has been done during SMOV but high intrinsic precision (accuracy ~ 1%) polarimetric measurements should be possible with NICMOS. However, uncertainties in the darks and flat-fielding could degrade the performance of the polarizers and reduce the level of accuracy mentioned above.

Grisms

The wavelength calibration and absolute sensitivity of the grisms will be measured once NIC3 science observations are enabled. The wavelength dispersion solutions for each grism will be obtained by observing a compact planetary nebula (proposal ID 7695). Changes in the dispersion solution as a function of location in the detector will also be measured by taking spectra of the planetary nebula at four different positions within the chip, i.e., one per quadrant.

Spectra of the HST absolute standards G191-B2B (white dwarf) and P330E (solar analog) will be obtained to establish the absolute sensitivity of the three grisms (proposal ID 7696).

Coronograph

The ability to position a star behind the coronographic mask will be enabled during SMOV. The PSF within the coronograph will also be characterized during SMOV. A contingency program designed to measure the stability of the coronograph performance will be executed as part of the cycle 7 calibration plan if large physical motions in the NIC2 camera are detected (proposal ID 7694). This program focuses on measuring the possible change in the scattering and diffracted energy rejection patterns as a function of target decentration in the mask.

At present there is sufficient motion of the projected position of the coronographic hole onto the NIC2 detector that an automatic hole location task is being developed for the NICMOS on-board flight software. This is expected to be available for Cycle 7-NICMOS observations.

As mentioned previously, an update on the SMOV results for coronography will become available on the STScI NICMOS WWW on 1 August 1997.

Point Spread Function

No calibration program specifically designed to measure the point spread function of the three cameras will be executed as part of the Cycle 7 calibration plan. Observers requiring PSFs in specific filters and/or locations within the field of view are advised to include these in their own program. NICMOS PSFs can however be modeled quite well using Tiny Tim V4.3.

Focus Monitoring

Since the NICMOS camera focii will continue to change as cryogen vents, the focus of all three cameras will be monitored throughout the entire Cycle 7 (prop ID 7608). During the first few months, focus measurements will be obtained every other week with the three cameras. The frequency of the monitoring will be decreased to once a month, after the first few months. The focus and physical motion of the cameras will be measured using phase retrieval, encircled energy and plate scale techniques. Updates to best focus positions will most likely occur a few times during Cycle 7. Information regarding these focus updates will be posted on the NICMOS focus Web page.

Photometric Calibration

Flux Standards for NICMOS Absolute Calibration

The absolute flux calibration of NICMOS will be calculated from observations of standard stars with known flux distributions $F(\lambda)$. The sensitivity as a function of wavelength for the dispersed spectra from the grisms is determined directly

from the known $F(\lambda)$ and the observed response, after any required corrections for flat field response. Sensitivities for the filters are calculated from observations of the standard stars according to the synthetic photometry procedure detailed in Koorneef *et al.* (1986). Since the pipeline calibration cannot utilize color information, the header of the reduced data will contain the calibration constant for the filter that specifies the equivalent flux for a constant spectral distribution as a function of wavelength. For convenience, this calibration constant appears twice, once in Jansky units and once in erg s^{-1} cm^{-2} Å^{-1} units. Color transformations could be defined for post-pipeline data analysis.

White Dwarf Absolute Standards

The flux distributions of our primary standard stars are defined by models for the four pure hydrogen white dwarfs in Table 15.3 (Bohlin, Colina, & Finley 1995). Bohlin (1996) transfers these calibrations to FOS and IUE data in the UV and to the optical spectra of Oke (1990) to obtain a set of standards with fluxes that are accurate to a few percent from 1150–9200Å. Observations of this set of standard stars produces consistent absolute flux calibrations on the WD scale for the current HST instrument complement. Currently, flux distributions to the limit of NICMOS coverage are only available for four WD (Table 15.3).

Table 15.3: WD Standard Stars

Star	K	Sp.T.	V	B-V
G191B2B	12.7	DAO	11.781	-0.33
GD71	13.8	DA1	13.032	-0.25
GD153	14.2	DA1	13.346	-0.27
HZ43	13.7	DA1	12.914	-0.31

Solar Analog Absolute Standards

In order to expand the set of IR standard stars in the appropriate flux range for NICMOS, M. Rieke, R. Thompson, and collaborators at the University of Arizona are making photometric observations of solar-analog stars, which will be used to normalize the solar spectrum to the observed IR magnitudes. This method consists of several steps:

1. The solar colors in the photometric system are determined by assuming that the average colors of the solar analogs are equal to those of the Sun (classified as a G2V star).

2. The zero point of the absolute flux density in each near-infrared photometric bandpass is calculated from the photometric magnitudes for the Sun and the absolute flux spectrum of the Sun.

3. The absolute solar flux density in each photometric band is scaled in proportion to the magnitude of the solar analog star relative to that of the Sun.

The final absolute flux accuracy achieved by the solar-analog method relies on two basic assumptions:

1. That the absolutely calibrated reference spectrum of the Sun is known with an uncertainty of a few percent (Colina, Bohlin, & Castelli 1996).

2. That the spectra of the solar-analogs are identical to the solar spectrum, i.e., agree within the 2% uncertainty in the shape of the flux distribution at infrared wavelengths.

The solar-analog method was used in the past to determine the absolute calibration of near-infrared photometry (Campins, Rieke, and Lebofsky, 1985) at ground-based observatories. The accuracy in the absolute calibration was at least 5%, and for some bands, 2% to 3% (Campins et al., 1985).

As a check on the solar analog method, the ground-based program includes observations of the WD G191B2B. Furthermore, FOS observations of three prime solar analog candidates listed in Table 15.4 were made during Cycle 6. The FOS red detector was used with the high resolution G780H, G570H, G400H and G270H to obtain high signal to noise spectra of these three candidates over the 2200 to 8500 angstroms range to verify agreement with the solar flux distribution. Additional STIS observations covering the 0.6–1.0 μm wavelength range will be obtained in Cycle 7.

Table 15.4: Prime Solar Analog Candidates

Star	V	K	E(B-V)	B-V	V-I	RA(1950)	DEC(1950)	No.[a]
P041-C	11.99	10.56	0.01	0.62	0.69	14:51:42.9	+71:55:26	4
P177-D	13.50	12.09	0.01	0.63	0.71	15:57:43.2	+47:45:07	5
P330-E	13.03	11.62	0.01	0.63	0.74	16:29:35.8	+30:15:09	5

a. No. indicates the number of observations in hand by the U. of Arizona group as of 96Feb22. For the Sun, B-V=0.633 (Taylor 1994), and V-I=0.703 (Bessell and Norris 1984).

Ground Based Calibrations

The existing near-infrared standard star lists used by ground-based telescopes are inadequate for NICMOS because they are too bright and there is a dearth of suitable observations to rule out low-level Near-IR variability for most stars. As we mentioned previously, to counter this problem, a large program of J, H, K photometry has been conducted by a team lead by Marcia Rieke of Steward Observatory. The star selection is based upon HST Guide Star Availability/Suitability Windows.

In the Northern Hemisphere observations have been performed with a NICMOS2 array on the Mt. Lemmon 60" & Kitt Peak 90" and in the Southern Hemisphere with a NICMOS3 array on the Las Campanas 40".

The primary goals of the program were:

• Relative flux references accurate to 1.5% for standard photometry.

• Color transformations between ground based and NICMOS systems.

• Relative absolute wavelength & spectrophotometric references for Grisms.

- Polarization standards.

Sample Selection

Solar analogs from HST Guide Star Photometric Survey (Lasker and Sturch) form the main flux references to bridge the gaps in atmospheric transmission. Solar analogs were chosen because:

- Dispersion in Near IR colors is very small in G-stars.

- Minimum number of strong spectral features in Near-IR.

- Solar spectrum available throughout range of NICMOS sensitivity.

References

- Bessell, M., and Norris, 1984, *ApJ*. 285, 622.

- Bohlin, R. C., 1996, *AJ*, 111, April.

- Bohlin, R. C., Colina, L., and Finley, D. S., 1995, *AJ*, 110, 1316.

- Campins, H., Rieke, G. H., and Levofsky, M. J., 1985, *AJ*, 90, 896.

- Colina, L., Bohlin, R. C., and Castelli, F., 1996, *AJ*, in press.

- Colina, L. & Bohlin, R.C. 1997 AJ 113, 1138

- Koornneef, J., Bohlin, R. C., Buser, R., Horne, K. D., and Turnshek, D. A. 1986, *Synthetic Photometry and the Calibration of the HST, Highlights in Astronomy*, Vol. 7, ed. J.-P. Swings (Reidel), p. 833; also Appendix 1 of Turnshek, D. A., Baum, W. A., Bohlin, R. C., Dolan, J. F., Horne, K. D., Koornneef, J., Oke, J. B., and Williamson, R. L. 1989, Standard Astronomical Sources for HST: 2. Optical Calibration Targets, STScI.

- Oke, J. B. 1990, *AJ*, 99, 1621.

- Taylor, 1994, *PASP*, 106, 444.

- Turnshek, D.A., Bohlin, R.C., Williamson R.L., Lupie, O.L. & Koornneef, J. 1990 AJ 99, 1243

- Whittet, D.C.B, Martin, P.G., Hough, J.H., Rouse, M.F., Bailey, J.A. & Axon, D.J. 1992 ApJ 386, 562

Glossary

The following terms and acronyms are used in this handbook.

A-D: Analog to digital.

CCD: Charge-coupled device. Solid-state, light detecting device.

CDBS: Calibration Data Base. System for maintaining reference files and tables used to calibrate HST observational datasets.

CIT: California Institute of Technology.

COBE: Cosmic Background Explorer.

COSTAR: Corrective Optics Space Telescope Axial Replacement.

CP: Call for Proposals.

CR: Cosmic ray.

CVZ: Continuous viewing zone.

DQ: Data quality.

DQE: Detector quantum efficiency.

DN: Data number.

ETC: Exposure Time Calculator.

FAQ: Frequently asked questions.

FGS: Fine Guidance Sensors.

FITS: Flexible Image Transport System. A generic IEEE- and NASA-defined standard used for storing image data.

FOC: Faint Object Camera.

FOM: Field Offset Mirror (or mechanism)

FOS: Faint Object Spectrograph.

FOV: Field of view.

FPA: Focal plane array.

FSW: Flight software.

FTP: File Transfer Protocol. Basic tool used to retrieve files from a remote system. Ask your system manager for information about using FTP.

FUV: Far ultraviolet.

FWHM: Full width at half maximum.

GASP: Guide Star Astrometric Support Program.

GEIS: Generic Edited Information Set. The multigroup format used by STSDAS for storing some HST image data.

GHRS: Goddard High-Resolution Spectrograph.

GO: General Observer.

GTO: Guaranteed Time Observer.

HSP: High-Speed Photometer.

HST: Hubble Space Telescope.

ICD: Interface control document. Defines data structures used between software or systems to ensure compatibility.

IDT: Instrument Development Team.

IR: Infrared.

IRAF: Image Reduction and Analysis System. The system on which STSDAS is built.

IUE: International Ultraviolet Explorer.

K: Degree Kelvin.

LSF: Line spread function.

MOS: Multi-object spectroscopy.

ND: Neutral density.

NICMOS: Near-Infrared Camera and Multi-Object Spectrograph.

NUV: Near ultraviolet.

OPUS: OSS and PODPS Unified Systems.

OSS: Observation Support System.

OTA: Optical Telescope Assembly.

PAM: Pupil Alignment Mirror (or mechanism).

PI: Principal investigator.

PODPS: Post-Observation Data Processing System.

PSF: Point spread function.

QE: Quantum efficiency.

RA: Right ascension.

rms: Root mean square.

SAM: Small angle motion.

SLTV: System level thermal vacuum (testing phase).

SMOV: Servicing Mission Orbital Verification.

S/N: Signal-to-noise ratio.

SSR: Solid state recorder.

ST-ECF: Space Telescope European Coordinating Facility.

STEIS: Space Telescope Electronic Information System. The World Wide Web host from which information, software, documentation, and other resources pertaining to the HST can be obtained.

STIS: Space Telescope Imaging Spectrograph.

STScI: Space Telescope Science Institute.

STSDAS: Space Telescope Science Data Analysis System. The complete suite of data analysis and calibration routines used to process HST data.

SV: Science verification. Process of taking observations that can be used for HST instrument calibration.

TAC: Telescope Allocation Committee.

TEC: Thermal electrically cooled.

URL: Uniform resource locator. Address for WWW.

UV: Ultraviolet.

VCS: Vapor cooled shield.

WF/PC: Wide Field/Planetary Camera.

WFPC2: Wide Field Planetary Camera-2. Replacement for WF/PC installed during first servicing mission of December 1993.

WWW: World Wide Web. Hypertext-oriented method for finding and retrieving information over the Internet.

YSO: Young stellar object.

Appendix

Bright Object Mode

The time taken to read through a quadrant on the array sets a fundamental limit on the fastest electron collection rate which can be achieved by resetting all the pixels. An inherent consequence of the methods of operating the NICMOS array detectors in the ACCUM, MULTIACCUM, and RAMP modes is therefore that there is a minimum possible exposure time, ~ 0.6 seconds (0.302 for MULTIACCUM), set by the time required to read the array. For a very bright object, such as the disk of Jupiter, the time between the reset of a pixel, and its final read is sufficiently long that the pixel saturates. Although the detector arrays are multiplexed by division into four quadrants, each pixel in a 128 x 128 pixel quadrant must be sampled in some order (note that there is no transfer of charge as is done in a CCD).

The solution adopted to this problem for NICMOS is the provision of a *bright object* mode which enables targets to be observed which are ~600 times brighter than is possible in the other modes without saturating. In BRIGHTOBJ mode, an ACCUM sequence of operations is performed on *one* pixel in each quadrant at a time. That is, the pixel is reset, read, integrated, and read again with the difference between the final and initial readouts being stored as the measured signal and the interval between the reads being the exposure time. This process is repeated sequentially for all pixels in each quadrant. Users can think of this as integrating on a single pixel at a time. The smallest integration time which can be used is 1.024 milliseconds. Figure 15.1 illustrates the operation of bright object mode. Initially the detector is reset and the first pixel (solid shading) in each quadrant is read. A reset is then made and the second pixel in each quadrant is read. The process continues until all 16,384 pixels in each quadrant have been read.

Figure 15.1: Bright Object Mode Operation
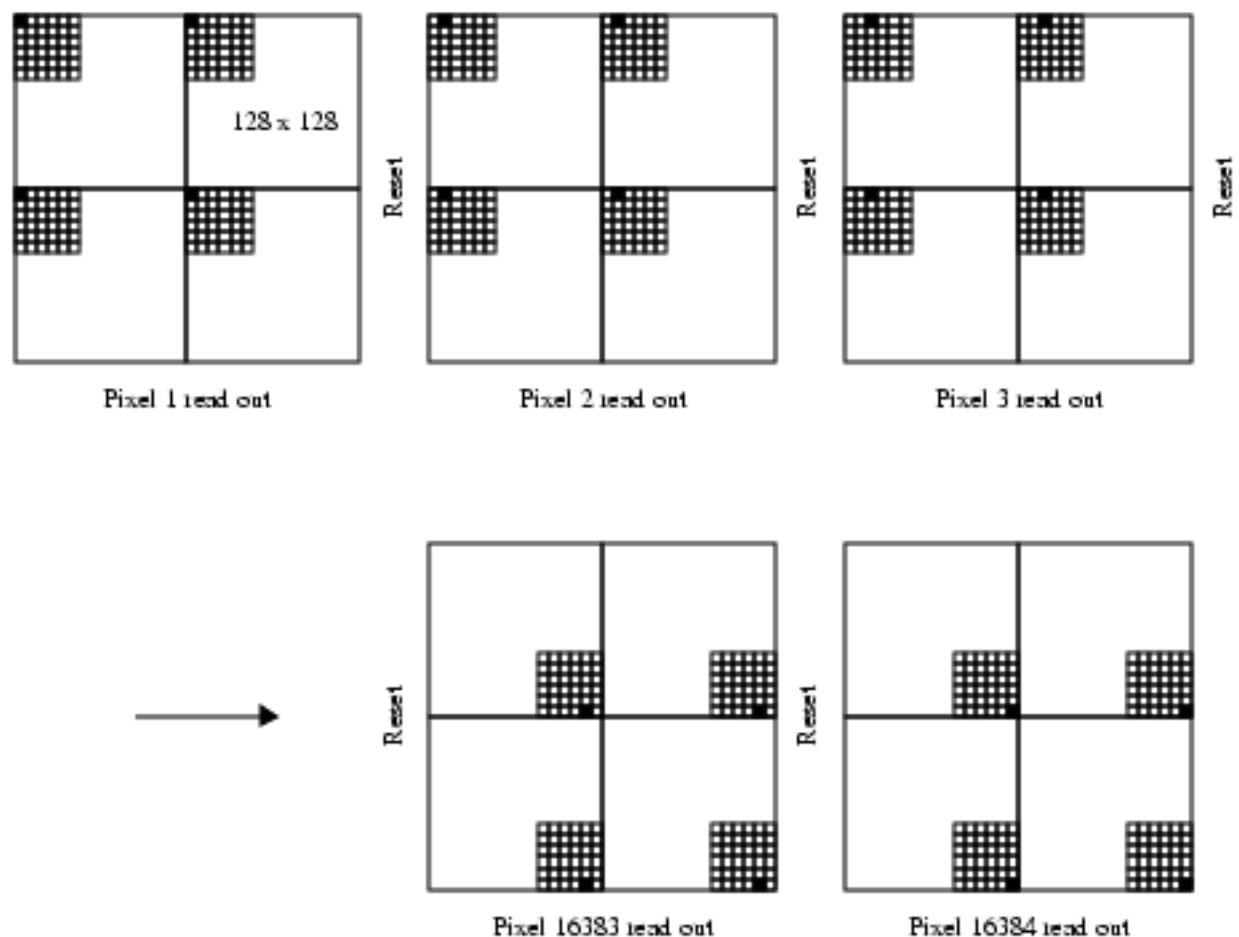
The time required to take a BRIGHTOBJ mode exposure can be rather long. Since photons are only collected in one pixel per quadrant at an time, the time associated with obtaining the frame is $0.206 + (EXPTIME \times 16384)$ where *EXPTIME* is the integration time per pixel (i.e. the observation time is approximately (128^2) x the exposure time). For example, if an integration time of 0.1 seconds is used to observe a bright target then the actual time required to complete the observation would be around 27 minutes! This means that allowing for acquisition time only two such exposures could be obtained in a single target visibility period. However, it is not always so serious. In the case of Jupiter for example the integration times required per pixel are only of the order of milliseconds and so the total integration time will only be around 20 seconds.

The longest exposure time which is possible in BRIGHTOBJ mode is 0.261 seconds, requiring 4278 seconds in total. Thus it is possible, in the worst case, for a single BRIGHTOBJ mode exposure to use more than an orbit. In general observers are strongly advised to consider the trade-off between relatively long BRIGHTOBJ mode exposures (which take the longest time) and short ACCUM

mode exposures (perhaps using a filter and camera combination with lower throughput).

One of the obvious uses of BRIGHTOBJ mode is for solar system targets. Due to the limitations of the Track 51 capability (linear tracking with orbital or planetary parallax correction) HST can only follow a moving target for 2048 seconds, of which 1980 seconds is available for an exposure. This therefore sets the longest integration time that is possible for a moving target in BRIGHTOBJ mode. Proposers will need to judge the real integration time and signal to noise ratio required for the observation time and adjust accordingly.

The advantage of this mode of operation is the ability to observe objects significantly brighter than the normal saturation limit of the detector.

The disadvantages are several:

- Due to the extremely large time penalties involved in this mode operation, *it cannot be used to accomplish time resolved observations on shorter time intervals than ACCUM mode.*

- Some observations will take a long time. BRIGHTOBJ mode exposures are therefore very sensitive to the quality of the pointing of HST. They should not be obtained using GYRO guiding mode. In addition, if the object changes (planetary rotation) or if the telescope pointing changes it will affect different parts of the image differently.

- The D.C. offset of the detector output is not removed in this mode of operation. In general, the signal is very high and the offset does not matter. In some cases it will and this can be a detriment to the signal accuracy.

- There is also no cosmic ray correction or saturation detection in this mode of operation. Although they are still susceptible to cosmic rays, events should be very rare as the integration time *per pixel* is very short.

Ramp Mode

The RAMP mode is an intrinsically different way of obtaining an image which can be thought of as an on-board hybrid between ACCUM and MULTIACCUM, providing a limited version of the advantages we described for MULTIACCUM with the simplicity of ACCUM, producing a single output image at the end of the exposure. RAMP mode is appropriate when high dynamic range or cosmic ray cleaned observations are required but the data volume is constrained. The basic ideas behind the RAMP mode are illustrated in Figure 7.4.

RAMP mode has not been tested on-orbit, and no plans exist for its validation. Given the proven capability of MULTIACCUM and the solid state recorder which effectively alleviates data rate concerns, RAMP is not believed to be useful.

Figure A.2: Basic Ramp-Mode for NSAMP = 6

Each readout is differenced ONBOARD with the previous readout and used to compute a running mean of the # of counts per sample interval, t, and an associated variance for each pixel.
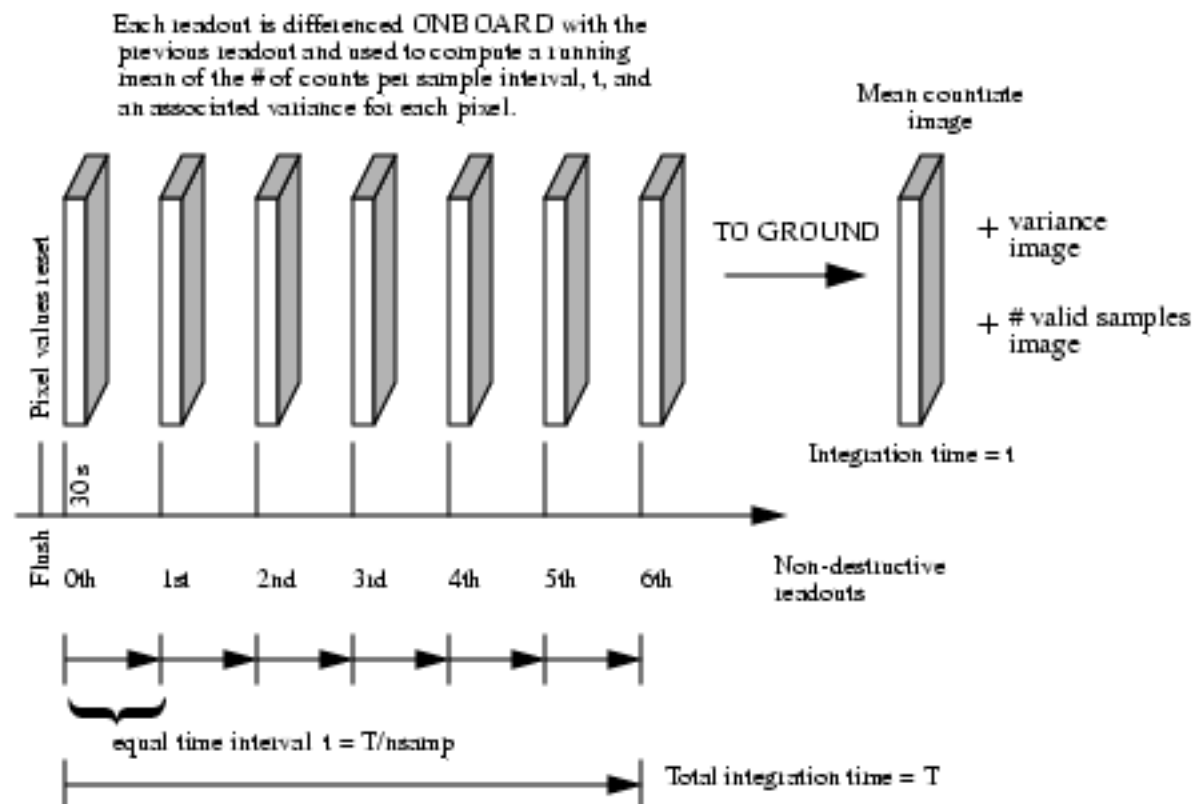
As in the case of the MULTIACCUM mode, in RAMP mode the initial detector readout, which obtains the initial pixel values, is followed by a number, NSAMP, of non-destructive readouts, up to a maximum of 254. Both the integration time T and the number of passes NSAMP are set by the observer in the proposal. Unlike the readouts of MULTIACCUM the intermediate readouts in RAMP mode must be at equal intervals during the exposure and are not individually downlinked to the ground. The integration time is the time between the initial non-destructive read of the first pixel and the last non-destructive read of the first pixel. If T is the total integration time the sub-reads occur at intervals of T/NSAMP. As illustrated in Figure 7.5. each of the ramp samples are formed by taking the difference between the cumulative signal recorded after the current read and that obtained at the previous read.

Figure A.3: The On-Board Ramp Mode Calculations

Each readout is differenced ONBOARD with the previous readout and used to compute a running mean of the # of counts per sample interval, t, and an associated variance for each pixel.

$$\bar{y} = \frac{1}{6} \sum_{i=1}^{6} y_i$$

TO GROUND

Mean countrate image

+ variance image

+ # valid samples image

Integration time = t

$y_1 = x_1 - x_0$ $y_2 = x_2 - x_1$ $y_3 = x_3 - x_2$ $y_4 = x_4 - x_3$ $y_5 = x_5 - x_4$ $y_6 = x_6 - x_5$

Pixel values reset

30 s

Flush

0th, x0   1st, x1   2nd, x2   3rd, x3   4th, x4   5th, x5   6th, x6

Non-destructive readouts

equal time interval t = T/nsamp

Total integration time = T
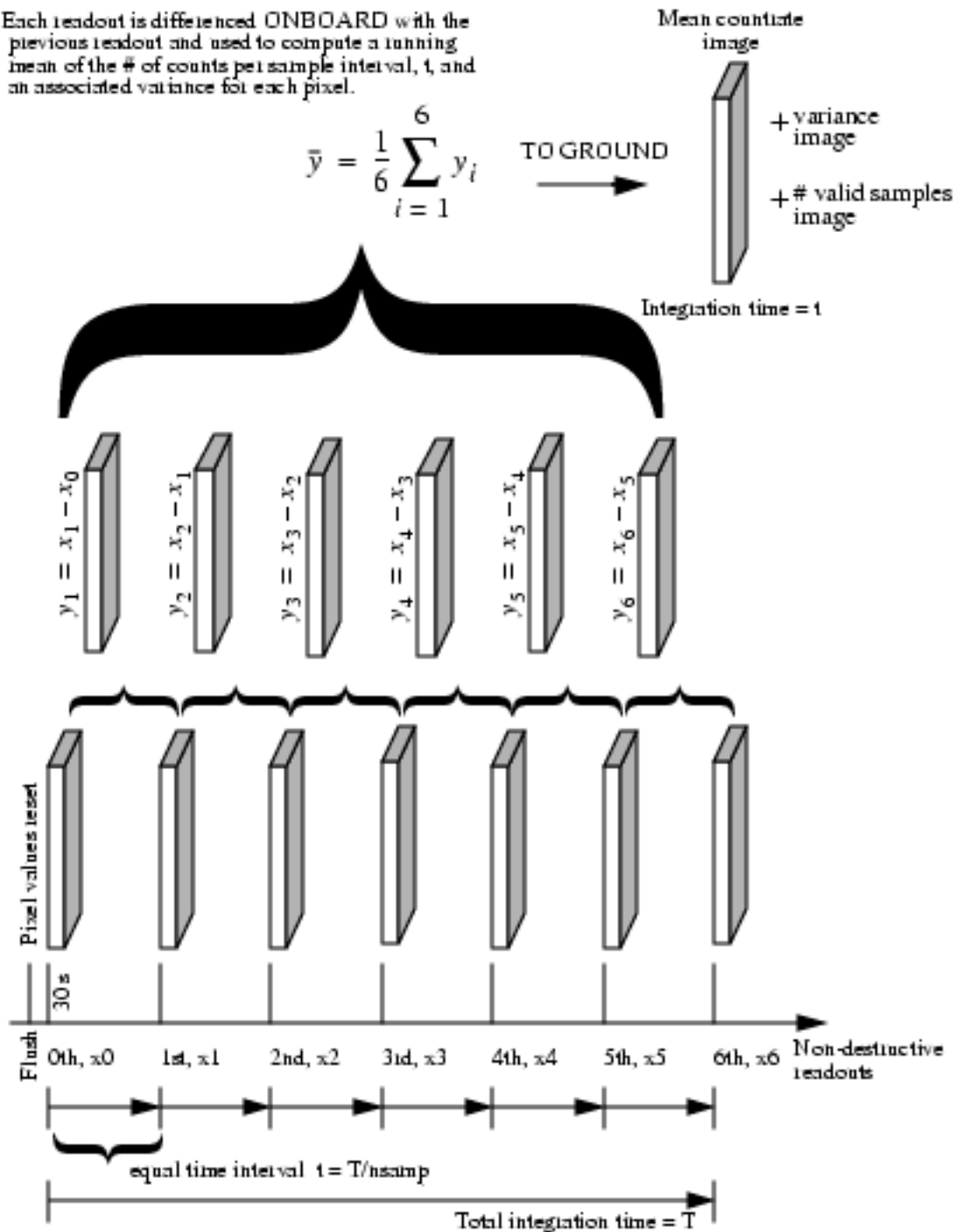
The time taken to perform the ramp calculation is ~7 seconds per camera and this sets the minimum time between successive ramp samples. Thus if 3 cameras are in use in ramp mode this restriction expands to > 21 seconds (there are other overheads involved). Ramp mode produces three data arrays; the image which contains the mean values of the slope or ramp of each pixel derived from the

difference images; the number of samples which were used to determine the slope, and the variance over all the samples used in the calculation of the image.[1]

The aware reader will have realized that if all the difference images are used to form this final mean the output of RAMP mode will be identical to that of an ACCUM for a time T/NSAMP. However, the great power of RAMP mode is that during the calculation of the slope it is also possible to detect pixel saturation and optionally cosmic rays, but not without penalties as we will explain shortly. A variety of ways of using this saturation and cosmic ray hit information are available to the user. The samples array becomes meaningful when one of these options is chosen.

Using Ramp Mode to Reject Cosmic Rays and Detect Saturation

Ramp mode provides processing mechanisms for the detection, and elimination of cosmic rays (CR) and for saturation detection. The optional parameter CR-ELIMINATION (see the proposal instructions) selects from four available processing modes for handling cosmic ray events. We have already described the first of these in which no action is taken, and the data returned is equivalent to a simple ACCUM exposure. Since the ramp mode computes a progressively updated variance at each sample cosmic ray events are detected by changes in slope which are more than 3σ away from the slope determined by the previous reads. The basic principles behind cosmic ray rejection are illustrated in Figure A.4 and Figure A.5.

In the CONTINUE method, which is the default setting, when a cosmic ray is detected at a given pixel the value from that ramp sample for that pixel is eliminated from the image and variance arrays. Other pixels are unaffected by the detection. The ramp sampling then continues until the end of the exposure, removing any subsequent suspect samples in the same way on a pixel-by-pixel basis.

In the RETAIN method when a cosmic ray is detected at a given pixel, processing for that pixel is suspended and the mean pixel and variance values obtained up to the sample in which the CR hit occurred are recorded and the number of valid samples is set to that before the hit occurred. As before, other pixels are unaffected by the detection. The ramp sampling continues processing these until either they also receive a CR hit, and are themselves suspended, or the end of the exposure is reached.

In The MARK method any pixel which receives a detected CR hit is flagged as bad (set = 0) in the data quality array, but the sample in which this occurred, and all subsequent samples, are still used in the variance and pixel value calculations.

---

1. The term *ramp* came from the original concept of performing an updating linear least-squares fit to the data, which was not implemented due to the limited computer power of the NICMOS computer. Over 20 seconds would be required to compute the LSQ-fit at each ramp step.

The user then has the responsibility for deciding what to do with suspect pixels during analysis.

Figure A.4 shows the ramp mode operation for an uncontaminated signal. In the top panel we see the cumulative counts with time. Marked is the time interval between ramp samples, t, and the signal associated with each ramp sample. The middle panel shows a plot of the signals measured in each of the ramp samples. Since there is no cosmic ray contamination, this is essentially a constant except for statistical fluctuations. The bottom panel shows how the data quality flag would have been evaluated for each ramp sample by the flight software. In this case all samples are good.

Figure A.4: Ramp Mode Operation for Uncontaminated Signal
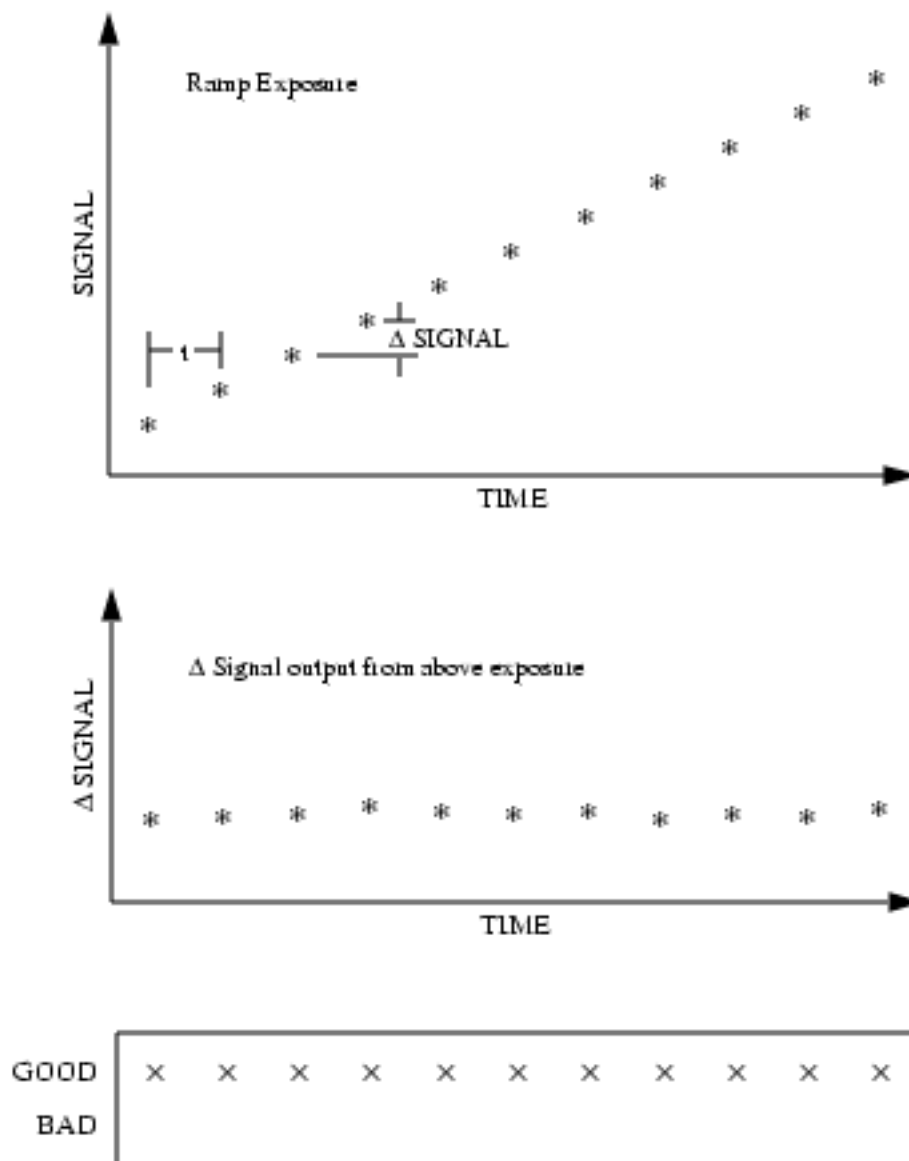
Figure A.5 shows ramp mode operation for a signal contaminated with cosmic rays. In the top panel we again see the cumulative counts with time. Two cosmic ray events are marked. The middle panel again shows a plot of the signals measured in each of the ramp samples. Notice that the samples effected by the cosmic rays are outliers from the trend we saw in Figure A.4. The bottom panel shows how the quality flag would have been evaluated for each ramp sample by the flight software. The two samples with cosmic ray hits have been identified as bad and are not used in the final calculation of the mean signal.

Figure A.5: Ramp Mode Operation for Signal Contaminated by Cosmic Rays
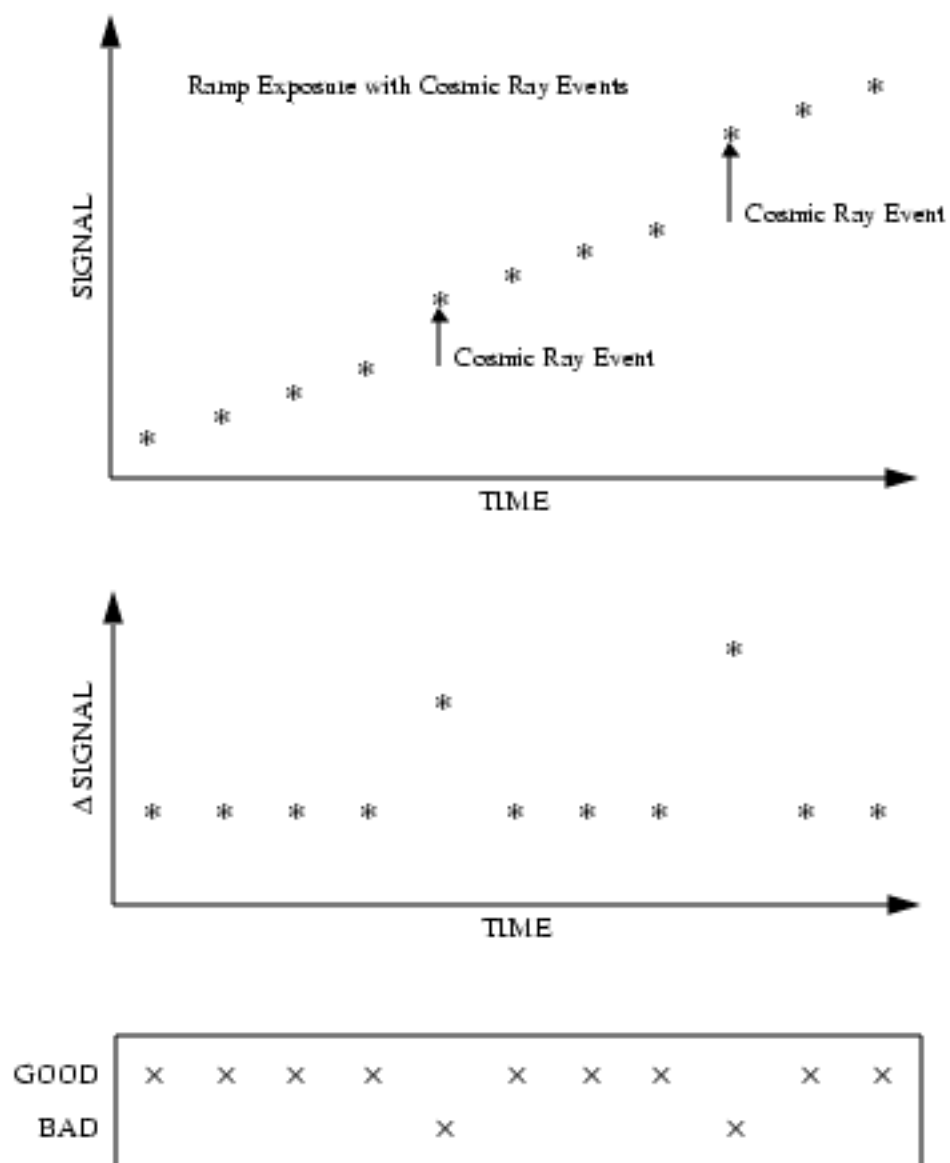
RAMP mode also discontinues the processing on a pixel once the signal in the pixel reaches a level in which the deviation from linearity is > 2%. As shown in Figure A.6, the result up to that time, and the number of samples which had been collected are stored and downlinked. This can be very useful in images where the expected flux levels are not well known and in serendipitous or survey observations. Figure A.6 shows ramp mode operation for a signal which reaches the saturation or nonlinear limit prior to the end of the exposure. In the top panel we again see the cumulative counts with time. The horizontal line marks the saturation or nonlinear threshold. The bottom panel shows how the quality flag would have been evaluated for each ramp sample by the flight software. All the samples which occur after the saturation limit have been identified as bad and are not used in the final calculation of the mean signal.

Figure A.6: Ramp Mode Operation for Signal Reaching Saturation Before Exposure End
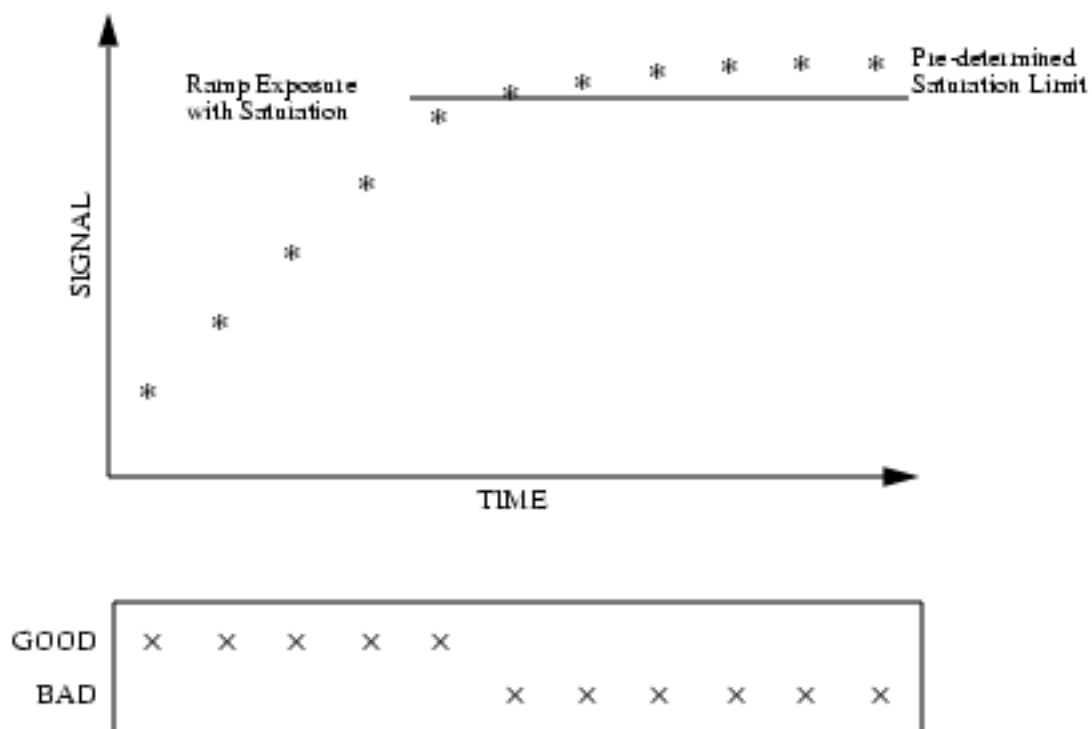
Saturation Detection does not rely on Δ SIGNAL.
Saturation Detection is *always* enabled for Ramp Exposures.
Only the GOOD values will be used to determine the final pixel value.

Limitations of Ramp Mode

Dark Current Removal

The real science data sits on a plateau of dark current which is a varying function of time since reset (the shading effect—see Chapter 7). As this dark current varies significantly, at least in the first minute, in order to update the mean and variance without bias its contribution has to be removed. Moreover, with either or both the *saturation* and *rejection* actions turned on, each pixel can essentially have a different integration time (number of valid samples). Since the ramp mode will return an output array without the dark current removed this has to be accounted for in the subsequent data reduction, either using an empirical correction or a model. How this model is implemented is therefore *crucial* to the functioning of the mode as a failure to treat it properly will invalidate ramp mode data for faint sources. At present it is not clear how well this can be done. One must ensure that sufficient ramp samples are obtained in order for the ramp calculations to be reliable. Ideally this should be a number > 30, but numbers as low as 16 or so might well suffice, if the frequency of cosmic ray hits on orbit is

not too high. Because the start of the ramp calculation has to be delayed for ~30 seconds to avoid the effects of shading ramp mode will not be useful for bright sources

Cosmic Ray ADU Distribution Function

In an automatic sigma clipping procedure a crucial parameter is the *threshold* at which the rejection occurs. If this is set too high then there can be many low level cosmic rays which are not removed. With the ramp mode data it will not be possible to remove them without interpolating over them. Even detected CR hits will potentially have *halos* of distributed charge around them which might still contaminate the data if the CR hits turn out to not be confined to single pixels. This is a significant disadvantage compared to MULTI-ACCUM mode. More seriously if it is set too low then the underlying statistical distribution of the real events is censored invalidating the basic assumptions implicit in standard error analysis. This difficulty has led statisticians to develop robust iterative techniques for such problems. However these are computationally expensive, and require all the data to be kept in memory, so that a dynamic adjustment of the rejection criteria can take place. On board HST, the timing restriction created by the limited computing power of the flight computers eliminate this as a practical possibility.

Cosmic Rays that Won't be Detected

Detection of cosmic rays (CR) in RAMP mode relies on discontinuities in the detected count rate for a pixel. However, three readouts are needed in order to make an estimate of the count rate. Cosmic ray hits before the fourth readout are therefore not detected. The first readout cannot occur earlier than 30 seconds into the integration, and the minimum time between readouts in RAMP mode is about 7 seconds. Therefore, the fourth readout cannot occur any sooner than 51 seconds into the integration. There is a significant probability that cosmic ray hits will occur during the first minute of an integration. These hits will not be detected or removed in RAMP mode (in MULTIACCUM, on the other hand, since all the readouts are accessible to the pipeline calibration software, cosmic rays can be detected at any stage during the integration).

Index